

**SYNTHESIS, STRUCTURE AND PROPERTIES  
OF ELECTROCHEMICALLY ACTIVE  
NANOCOMPOSITES**

**IL-SEOK KIM**

**Department of Materials Science and Engineering  
Carnegie Mellon University  
Pittsburgh PA 15213  
May 2003**

**Submitted to the Carnegie Institute of Technology in partial fulfillment  
of the requirements for the degree of Doctor of Philosophy  
in Materials Science and Engineering**

Report Documentation Page				Form Approved OMB No. 0704-0188	
Public reporting burden for the collection of information is estimated to average 1 hour per response, including the time for reviewing instructions, searching existing data sources, gathering and maintaining the data needed, and completing and reviewing the collection of information. Send comments regarding this burden estimate or any other aspect of this collection of information, including suggestions for reducing this burden, to Washington Headquarters Services, Directorate for Information Operations and Reports, 1215 Jefferson Davis Highway, Suite 1204, Arlington VA 22202-4302. Respondents should be aware that notwithstanding any other provision of law, no person shall be subject to a penalty for failing to comply with a collection of information if it does not display a currently valid OMB control number.					
1. REPORT DATE <b>01 MAY 2003</b>		2. REPORT TYPE <b>N/A</b>		3. DATES COVERED <b>-</b>	
4. TITLE AND SUBTITLE <b>Synthesis, Structure And Properties Of Electrochemically Active Nanocomposites</b>				5a. CONTRACT NUMBER	
				5b. GRANT NUMBER	
				5c. PROGRAM ELEMENT NUMBER	
6. AUTHOR(S)				5d. PROJECT NUMBER	
				5e. TASK NUMBER	
				5f. WORK UNIT NUMBER	
7. PERFORMING ORGANIZATION NAME(S) AND ADDRESS(ES) <b>Department of Materials Science and Engineering Carnegie Mellon University Pittsburgh PA 15213</b>				8. PERFORMING ORGANIZATION REPORT NUMBER	
9. SPONSORING/MONITORING AGENCY NAME(S) AND ADDRESS(ES)				10. SPONSOR/MONITOR'S ACRONYM(S)	
				11. SPONSOR/MONITOR'S REPORT NUMBER(S)	
12. DISTRIBUTION/AVAILABILITY STATEMENT <b>Approved for public release, distribution unlimited</b>					
13. SUPPLEMENTARY NOTES <b>The original document contains color images.</b>					
14. ABSTRACT					
15. SUBJECT TERMS					
16. SECURITY CLASSIFICATION OF:			17. LIMITATION OF ABSTRACT <b>UU</b>	18. NUMBER OF PAGES <b>225</b>	19a. NAME OF RESPONSIBLE PERSON
a. REPORT <b>unclassified</b>	b. ABSTRACT <b>unclassified</b>	c. THIS PAGE <b>unclassified</b>			

# Abstract

The need for miniaturization of high-speed and high-power devices to meet consumer demand for easy access and portability has placed stringent demands on the energy requirements. There is therefore a need for high-energy density lightweight energy storage systems to meet these challenging demands of portable devices. The Li-ion battery since its commercialization by Sony in 1990 is still the major choice of rechargeable energy source for portable consumer electronic devices such as camcorders, laptops and cellular phones. Since 1990 however, the materials systems used in Li-ion batteries have considerably matured. The area of cathodes has witnessed considerable research activity and a number of systems have been identified with potential capacities for use in high-energy systems. In the area of anodes however, graphite still appears to be the material of choice. There is therefore a need to identify alternative electrochemically active anode systems better than carbon that could be competitive with existing and advanced cathode systems of the future while at the same time meeting the challenges posed by high-energy devices.

Several metals are known to react with lithium to form useful anode materials exhibiting high capacity for Li-ion battery application. However, the cycle life of these materials is generally poor since the large volume changes ( $\cong 300\sim 600\%$ ) caused by the reaction of lithium with these metals inevitably leads to decrepitation, cracking and crumbling of the electrode. In order to overcome this problem, researchers have invoked the concept of 'active-inactive' composites, which can help to reduce or prevent mechanical damage caused by the ensuing volume expansion of the anode during electrochemical cycling. Most of the approaches studied involve generation of the 'active-inactive' composites after reaction with lithium and the inherent chemical and electrochemical stability of such systems is always questionable. In the present work, efforts have been made to directly synthesize directly nanocomposites comprising the active and inactive species. Such an approach promises better control of the electrochemical property since the thermodynamic and chemical stability of the system

is determined apriori, before synthesizing the nanocomposites. In this study, silicon and tin have been used as active components because of their high theoretical capacity of 4000 mAh/g, and 990 mAh/g, respectively. In order to generate the active-inactive nanocomposite, carbon and non-oxide ceramics have been studied as the primary inactive components.

High-energy mechanical milling (HEMM) and solution based soft-chemistry based approaches were chosen for synthesizing the tin/carbon, tin/titanium nitride and silicon/non-oxide nanocomposites because of the reasons described in the following. Tin metal is typically malleable at room temperature and mechanical milling of Sn to form nanosized particles is extremely difficult. Hence a chemical route has been employed to synthesize Sn/C and Sn/transition metal non-oxide nanocomposites. On the other hand, Si exhibiting high mechanical brittleness (Knoop hardness: 820 kg/mm<sup>2</sup>) can be easily pulverized into nanosized particles by mechanical milling. However, the generation of nanosized Si by chemical routes poses significant challenges. As a result, high-energy mechanical milling has been utilized to generate nanocomposites of Si/TiN, Si/TiB<sub>2</sub> and Si/SiC.

XRD results of the silicon based nanocomposite materials generated by HEMM show that the powders are composed of amorphous Si and nanocrystalline inactive phases. The electrodes prepared from Si-based nanocomposites exhibit a stable capacity in the range of 300~400mAh/g. The capacity of the nanocomposite electrodes is inversely proportional to the milling time, while the stability of the capacity is closely related to the duration of milling. Therefore, optimization of the milling time is very important to achieve high capacity and stability. The electrodes prepared by HEMM do not exhibit any change in the phases formed as well as the microstructure, indicating the structural stability of the nanocomposites. However the nanocomposites obtained from HEMM generally exhibit a loss in capacity after extended milling. Detailed systematic impedance analysis, electronic conductivity measurement and high-resolution electron microscopy studies have shown that the loss in capacity is caused by embedding of the extremely fine Si particles (10~20 nm) within the inactive matrices. This results in high charge-transfer resistances on the order of ~600 ohm thereby preventing the Li-ions from alloying and de-alloying with Si resulting in an inactive material.

Tin-based nanocomposites on the other hand, have been synthesized by pyrolyzing the precursors generated by the infiltration of organotin compounds such as tetraethyl tin into mechanically milled PS-resin. The Sn/C electrodes exhibit a promising initial discharge capacity of ~480mAh/g that lowers to a value of 460 mAh/g after 30 cycles. The nanocomposite consists of spherical nano-particles of tin (~200nm) dispersed in amorphous carbon particles determined by TEM analysis. Results of the studies so far have shown that Sn and Si-based nanocomposites appear to be quite promising anode systems for Li-ion application.

# **Table of Contents**

I.	<b>INTRODUCTION</b>	1
II.	<b>BACKGROUND</b>	6
2. 1.	Li-ion Batteries and its Components	6
1.	Rocking-Chair Cells	6
2.	Theoretical Capacity, Energy Density and Differential Capacity	7
3.	Design Consideration	10
4.	Materials for Li-ion Batteries	15
2. 2.	Active-Inactive Nanocomposite Anodes	28
1.	Materials Selection	30
2.	Synthetic Methods	40
III.	<b>OBJECTIVES</b>	57
3. 1.	Overall Objectives	57
3. 2.	Research Goals	57
1.	Synthesis of Nanocomposite Anode Materials	57
2.	Study of Electrochemical Properties	58
3.	Structural and Microstructural Analyses to Generate Improved Nanocomposites	59
IV.	<b>EXPERIMENTAL PROCEDURES</b>	60
4. 1.	Preparation of Nanocomposites	60
1.	High-energy Mechanical Milling (HEMM)	60
2.	Chemical Synthesis of Sn-based Nanocomposites	64
4. 2.	Characterization of Nanocomposites	70
4. 3.	Characterization of Electrodes	74
V.	<b>RESULTS AND DISCUSSION</b>	78
	<i><u>Part I. Nanocomposite Electrodes Synthesized using HEMM</u></i>	

5. 1. Silicon/Titanium Nitride Nanocomposites	78
1. Effect of Composition on the Nanocomposite	79
2. Effect of Milling Time on the Nanocomposite	84
3. Analyses of the Morphologies and the Microstructure of the As-Milled Powder and the Electrodes	89
5. 2. Silicon/Titanium Boride Nanocomposites	98
1. Effect of Milling Time on the Nanocomposite	98
2. Morphology and Phase Analyses	100
3. Effect of Premilling of TiB <sub>2</sub>	104
5. 3. Silicon/Silicon Carbide Nanocomposites	117
1. Phase Analysis of the As-milled Powders	117
2. Electrochemical Characteristics of Si/SiC Nanocomposites	120
3. Microstructural/Morphological Analysis of the Si/SiC Nanocomposites	126
5. 4. Study of the Inactivity of Nanocomposites Generated by Extended HEMM	130
1. Electrical Resistivity of Nanocomposites	133
2. Impedance Analyses of Nanocomposites	137
3. Chemical Stability of the Active-inactive Nanocomposites	145
4. High Resolution TEM (HR-TEM) Analyses	151
5. Addition of Particle Size Reducers	156
 <i><u>Part II. Sn-based Nanocomposite Electrodes obtained by Chemical Synthesis</u></i>	
5. 5. Sn/Non-oxide Nanocomposites	164
1. Sn/TiN Nanocomposites	164
2. Sn/C Nanocomposites	172
1) Tin (IV) Chloride + Poly(methacrylonitrile)	172
2) Sn/C Nanocomposites Derived from Alkyl tin + PS-resin	183
 VI. <b>CONCLUSIONS</b>	 206
1. Silicon/Titanium Nitride Nanocomposites	206

2. Silicon/Titanium Boride Nanocomposites	207
3. Silicon/Silicon Carbide Nanocomposites	208
4. Study of the Inactivity of Si after Extended Milling	208
5. Tin/Titanium Nitride Nanocomposites	209
6. Tin/Carbon Nanocomposites from Tin (IV) Chloride + Poly(methacrylonitrile)	209
7. Tin/Carbon Nanocomposites from Alkyl Tin compounds + PS-resin	210

## **Appendix A**

Hydrazide Sol-Gel Process: A Novel Approach for Synthesizing Nanostructured Titanium Nitride	211
---	-----

## **Appendix B**

Hydrazide Sol-gel Synthesis of Nanostructured Titanium Nitride: Precursor Chemistry and Phase Evolution	250
--	-----

## **Appendix C**

Synthesis of Nanocrystalline Sn by Hydrazide Sol-gel (HSG) Process	286
--	-----

## **Appendix D**

Electrochemical Impedance Spectroscopy (EIS)	293
--	-----



## **List of Figures**

Fig. 2-1. Schematic representation of a “rocking-chair” battery during the discharge process.

Fig. 2-2. The direction of propagation or transport of electron and ion during charge and discharge process.

Fig. 2-3. A typical polarization curve for a prototype electrochemical cell.

Fig. 2-4 Schematic representation of the relative energies of the electrolyte and the electrodes.

Fig. 2-5 The structure of lithiated graphite ( $\text{LiC}_6$ ). (a) A schematic drawing of the AA stacking of graphene layers, (b) In plane distribution of Li.

Fig. 2-6 (a) Specific gravimetric and (b) Volumetric capacity of several promising anode materials [78].

Fig. 2-7 Molar volumes change of anode materials before/after lithiation. The percentage increase in volume after full lithiation is shown respectively [78].

Fig. 2-8 A schematic model of the active-inactive nanocomposite and the morphological change occurring during lithium insertion.

Fig. 2-9 (a) Phase diagrams, and (b) Compositional dependence of the potential in Li-Si and Li-Sn systems.

Fig. 2-10 Crystal structures of the inactive matrix components. (a) TiN with NaCl structure, (b)  $\text{TiB}_2$  with  $\text{AlB}_2$  structure, and (c)  $\beta\text{-SiC}$  with ZnS structure, respectively [115].

Fig. 2-11 Differential capacity vs. cell potential curves of commercially obtained from non-oxide powders of (a) TiN, (b) TiB<sub>2</sub> and (c) SiC, respectively. (Current rate : 100 $\mu$ A/ cm<sup>2</sup>, Potential : 0.02~1.2 V)

Fig. 2-12 Schematic flow-chart illustrating the expected physical and structural changes possible during mechanical milling [125].

Fig. 2-13 Schematic atomic arrangement in nanocrystalline materials [124].

Fig. 2-14 Schematic illustration of the reactions and processes occurring during high-energy mechanical milling.

Fig. 4-1. A schematic flow chart of the HEMM process used for generating Si/TiN nanocomposites.

Fig. 4-2. Schematic flow chart of the HEMM process used for synthesizing Si/TiB<sub>2</sub> nanocomposites.

Fig. 4-3. A schematic flow chart of the HEMM process used for synthesizing Si/SiC nanocomposites.

Fig. 4-4. A schematic flow chart showing the chemical synthesis procedure used to obtain Sn/C or Sn/TiN nanocomposites.

Fig. 4-5. A schematic flow chart showing the chemical synthesis procedure used to obtain Sn/ nanocomposites from alkyl tin and PS-resin.

Fig. 4-6. Schematic cross-section of the prototype “hockey-puck” cell used for the characterization of the electrochemical response of the synthesized nanocomposites.

Fig. 4-7. Schematic cross-section of the “CR 2016” type coin cell used for the characterization of the electrochemical response.

Fig. 5-1 X-ray diffraction patterns of various compositions of Si/TiN nanocomposites obtained after milling for 18h (a) Si:TiN=1:1, (b) Si:TiN=1:1.5 and (c) Si:TiN=1:2, respectively.

Fig. 5-2 Capacity as a function of cycle number for the different Si/TiN nanocomposites obtained after milling for 18h, (a) Si:TiN=1:1, (b) Si:TiN=1:1.5 and (c) Si:TiN=1:2, respectively. (Current rate:  $250\mu\text{A}/\text{cm}^2$ , Potential: 0.02~1.2 V)

Fig. 5-3 Differential capacity vs. cell potential curves for the first twenty cycles of the different nanocomposites with a molar ratio of (a) Si:TiN=1:1 and (b) Si:TiN=1:1.5, and (c) Si:TiN=1:2 obtained after milling for 18 h. (Current rate:  $250\mu\text{A}/\text{cm}^2$ , Potential: 0.02~1.2 V)

Fig. 5-4 X-ray diffraction patterns of Si:TiN=1:2 composites obtained after milling for 6 h, 12 h and 18 h, respectively.

Fig. 5-5 Capacity as a function of cycle number for Si:TiN=1:2 nanocomposites obtained after milling for 6 h, 12 h and 18 h each. (Current rate:  $250\mu\text{A}/\text{cm}^2$ , Potential: 0.02~1.2 V)

Fig. 5-6 Differential capacity vs. cell potential curves for the first twenty cycles of the nanocomposite with Si:TiN = 1:2 molar ratio obtained after milling for (a) 12 h and (b) 6h. (Current rate:  $250\mu\text{A}/\text{cm}^2$ , Potential: 0.02~1.2 V)

Fig. 5-7 Cell potential vs. specific capacity curves for the first twenty cycles of the nanocomposite corresponding to Si:TiN = 1:2 molar ratio obtained after milling for 12 h. (Current rate:  $250\mu\text{A}/\text{cm}^2$ , Potential: 0.02~1.2 V)

Fig. 5-8 (a) SEM micrograph of the Si:TiN = 1:2 composite showing the nanocrystalline particles (100~300nm). Chemical map of (b) Ti and (c) Si, respectively, using EDX for the Si/TiN composite corresponding to Si:TiN = 1:2 molar ratio obtained after milling for 12 h. (Both images are taken at the same scale.)

Fig. 5-9 SEM micrographs of the electrode before and after 30 cycles fabricated from the Si/TiN composite corresponding to Si:TiN = 1:2 molar ratio obtained after milling for 12 h.

Fig. 5-10 XRD pattern collected on the electrode after 30 cycles prepared with the Si/TiN composite corresponding to Si:TiN = 1:2 molar ratio obtained after milling for 12 h.

Fig. 5-11 TEM micrographs of the Si/TiN nanocomposite containing 33 mol% Si obtained after milling for 12 h; (a) BF image, (b) DF image, and (c) SA diffraction pattern (camera length = 66cm, reduced to 30% of its original size).

Fig. 5-12 (a) HRTEM micrographs of the Si/TiN nanocomposite containing 33 mol% Si obtained after milling for 12 h, (b) Elemental map of Si, (c) Elemental map of Ti, which are analyzed by electron energy-loss spectroscopy (EELS). (The arrows represent the same position.)

Fig. 5-13 X-ray diffraction patterns of Si:TiB<sub>2</sub>=1:2 composites obtained after milling for 6 h.

Fig. 5-14 Capacity as a function of cycle number for Si/TiB<sub>2</sub> nanocomposites containing 40 mol% Si obtained after milling for 10 h, 15 h, 20h and 25 h each. (Current rate: 100 $\mu$ A/ cm<sup>2</sup>, Potential: 0.02~1.2 V)

Fig. 5-15 Differential capacity vs. cell potential curves for the first fifteen cycles of the nanocomposite containing Si:TiB<sub>2</sub> = 2:3 molar ratio (40 mol % Si) obtained after milling for (a) 10 h , (b) 15 h, (c) 20 h and (b) 25 h, respectively. (Current rate: 100 $\mu$ A/ cm<sup>2</sup>, Potential: 0.02~1.2 V)

Fig. 5-16 (a) SEM micrograph of the Si:TiB<sub>2</sub> = 2:3 composite obtained after milling for 20h. Chemical map of (b) Si and (c) Ti, respectively, using EDX. (All images are taken at the same scale as shown in (a).)

Fig. 5-17 HR-TEM micrographs of the electrode prepared with the Si/TiB<sub>2</sub> composite corresponding to Si:TiB<sub>2</sub> = 2:3 molar ratio obtained after milling for 20 h (a) bright field image, (b) dark field image, (c) bright field image taken at a higher magnification, and (d) SADP (CL=66 cm) showing nanocrystalline TiB<sub>2</sub>.

Fig. 5-18 SEM micrographs of the electrode (a) before and (b) after 20 cycles, comprising Si/TiB<sub>2</sub> nanocomposite corresponding to Si:TiB<sub>2</sub> = 2:3 molar ratio obtained after milling for 20 h.

Fig. 5-19 XRD pattern of the electrode before and after 20 cycles prepared with the composite corresponding to Si:TiB<sub>2</sub> = 2:3 molar ratio obtained after milling for 20 h.

Fig. 5-20 Long scan (scan step: 0.013°, dwell time:50 sec) XRD patterns corresponding to commercial and premilled TiB<sub>2</sub> powders. The  $B$  values (the peak width at  $I_{max}/2$ ) are marked. (a) commercial, (b) premilled for 12h, (c) 18h and (d) 24h, respectively.

Fig. 5-21 Capacity as a function of cycle number for Si/TiB<sub>2</sub> nanocomposites with a molar ratio 1:2 obtained after milling for 10h. TiB<sub>2</sub> used was pre-milled for 12h, 18h and 24h respectively. (Current rate: 100 $\mu$ A/ cm<sup>2</sup>, Potential: 0.02~1.2 V)

Fig. 5-22 Differential capacity vs. cell potential curves for the first twenty cycles of the nanocomposite containing Si:TiB<sub>2</sub> = 1:2 molar ratio obtained after milling for 10 h using TiB<sub>2</sub> premilled for (a) 24 h, (b) 12 h and (c) 18 h. (Current rate: 100 $\mu$ A/ cm<sup>2</sup>, Potential: 0.02~1.2 V)

Fig. 5-23 X-ray diffraction patterns of powders milled for 24h using HEMM (a) Si:SiC = 1:2, (b) Si:C = 3:2.

Fig. 5-24 Binary phase diagram of Si-C system [6].

Fig. 5-25 Capacity as a function of cycle number for Si/SiC nanocomposites obtained after milling (a) Si and SiC using the molar ratio of Si:SiC=1:2, (b) Si and C using the molar ratio of Si:C=3:2. (Current rate: 100 $\mu$ A/ cm<sup>2</sup>, Potential: 0.02~1.2 V)

Fig 5-26 The differential capacity plots of the nanocomposites prepared from Si:SiC=1:2 obtained after milling for (a) 20 h, (b) 25 h and (c) 30h. The differential capacity plots obtained from Si:C=3:2 obtained after milling for (d) 12 h and (e) 24 h. (Current rate: 100 $\mu$ A/ cm<sup>2</sup>, Potential: 0.02~1.2 V)

Fig. 5-27 TEM micrographs of the Si/SiC nanocomposite obtained after milling Si and C in the molar ratio (Si:C=3:2) for 24 h; (a) BF image, (b) DF image, (c) BF image at a lower magnification, and (d) SA diffraction pattern (camera length = 66cm, reduced to 70% of its original size).

Fig. 5-28 (a) HRTEM micrographs of the Si/SiC nanocomposite obtained after milling Si and C in the molar ratio (Si:C=3:2) for 24 h, (b) Elemental map of carbon, which are analyzed by electron energy-loss spectroscopy (EELS).

Fig. 5-29 Capacity as a function of cycle number for commercial amorphous and crystalline silicon. Note the first discharge capacity of both samples is similar. (Current rate:  $250\mu\text{A}/\text{cm}^2$ , Potential: 0.02~1.2 V)

Fig. 5-30 Schematic drawing of the four point probe layout used for bulk resistivity measurement.

Fig. 5-31 The resistivity of the Si:TiN=1:2 nanocomposites obtained after milling for 4, 6, 9 and 18 h, respectively.

Fig. 5-32 Capacity as a function of cycle number for Si/TiN nanocomposites containing 33 mol% Si obtained after milling for 6 h and 9 h each. (Current rate:  $100\mu\text{A}/\text{cm}^2$ , Potential: 0.02~1.2 V)

Fig. 5-33 Impedance spectra collected at different discharge voltages on the Si/TiN (Si:TiN=1:2) nanocomposite electrode obtained after milling for (a) 6h, (b) 9h respectively, during the first discharge process.

Fig. 5-34 Equivalent circuit used for the interpretation of the Si/TiN nanocomposite electrodes. ( $R_{\Omega}$ : ohmic resistance,  $R_{ct}$ : charge transfer resistance, CPE: constant phase element,  $Z_w$ : Warburg impedance and  $f$ : frequency).

Fig. 5-35 The plots of (a) Charge transfer resistance ( $R_{ct}$ ) vs. discharge potential, (b) Double layer capacitance vs. discharge potential, and (c)

Diffusion coefficient of  $\text{Li}^+$  ions vs. discharge potential of the Si/TiN (Si:TiN=1:2) electrodes obtained after milling for 6 h and 9 h, respectively.

Fig. 5-36 XRD spectrum obtained from the TiN thin film obtained after sputtering from Ti target in Nitrogen atmosphere. Note crystallographic data of TiN is shown with bars.

Fig. 5-37 SEM micrograph showing the Sn-TiN interface. Note the formation of Sn droplets with contour angle of  $137.2^\circ$  indicating the non-wetting of Sn on TiN.

Fig. 5-38 XRD analysis result obtained from the heat-treatment of Si and TiN mixture at  $1500^\circ\text{C}$  for 5 h in UHP-Ar.

Fig. 5-39 (a) and (c) HRTEM micrographs of the Si/TiN nanocomposite containing 33 mol% Si obtained after milling for 9 h, (b) EELS elemental map of Si obtained from (a), (d) EELS elemental map of Ti obtained from (c). (The arrows represent the same position in (a) and (b), (c) and (d), respectively.)

Fig. 5-40 HRTEM micrographs of the interface between nanocrystalline TiN and amorphous Si, taken from the Si/TiN nanocomposite containing 33 mol% Si obtained after milling for 9 h.

Fig. 5-41 Capacity as a function of cycle number for Si/TiN nanocomposites obtained after milling for 12 h using Si:TiN=1:2 mixture. (Current rate:  $100\mu\text{A}/\text{cm}^2$ , Potential: 0.02~1.2 V)

Fig 5-42 The differential capacity plots of the nanocomposites prepared from Si:TiN=1:2 obtained after milling for 12 h using a particle size reducer



corresponding to (a) 0 wt.% NaCl and (b) 5 wt% NaCl. (Current rate:  $100\mu\text{A}/\text{cm}^2$ , Potential: 0.02~1.2 V)

Fig. 5-43 Capacity as a function of cycle number for Si/SiC nanocomposites obtained after milling 24 h using Si:C=3:2 mixture. (Current rate:  $100\mu\text{A}/\text{cm}^2$ , Potential: 0.02~1.2 V)

Fig 5-44 The differential capacity plots of the nanocomposites prepared from Si:C=3:2 obtained after milling for 24 h using a particle size reducer of (a) 0 wt% NaI, (b) 5 wt% NaI and (b) 10 wt% NaI. (Current rate:  $100\mu\text{A}/\text{cm}^2$ , Potential: 0.02~1.2 V)

Fig. 5-45 Capacity as a function of cycle number for Sn/TiN nanocomposites corresponding to (a) SnTiN = 1:2 and (b) Sn:TiN = 1:1 obtained after heat treatment for 5 h in UHP-Ar at 800 and 1000°C, respectively. (Current rate :  $100\mu\text{A}/\text{cm}^2$ , Potential : 0.02~1.2 V)

Fig. 5-46 X-ray diffraction patterns of Sn/TiN nanocomposites corresponding to Sn:TiN = 2:1 obtained after heat treatment for 5 h in UHP-Ar at (a) 800 and (b) 1000 °C, respectively.

Fig. 5-47 Capacity as a function of cycle number for Sn/TiN nanocomposites obtained after heat treatment for 5 h in UHP-Ar at 800 and 1000°C, respectively. The first irreversible loss of each nanocomposite is shown in the box. (Current rate :  $100\mu\text{A}/\text{cm}^2$ , Potential : 0.02~1.2 V)

Fig. 5-48 Differential capacity vs. cell potential curves of the Sn/TiN nanocomposites obtained after heat treatment for 5 h in UHP-Ar at (a) 800 and (c) 1000°C, respectively. (Current rate :  $100\mu\text{A}/\text{cm}^2$ , Potential : 0.02~1.2 V)

Fig. 5-49 A schematic representation of the processes involved in the formation of Sn/C nanocomposite using the chemical approach.

Fig. 5-50 The TGA/DTA analyses of the (a) polymethacrylonitrile and (b) as-prepared precursor showing the formation of C and Sn/C nanocomposites, respectively.

Fig. 5-51 X-ray diffraction patterns of Sn/C nanocomposites obtained after heat treatment for 5 h each in UHP-Ar at (a) 400, (b) 600 and (c) 800°C, respectively.

Fig. 5-52 Capacity as a function of cycle number for Sn/C nanocomposites obtained after heat treatment for 5 h each in UHP-Ar at 400, 600 and 800°C, respectively. The first irreversible loss of each nanocomposite electrode is shown in the box. (Current rate :  $100\mu\text{A}/\text{cm}^2$ , Potential : 0.02~1.2 V)

Fig. 5-53 Differential capacity vs. cell potential curves of the Sn/C nanocomposites obtained after heat treatment for 5 h each in UHP-Ar at (a) 400, (b) 600 and (c) 800°C, respectively. (Current rate :  $100\mu\text{A}/\text{cm}^2$ , Potential : 0.02~1.2 V)

Fig. 5-54 Schematic structure of PS-resin cross-linked by divinylbenzene.

Fig. 5-55 The TGA analysis of the PS-resin in UHP-Ar showing the formation of carbon.

Fig. 5-56 Capacity as a function of cycle number for Sn/C nanocomposites obtained from (a)  $\text{Sn}_2\text{Cl}_4 \cdot 5\text{H}_2\text{O}$  + PS-resin beads and (b) corresponding differential capacity plot; (c)  $\text{Sn}_2\text{Cl}_4 \cdot 5\text{H}_2\text{O}$  + mechanically milled PS-resin powder and (d) corresponding differential capacity plot, respectively. Both

nanocomposites were obtained after heat treatment for 5 h in UHP-Ar at 800°C. (Current rate : 100 $\mu$ A/ cm<sup>2</sup>, Potential : 0.02~1.2 V)

Fig. 5-57 SEM micrographs showing pores in (a) PS-resin beads and (b) mechanically milled PS-resin powder. Note the density of pores is higher in the case of PS-resin powder obtained after mechanical milling for 30 min.

Fig. 5-58 Capacity as a function of cycle number for Sn/C nanocomposites corresponding to a Sn:C =1:1 composition obtained from mechanically milled PS-resin powder infiltrated with (a) tetramethyl tin, (b) tetraethyl tin, and (c) tetra-n-octyl tin, respectively, followed by pyrolysis for 5 h in UHP-Ar at 600°C. The insets show the differential capacity vs. cell potential plots for each of the nanocomposites. (Current rate : 100 $\mu$ A/ cm<sup>2</sup>, Potential : 0.02~1.2 V)

Fig. 5-59 The TGA analysis of the precursor obtained from PS-resin infiltrated with tetraethyl tin corresponding to the composition of Sn:C=1:1 in UHP-Ar using a heating rate of 10°C/min.

Fig. 5-60 X-ray diffraction pattern of Sn/C nanocomposite obtained from PS-resin infiltrated with tetraethyl tin corresponding to a composition of Sn:C=1:1, after heat treatment for 5 h in UHP-Ar at 600 °C.

Fig. 5-61 TEM micrographs of the Sn/C nanocomposite obtained from PS-resin infiltrated with tetraethyl tin corresponding to a composition of Sn:C=1:1 after heat treatment for 5 h in UHP-Ar at 600 °C; (a) BF image, (b) SA diffraction pattern (camera length = 61cm, reduced to 40% of its original size).

Fig. 5-62 (a) Plots of capacity as a function of cycle number, (b) Differential capacity vs. cell potential curves obtained from the PS-resin infiltrated with

tetraethyl tin corresponding to the composition of Sn:C=1:1 after heat treatment for 5 h in UHP-Ar at 600 °C. (Current rate : 100 $\mu$ A/ cm<sup>2</sup>, Potential : 0.02~1.2 V)

Fig. 5-63 (a) Plot of capacity as a function of cycle number (b) Differential capacity vs. cell potential curves obtained from the carbon obtained after heat-treatment of PS-resin at 600°C for 5h in Ar. (Current rate : 100 $\mu$ A/ cm<sup>2</sup>, Potential : 0.02~1.2 V).

## **List of Tables**

Table 2-1 Examples of practical electrolyte used in Li-ion batteries [29].

Table 2-2 Ionic conductivity of lithium oxide-based glasses with various compositions [2].

Table 2-3 Ionic conductivity of various electrolyte membranes at room temperature. [58].

Table 2-4 Examples of active-inactive composite anodes studied in the literature.

Table 2-5 Crystal Structures and volumes per atom of Li-Sn and Li-Si systems [88].

Table 2-6 Electronic and mechanical properties of active and inactive components used for this study [114, 117-122].

Table 5-1 Results of EDX analysis of the nanocomposite corresponding to a molar composition Si:TiN=1:2 obtained after milling for 12h. (All quantities are given in atomic percentages.)

Table 5-2 Approximate crystallite size of the premilled TiB<sub>2</sub> particles obtained after milling for 12h, 18h and 20h, respectively, calculated using the Scherrer formula.

# *Chapter 1*

## **Introduction**

Li-ion batteries are the state-of-the-art power sources for consumer electronic devices because of their high volumetric and gravimetric capacities. However while considerable research efforts have been focused on cathode systems, anodes materials remain relatively unexplored. Graphite has been the customary anode material for lithium ion batteries with a theoretical capacity of 372 mAh/g or volumetric capacity of 830 Ah/L [1]. During the last few years however, there has been a surge of activity focused at identifying alternative anode materials due to an incessant demand for high capacity energy sources desired for a number of wireless cellular phones and consumer portable electronic devices.

While graphite has been the anode of choice, metals have been studied as anodes since 1970 [2-4] because of its higher capacity than graphitic materials. Among the metals, which form Li-alloys, Sn and Si are well known since both electrochemically react with up to 4.4 atoms of Li each Si or Sn atom generating a capacity of 4000 and 990 mAh/g, respectively [5]. However, a major problem with lithium alloys as anodes is the very large change in volume during charge/discharge resulting in cracking or crumbling of the anodes causing loss in capacity during cycling. A number of studies have been conducted to overcome this problem. Most recent developments to date include fabrication of nanocomposites of intermetallics, comprising electrochemically ‘active-inactive’ phases. The discovery of tin oxide glass nanocomposites actually set the trend for this strategy [6-15]. The tin-oxide based glass composite was first invented by researchers in Fuji [16], which appears to solve the problems related to the cyclability. Research in our group has also demonstrated the potential of sol-gel derived doped tin oxide-based glass composites [17]. However, the

tin oxide-based anodes have a large irreversible capacity on the order of 55~60 % resulting from the electrochemical reduction reaction of Li with oxygen bonded to Sn. Because of the irreversible capacity loss, oxide-based materials have not been pursued actively for use as anodes in Li-ion batteries [7]. In order to preserve and stabilize the original morphological state of the anode and thereby attain good electrochemical properties, various material systems other than oxide-based composites have been analyzed to minimize the mechanical stress induced by the large ensuing volumetric changes undergone by the active phase. Most of the current studies on anode materials other than carbon have focused on creating a composite microstructure comprising an inactive host matrix containing a finely dispersed active phase. It has been shown that a nanocrystalline state helps to preserve the crystallographic stability minimizing the drastic effects of the large volume changes probably due to the reduced density of atoms in a nanosized grain [18]. Dahn et al. have reported Sn-Fe-C based nanocomposite systems, and Thackeray et al. have studied the  $\text{Cu}_6\text{Sn}_5$  and InSb systems for anode applications [5, 8-11]. Similarly, SnSb-based systems have also been investigated [12]. All of these systems are based on the concepts and employing a strategy analogous to tin oxide glasses, and the electrochemically active phase is generated after electrochemical insertion of lithium. Although these systems are promising, there are problems related to either capacity or cyclability. The chemical and electrochemical stability are also difficult to control in these systems. As a result, there is a need for further improving the demonstrated concept of ‘active-inactive’ composites.

Our research has been focused on directly synthesizing ‘active-inactive’ nanocomposites containing Sn and Si as active components due to their high capacities. Regarding inactive components, carbon and non-oxide ceramics have been chosen to attain the nanocomposite structure. The chapter on results is therefore divided into two parts according to the synthetic approaches. The first part describes the synthesis of Si nanocomposite using high-energy mechanical milling (HEMM). Si is relatively brittle compared to Sn, which makes HEMM appropriate to generate the desired nanocomposite structure. HEMM process has several advantages such as homogeneous nanoscale mixing, economy of the process and the ability to easily scale-up for large-scale production [19]. The details regarding the mechanisms involved, the preparation of the precursors as well as the techniques used for obtaining nanocomposites will be

## ***Chapter 1. Introduction***

described later. In addition, phase and microstructure analyses, and their combined influence on the electrochemical properties will also be outlined. The second part describes the synthesis of Sn/C nanocomposite prepared by chemical approaches. The major problem with the generation of Sn nanocomposite by milling is that it is very difficult to make nano-sized Sn particles due to its malleable nature [20, 21]. On the other hand, it is difficult to design chemical approaches to generate nanosized Sn in an inactive matrix. The difficulty arises from the need for high temperature treatments to generate any of the non-oxide inactive phases. These temperature which tend to be higher than the melting point of Sn inevitably lead to coarsening and growth of Sn crystallites. As a result the advantages of the nanocrystalline structure will be lost. A detailed study of the reactions and the results of the electrochemical tests along with phase and microstructure analyses will also be presented.

The main goal of the present study is to develop active-inactive nanocomposite anodes exhibiting capacities higher than carbon. Accordingly, there are several challenging scientific issues that need to be addressed. The first issue is the synthesis of nanocomposite containing Si or Sn by HEMM and chemical approaches, respectively and their structural analyses using primarily X-ray diffraction (XRD). A second issue is the imperative need to study experimental factors such as starting compositions of active and inactive components, duration of processing time, etc. The morphology and microstructure have been studied using scanning electron microscopy (SEM) equipped with energy dispersive X-ray analysis (EDX) and, conventional and high-resolution transmission electron microscopy (TEM & HR-TEM) coupled with electron energy loss spectroscopy (EELS). Finally, the study addresses the major issue of evaluating the electrochemical property of all the synthesized composites. A systematic analysis has therefore been conducted to study the electrochemical performance of all the resultant nanocomposites. Results of these studies are presented and discussed further in detail in the subsequent chapters.



**References**

1. R. A. Huggins, Solid State Ionics, 113-115, 57-67 (1998).
2. M. Winter and J. O. Besenhard, Electrochim. Acta, 45, 31 (1999).
3. Sanyo Electric, US Patent No. 4,820,599, 1989.
4. B. A. Boukamp, G. C. Lesh, R. A. Huggins, J. Electrochem. Soc., 128, 725 (1981).
5. O. Mao and J. R. Dahn, J. Electrochem. Soc., 146, 405 (1999).
6. I. A. Courtney, W. R. McKinnon and J. R. Dahn, J. Electrochem. Soc., 146, 59 (1999).
7. O. Mao, R. L. Turner, I. A. Courtney, B. D. Fredericksen, M. I. Buckett, L. J. Krause and J. R. Dahn, Electrochemic. Solid-State Lett., 2, 3 (1999).
8. O. Mao and J. R. Dahn, J. Electrochem. Soc., 146, 414 (1999).
9. O. Mao and J. R. Dahn, J. Electrochem. Soc., 146, 423 (1999).
10. K. D. Kepler, J. T. Vaughey and M. M. Thackeray, Electrochemic. Solid-State Lett., 2, 307 (1999).
11. J. T. Vaughey, J. O'Hara and M. M. Thackeray, Electrochemic. Solid-State Lett., 3, 13 (2000).
12. J. Yang, , M. Wachtler, M. Winters and J. O. Besenhard, Electrochemic. Solid-State Lett., 2, 161 (1999).
13. G. M. Ehrlich, C. Durand, X. Chen, T. A. Hugener, F. Spiess and S. L. Suib, J. Electrochem. Soc., 147, 886 (2000).
14. H. Kim, J. Choi, H. Sohn and T. Kang, J. Electrochem. Soc., 146 4401 (1999).
15. H. Kim, B. Park, H. Sohn and T. Kang, J. Power Sources, 90, 59 (2000).
16. Y. Idota, T. Kubota, A. Matsufuji, Y. Maekawa and T. Miyasaka, Science, 276, 1395 (1997).
17. J. Y. Kim, D. E. King, P. N. Kumta and G. E. Blomgren, J. Electrochem. Soc., 147, 4411 (2000).
18. L. Y. Beaulieu, D. Larcher, R. A. Dunlap, and J. R. Dahn, J. Electrochem. Soc., 147, 3206 (2000).
19. K C. Suryanarayana, Prog. Mater. Sci., 46, 1 (2001).

## ***Chapter 1. Introduction***

20. B. Yeung and J. Jang, Mater. Sci. Lett., 21, 723 (2002).
21. F. Vnuk, M. Sahoo, D. Baragar and R. W. Smith, J. Mater. Sci., 15, 2573 (1980).

## Chapter 2

# Background

## 2.1 Li-ion Batteries and its Components

Rechargeable batteries with high energy density have been studied recently as energy sources for various compact portable electronic devices, hybrid motor vehicles, etc. Furthermore, Li-ion batteries are considered to be most promising among various secondary batteries since the commercialization of the first Li-ion battery by Sony in 1991. Although Li-ion batteries are state-of-the-art in terms of power sources, there is a need to further improve the energy density and capacity to provide adequate power and meet the growing demand of portable high-tech electronic devices. In this section, the general thermodynamic theory and the electrochemical reaction mechanisms of Li-ion batteries will be discussed. In addition, the typical materials comprising batteries namely, the cathode, anode and electrolyte will be described.

### 2.1.1 Rocking-Chair Cells

The first practical nonaqueous lithium rechargeable cells have been developed using lithium metal as the negative electrode (anode). However, lithium metal anodes exhibit several problems, which prevent the utilization of lithium rechargeable batteries for practical purposes. The first problem is that lithium becomes electrochemically inactive during the charging process due to dendrite formation [1]. Since the dendrite formation reduces battery life significantly, excess amount of lithium metal is required to be used as an anode. Secondly, there is a high cost associated with the battery production facilities necessary for using lithium metal as the anode. This is because of

high reactivity of lithium metal to air and moisture. This also causes safety problems during operation.

As a result, other types of anode materials have been proposed to be used in lithium rechargeable batteries. The main concept is the use of lithium intercalation (insertion) compounds for both cathodes and anodes, which gave rise to the so-called “rocking chair” cells. The term “rocking chair cell” arises from the fact that both electrodes undergo intercalation and de-intercalation during electrochemical cycling, which includes the charge and discharge processes.  $\text{Li}^+$  ions de-intercalate from the cathode that includes lithium and intercalate into the anode during the charge reaction, while the reverse reaction occurs at both electrodes during the discharge process. Fig. 2-1 shows the schematic representation of the “rocking chair cell” and an example of the basic charge and discharge process is also described below. The output voltage of such cells is determined by the difference between the electrochemical potential of lithium of the two compounds used for the cathode and the anode. Some of the electrode materials commonly used for the “rocking chair cell” will be described in detail in the following section.

### **2. 1. 2 Theoretical Capacity, Energy Density and Differential Capacity**

Batteries are portable energy sources, and therefore, the most important consideration would be the amount of stored electrochemical energy, which converts to electrical energy in practical applications. In order to represent the energy density, the “capacity” of the battery is typically measured and compared to its theoretical value. In other words, the capacity of the electrochemical cells reflects the energy that is stored by the electrodes within. Theoretical capacities in Li-ion batteries can be calculated by the number of Li-ions or electrons involved in the charge/discharge reactions per equivalent, such as mass (gravimetric capacity) or volume (volumetric capacity). Each capacity can be obtained using the equations below [2]. As seen in the equations, the theoretical capacity of a cell is expressed in terms of coulombs or ampere-hours.

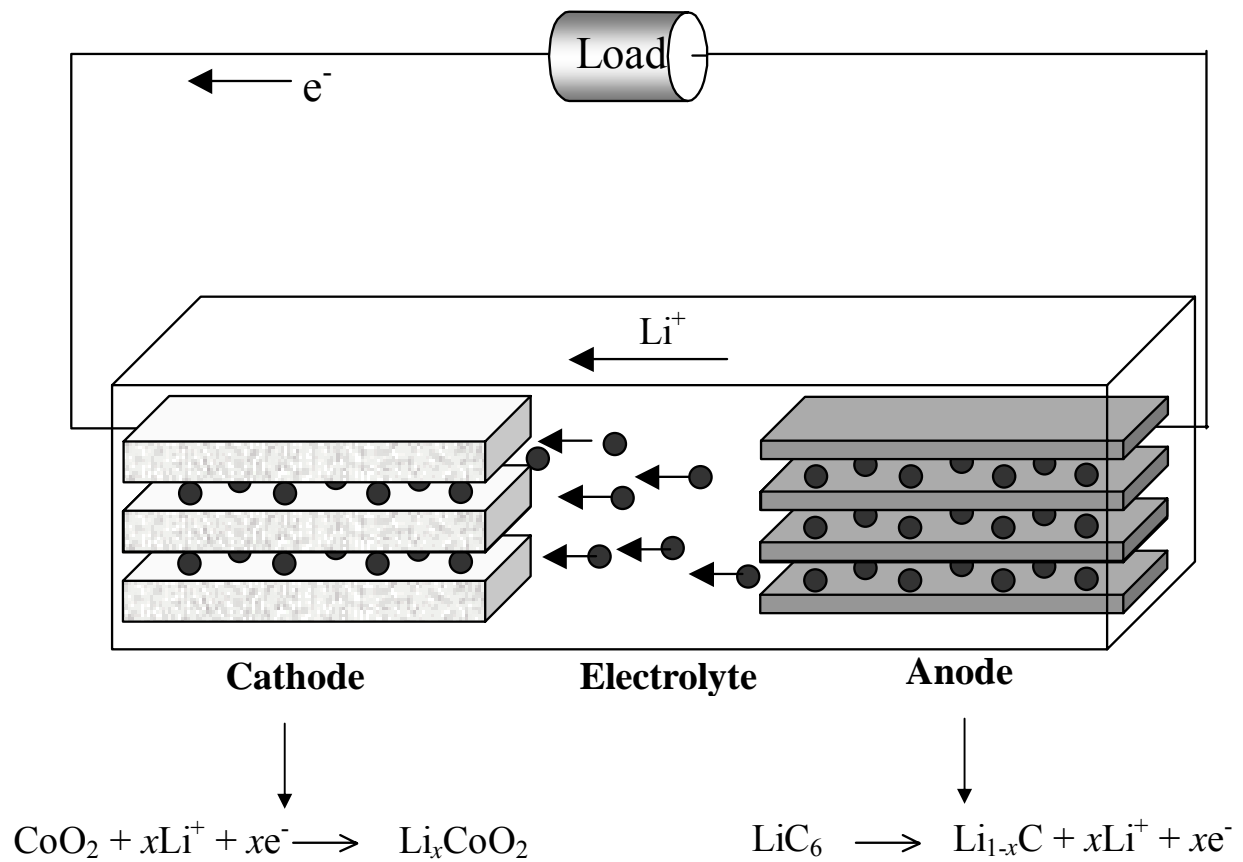


Fig. 2-1. Schematic representation of a “rocking-chair” battery during the discharge process.

$$\begin{aligned}
 \text{Gravimetric Capacity} &= \frac{N \times F}{M} \left( \frac{\text{Coulomb}}{g} \right) \\
 &= \frac{N \times F}{3.6M} \left( \frac{\text{mAh}}{g} \right)
 \end{aligned} \tag{2-1}$$

$$\text{Volumetric Capacity} = \text{Gravimetric Capacity} \times \text{density}$$

$N$  = moles of transportable Li-atoms (=electrons) per each mole of material

$F$  = Faraday's constant (= 96487Coulomb or 26.8 Ah)

$M$  = Formula weight of the material

The energy density is simply written as  $\varepsilon = V_{av}Q$ , the product of average voltage and the capacity, which can be represented in terms of mass (Wh/kg) or volume (Wh/l) [2]. However, the performance of a battery in actual practice is less than the theoretical value of the electrode materials because it also includes either the mass or the volume of non-active components such as electrolyte, separator, etc. The average voltage can be approximately calculated using the maximum degree of insertion,  $x_m$ . Hence the energy density of a battery is expressed as follows:

$$\text{Energy Density } \varepsilon = \frac{N \times F}{M} \int_0^{x_m} V dx \left( \frac{\text{Wh}}{\text{kg}} \right) \tag{2-2}$$

$x_m$  = the maximum degree of insertion of lithium ions

The method commonly used for the characterizing the electrochemical properties of electrodes used in our study as well is the constant current cycling or the galvanostatic technique, wherein the voltage changes with time by the application of a constant current. The plot of the differential capacity vs. cell voltage is very useful for ascertaining the presence of electrochemical reactions since the rate of lithium insertion into electrode materials is generally controlled by diffusion. The basic idea of differential capacity measurements is described by the equation below, where  $I$ ,  $Q$ ,  $V$  and  $t$  correspond to current, charge/capacity, voltage and time of charge and discharge

of the cell, respectively.

$$I = \left( \frac{dQ}{dt} \right) = \left( \frac{dQ}{dV} \right) \left( \frac{dV}{dt} \right) \quad (2-3)$$

When lithium is inserted into an electrode such as intercalation of lithium ions into graphite as mentioned earlier, the intercalation or insertion is mainly controlled by diffusion. In such a case where two phases coexist during insertion, the two different phases are differentiated by the concentration of lithium, wherein a plateau of voltage profile exists during phase changes. Since constant current is used, the value of differential capacity,  $dQ/dV$  increases dramatically and is represented in a plot when the  $dV/dt$  term becomes really small such as at voltage plateaus. Therefore, differential capacity vs. voltage can be used to determine the potential at which phase changes occur during electrochemical reactions such as the discharge and charge processes.

### 2. 1. 3 Design Consideration

Rechargeable batteries convert chemical energy to electric energy during discharge process and vice versa during charge. During the discharge of a cell, electrons move from the anode to the cathode through an external load of resistance  $R$  and ions flow inside the cell to convert chemical energy to electrical energy. The electric current which passes through the external load,  $I$ , is equal to the ionic current within the cell. During the charge process, electrons move in the other direction by an externally applied electric motive force (emf) or voltage that converts electrical energy to chemical energy. In other word, due to the chemical potential difference between a cathode and an anode, ionic species such as  $\text{Li}^+$  ions for example, tend to move according to the chemical potential difference and as a result, electric current is generated to compensate the ionic current through a electrolyte inside the cell. Fig. 2-2 shows the schematic of charge and discharge process and the directions of ionic and electric current.

In this case, the internal resistance of the cell is represented as [3]:

$$R = (L / \sigma_i A) + R_{\text{int}} + R_e \quad (2-4)$$

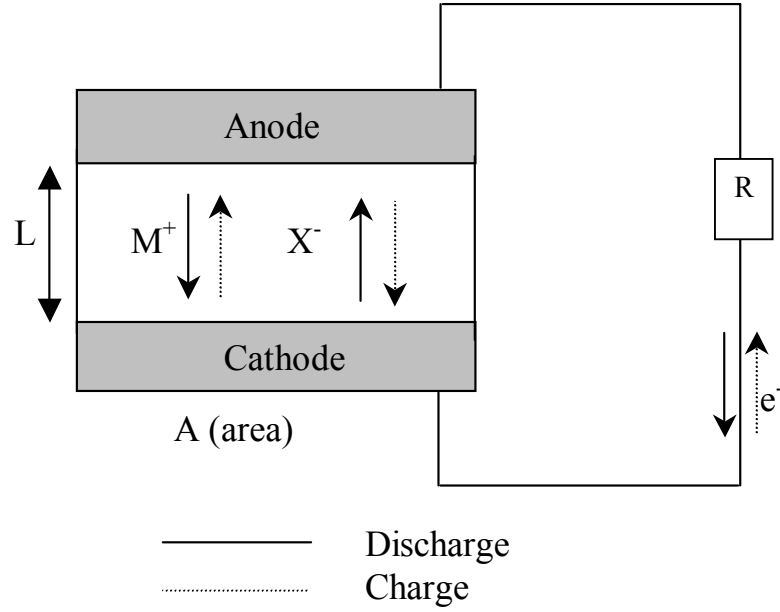


Fig. 2-2. The direction of propagation or transport of electron and ion during charge and discharge process.

where  $L/A$  is the thickness/area ratio of an electrolyte separator between two electrodes,  $\sigma_i$  is the ionic conductivity of the electrolyte,  $R_{\text{int}}$  is the resistance to ionic transfer across the electrolyte, and  $R_e$  is the internal resistance of the cell including the cathode and anode. The open-circuit voltage is represented by the chemical potential difference between a cathode and an anode:

$$V_{oc} = (\mu_A - \mu_C) / (-nF) \quad (2-5)$$

In this equation, ' $n$ ' represents the mole of electrons and ' $F$ ' is the Faraday's constant. By using equation (2-4) and (2-5), the operating voltage of the cell can be expressed:



$$V = V_{oc} - IR \quad (2-6)$$

Fig 2-3 exhibits a typical voltage vs. current curve during discharge of a battery and this is also called the polarization curve [3]. From the voltage drop,  $V_{oc}-V$ , the resistance of the battery can be measured by dividing the voltage drop with the measured current. From the polarization plot, the I-V curve can be divided into three regions according to the slope as seen in the figure. The rapid voltage drop in the region (I) reflects an increase in the interfacial resistance  $R_{int}$  between the electrodes and the electrolyte, which results from the increase of the current during discharge that eventually saturates.

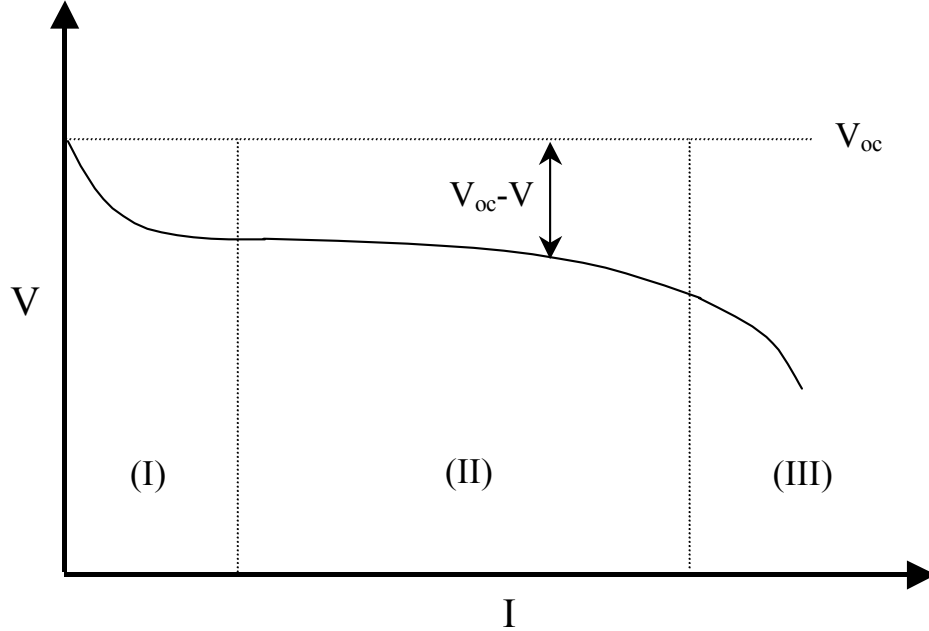


Fig. 2-3. A typical polarization curve for a prototype electrochemical cell.

The relatively smaller slope in region (II) is caused by the ionic conductivity  $\sigma_i$  of the electrolyte, while the other resistance values do not change much. The higher current in region (III) is limited by the diffusion of ionic species at the electrode/electrolyte interface because the movement of the ionic species is not very rapid to retain the equilibrium states. A large value of  $\sigma_i$  shifts the region (III) to higher currents and increases the power output of a battery when considering that the power corresponds to the area under the curve.

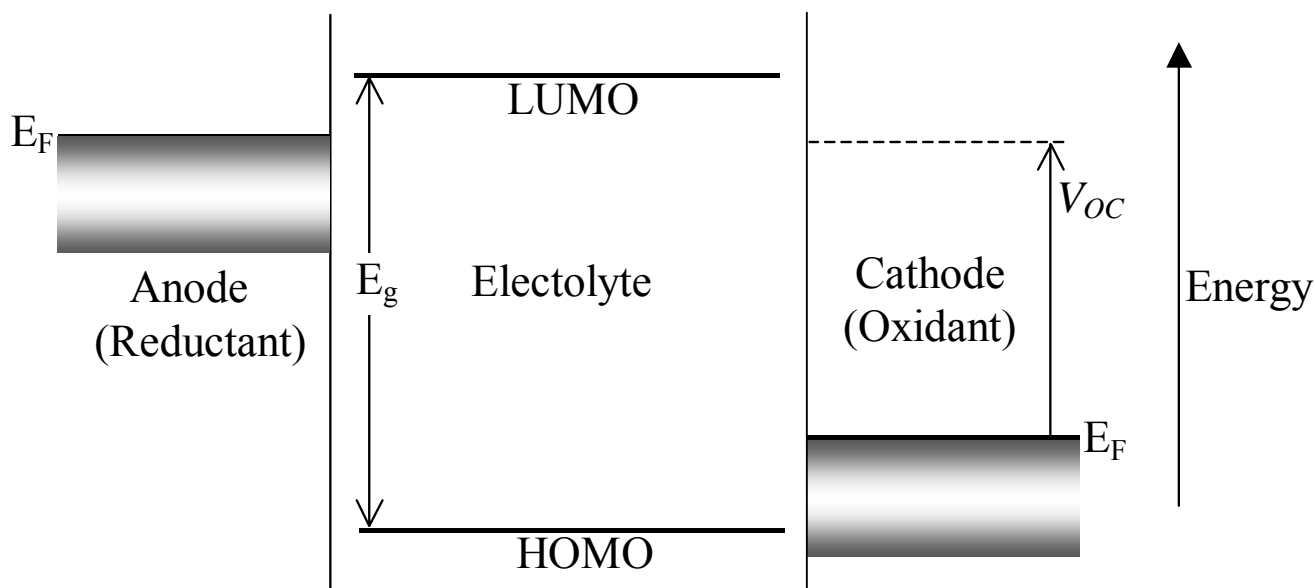


Fig. 2-4 Schematic representation of relative energies of the electrolyte and the electrodes.

As mentioned above, the driving force of the electric current is the chemical potential difference between the cathode and the anode and the open circuit voltage is also determined by the chemical potential difference. Therefore, the discharge process, which is a spontaneous reaction, should continue to progress until the chemical potential

of the cathode becomes same as that of the anode and this could also be explained using the Fermi energy levels of the electrodes and the energy window of the electrolyte. Fig. 2-4 shows a schematic of the relative energy levels of the electrodes and the electrolytes. When a cell with liquid electrolyte undergoes discharge, as illustrated in the energy diagram, the highest level of the electron distribution ( $E_F(A)$ ) should lie below the lowest unoccupied molecular orbital (i.e. LUMO: the lowest electron acceptor states) to achieve thermodynamic stability. Similarly, the Fermi level of the cathode should be present above the highest occupied molecular orbital level (HOMO: the highest electron donor states) of the electrolyte in order to maintain the stability between the electrolyte and the cathode. Failure to do so will cause the cathode to drag electrons from the electrolyte causing oxidation of the electrolyte. As a result,  $E_F$  or the chemical potential should exist between LUMO and HOMO levels of the electrolyte although a larger ( $\mu_A - \mu_C$ ) is beneficial to maximize the voltage output.

Based on the above considerations, the various battery components are expected to possess certain properties in order to ensure good performance of the battery. Since the power output of the cell is represented as  $P = IV$ , a combination of high current and high voltage are required to obtain a large power output. However the operating voltage is limited by the open circuit voltage of the cell, and a high current is necessary to attain better power output. The internal loss of the cell corresponds to  $I^2R$  and therefore, smaller internal resistance is also required to lower the internal  $IR$  drop. From equation (2-4), in order to minimize the inherent materials related terms such as  $R_e$  and  $\sigma_i$  some conditions need to be met by the materials. First, electrodes materials should have good electronic conductivity, therefore metallic or semiconductor materials are preferred rather than insulators. Second, in order to lower the internal resistance, an electrolyte with high ionic conductivity is necessary and typically the non-aqueous electrolyte for Li-ion batteries should have  $\sigma_i$  larger than 0.1S/cm.  $R_{int}$  is closely related to the interface of the electrodes-electrolyte and can be decreased by increasing the area of the interface using electrodes with porous or smaller particle size. It is also important to control the shape factor of a cell ( $L/A$ ) by designing the battery efficiently. This will contribute to an increase in the ionic current as well as reduce the internal resistance of the cell.

## **2. 1. 4 Materials for Li-ion Batteries**

### **1. Cathodes**

All cathode materials in Li ion battery applications are based on lithium ion intercalation compounds. Since 1970 the first operational rocking chair batteries were assembled using lithium metal as the negative electrode (anode) and non-lithiated positive electrode materials. Some layered materials such as  $\text{TiS}_2$ ,  $\text{NbS}_2$ , and  $\text{NbSe}_2$  were tested along with lithium. However, these systems were not developed further due to the low voltage, oxidation and decomposition of the sulfide.

In the early 1980's,  $\text{LiCoO}_2$  was found to de-lithiate at high temperatures [4] and was studied extensively for Li battery applications [5]. Other types of ternary lithium transition metal non-oxide systems  $\text{LiMX}$  ( $\text{M}$  = transition metals,  $\text{X}$  = S, Se, Te) have also been reported as candidates for cathode materials [6]. However, their operating voltages and volumetric capacities are lower than  $\text{LiMO}_2$ . Research in the area of cathode materials recently is mainly focused on transition metal oxides due to the high theoretical capacity and high energy density.  $\text{LiCoO}_2$  is known to be the most popular cathode material for practical applications since Sony first commercially developed the  $\text{LiCoO}_2/\text{C}$  cell [5]. This cathode material has several advantages such as high operating voltage, high energy density and capacity with low formula weight, which renders the material attractive as a compact energy source. However, the problems related to the decomposition of electrolytes [7, 8], high production cost and toxicity related to cobalt still exists and need to be improved.

A number of other layer oxides such as  $\text{LiNiO}_2$ , have also been examined and reported in the literature [9, 10]. Although  $\text{LiNiO}_2$  has relatively low operating voltage compare to  $\text{LiCoO}_2$ , it offers many advantages as a cathode material [11], which are good high temperature performance, good charge retention, ability to cycle over a wide compositional range and low production cost. In this system, however, Ni atoms tend to migrate into Li sites when Li content is low (deficient state) thereby degrading overall performance. It was shown that the substitution of Ni with Co or doping of other elements could stabilize the structure and reduce the defect concentration [12]. In addition, there is oxygen evolution due to the oxide decomposition and thermal run away problems that has slowed its commercialization [13].

## ***Chapter 2. Background***

$\text{LiMn}_2\text{O}_4$  is another class of cathode materials, which is being studied extensively [14-16] since Hunter first showed its ability to remove lithium while maintaining the spinel framework structure [17]. Bellcore researchers and others have since demonstrated its potential as a cathode [18]. This system is more advantageous compared to  $\text{LiCoO}_2$  and  $\text{LiNiO}_2$  systems since Mn is more abundant, less expensive and nontoxic. However, the stable form of  $\text{LiMn}_2\text{O}_4$  is not layered but a spinel structure, and as a result, it is known to have relative a lower capacity [19, 20]. A layered compound with the formula  $\text{LiMnO}_2$  would be ideal with high theoretical capacity but several initial attempts to synthesize layered  $\text{LiMnO}_2$  using low temperature methods [21, 22] were not successful because of the low crystallinity of the products. Recently, layered  $\text{LiMnO}_2$  compounds have been reported with better properties using the chimie douce method involving ion-exchange reaction between  $\text{NaMnO}_2$  and  $\text{LiBr}$  in hexanol [23, 24]. The synthesis of layered manganese oxide is still an important goal of solid-state chemists, materials scientists and intercalation chemists for Li-ion battery applications [25-28]. Although methods have been identified to synthesize the layered form of  $\text{LiMnO}_2$  bearing structural similarity to  $\text{LiCoO}_2$  and  $\text{LiNiO}_2$ , the system is very much prone to conversion to spinel with removal of 50% of the lithium. This irreversible transformation has largely prevented its rapid use. Stabilization of the layered structure remains one of the most challenging aspects in the development of new cathode materials for Li-ion batteries.

### **2. Electrolytes**

As mentioned earlier, electrolytes for Li-ion batteries are generally required to have the following fundamental properties: 1) high ionic conductivity, 2) chemical stability or inertness against other components of the battery such as cathode/anode, current collector and separator, 3) thermal stability within the operating temperature range, 4) wide bandgap or voltage window for electrochemical stability, 5) non-toxicity. Electrolytes for secondary batteries can be categorized into organic (non-aqueous), crystalline/amorphous solid and polymer electrolytes according to their respective stable physical states.

Given in table 2-1 below is a list of some organic electrolytes, which have been used or proposed for Li-ion rechargeable battery systems [29]. The main component of

## ***Chapter 2. Background***

the electrolyte is the lithium salt exhibiting good lithium ion conductivity. Lithium salts with monovalent anions are generally preferred since electrolytes can have a higher degree of dissociation of salts and a higher mobility accordingly. Several candidates have been proposed like  $\text{LiClO}_4$ ,  $\text{LiBF}_6$ ,  $\text{LiPF}_6$  and  $\text{LiAsF}_6$ , however  $\text{LiClO}_4$  is known to be unstable under conditions used for the anode among these candidates [29]. The other component is organic solvent that dissolves lithium salts to form electrolytes. The solvents need to have lower melting points, higher boiling temperature, and low vapor pressure to be functional over a wide range of operating temperature. In addition, high relative permittivity (5~90) and low viscosity (0.2~2.5 cP) are necessary for the electrolyte solution to display higher ionic conductivity. The most acceptable solvents are alkyl carbonates such as propylene carbonate (PC), ethylene carbonate (EC) dimethyl carbonate (DMC), diethyl carbonate (DEC), etc. that exhibit a Li ionic conductivity in the range of 0.2~ 47  $\text{ms/cm}^{-1}$  for all the family of lithium salts mentioned above [30]. PC and EC belong to the cyclic alkyl carbonate family, which show higher permittivity due to their polarity. However the viscosity of these solvents are relatively high compared to other linear alkyl carbonate like DMC and DEC. Thus mixing of solvents is an effective way to overcome the disadvantages of the two different carbonate [31, 32] and hence, a mixture of these two different carbonate are generally used in commercial electrolytes as shown in Table 2-1.

Another type of electrolyte is a solid Li-ion conductor, comprising crystalline and amorphous phases. The ionic conductivity of solids is attributed to the atomic motions through vacant (Schottky) or/and interstitial (Frenkel) sites present or created in the materials. One of the well-known examples is  $\text{LiI}$  with a low ionic conductivity of about  $2 \times 10^{-7} \text{Scm}^{-1}$  at room temperature [33], although the energy of formation of vacancies is low enough to generate a considerable vacancy concentration to permit diffusion. To date, solid electrolytes have rarely been used for practical purpose due to their low ionic conductivity at room temperature. However, in the interest of safety and the need for high power/capacity batteries there has been an increased focus on safety considerations because most organic solvents used in electrolytes are flammable. This interest and demand has expanded the search for more reliable solid electrolytes. In order to increase the ionic conductivity of the solid electrolyte, additives such as  $\text{Al}_2\text{O}_3$  [34] have been used to form what are called nanocomposite electrolytes. These

## Chapter 2. Background

composite electrolytes are composed of dispersed second phases in the host matrix which show enhanced ionic conductivity [34, 35].

**Table 2-1 Examples of practical electrolyte used in Li-ion batteries [29].**

Rechargeable Battery Cathode/Anode	Electrolyte (Salt/Solvent)	Company or Institute
Li-Al/TiS <sub>2</sub>	LiPF <sub>6</sub> /MeDOL+DME+additive	Hitachi Maxwell (Jap)
Li/MoS <sub>2</sub>	LiAsF <sub>6</sub> /PC+cosolvent	Moli Energy (Can)
Li-alloy/C	LiClO <sub>4</sub> /PC	Matsushita Battery (Jap)
Li-Al/Polyaniline	LiClO <sub>4</sub> /PC	Bridgestone-Seiko (Jap)
Li-C/LiCoO <sub>2</sub>	LiPF <sub>6</sub> /PC+DEC	Sony Energytec (Jap)
Li-C/LiCoO <sub>2</sub>	LiBF <sub>6</sub> /PC+EC+BL*	A&T Battery (Jap)
Li-C/LiCoO <sub>2</sub>	LiPF <sub>6</sub> /EC+DEC+cosolvent	Matsushita Battery (Jap)
Li-C/LiCoO <sub>2</sub>	LiPF <sub>6</sub> /EC-cosolvent	Sanyo (Jap)
Li-C/Li <sub>1+x</sub> Mn <sub>2</sub> O <sub>4</sub>	LiPF <sub>6</sub> /EC+DMC	Bellcore (USA)
Li-C/LiNiO <sub>2</sub>	LiPF <sub>6</sub> /EC+cosolvent	Rayovac (Jap)
Li/Li <sub>x</sub> MnO <sub>2</sub>	Organic eletrolyte	Tadiran (Israel)
Li/TiS <sub>2</sub>	LiI-LiPO <sub>4</sub> -P <sub>2</sub> S <sub>2</sub>	Everready (USA)
Li/V <sub>6</sub> O <sub>13</sub>	LiX/PEO-based polymer (X: halide)	Valence Technology (USA)

\* BL: Butyrolactone

Amorphous solid materials also have been studied extensively as solid electrolytes [36-40]. Glassy solid are known to have several advantages compared to crystalline solids. Amorphous solids have a wide range of composition, which enable higher ionic conductivity to be achieved. The absence of grain boundaries promotes faster diffusion of ionic species in comparison to crystalline solids. Lithium ion

## Chapter 2. Background

conducting glasses can be categorized into two groups, oxide and sulfide-based glasses. Oxide systems such as  $\text{Li}_2\text{O}-\text{B}_2\text{O}_3$ ,  $\text{Li}_2\text{O}-\text{SiO}_2$ ,  $\text{Li}_2\text{O}-\text{B}_2\text{O}_3-\text{Li}_2\text{SO}_4$ , and sulfide systems such as  $\text{SiS}_2-\text{Li}_2\text{S}$  [41],  $\text{SiS}_2-\text{Li}_2\text{S}-\text{Al}_2\text{S}_3$  [42, 43] have been reported. Some examples of amorphous electrolytes and their ionic conductivities are tabulated in Table 2-2.

**Table 2-2 Ionic conductivity of lithium oxide-based glasses with various compositions [2].**

Material (Composition)	Conductivity (S/cm)	Temperature of measurement (°C)
$\text{Li}_2\text{B}_4\text{O}_7$	$1.0 \times 10^{-4}$	300
$\text{LiBO}_2$	$4.0 \times 10^{-3}$	300
$\text{Li}_2\text{O}-\text{B}_2\text{O}_3$ (42.5-57.5)	$6.1 \times 10^{-3}$	350
$\text{Li}_2\text{O}-\text{B}_2\text{O}_3$ (63-37)	$6.3 \times 10^{-11}$	25
$\text{Li}_4\text{B}_7\text{O}_{12}\text{Cl}$	$2.5 \times 10^{-4}$	200
$\text{Li}_4\text{B}_7\text{O}_{12}\text{Cl}$	$8.0 \times 10^{-3}$	300
$\text{Li}_2\text{O}-\text{Li}_2\text{Cl}_2-\text{Li}_2\text{SO}_4-\text{SiO}_2-\text{B}_2\text{O}_3$ (35-10-30-12.5-12.5)	$9.7 \times 10^{-2}$	350
$\text{Li}_2\text{O}-(\text{LiCl})_2-\text{B}_2\text{O}_3$ (31.8-12.3-55.9)	$1.7 \times 10^{-2}$	300
$\text{Li}_2\text{O}-(\text{LiCl})_2-\text{Al}_2\text{O}_3-\text{B}_2\text{O}_3$ (29-24-3-44)	$1.5 \times 10^{-2}$	350
$\text{Li}_2\text{O}-\text{LiF}-\text{B}_2\text{O}_3$ (20-36-44)	$3.1 \times 10^{-4}$	200
$\text{Li}_2\text{O}-\text{Li}_3\text{PO}_4-\text{B}_2\text{O}_3$ (25-10-65)	$1.0 \times 10^{-3}$	330
$\text{Li}_2\text{O}-\text{Li}_2\text{SO}_4-\text{B}_2\text{O}_3$ (0.5-0.15-1)	$2.4 \times 10^{-3}$	350
$\text{Li}_2\text{O}-\text{Li}_2\text{SO}_4-\text{B}_2\text{O}_3$ (0.71-1.1-1)	$2.1 \times 10^{-2}$	300
$\text{Li}_2\text{Si}_2\text{O}_5$	$1.9 \times 10^{-3}$	350
$\text{Li}_2\text{O}-\text{Si}_2\text{O}_2$ (40-60)	$1.0 \times 10^{-6}$	100
$\text{Li}_2\text{Al}_2\text{Si}_4$	$4.0 \times 10^{-4}$	300
$\text{Li}_2\text{O}-\text{Nb}_2\text{O}_3$	$6.1 \times 10^{-4}$	200
$\text{Li}_2\text{O}-\text{B}_2\text{O}_3-\text{LiNbO}_3$ (40-35-25)	$8.0 \times 10^{-4}$	350
$\text{Li}_2\text{O}-\text{Al}_2\text{O}_3-\text{SiO}_2$ (25-25-50)	$6.1 \times 10^{-4}$	250
$\text{Li}_2\text{O}-\text{B}_2\text{O}_3-\text{SiO}_2$ (39-13-48)	$1.5 \times 10^{-3}$	350
$\text{Li}_2\text{Si}_2\text{O}_5-\text{Li}_2\text{SO}_4$ (71.5-28.5)	$8.7 \times 10^{-3}$	350
$\text{LiNbO}_2-\text{SiO}_2$ (65-35)	$1.0 \times 10^{-4}$	200
$\text{Li}_2\text{O}-\text{Y}_2\text{O}_3-\text{SiO}_2$ (40-6-54)	$1.4 \times 10^{-3}$	300
$\text{LiPO}_3-\text{LiF}$ (60-40)	$6.7 \times 10^{-9}$	25
$\text{LiPO}_3-\text{LiCl}$ (70-30)	$1.0 \times 10^{-3}$	220
$\text{LiPO}_3-\text{LiI}$ (67-33)	$1.0 \times 10^{-3}$	194
$\text{LiPO}_3-\text{LiBr}$ (67-33)	$1.3 \times 10^{-3}$	220
$\text{LiPO}_3-\text{Li}_2\text{SO}_4$ (67-33)	$3.5 \times 10^{-3}$	250
$\text{B}_2\text{O}_3-0.56\text{Li}_2\text{O}-0.08\text{LiF}$	$6.3 \times 10^{-4}$	300
$\text{B}_2\text{O}_3-0.56\text{Li}_2\text{O}-0.08\text{LiI}$	$3.2 \times 10^{-3}$	300
$\text{Li}_2\text{O}-\text{LiF}-\text{Al}(\text{PO}_3)_3$ (30-50-20)	$1.0 \times 10^{-2}$	300
$\text{Li}_2\text{O}-\text{LiF}-\text{Al}(\text{PO}_3)_3$ (15-70-15)	$1.3 \times 10^{-3}$	220
$\text{Nb}_2\text{O}_5-\text{Li}_2\text{O}$ (50-50)	$5.3 \times 10^{-3}$	350
$\text{Ta}_2\text{O}_5-\text{Li}_2\text{O}$ (50-50)	$6.4 \times 10^{-3}$	350



Solid electrolytes exhibit a higher propensity to be fabricated into thin films since they can be synthesized *in-situ* using thin film technology. Furthermore, the electrolyte layer forms a good solid-solid contact with the electrodes depending on the manufacturing methods. The electrolyte layer in thin film batteries are on the order of 1~3 $\mu$ m. Under these dimensions, the resistances are quite small and the solid electrolyte thus is not required to have high ionic conductivity as opposed to conventional bulk Li-ion secondary batteries. Although the use of crystalline or glassy electrolytes for thin film battery applications have been reported extensively [44-49], there are several problems yet to be solved such as mechanical strength, integrity and the brittle nature of the ceramic.

Polymer or plastic electrolytes are relatively unexplored in the solid-state ionics field. The new electrolyte systems are expected to reduce the production cost and be more conducive to large-scale production. The absence of a liquid phase essentially promises batteries to be packed into lightweight plastic containers rather than metallic casings. The term “polymer electrolytes” can be applied to a family of several systems comprised as the following [50]: 1) A system comprising a salt dissolved in a high molecular weight polar polymer matrix, 2) A gel electrolyte made by dissolving a salt in a polar solvent and adding an inactive polymer to give a mechanically stable system, 3) A plasticized electrolyte obtained by adding small amount of liquid with high dielectric constant into a polymer electrolyte to obtain improved ionic conductivity, 4) A membrane ionomer prepared using polymer electrolyte with inert backbone materials.

The development of polymer electrolyte membrane was initiated using complexes of lithium salt LiX (LiClO<sub>4</sub>, LiCF<sub>3</sub>SO<sub>3</sub>, LiBF<sub>4</sub>, etc) and high molecular weight polymers containing coordinated lithium within, such as polyethylene oxide (PEO), where lithium is coordinated with oxygen atoms [51]. Since the amorphous polymer host for lithium salts show poor ionic conductivity and there is an inherent difficulty related to synthesizing crystalline PEO, attempts have been made to replace the polymer host using copolymers [52-55]. However the major drawback of these copolymers is the unsatisfactory electrochemical stability. Recently gel polymer electrolytes have attracted considerable attention because of their higher and practical ionic conductivities. There are two methods to generate gel polymer electrolytes: The

## ***Chapter 2. Background***

first method involves loading a liquid electrolyte into a matrix e.g., porous polyethylene [56], and the second is increasing the viscosity of the liquid electrolyte by adding soluble polymers, e.g., PEO, polymethyl methacrylate (PMMA), polyvinylidene fluoride (PVDF), etc [57]. Although commercialization of Li-ion polymer batteries is imminent, the search for methods and strategies to optimize the properties such as mechanical strength and cation mobility (conductivity) continues. Table 2-3 exhibits some examples of polymer electrolytes and their ionic conductivities at room temperature.

### **3. Anodes**

Li metal has been used widely as anodes for primary battery application because  $\text{Li}^+$  is the lightest and the most mobile ion available in non-aqueous electrolyte conditions next to hydrogen. Despite various attempts to use Li metal for rechargeable battery applications [59-61] it has major problems. Li metal anodes form dendritic morphologies after a limited number of charge/discharge cycles and these dendrites make contact with the cathode thereby short-circuiting the cell. The dendrites also affect the cycling efficiency because some dendrites lose contact with the electrode resulting in electrochemically inactive portions during deposition/dissolution, which are related to the charge/discharge processes respectively. Another problem is a safety issue related to the cells containing Li metal anodes. Heating of the cell due to reasons such as internal short-circuit, high current applications, overcharge, etc., can cause excess heat to be generated which causes decomposition and/or adverse reactions. If a liquid electrolyte is used the cell would thus spontaneously ignite. The causes of excess internal heat generation are: 1) A reaction between the electrolyte and the anode or cathode, 2) the thermal decomposition of the electrolyte, 3) the thermal decomposition of the electrode, 4) current passing through a cell with a large electric resistance. Therefore, the use of Li metal as an anode is not considered satisfactory for commercialization although it has an incredibly large capacity as high as 3860 mAh/g [62]. The need for alternative anode materials to replace lithium is therefore very imminent in the electrochemical community.

Carbon materials began to attract considerable attention in the late 1980's as alternative anode materials to lithium. Carbon anode electrochemically intercalates

## Chapter 2. Background

lithium, which resulted in the development of the “rocking chair” rechargeable battery combined with high performing lithium intercalating cathodes such as  $\text{LiCoO}_2$ ,  $\text{LiNiO}_2$  and  $\text{LiMnO}_4$ . Since carbon anodes do not have lithium and need to be charged initially, these Li-containing intercalation cathodes complete the definition of the “rocking chair” cell. Furthermore, a carbon anode shows less reactivity, good reversibility and a negative potential profile close to lithium, thus solving the safety issue problem associated with lithium metal anodes.

**Table 2-3 Ionic conductivity of various electrolyte membranes at room temperature. [58].**

Material	Composition	Conductivity (S/cm) $\times 10^{-3}$
$\text{LiClO}_4$ -EC-PC-PAN	4.5-56.5-23.0-16.0	1.1
$\text{LiClO}_4$ - $\gamma$ BL-PAN	4.5-79.5-16.0	2.8
$\text{LiAsF}_6$ -EC-PC-PAN	4.5-56.5-23.0-16.0	0.9
$\text{LiAsF}_6$ - $\gamma$ BL-PAN	4.5-79.5-16.0	4.1
$\text{LiN}(\text{CF}_3\text{SO}_2)_2$ -EC-PC-PAN	4.5-56.5-23.0-16.0	1.0
$\text{LiN}(\text{CF}_3\text{SO}_2)_2$ -EC- $\gamma$ BL-PAN	4.5-56.5-23.0-16.0	2.6
$\text{LiClO}_4$ -EC-PC-PMMA	4.5-46.5-19.0-30.0	0.7
$\text{LiAsF}_6$ -EC-PC-PMMA	4.5-46.5-19.0-30.0	0.8
$\text{LiN}(\text{CF}_3\text{SO}_2)_2$ -EC-PC-PMMA	4.5-46.5-19.0-30.0	0.7
$\text{LiN}(\text{CF}_3\text{SO}_2)_2$ -EC-DMC-PMMA	5-50-20-25	1.1
$\text{LiN}(\text{CF}_3\text{SO}_2)_2$ -EC-DBP-PVDF	3.5-36.5-30-30	0.017
$\text{LiN}(\text{CF}_3\text{SO}_2)_2$ -PEGDME-PEO	4.8-80.9-14.3	0.1
$\text{LiN}(\text{CF}_3\text{SO}_2)_2$ -PEGDME-DEC-PEO	6.7-64.1-21.3-7.9	0.1
$\text{LiN}(\text{CF}_3\text{SO}_2)_2$ -PEGDME-DMC-PEO	6.6-62.4-20.8-10.2	0.2
$\text{LiN}(\text{CF}_3\text{SO}_2)_2$ -PEGDME-EC-PEO	6.6-56.0-18.7-18.7	1.9
$\text{LiN}(\text{CF}_3\text{SO}_2)_2$ -PEGDME-PC-PEO	6.7-63.2-21.0-9.1	1.0

\*PEO : poly(ethylene oxide), PC : propylene carbonate, EC : ethylene carbonate,  
BL :  $\gamma$ -butyrolactone, PAN : poly(acrylonitrile), PMMA : poly(methyl methacrylate),  
PVDF : poly(vinylidene fluoride), PEGDME : poly(ethylene glycol-dimethylether),  
DMC : dimethyl carbonate, DEC : diethyl carbonate, DBP : dibutyl phthalate

Carbon materials have attracted much interest because of the diverse carbon structures, which play an important role in electrochemistry. The structure of the carbonaceous materials is generally influenced by the starting materials [63]. For example, carbon prepared from the solid phase such as organic polymer has a highly disordered structure while the carbon synthesized from the liquid phase has a crystalline structure, namely, artificial graphite. The quantity of sites where lithium atoms can intercalate/de-intercalate reversibly depends on the crystallinity, texture and morphologies of carbonaceous materials [64-71]. In addition, the electrochemical responses such as potential characteristics are determined by the type of carbonaceous materials. In spite of the various types of carbon, most carbonaceous materials which intercalate lithium electrochemically can be classified generally as graphitic (ordered) and non-graphitic (disordered) carbons.

Graphitic material consists of the stacking with “graphene sheets” and these layers are weakly bonded together by van der Waals forces. There are mainly two kinds of stacking, one is ABAB type (hexagonal) and the other is ABCABC (rhombohedral). However, pure single type of graphite is very difficult to obtain because the energy required to induce phase transformation between these two phases is quite small. An intercalation into graphite materials results in the occupation of empty layered gaps between graphene layers with lithium atoms. It is noted that the ABAB stacking of graphene layers slide and form the AAA stacking during intercalation as shown in Fig2-5. Lithiated graphite can be expressed as  $\text{Li}_x\text{C}_6$  ( $x = 0\sim 1$ ) and fully Lithiated  $\text{LiC}_6$  forms an energetically AA favorable stacking, which has a theoretical capacity as high as 372mAh/g [72]. Graphitic materials have been used as standard anodes for “rocking chair” cells since Sony Energytec Inc. commercialized the Li-ion rechargeable battery.

Non-graphitic carbon has attracted much interest recently because of its ability to exhibit higher capacity than graphite. Non-graphitic carbon or disordered carbon provides additional sites for lithiation. As a result, it has the ability to host a larger number of Li, i.e.  $x > 1$  in  $\text{Li}_x\text{C}_6$ . Research on disordered carbon includes the modification of graphitic surface using mild oxidation [73, 74], the use of carbon with a smaller particle size [75, 76], creating extensive disorder by mechanical milling [77], etc. However, there are still problems to be solved despite their high capacities such as high irreversible loss and poor cycling performance.

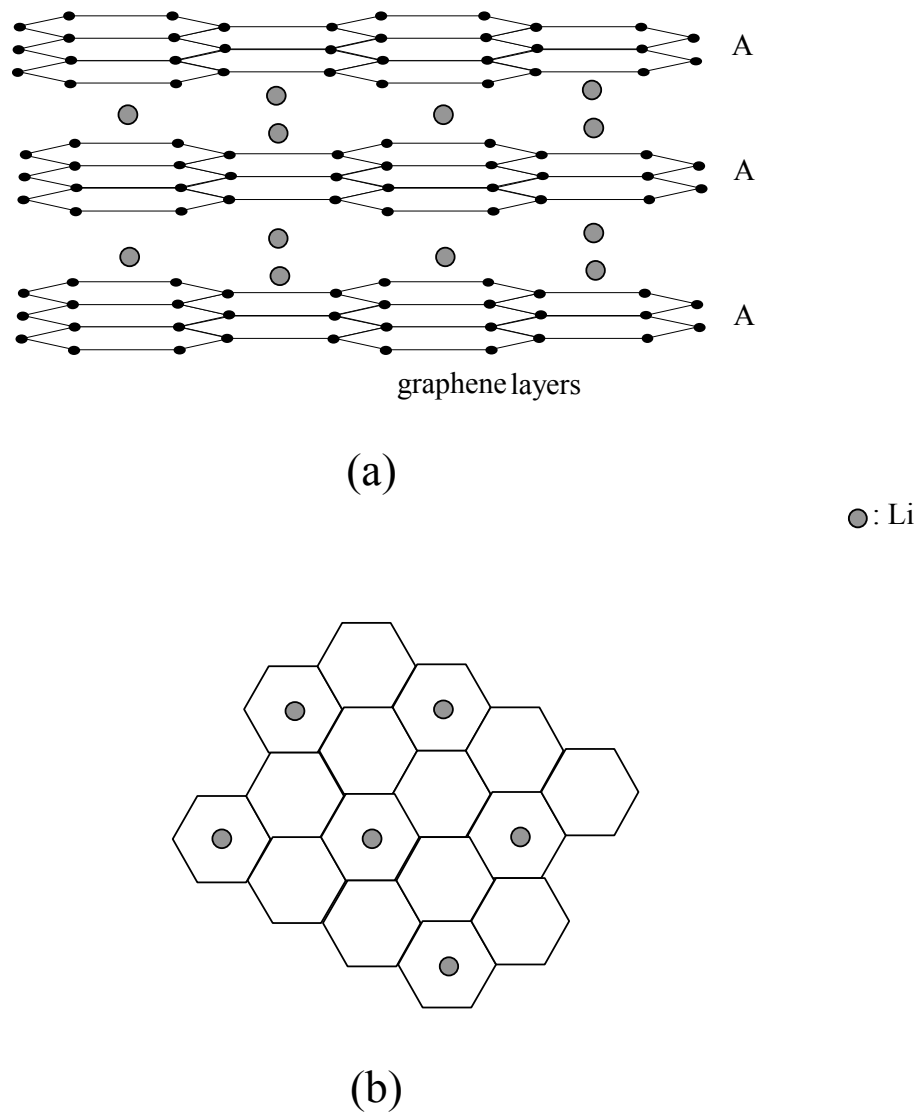
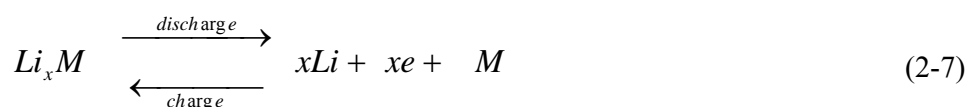


Fig. 2-5 The structure of lithiated graphite ( $\text{LiC}_6$ ). (a) A schematic drawing of the AA stacking of graphene layers, (b) In plane distribution of Li.

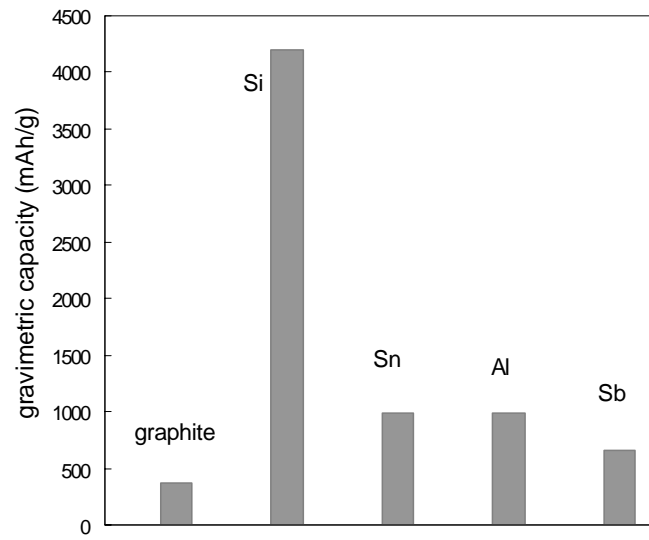
## Chapter 2. Background

While graphitic anodes show good performance in the market for Li-ion batteries, there has been a continuous effort to improve the performance of lithium metal anodes. Lithium-alloy anodes for Li-ion rechargeable battery application have been studied since early 1970 because lithium is known to form intermetallics phases ( $\text{Li}_x\text{M}$ ) with numerous metals such as Mg, Ca, Al, Si, Ge, Sn, Sb, Bi, As, Ag, Au, Pt, Cd, etc. electrochemically at room temperature [78].

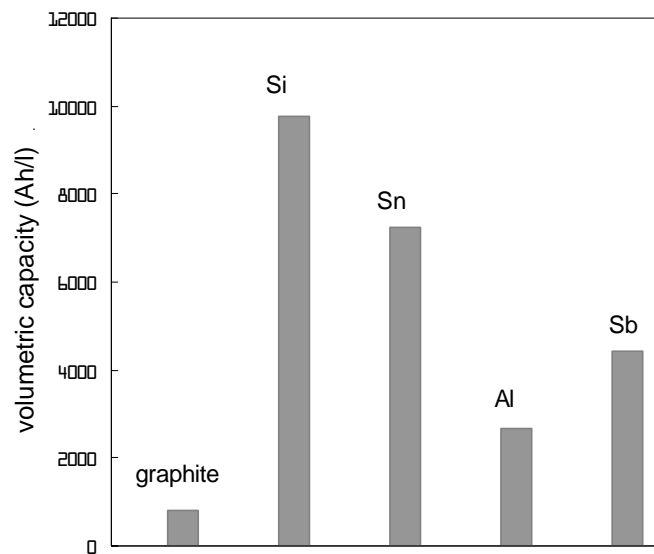


The reaction above is generally quite reversible and the amount of lithium accommodation or capacity can be easily calculated by knowing  $x$ . The gravimetric capacity and volumetric capacity of lithiated metals is shown in Fig 2-6. As seen from Fig 2-6 (a) and (b), both the specific gravimetric and volumetric capacities of lithium-alloys are generally higher than lithiated graphite. The lithium alloys are also advantageous over graphite materials because the solvent molecules do not intercalate with lithium alloys whereas graphite materials have problems with solvent intercalation [79].

Despite these advantages, lithium alloys have not been used commercially as anodes in Li-ion batteries because the metals undergo significant changes in structure and in volume during the reaction with lithium. The change in volume of metals upon alloying with lithium is shown in Fig. 2-7 and the increase in volume can be as high as 358% in the case of Sn [80]. Besides, lithium-alloys are generally brittle due to their highly ionic character, a characteristic of the so-called family of ‘Zintl-phases’ that these alloys belong to [81]. Due to these reasons, an incredibly large mechanical stress results during lithiation that leads to mechanical failure of the lithium-alloy electrode, and the electrode undergoes extensive cracking and crumbling. As a consequence, particles consisting of lithium-alloy anodes lose contact and the electrical conductivity is lost. Consequently, the electrodes fail to exhibit the desired electrochemical performance eventually after several cycles or almost immediately in some cases wherein the alloy particles are used alone.



(a)



(b)

Fig. 2-6 (a) Specific gravimetric and (b) Volumetric capacity of several promising anode materials [78].

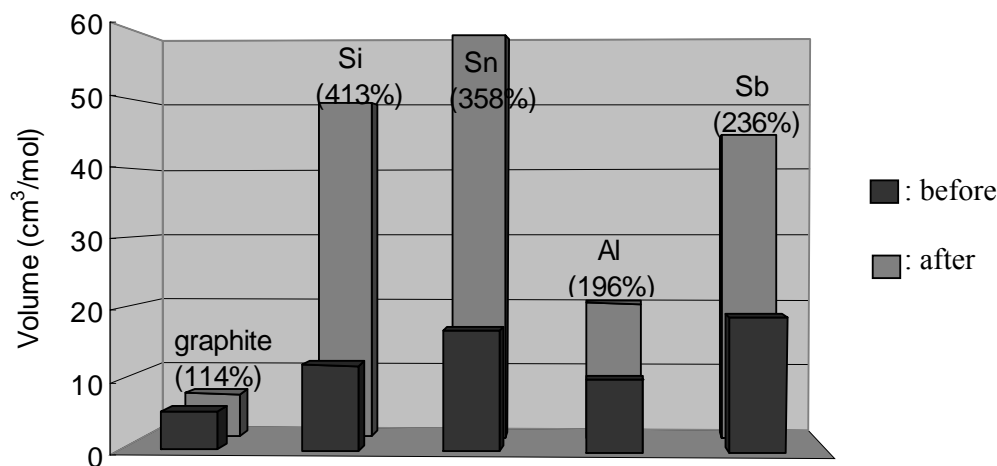


Fig. 2-7 Molar volumes change of anode materials before/after lithiation. The percentage increase in volume after full lithiation is shown respectively [78].

Lithium-alloy anodes were first introduced in the market in late 1970 by Matsushita-Panasonic [78], who designed the cell using Bi-Pb-Sn-Cd alloy as the anode, and similar types of materials were also reported in the literature [82, 83]. These systems could attain reasonable cyclability only when the cycling was limited to very 'shallow' reaction, utilizing less than 10% of its electrochemical capability (capacity) in order to prevent any mechanical failure during the alloying and de-alloying process. Therefore, the resultant capacities are very low with respect to their theoretical capacities. Recently, Fuji Photo Film Celltec Co. reported tin-based amorphous composite oxide (TCO), which have been claimed to have a specific capacity of 800mAh/g with good reversibility [84]. The TCO is made from SnO, B<sub>2</sub>O<sub>3</sub>, Sn<sub>2</sub>P<sub>2</sub>O<sub>7</sub>, Al<sub>2</sub>O<sub>3</sub>, and other precursors.

According to their result, Sn (II) compounds only react with Li, whereas other oxides including B, P, and Al are electrochemically inactive. There are two important aspects that can be learned from their discovery. The first aspect is that this system shows reasonably good cyclability in spite of the large volume expansion of Sn during the charge/discharge processes. The reason for good reversibility can be attributed to the



fine particle size, and the employment of electrochemically inactive components as mentioned above. Nanosized active materials are less prone to subdivision because of the smaller absolute volumetric changes and reduced effective mechanical stresses within the particles [85, 86]. In addition, ultra fine particles have also relatively a low number density of atoms per grain, which leads to relatively smaller volume change during cycling. The atoms are segregated to the grain boundaries in nanosized materials and hence the grain boundary dynamics play an important role with regards to stabilizing the materials. Furthermore, the mechanical stresses caused by volume expansion of Sn during cycling is reduced or relieved by the presence of electrochemically inert materials, which play a very important role in maintaining the mechanical integrity of the electrode system. Another aspect of selecting a nanosized inactive matrix is that the matrix could undergo plastic deformation due to the stress resulting from volume expansion of the active element. It is known that some ceramic materials such as  $\text{TiO}_2$  or  $\text{ZrO}_2$  exhibit superplastic deformation due to their nano-particle size [87]. A similar response can therefore be expected from the nanosized systems selected. The specific systems selected for this study are described later. The major problem of TCO is the first irreversible capacity loss, resulting from the reaction of Li with SnO and the formation of  $\text{Li}_2\text{O}$ . Nevertheless, the development of TCO was the first demonstration of the potential of creating the so-called ‘active-inactive’ nanocomposite anode materials by the electrochemical insertion of lithium into the tin-oxide based amorphous glass. The rationale and characteristics of the ‘active-inactive’ nanocomposite concept will be explained in detail in the next session.

### **2.2 Active-Inactive Nanocomposite Anodes**

The particle size of the active component is known to relate closely with the cycling behavior [78]. However, it is very difficult to maintain a reasonable cyclability when only an active component is used as an anode since the anode has limited mechanical strength due to the fine porous structure, which can be generated during electrochemical cycling. Furthermore, the anode suffers from time-dependent structural changes such as particle growth during cycling. Several approaches have been used to

show that the use of dense electronically conductive species along with a finely dispersed Li reactant can improve the electrochemical performance [88, 89].

Following the discovery and reports of TCO, the concept of ‘active-inactive’ nanocomposite has been studied extensively. The main idea of active-inactive nanocomposite is that the cycling performance of materials reactive to lithium termed as active can be improved significantly when materials that are inert or non-reactive to lithium termed as ‘inactive’ act as the host or matrix. The inactive component plays a very important role as a ‘buffer’ or a ‘matrix’, which endures the large volumetric stresses related to the active species thereby alleviating the mechanical stress arising from volume expansion/contraction during electrochemical cycling, as mentioned earlier. The inactive component can also act as a skeleton for the resulting microstructure, which provides the sites for the reaction at the interface between the active and inactive components. In other words, the microstructure of the nanocomposite should be able to accommodate any structural change during cycling in order to retain good cyclability. The ratio between active and inactive components is also important in obtaining the desired cyclability because the aggregation of active particles is inversely proportional to the amount of the matrix components used [90]. However with increase in the amount of the inactive component, there is significant reduction in the utilizable capacity. The matrix component is also required to allow the transport of lithium ions and provide electron conduction. A schematic model of an ‘active-inactive’ nanocomposite is shown in Fig. 2-8.

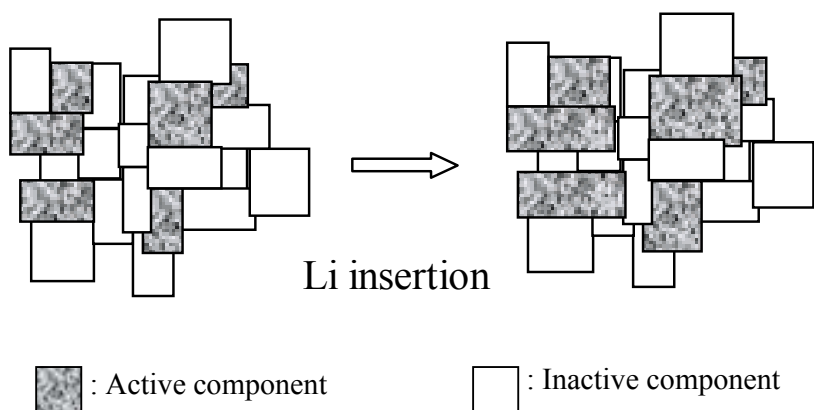


Fig. 2-8 A schematic model of the active-inactive nanocomposite and the morphological change occurring during lithium insertion.

## Chapter 2. Background

Dahn et al. have reported studies on Sn-Fe-C based nanocomposite, consisting of active  $\text{Sn}_2\text{Fe}$  and almost inactive  $\text{SnFe}_3\text{C}$  [91-94]. The real reactant in this system, however, is Sn while Fe is the inactive element. They have claimed that the anode has a capacity of  $\sim 200\text{mAh/g}$  with good reversibility. A similar concept of creating the active-inactive composite upon lithium insertion has been explored in the  $\text{Cu}_6\text{Sn}_5$ , InSb and MnSb systems by Thackeray et al. [95-97]. Similarly, SnSb-based systems have also been examined [97]. In Table 2-4, examples of several active-inactive anode systems and their characteristics reported in the literature [98-100] have been tabulated.

**Table 2-4 Examples of active-inactive composite anodes studied in the literature.**

Material	Inactive Component(s)	Specific Capacity (mAh/g)	Ref
$\text{Sn}_2\text{Fe}/\text{SnFe}_3\text{C}$	Fe+ $\text{SnFe}_3\text{C}$	180	[91-94]
$\text{Cu}_6\text{Sn}_5$	Cu	200	[95]
InSb	$\text{In}_x$ ( $x < 1$ )	290	[96]
SnSb	$\text{Sn}_x$ ( $x < 1$ )	585	[98]
MnSb	Mn	300	[97]
$\text{Ni}_3\text{Sn}_2+\text{C}$	Ni+C	280	[99]
$\text{Mg}_3\text{Ni}$	$\text{Mg}_2\text{Ni}$	290	[100]

### 2. 2. 1 Materials Selection

#### 1. Active Components

Silicon and Tin have attracted significant interest as anode materials for Li-ion battery because they have very large gravimetric and volumetric capacities compared to other Li-reacting metals as shown earlier. The introduction of lithium into silicon or tin

results in a simple compositional change, and the formation of a solid solution and new crystalline species. Table 2-5 presents the crystallographic data of the various phases and compounds observed in the Li-Sn and Li-Si systems [88].

**Table 2-5 Crystal Structures and volumes per atom of Li-Sn and Li-Si systems [88].**

Compound	Crystal Structure	Volume per Sn-atom ( $\text{\AA}^3$ )	Compound	Crystal Structure	Volume per Si-atom ( $\text{\AA}^3$ )
Sn	Tetragonal	16.3	Si	Cubic	20.0
LiSn	Monoclinic	41.1	Li <sub>12</sub> Si <sub>7</sub>	Orthorhombic	58.0
Li <sub>7</sub> Sn <sub>3</sub>	Monoclinic	61.2	Li <sub>14</sub> Si <sub>6</sub>	Rhombohedral	51.5
Li <sub>5</sub> Sn <sub>2</sub>	Rhombohedral	64.3	Li <sub>18</sub> Si <sub>4</sub>	Orthorhombic	67.3
Li <sub>13</sub> Sn <sub>5</sub>	Hexagonal	65.5	Li <sub>22</sub> Si <sub>5</sub>	Cubic	82.4
Li <sub>7</sub> Sn <sub>2</sub>	Orthorhombic	80.3			
Li <sub>22</sub> Sn <sub>5</sub>	Cubic	96.7			

Huggins et al. have shown the electrochemical potential of Li-Si and Li-Sn systems at a temperature of 415°C, which is the operating temperature of batteries using molten salts [88]. When compared with their phase diagrams, the potential plateaus almost match with the two phase regions in the phase diagrams (Fig. 2-9 (a) and (b)) since the potential of the cell can be expressed simply by the Nernst equation [101].

$$\Delta E_{cell} = \frac{RT}{nF} \ln \frac{a_2}{a_1} \quad (2-8)$$

$a_1$  : the activity of cathode,  
 $a_2$  : the activity of anode ( $a_2 > a_1$ ),  
 $n$  : number of electrons involved,  
 $F$  : Faraday's const.,  
 $R$  : Gas const.,  
 $\Delta E_{cell}$  : the potential of a cell

However, the potential plateaus are not relatively well defined at room temperature because of kinetic aspects such as low  $\text{Li}^+$  diffusivity [102].

Although fully lithiated  $\text{Li}_{4.4}\text{Si}$  or  $\text{Li}_{4.4}\text{Sn}$  exhibit high theoretical specific capacities, extensive volume changes are expected during lithiation as seen in Table 2-5, which leads to severe mechanical stress. Limiting the degree of lithiation in the active material can decrease the mechanical stress by avoiding the large volume changes that correspond to full lithiation, but it will also limit the full utilization of the active components, resulting in significant loss in available capacity. That is why the selection of the matrix material is very important in order to improve the dimensional stability. The inactive matrix components that are selected for this study will be described in the next paragraph.

## **2. Matrix Materials**

As seen earlier, most examples of nanocomposites for anode materials are based on the alloys or compounds (e.g.  $\text{Sn}_2\text{Fe}$ ,  $\text{InSb}$ ,  $\text{SnO}$ ,  $\text{SnSb}$ , etc), which forms an inactive component during lithiation. Therefore, the selection of inactive components is relatively limited because of the availability of such alloys. From this point of view, direct synthesis of active/inactive composite, which does not undergo any alteration of each component is advantageous. In order to generate nanocomposite anodes without inducing any reaction between the active and inactive components, inactive matrix materials need to be chemically inert against active elements such as Sn and Si. In addition to the chemical inertness, electrochemical inertness is also required to achieve structural integrity, which essentially eliminates oxides and metals. The choice of the inactive matrix materials is therefore limited to only non-oxide materials, which exhibit good electronic and/or ionic conductivity, good mechanical strength, and are light weight. Carbon is also a preferred matrix due to its good electronic conductivity and

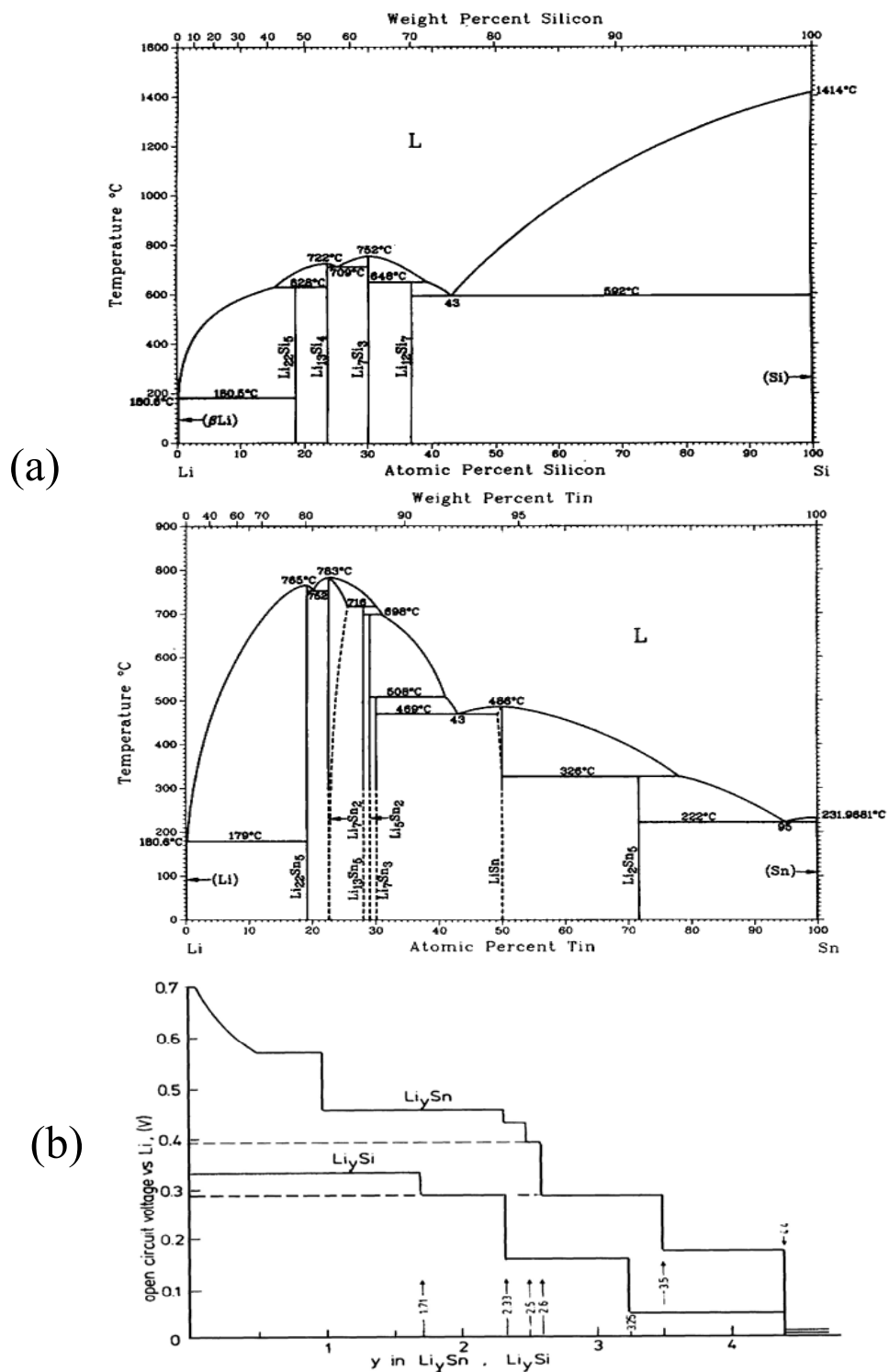


Fig. 2-9 (a) Phase diagrams, and (b) Compositional dependence of the potential in Li-Si and Li-Sn systems.

established lubricating characteristics. Furthermore, carbon is also a light-weight element. The inactive materials that were selected for this study are described below:

### **1) Titanium Nitride (TiN)**

Titanium nitride is golden-brown in color and has a NaCl structure as shown in Fig. 2-10 (a). Its high hardness ( $\approx 2000 \text{ kg/mm}^2$ ) and high melting temperature ( $\approx 3000^\circ\text{C}$ ) make TiN a useful material for coating cutting tools for obtaining improved hardness and wear resistance [103-105]. TiN has also been used as a self-heating crucible or as a conductor for electronic application due to its very high electrical conductivity of  $2\sim 5 \times 10^4 \text{ } \Omega^{-1}\text{cm}^{-1}$  [106-108]. Good electronic conductivity of TiN with high surface area has also attracted its interest for use in supercapacitors [109, 110].

### **2) Titanium Boride (TiB<sub>2</sub>)**

Titanium boride (TiB<sub>2</sub>) is the most stable compound in the Ti-B binary system. It is dark gray in color, and exhibits the AlB<sub>2</sub>-type hexagonal crystalline structure, (Fig. 2-10 (b)). Typical mechanical properties for hot-pressed TiB<sub>2</sub> include a hardness of  $1800\sim 2700 \text{ kg/mm}^2$  and a fracture toughness of  $57 \text{ MPa}\cdot\text{m}^{1/2}$  [111]. Its very high melting temperature ( $\sim 2980^\circ\text{C}$ ) and exceptional resistance to attack by molten metals make it a very good crucible material for metallizing boats. Titanium boride also has a very low electrical resistivity  $\sim 15 \times 10^{-6} \text{ } \Omega\text{cm}$  [111].

### **3) Silicon Carbide (SiC)**

Silicon carbide is very well known for its application as a wide band gap semiconductor ( $2.2\sim 3.3 \text{ eV}$ ). It has attracted significant interest due to its good properties such as thermal stability and conductivity, chemical resistance against hostile environment and high hardness ( $2400\sim 2500 \text{ kg/mm}^2$ ) [112-114]. Although SiC exhibits over 170 different polytypes according to the stacking sequence, the most common structures are 6H  $\alpha$ -SiC and cubic  $\beta$ -SiC. Cubic type SiC, which has been used in this study can be represented by the basic zinc blende structure as shown in Fig. 2-10 (c). SiC has a low resistivity of  $107\sim 200 \text{ } \mu\Omega\text{cm}$  and a high melting temperature ( $2093^\circ\text{C}$ ) [114].

The inactive materials listed above were tested for their electrochemical activity and Fig. 2- shows the differential capacity vs. voltage plots of TiN, TiB<sub>2</sub> and SiC respectively, since differential capacity plots are very useful to identify any

electrochemical reaction in the system during cycling. The peaks shown during the first discharge at  $\sim 1.25\text{V}$  and  $0.75\text{V}$  (see Figs. 2-11 (a), (b) and (c)) are caused by a surface oxide layer and the formation of a passivation layer, respectively. All plots appear to be similar without any peaks during subsequent charge/discharge cycles, confirming that the materials are electrochemically inactive within the voltage window ( $0.02\text{V}\sim 1.2\text{V}$ ) used for testing.

### **4) Carbon**

As mentioned earlier, carbon materials consist of graphitic and non-graphitic carbons. Since graphitic carbons are electrochemically active and well-known anode materials, only non-graphitic carbons are considered for use as an inactive matrix. However, there are a variety of non-graphitic materials depending on various sources and treatments used to generate them [115]. It is therefore very difficult to provide the specific properties of non-graphitic carbon. Carbons used as an inactive matrix in the present research are generated from polymeric precursors or chemical pyrolysis and are therefore amorphous. The general properties of amorphous carbon are shown in Table 2-6. Although amorphous carbon does not have excellent mechanical properties, it is still a very suitable candidate due to its good electrical conductivity and low atomic mass. Results of the study using amorphous carbon materials as inactive elements will be presented later. Table 2-6 also lists the most important relevant electronic and mechanical properties of inactive matrices as well as active elements, tin and silicon.



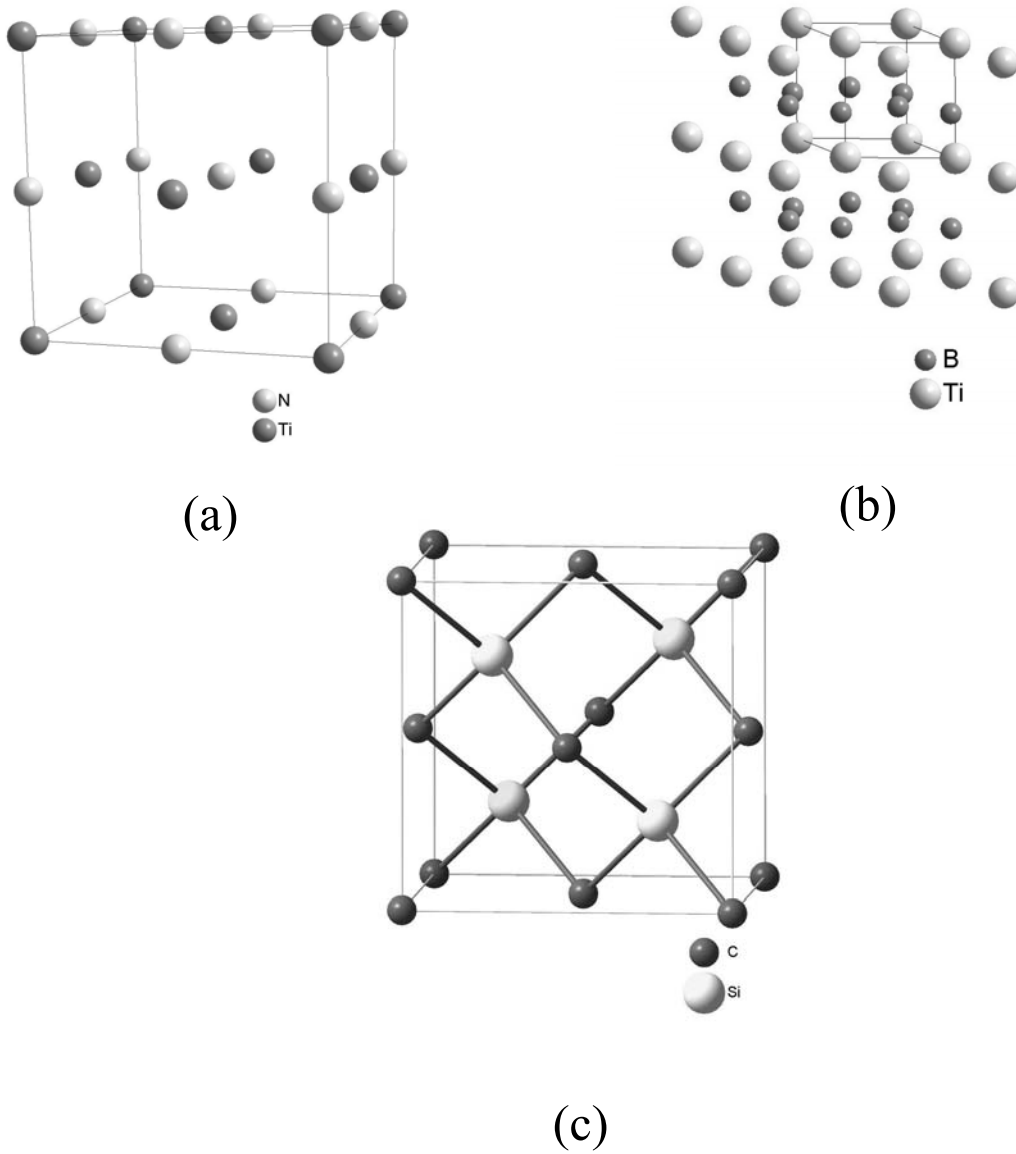
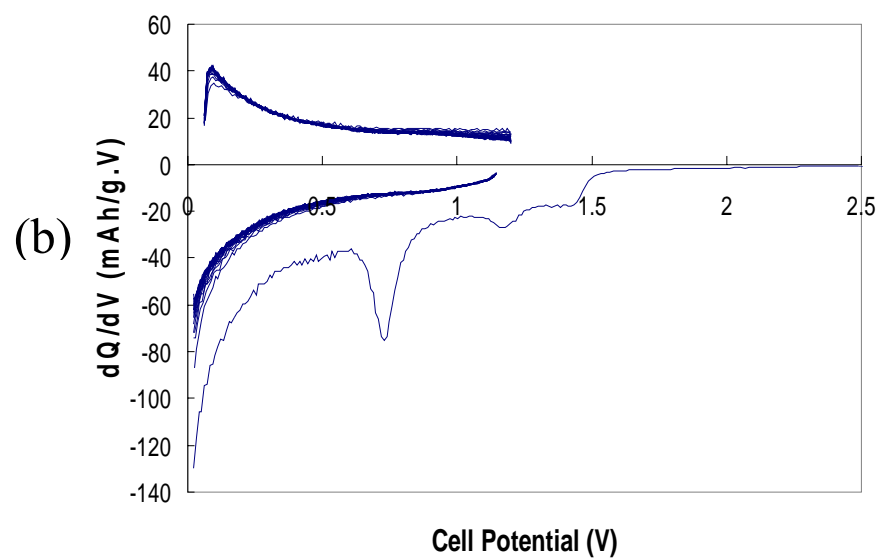
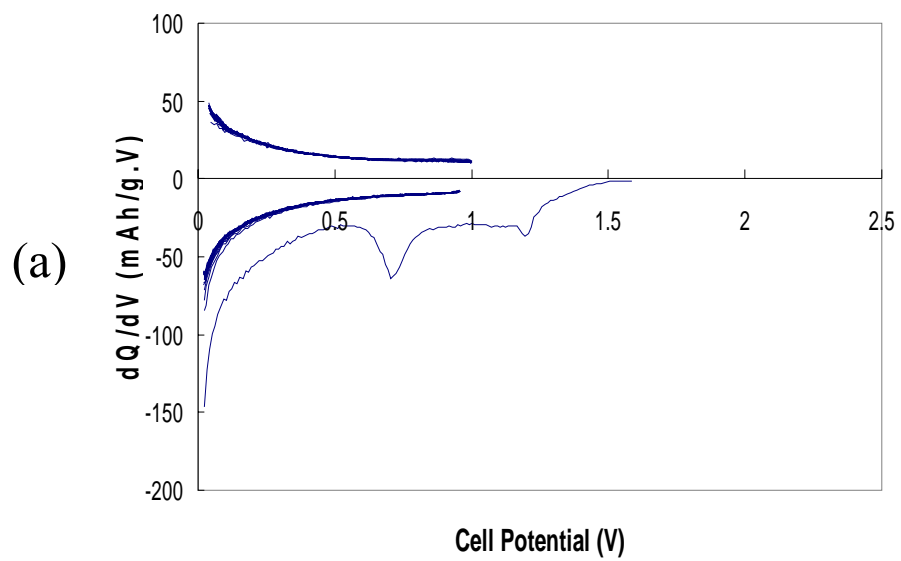


Fig. 2-10 Crystal structures of the inactive matrix components. (a) TiN with NaCl structure, (b) TiB<sub>2</sub> with AlB<sub>2</sub> structure, and (c)  $\beta$ -SiC with ZnS structure, respectively [115].



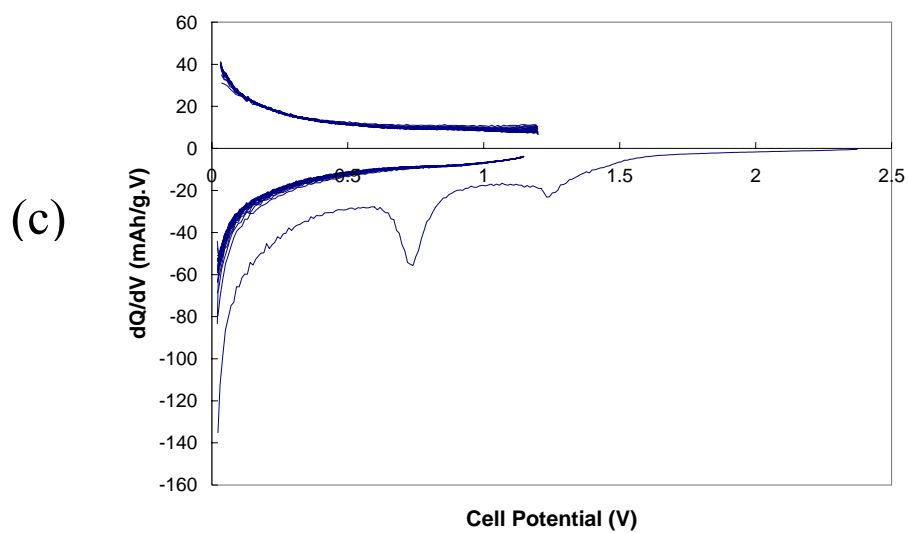


Fig. 2-11 Differential capacity vs. cell potential curves of commercially obtained from non-oxide powders of (a) TiN, (b) TiB<sub>2</sub> and (c) SiC, respectively. (Current rate : 100 $\mu$ A/ cm<sup>2</sup>, Potential : 0.02~1.2 V)

**Table 2-6 Electronic and mechanical properties of active and inactive components used for this study [114, 117-122].**

	Electronic Resistivity [ $\mu\Omega\text{cm}$ ]	Vickers Hardness [Kg/mm <sup>2</sup> ]	Tensile Strength [10 <sup>3</sup> psi]	Young's Modulus [Gpa]	Ultimate Tensile Stress [MPa]	Flexural Strength [MPa]	Fracture Toughness [MPam <sup>1/2</sup> ]
Si	$3.3 \times 10^6$	820	0.4	12.4	300	n.a. <sup>1</sup>	0.75.
Sn	12.6	255	2.1.	49.9	14.5	n.a.	n.a.
TiN	23	1900	9.0	248	n.a	n.a.	8.7
TiB <sub>2</sub>	15	3370	18.4	372-551	131	240	6.7
$\beta$ -SiC	107-200	2400-2500	5-20	262-468	550	131	3.4-4.4.
Vitreous Carbon® <sup>2</sup>	5500	225	n.a.	28	n.a.	100	n.a.

<sup>1</sup> n.a.: Not available

<sup>2</sup> Commercial amorphous carbon product by Le Carbone Lorraine, Paris, France.

### **3. 2. 2 Synthetic Methods**

The efficacy of nanocomposites for battery materials is largely dependent on the synthesis of nanosized powders. Ultra fine materials can be prepared by several methods [123] such as vapor phase, solid-state and chemical reactions in liquid. In order to generate materials useful for batteries, the yield as well as the purity of the powder is important. Therefore vapor phase reactions such as sputtering, chemical vapor deposition, etc. are not suitable due to the low yield of these processes. It is necessary to identify approaches that would not only yield nanostructured materials, but are also easily amenable to the battery industry. As discussed earlier, two such different synthetic approaches have been used in this study. The approaches have been largely determined by the ability to generate nanosized forms of the active component, Si or Sn. In this section, the syntheses techniques that have been used for the generation of the nanocomposites are described.

#### **1. High-Energy Mechanical Milling**

Mechanical milling is a powder processing technique that allows the production of homogeneous materials from mixture of powders. Mechanical energy during milling is stored as deformation energy, which enables the attainment of the desired microstructure. Mechanical milling is a process that involves synthesizing the non-equilibrium state by “energizing and quenching” similar to rapid solidification [124]. The technique has therefore good potential for developing metastable materials. Recently, different types of high-energy mechanical milling (HEMM) equipments are used to obtain higher milling energy and all the milling processes mentioned in the text therefore refer to HEMM. Fig 2-12 shows the microstructural changes that are expected to occur during mechanical milling [125].

The attributes of HEMM can be summarized as follows [126, 127]: 1) Generation of nanocrystalline or amorphous materials, 2) Expansion of solid solubility limit, 3) Refinement of grain sizes to nanometer range, 4) Synthesis of novel crystalline and quasicrystalline phases, 5) Production of a fine dispersion of secondary phases, 6) Disordering of ordered intermetallics, and 7) Synthesis of metastable alloys, 8) Ability

## ***Chapter 2. Background***

to induce chemical reactions at low temperatures. Among these, the generation of nanocrystalline materials is the most interesting application of HEMM useful for synthesizing nanocomposite anodes.

Nanocrystalline materials are single or multi-phase materials, the crystal size of which is in the range of about 1~100nm. Because of the large fraction of the atoms that are located at grain boundaries as shown in Fig. 2-13, nanocrystalline materials generally exhibit increased mechanical hardness, fracture toughness and ductility, lower saturation magnetization, and so on compared to the materials exhibiting large grain sizes [128]. Therefore, the employment of nanocrystalline composite materials for nanocomposite anodes will enhance not only the diffusion rates due to higher grain boundary diffusion but also the overall mechanical properties including fracture toughness and hardness.

Li et al. have proposed a theoretical model to explain the change in grain size occurring during mechanical milling. They indicate that the grain size in the early stages of milling follows the relation below with milling time [129]:

$$d = Kt^{-2/3} \quad (2-9)$$

where  $d$  is a grain size,  $K$  is constant and  $t$  corresponds to milling time. It has also been reported that the minimum grain size obtainable by milling is dictated by complicated factors such as plastic deformation, dislocation motion, and the recovery and recrystallization behavior of materials [129, 130]. On the other hand, the minimum grain size attainable in the case of metals with f.c.c. structure like Al, Ag, Cu, and Ni appears to be inversely proportional to the melting temperature of the metals [131]. In the case of nanocomposites, it is proposed that grain growth can be minimized or prevented due to the possible presence of amorphous phase [132].

When powders of two different elements are milled by high-energy, particles of this mixture are trapped between two balls (or other type of milling media) or a ball and the wall of a vial and are subjected to severe mechanical deformation. The particles undergo mechanical stresses as high as 200MPa in a few microseconds [133]. This impact energy leads to the deformation and cold-welding of particles, which results in

fracture due to work hardening. A balance between fragmentation and coalescence will lead to slow change in the particle size. The schematic illustration of alloying or reaction occurring during the high-energy mechanical milling is shown in Fig. 2-14. The thermal energy generated during milling plays a major role in the case of mechanical alloying because it provides the energy for overcoming the activation barrier for the reaction.

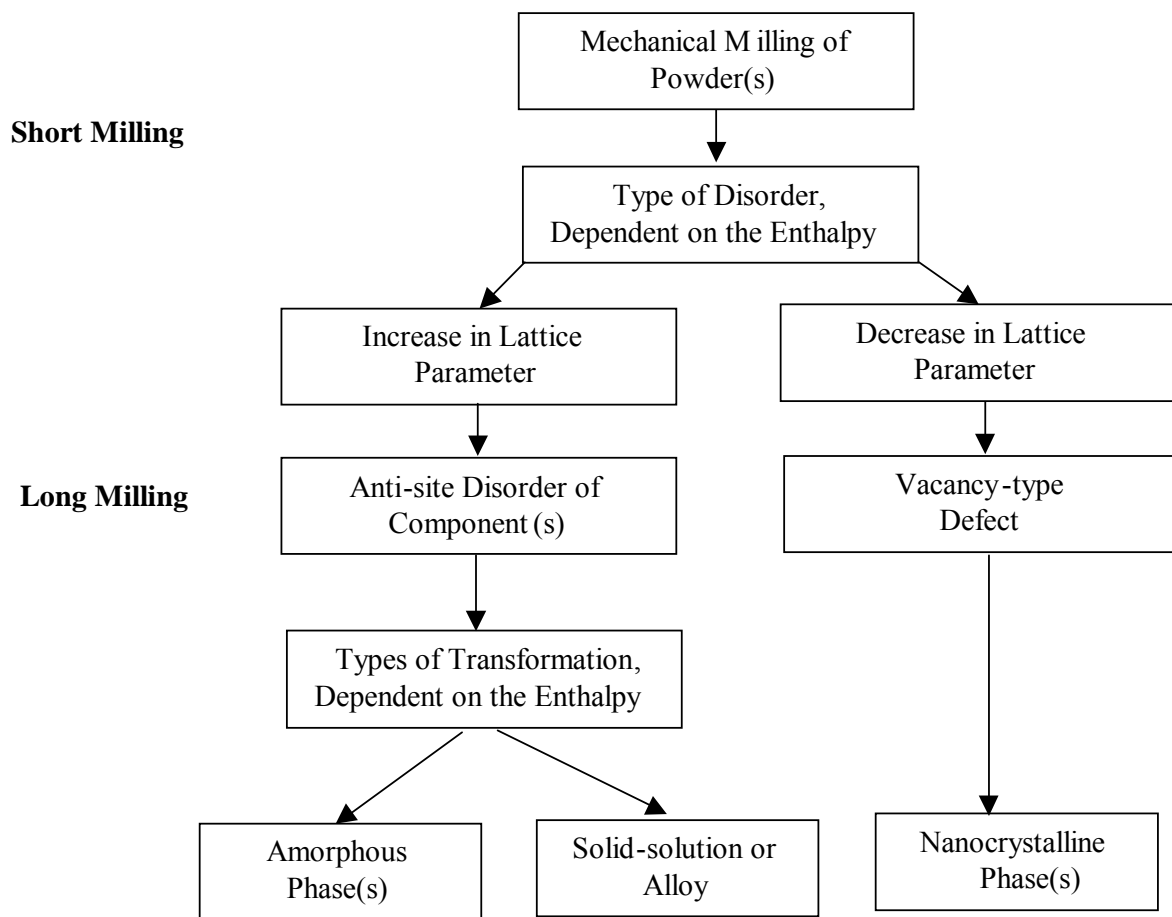


Fig. 2-12 Schematic flow-chart illustrating the expected physical and structural changes possible during mechanical milling [125].

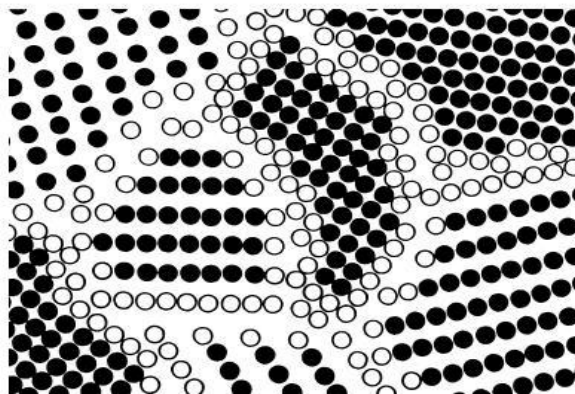


Fig. 2-13 Schematic atomic arrangement in nanocrystalline materials [124].

The milled powders may have a significant difference in morphology according to the mechanical property of the starting materials. Since the nanocomposite anode materials that will be discussed in this paper comprise two brittle materials, the alloying is not likely to occur analogous to materials that are ductile or a mixture of ductile and brittle materials. Although brittle components undergo continuous fragmentation without coalescence, the particles tend to behave in a ductile fashion at very small sizes, which results in no further reduction in the particle size. It should be also noted that elements, which are more brittle, tend to be easily fragmented and embedded in elements that are not as brittle [124].

Mechanical milling is a complex process, and its effectiveness is dependent on controlling the various milling parameters such as milling time, charge (ball-to-powder) ratio, milling temperature, milling atmosphere, etc. Milling time is one of the most important parameters because the energy transferred to the reacting media is directly related to the milling time. The time required for milling is generally chosen as the steady state condition, where fragmentation and coalescence are balanced. It should be noted that there is a strong possibility of contamination of powders arising from the milling media. The tendency to induce contamination increases when the powder is



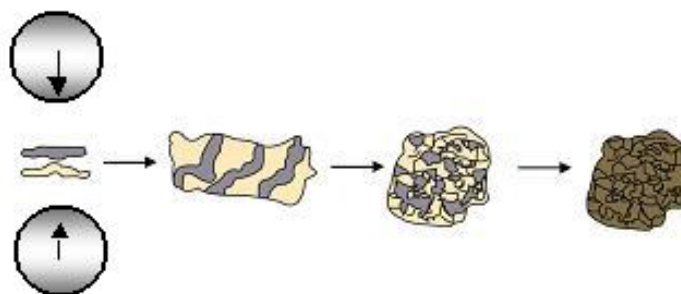


Fig. 2-14 Schematic illustration of the reactions and processes occurring during high-energy mechanical milling.

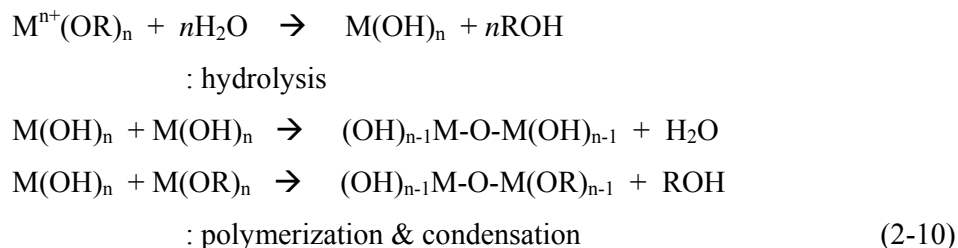
milled for an extended period beyond what is desirable. Hence it is important to select the appropriate milling time to achieve the desired product. The charge ratio is also important because an increased number of balls will increase the probability of occurrence of collision, which directly relates to milling energy. The rise in temperature during milling also has a significant effect on the product, since diffusional processes are dominant during milling. The rise in temperature is determined by complex factors including milling time, charge ratio and the temperature outside of the milling container. In order to prevent the rise in temperature, external cooling agents such as water and liquid nitrogen are intentionally used in some cases. The presence of air can also oxidize the reactive metallic powders. Hence there is a need for the use of inert atmospheres to avoid any possible oxide contamination. Different atmospheres are also used depending on the desired product. For example, nitrogen or ammonia gas is used when synthesizing nitrides.

Although HEMM appears to be promising for the generation of nanocomposite materials, there are some limitations to the technique. These limitations are due in part, to powder contamination and difficulty in milling of soft, low-melting, ductile materials, etc, as mentioned earlier. Hence chemical approaches are also investigated for the synthesis of nanocomposite materials. These methods provide an excellent pathway for

attaining good mixing of starting materials at a molecular level, thereby accelerating the formation of nanocomposites.

### 2. Chemical Routes

The sol-gel process is well known for its capability to generate oxide glasses and ceramics. The traditional sol-gel method involves hydrolysis of metal alkoxides and subsequent condensation to yield amorphous polymeric gels. The gels can then be dried in air, with the help of drying control additives supercritically to form xerogels, ambigels or aerogels, respectively [134, 135]. The dried gels when heat-treated transform to yield crystalline oxides. Metal alkoxides ( $M^{n+}(OR)_n$ ) are compounds, where the metal species (M) are bound to the organic carbon via oxygen. The metal centers in alkoxides are susceptible to attack by strong nucleophiles such as  $OH^-$  resulting in the formation of catenated oxide chains. The alkoxy group ( $OR^-$ ) in a metal alkoxide is a Lewis base that undergoes hydrolysis to form a metal oxide or hydroxide as follows [136]:



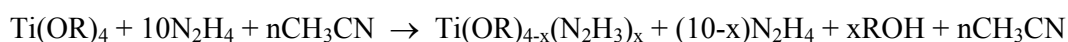
The sol-gel method can be generally utilized to generate crystalline or amorphous oxides depending on the experimental conditions such as pH in the solution, temperature and the amount of catalysts used for inducing hydrolysis, etc. The sol-gel approach can provide amorphous or crystalline oxides of high purity, fine particle size and variable compositions. The approach is particularly useful for generating metastable phases and morphologies of various materials. It has been very well exploited for synthesizing materials at lower temperature, which form typically at high temperatures

Although the term ‘sol-gel’ has been traditionally used to describe the process of formation of oxide gels or powders, as described by Brinker and Sherrer [137], the process has also been used to include several other non-oxygen containing components

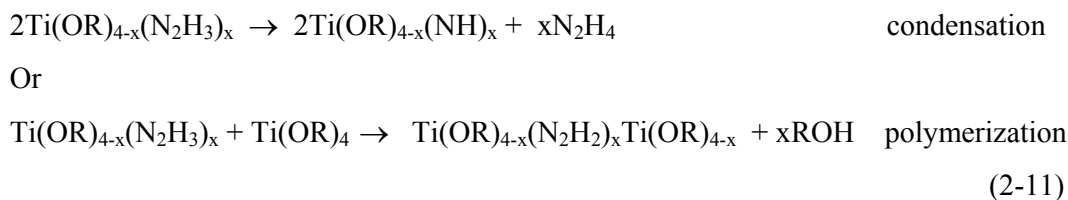
## ***Chapter 2. Background***

in recent years [138]. The broad definition of sol-gel reactions includes not only the formation of oxides but also non-oxides such as nitrides and sulfides from either gels or colloidal dispersions. Hence the approach may also be extended for synthesizing sulfides and nitrides by subjecting the metal alkoxides to nucleophilic attack by nucleophiles such as  $\text{SH}^-$  and  $\text{NHNH}_2^-$ . Alkoxides can therefore be perceived as attractive starting materials for synthesizing non-oxide materials including sulfide or nitride materials. Similarly, metal alkoxides can also be perceived as useful precursors for initiatory chemical reactions to form non-oxide ceramics. Although the sol-gel process has received widespread attention because of its tremendous flexibility in generating metal oxide gels, fine particles and thin films, their potential for directly synthesizing oxides, non-oxides, such as sulfides or nitrides, is relatively unexplored due to the extreme moisture sensitivity of the alkoxide. The precursor therefore needs to be handled carefully to prevent oxidation by exposure to air or moisture, which renders the process quite challenging.

Our research group has shown the utility of these sol-gel based approaches for directly synthesizing non-oxides, wherein non-oxygen containing nucleophiles directly replace the alkoxy groups as well as chlorine groups. We have accordingly synthesized  $\text{TiS}_2$  and  $\text{NbS}_2$  by the reaction of alkoxides with  $\text{SH}^-$  containing nucleophiles [139, 140], and studied the synthesis of  $\text{AlN}$  and  $\text{Mo}_2\text{N}$  using the reaction of corresponding alkoxides and metal chlorides with hydrazine ( $\text{N}_2\text{H}_4$ ) [141-144]. These approaches have been accordingly referred to as the thio sol-gel (TSG) and the hydrazide sol-gel (HSG) processes. As mentioned earlier, non-oxide ceramics such as titanium nitride are good candidates to serve as a matrix for nanocomposite anode. We have recently synthesized nanocrystalline  $\text{TiN}$  using the hydrazide sol-gel process (see Appendix A), which shows that very fine particle size less than 100nm can be obtained by the alkoxide-hydrazine reaction [145]. The main reaction mechanism is the replacement of isopropoxy groups in Ti alkoxide with hydrazide groups in acetonitrile used as a solvent followed by a condensation and/or polymerization reaction as described below:

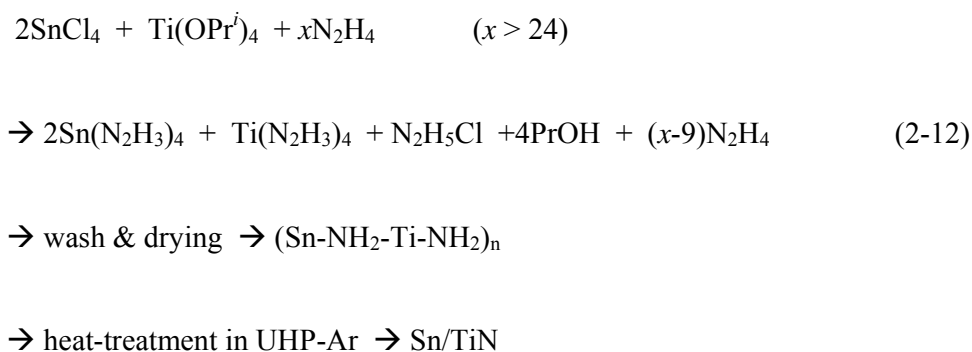


## Chapter 2. Background



Where  $x \leq 4$ , R is  $\text{C}_3\text{H}_7$  and 'n' indicates the amount of solvent.

It should be also noted that the HSG process is not limited to only generating metal nitrides. In those special systems where the corresponding nitride phase is metastable or unstable, the precursor synthesized by the HSG process renders nano-sized metal clusters instead of a nitride. Thus nano-particles of Sn have also been synthesized by the HSG process [146], which have strong affinity towards lithium. The result is shown in Appendix C. We have demonstrated that the HSG method could also be used to obtain active-inactive nanocomposites such as Sn/TiN, when titanium alkoxide and tin chloride are reacted with hydrazine resulting in the formation of a co-precipitated precursor [146]. The reactions below are proposed to describe the basic mechanism for the co-precipitation reaction resulting in the generation of Sn/TiN nanocomposite by the HSG process.



The synthesis of Sn/TiN nanocomposites, however, has a limitation that Sn particles may grow during the subsequent heat-treatments necessary for forming TiN. It has also been observed that carbonaceous species play an important role in preventing particle growth according to our previous study [145]. Thus carbon has also been investigated as a candidate matrix component for Sn-based nanocomposites. In addition, C being lighter in comparison to TiN will contribute to the nanocomposite exhibiting

## ***Chapter 2. Background***

much higher capacity in general. Although it is difficult to synthesize carbon by chemical approaches, carbonaceous materials can be easily prepared from most polymers after pyrolysis at moderate temperatures. In order to synthesize Sn/C nanocomposites, the metathetic reduction of tin halides with hydrazine has been adopted for generating Sn using appropriate solvents in the presence of a solubilized polymer, wherein the dissolved polymer acts as a source for carbon. Hydrazine is known to be a good reducing agent and has been used frequently for reducing metal halides particularly of noble metals such as Pt and Ru [147]. The HSG and metathetic reduction processes are thus very promising for synthesizing Sn-based nanocomposites. The results of these experiments will be discussed in subsequent sections.

**References**

1. I. Yoshimatsu, T. Hirai and J. Yamaki, *J. Electrochem. Soc.*, 135, 2442 (1988).
2. C. Julien and G. Nazri in *Solid State Batteries: Materials Design and Optimization*, (Kluwer Academic Publisher, Norwell, 1994).
3. J. B. Goodenough in *Lithium Ion Batteries* ed. M. Wakihara and O. Yamamoto (Wiley-Vch, Weinheim, 1998).
4. K. Mitzushima, P. C. Jones, P. J. Wiseman and J. B. Goodenough, *Mater. Res. Bull.*, 17, 785 (1980).
5. K. Ozawa, *Solid State Ionics*, 69, 212 (1994).
6. K. M. Abraham, *Electrochim. Acta*, 38, 1233 (1993).
7. J. R. Dahn, E.W. Fuller, M. Obrovac and U. von Sacken, *Solid State Ionics*, 69, 265 (1994).
8. Z. Zhang, D. Fouchard and J. R. Rea, *J. Power Sources*, 70, 16 (1998).
9. J. R. Dahn, U. von Sacken, M. W. Juzkow and H. Al-Janaby, *J. Electrochem. Soc.*, 138, 2207 (1991).
10. M. Broussely, F. Pertion, J. Labat, R. J. Staniewicz and A. Romero, *J. Power Sources*, 43, 209 (1993).
11. W. Ebner, D. Fouchard and L. Xie, *Solid State Ionics*, 69, 238 (1994).
12. C. C. Chang, Ph. D. thesis (Carnegie Mellon University, 1999).
13. C. C. Chang, J. Y. Kim and P. N. Kumta, *J. Power Sources*, 81, 56 (2000).
14. M. N. Richard, E. W. Fuller and J. R. Dahn, *Solid State Ionics*, 69, 59 (1994).
15. A. Yamada, K. Miura, K. Hinokuma and M. Tanaka, *J. Electrochem. Soc.*, 142, 2149 (1995).
16. M. Hosoya, H. Ikuta, T. Uchida and M. Wakihara, *J. Electrochem. Soc.*, 144, L52 (1997).
17. J. C. Hunter, *J. Solid State Chem.*, 39, 142 (1981).
18. J. M. Tarascon and D. Guyomard, *J. Electrochem. Soc.*, 138, 2864 (1991).
19. H. Huang and P. G Bruce, *J. Electrochem. Soc.*, 141, L106 (1994).
20. H. Huang and P. G Bruce, *J. Power Sources*, 54, 52 (1995).
21. F. Leroux, D. Guyomard and Y. Piffard, *Solid State Ionics*, 80, 307 (1995).
22. F. L. Cras, S. Rohs, M Anne and P. Strobel, *J. Power Sources*, 54, 319 (1995).

## ***Chapter 2. Background***

23. A. R. Armstrong and P. G. Bruce, *Nature*, 381, 499 (1996).
24. C. Masquelier, A. Konde and R. Kanno, *J. Electrochem. Soc.*, 145, L49 (1998).
25. K. Numata and S. Yamanaka, *Solid State Ionics*, 118, 117 (1999).
26. P. G. Bruce, A. R. Armstrong and R. L. Gitzendanner, *J. Mater. Chem.*, 9, 193 (1999).
27. Y. I. Jang and Y. M. Chiang, *Solid State Ionics*, 130, 53 (2000).
28. B. Ammundsen, J. Desilvestro, T. Groustso, D. Hassell, J. B. Metson, E. Regan R. Steiner and P. J. Pickering, *J. Electrochem. Soc.*, 147, 4078 (2000).
29. M. Morita, M. Ishikawa and Y. Matsuda in *Lithium Ion Batteries* ed. M. Wakihara and O. Yamamoto (Wiley-Vch, Weinheim, 1998).
30. J. Barthel and H. J. Gores in *Handbook of Battery Materials* ed. J. O. Besenhard (Wiley-Vch, Weinheim, 1998).
31. Y. Matsuda and H. Satake, *J. Electrochem. Soc.*, 127, 877 (1980).
32. Y. Matsuda, H. Nakashima, M. Morita and Y. Takasu, *J. Electrochem. Soc.*, 128, 2552 (1981).
33. C. C. Liang, A. V. Joshi and N. T. Hamilton, *J. Appl. Electrochem.* 8, 445 (1978).
34. B. V. R. Chowdar, R. G. V. Subba and G.Y. H. Lee, *Solid State Ionics*, 136-137, 1067 (2000).
35. G. Nagasubramanian, A. I. Attia, G. Halpert, E. Peled, *Solid State Ionics*, 67, 51 (1993).
36. D. P. Button, R. P. Tandon, H. L. Tuller and D. R. Uhlmann, *Solid State Ionics*, 9-10, 585 (1983)
37. D. P. Button, R. P. Tandon, H. L. Tuller and D. R. Uhlmann, *Solid State Ionics*, 9-10, 655 (1983)
38. A. Levasseur, M. Kbala, J. C. Brenthous, J. M. Reau, P Hagenmuller and M. Couzi, *Solid State Commun.*, 32, 839 (1979)
39. S. Rokade, K. Singh and V. K. Deshpande, *Solid State Ionics*, 18-19, 374 (1986).
40. A. Levasseur, J. C. Brenthous, J. M. Reau, P Hagenmuller and M. Couzi, *Solid State Ionics*, 1, 177 (1979).
41. J. K. Kennedy, S. Sahami, S. W. Shea and Z. Zhang, *Solid State Ionics*, 18-19, 369 (1986).

## **Chapter 2. Background**

42. V. K. Deshpande, A. Pradel and M. Ribes, *Solid State Ionics*, 28-30, 743 (1988).
43. J. K. Kennedy, Z. Zhang, and H. Eckert, *J. Non-Cryst. Solids*, 123, 328 (1990).
44. H. Ohtsuka, S. Okada and J. Yamaki, *Solid State Ionics*, 40-41, 964 (1990)
45. E. J. Plichta, W. D. Behl, D. Vujic, W. H. S. Chang and D. M. Schleich, *J. Electrochem. Soc.*, 139, 1509 (1992).
46. J. B. Bates, G. R. Grunzalski, R. A. Zuhr, A. Choudhury, C. F. Luck and J. D. Robertson, *J. Power Sources*, 43-44, 103 (1993).
47. K. West, B. Zachau-Christiansen, T. Jacobsen and S. Skaarup, *J. Power Sources*, 43-44, 127 (1993).
48. B. V. R. Chowdar and K. Radhakrishnan, *Solid State Ionics*, 44, 325 (1991).
49. A. Levasseur, M. Kbal, P. Hagenmuller, G. Couturier and Y. Danto, *Solid State Ionics*, 9-10, 1439 (1983).
50. F. Gray and M. Armand in *Handbook of Battery Materials* ed. J. O. Besenhard (Wiley-Vch, Weinheim, 1998).
51. M. Armand, *Advan. Mater.*, 2, 278 (1990).
52. X. Andrieu, J. F. Fauvarque, A. Goux, T. Hamaide, R. R'Hamdi and T. Vicedo, *Electrochim. Acta*, 40, 2295 (1995)
53. F. Alloin, J.-Y. Sanchez and M. Armand, *Solid State Ionics*, 60, 3 (1993).
54. F. Alloin, J.-Y. Sanchez and M. Armand, *Electrochim. Acta*, 37, 1729 (1992).
55. F. M. Gray, J. R. MacCallum, C. A. Vincent and J. R. M. Giles, *Macromolecules* 21, 392 (1988).
56. T. Itoh, K. Saeki, K. Kohno and K. Koseki, *J. Electrochem. Soc.*, 136, 3551 (1989).
57. R. Koksang, I. I. Olsen and D. Shackle, *Solid State Ionics*, 69, 320 (1994).
58. B. Scrosati in *Lithium Ion Batteries* ed. M. Wakihara and O. Yamamoto (Wiley-Vch, Weinheim, 1998).
59. D. Rauh, T. F. Reise and S. B. Brummer, *J. Electrochem. Soc.*, 130, 101 (1983).
60. F. C Laman and K. Brandt, *J. Power Sources*, 24, 195 (1988).
61. J. O. Besenhard, J. Guertler and P. Komenda, *J. Power Sources*, 20, 253 (1987).
62. J. Yamaki and S. Tobishima in *Lithium Ion Batteries* ed. M. Wakihara and O. Yamamoto (Wiley-Vch, Weinheim, 1998).



## **Chapter 2. Background**

63. N. Imanishi, Y. Takeda and O. Yamamoto in *Lithium Ion Batteries* ed. M. Wakihara and O. Yamamoto (Wiley-Vch, Weinheim, 1998).
64. K. Sawai, Y. Iwakoshi and T. Ohzuku, *Solid State Ionics*, 69, 273 (1994).
65. J. R. Dahn, A. K. Sleight, H. Shi, J. N. Reimers, Q. Zhong and B. M. Way, *Electrochim. Acta*, 38, 1179 (1993).
66. R. Yazami and D. Guerad, *J. Power Sources*, 43-44, 39 (1993).
67. N. Takami, A. Satoh, M. Hara and T. Ohsaki, *J. Electrochem. Soc.*, 142, 371 (1995).
68. A. Satoh, N. Takami and T. Ohsaki, *Solid State Ionics*, 80, 291 (1995).
69. T. Zheng, J. S. Xue and J. R. Dahn, *Chem. Mater.* 8, 389 (1996).
70. O. Yamamoto, N. Imanish, Y. Takeda and H. Kashiwagi, *J. Power Sources*, 54, 72 (1995).
71. G. Li, R. Xue, L. Chen and Y. Huang, *J. Power Sources*, 54, 271 (1995).
72. M. Winter and J. O. Besenhard in *Handbook of Battery Materials* ed. J. O. Besenhard (Wiley-Vch, Weinheim, 1998).
73. E. Peled, C. Menachem, D. Bar-Tow and A. Melman, *J. Electrochem. Soc.*, 143, L4 (1996).
74. C. Menachem, E. Peled, L. Burstein and Y. Rosenberg, *J. Power Sources*, 68, 227 (1997)
75. W. S. Li, L. C. Jiang, G. Y. Xie and X. Jiang, *J. Power Sources*, 58, 235 (1996).
76. H. Xiang, S. Fang and Y. Jiang, *J. Electrochem. Soc.*, 144, L187 (1997).
77. T. S. Ong and H. Yang, *J. Electrochem. Soc.*, 149, A1 (2002).
78. M. Winter and J. O. Besenhard, *Electrochim. Acta*, 45, 31 (1999).
79. J. O. Besenhard, J. Yang and M. Winter, *J. Power Sources*, 68, 87 (1997).
80. J. T. Vaughey, J. O'Hara and M. M. Thackeray, *Electrochem. Solid-State Lett.*, 3, 13 (2000).
81. R. Nesper, *Prog. Solid State Chem.*, 20, 1 (1990).
82. Sanyo Electric, US Patent No. 4,820,599, 1989.
83. T. Nohma, S. Yoshimura, K. Nishio, Y. Yamamoto, S. Fukuoka and M. Hara, *J. Power Sources*, 58, 205 (1996).
84. Y. Idota, T. Kubota, A. Matsufuji, Y. Maekawa and T. Miyasaka, *Science*, 276, 1395 (1997).

## ***Chapter 2. Background***

85. J. Yang,, Solid State Ionics 135,175 (2000).
86. L. Y. Beaulieu, D. Larcher, R. A. Dunlap, and J. R. Dahn, J. Electrochem. Soc., 147, 3206 (2000).
87. M. J. Mayo, Nanostructured Materials, 9, 717 (1997).
88. B. A. Boukamp, G. C. Lesh, R. A. Huggins, J. Electrochem. Soc., 128, 725 (1981).
89. R. A. Huggins and B. A. Boukamp, U. S. Patent 4,436,796 (1984).
90. I. A. Courtney, W. R. McKinnon and J. R. Dahn, J. Electrochem. Soc., 146, 59 (1999).
91. O. Mao, R. L. Turner, I. A. Courtney, B. D. Fredericksen, M. I. Buckett, L. J. Krause and J. R. Dahn, Electrochemic. Solid-State Lett., 2, 3 (1999).
92. O. Mao and J. R. Dahn, J. Electrochem. Soc., 146, 405 (1999).
93. O. Mao and J. R. Dahn, J. Electrochem. Soc., 146, 414 (1999).
94. O. Mao and J. R. Dahn, J. Electrochem. Soc., 146, 423 (1999).
95. K. D. Kepler, J. T. Vaughey and M. M. Thackeray, Electrochemic. Solid-State Lett., 2, 307 (1999).
96. J. T. Vaughey, J. O'Hara and M. M. Thackeray, Electrochemic. Solid-State Lett., 3, 13 (2000).
97. L. M. L. Fransson, J. T. Vaughey, K. Edstrom and M. M. Thackeray, J. Electrochem. Soc., 150, A86 (2003).
98. J. Yang, , M. Wachtler, M. Winters and J. O. Besenhard, Electrochemic. Solid-State Lett., 2, 161 (1999).
99. G. M. Ehrlich, C. Durand, X. Chen, T. A. Hugener, F. Spiess and S. L. Suib, J. Electrochem. Soc., 147, 886 (2000).
100. H. Kim, B. Park, H. Sohn and T. Kang, J. Power Sources, 90, 59 (2000).
101. D. R. Crow, Principles and Applications of Electrochemistry, (Blackie Academic & Professional, London, 1994).
102. A. Anani, S. Crouch-Baker and R. A. Huggins, 134, 3098 (1987).
103. H. Zheng, K. Oka and J. D. Mackenzie, Mat. Res. Soc. Symp. Proc. **271**, 893 (1992).
104. T. Graziani and A. J. Bellosi, Mater. Sci. Lett. **14**, 1078 (1995).
105. K. Kamiya and T. Nishijima, J. Am. Ceram. Soc. **73**, 2750 (1990).

## ***Chapter 2. Background***

106. I. N. Mihailescu, E. Gyorgy, N. Chitica, V. S. Teodorescu, G. Mavin, A. Luches, A. Perrone, M. Martino and J. Neatmtu, *J. Mater. Sci.* **31**, 2909 (1996).
107. A. J. Silvestre, O. Conde, R. Vilar and M. Jeandin, *J. Mater. Sci.* **29**, 404 (1994).
108. V. White and K. J. D. Mackenzie, *J. Mater. Sci.* **27**, 4287 (1992).
109. C. F. Jr. Windisch, J. W. Virden, S. H. Elser, J. Liu and M. H. Engelhard, *J. Electrochem. Soc.* **145**, 1211 (1998).
110. M. R. Wixom, D. J. Tarnowski, J. M. Parker, J. Q. Lee, P. L. Chen, I. Song and L. T. Thompson, *Mat. Res. Soc. Symp. Proc.* **496**, 643 (1997).
111. Cathleen Mroz Advanced Refractory Technology Inc., American Ceramic Society Bulletin, June, 55 (2000).
112. H. Morkoc, S. Strite, G. B. Gao, M. E. Lin, B. Sverdlov and M. Burns, *J. Appl. Phys.* **76**, 1363 (1994)
113. R. Verucchi, L. Aversa, G. Ciullo, A. Podesta, P. Milani and S. Iannotta, *Eur. Phys. J. B* **26**, 509 (2002).
114. F. Cardarelli, *Material Handbook; A Concise Desktop Reference*, (Springer, London, 2000).
115. M. Noel and V. Suryanarayanan, *J. Power Sources*, **111**, 193 (2002).
116. JCPDS – International Centre of Diffraction Data, (Newtown square, PA, 2002).
117. J. F. Shackelford and W. Alexander, *Materials Science and Engineering Handbook*, Third ed., (CRC Press LLC., Boca Raton, 2001).
118. Charles T. Lynch, *CRC Handbook of Materials Science Vol. I*, (CRC Press Inc., Cleveland, 1974).
119. C. P. Chen and M. H. Leipold, *Am. Cer. Soc. Bull.*, **59**, 469 (1980).
120. R. B. Ross, *Metallic Materials Specification Handbook*, fourth ed., (Chapman & Hall, London, 1992).
121. *Metals Handbook Ninth Edition*, Vol. 2, Properties and Selection: Nonferrous Alloys and Pure Metals, (American Society for Metals, Metals Park, 1979).
122. *ASM Handbook*, Vol. 2, Properties and Selection: Nonferrous Alloys and Special Purpose Metals, (ASM International, 1992).
123. H. Gleiter, *Pog. Mater. Sci.*, **33**, 223 (1989).

## ***Chapter 2. Background***

124. C. Suryanarayana, *Prog. Mater. Sci.*, 46, 1 (2001).
125. H. Bakker, I. W. Modder, G. F. Zou and H. Yang, *Mater. Sci. Forum*, 235-238, 477 (1997).
126. A. W. Weeber and H. Bakker, *Physica*, B153, 93 (1988).
127. H. Bakker, G. F. Zou and H. Yang, *Prog. Mater. Sci.*, 39, 159 (1995).
128. H. Gleiter, *Prog. Mater. Sci.*, 33, 223 (1989).
129. S. Li, K. Wang, L. Sun and Z. Wang, *Z. Scripta Metall Mater.*, 27, 437 (1992).
130. J. Eckert, J. C. Holzer, C. E. Krill III and W. L. Johnson, *J. Mater. Res.*, 7, 1751 (1992).
131. I. Börner and J. Eckert, *J. Mater. Sci. Forum*, 225-227, 377 (1996).
132. C. C. Koch, *Nanostructured Mater.* 9, 13 (1997).
133. R. B. Schwarz, *Mater. Sci. Eng.*, 97, 71 (1988).
134. T. Woignier, G. W. Scherer and A. Alaoui, *J. Sol-gel Sci. Tech.*, 3, 141 (1994).
135. H. Hirashima and K. Sudoh, *J. Non-Cryst. Solids*, 145, 51 (1992).
136. K. Kamiya and S. Sakka in *Fine Ceramics* ed. S. Saito (Elsevier, New York, 1988).
137. C. J. Brinker and G. W. Scherer, *Sol-Gel Science* (Academic press, San Diego, 1990).
138. A. C. Pierre, *Introduction to Sol-Gel Processing*, (Kluwer Academic Publishers, Norwell, 1998), pp4, 5.
139. M. A. Sriram and P. N. Kumta, *J. Mater. Chem.*, 8, 2441 (1998).
140. M. A. Sriram and P. N. Kumta, *J. Mater. Chem.*, 8, 2453 (1998).
141. J. Y. Kim, M. A. Sriram, P. H. McMichael, P. N. Kumta, B. L. Phillips and S. H. Risbud, *J. Phys. Chem. B*, 101, 4689 (1997).
142. J. Y. Kim, M. A. Sriram, P. N. Kumta, B. L. Phillips and S. H. Risbud, *J. Phys. Chem. B*, 104, 7895 (2000).
143. J. Y. Kim, M. A. Sriram, P. N. Kumta, B. L. Phillips and S. H. Risbud, in *Innovative Processing/Synthesis: Ceramics, Glasses, Composites*, *Ceramic Transaction*; Vol. 85, pp. 167-79, (American Ceramic Society, Westerville, 1997).
144. M. A. Sriram, P. N. Kumta, J. P. Matoney and E. I. Ko, *J. Mater. Sci. Lett.*, 14, 906 (1995).

## ***Chapter 2. Background***

145. I. S. Kim and P. N. Kumta, Mater. Sci. Eng. B, 98(2), 123 (2003).
146. I. S. Kim and P. N. Kumta, unpublished work.
147. E. W. Schmidt, Hydrazine and its derivatives: preparation, properties, applications, 2<sup>nd</sup> ed., (New York, Wiley-Interscience, 2001).

## Chapter 3

# Objectives

### 3. 1 Overall Objectives

The main objective of the present research is to develop nanocomposite anode materials for Li-ion applications and studying their electrochemical properties such as charge/discharge capacity, loss in capacity, and capacity retention. Accordingly, the overall objectives are outlined as three steps. The first objective is to synthesize nanocomposite anode materials using high-energy mechanical milling (HEMM) and chemical based approaches. Due to the difficulty in synthesizing Si-based nanocomposite by chemical methods and generating Sn-based composite by mechanical milling, two different synthetic approaches have been developed. The second objective of this research is to study the fundamental aspects of the electrochemical properties of each synthesized nanocomposite anode. The processing parameters and variables have accordingly been studied and correlated to the electrochemical results. The final objective is to study the structure/microstructure and obtain a basic understanding of the influence of structure, phase and microstructure on the observed electrochemical properties. The overall objective will therefore be described in detail including the specified research goals in the following.

### 3. 2 Research Goals

The research goals have been classified into three different categories:

### **3. 2. 1 Synthesis of Nanocomposite Anode Materials**

Two approaches have been used to synthesize nanocomposite anodes depending on the thermodynamic and chemical stability limitations posed by the different systems. Accordingly, high-energy mechanical milling (HEMM) and chemical based approaches have been utilized and developed to synthesize nanocomposites of various systems specified below depending on the preferred approach.

#### **1. Preparation of nanocomposites by HEMM**

Three different systems were selected.

- Silicon / Titanium nitride (Si/TiN)
- Silicon / Titanium boride (Si/TiB<sub>2</sub>)
- Silicon / Silicon carbide (Si/SiC)

All the systems listed above were prepared by HEMM. Although milling conditions varied from one system to another, the effect of milling parameters such as milling time and composition on the phase evolution, microstructure and the ensuing electrochemical properties will be discussed.

#### **2. Synthesis of nanocomposites by Chemical Approaches**

Tin-based nanocomposites were synthesized using the hydrazide sol-gel (HSG) and chemical reduction approaches. The following aspects were studied.

- 1) Choice of appropriate source materials for synthesizing the composites
- 2) Generation of Sn / TiN nanocomposites
- 3) Generation of Sn / Carbon nanocomposites
- 4) Phase evolution of the resultant precursor during heat-treatment
- 5) Reaction mechanisms involved in the formation of the desired nanocomposites using the chemical approaches.
- 6) Microstructural changes arising due to heat-treatment of the different precursors.

### **3. 2. 2 Study of Electrochemical Properties.**

The electrochemical responses of the nanocomposite anodes synthesized by

HEMM were evaluated and the effect of processing parameters was correlated to the observed electrochemical properties. Thus samples prepared using different milling times and different compositions were tested for their electrochemical characteristics. The Sn-based nanocomposites prepared by chemical approaches were also characterized with regards to the heat-treatment temperature in order to investigate the effect of heat-treatment on the phase evolution and electrochemical properties. The characterization methods include the evaluation of the capacity, cyclability and conducting systematic impedance analyses. The resultant electrochemical properties were also used as a basis to optimize the synthesis approach to generate nanocomposites that displayed improved performances.

#### **3. 2. 3 Structural and Microstructural Analyses to Generate Improved Nanocomposites**

Based on the results of electrochemical analyses, several analytical approaches were used to understand the role of structure and microstructure on the electrochemical properties. Thus high-resolution transmission electron microscopy (HR-TEM) equipped with electron energy-loss spectroscopy (EELS) was used to study the interface of the active and the inactive components and the compositional distribution of the components at the atomic and nanometer scale.

These analyses will give a better understanding of the microstructure, phase and chemistry of the nanocomposites generated by both HEMM and chemical approaches. Systematic understanding of the composition and microstructure will help to optimize the synthetic method so that nanocomposites exhibiting the optimum desired electrochemical response can be generated.



## Chapter 4

# Experimental Procedures

## 4. 1 Preparation of Nanocomposites

### 4. 1. 1 High-energy Mechanical Milling (HEMM)

The technique of HEMM as mentioned in chapter 2 is promising because of its ability to generate amorphous, metastable, and nanophase structures. This process has several advantages such as good mixing to achieve homogeneous microstructure, simplicity, ability to generate materials in a reproducible manner, and finally the process is easily scalable. Three different nanocomposites have been prepared using HEMM and a detailed description of the procedures is given in the following sections.

#### 1. The Silicon / Titanium Nitride (Si/TiN) System

The general procedure consists of milling commercially obtained materials using an airtight hardened steel vial (model 8009, round-ended). The atmosphere inside the vial is preferred to be inert because all materials used in this experiment are very reactive and easily oxidized when converted into the nano-sized state. Therefore, silicon and titanium nitride powders were batched in the vial inside an argon filled glove box. The SPEX mixer mill (SPEX CertiPrep, 8000 M) was used for milling. The repeated cyclic milling action combined with asymmetric lateral movements induce the milling media to impinge on the powder and the wall of the vial. The balls move with high-energy because of the amplitude (5cm) and speed (1200 rpm) of the clamp motion operating at a frequency (20Hz), thus generating a high-energy milling action. The exact

procedure is as follows:

2g of powder mixture comprising stoichiometric amounts of commercial Si (Aldrich, 99.5%, 325 mesh) and TiN (Aldrich, 99.5%, 325 mesh) were used for milling and the charge ratio (the weight of powder : the weight of milling media) used for HEMM is 1:25. A total 15 hardened steel balls (diameter: 8mm) were used as milling media. The milling mixture comprising of three different molar ratios of silicon and titanium nitride (1:1, 1:1.5 and 1:2) have been milled for 18 h to examine the effect of composition on the electrochemical property. The mixture of 1:2 molar ratio was also milled for different time periods (6, 12 and 18h). A schematic flow chart of the HEMM process used for generating the Si/TiN nanocomposites is shown in Fig. 4-1.

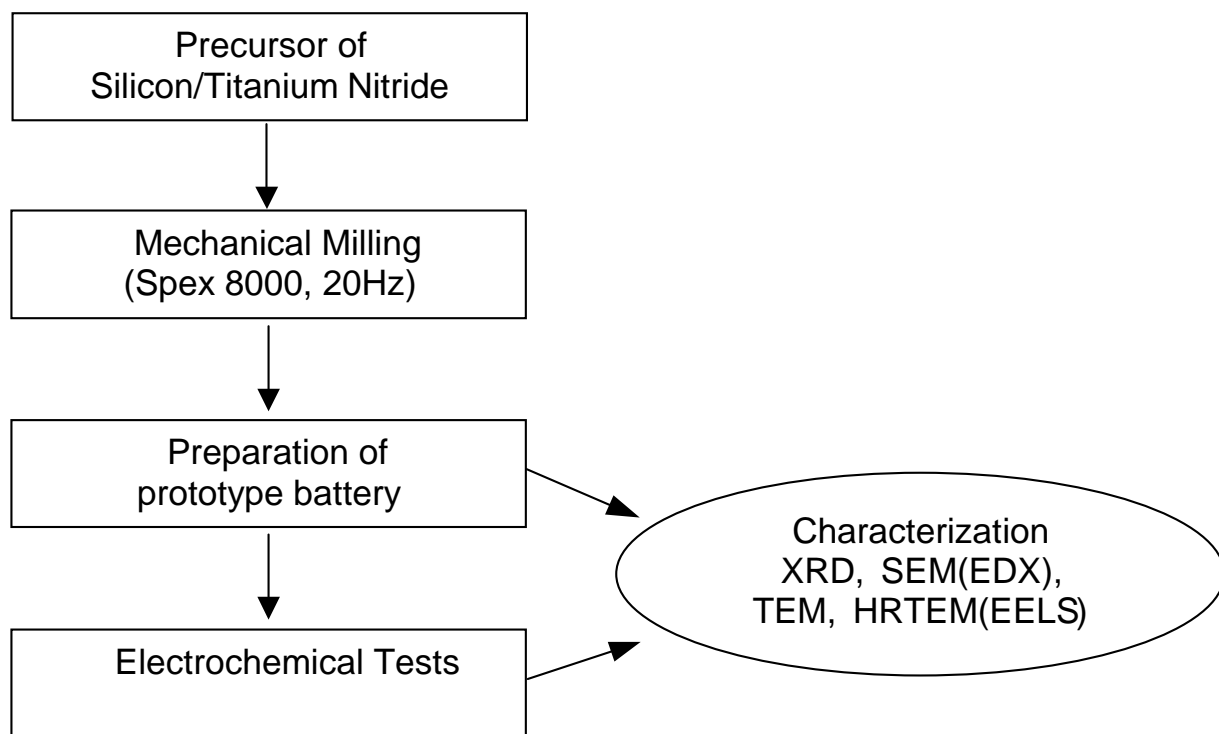


Fig. 4-1. A schematic flow chart of the HEMM process used for generating Si/TiN nanocomposites.

**2. Silicon / Titanium Boride (Si/TiB<sub>2</sub>)System**

Silicon and titanium boride nanocomposites were also synthesized using the HEMM process that was used for generating Si/TiN nanocomposites. In this system, also, 2g of the mixture of commercial powders containing 40 mol % Si (Aldrich, 99.5%, 325 mesh) (Si:TiB<sub>2</sub>=2:3) and 33.3 mol % Si (Si:TiB<sub>2</sub>=1:2) have been batched into an air-tight vial in an Ar filled glove box and then milled using different milling times, as described below. The HEMM was conducted in both cases using an air-tight hardened steel vial containing 15 balls (diameter: 8 mm) employing a charge ratio of 25:1. All experimental details are very similar to that of Si/TiN nanocomposites. The Si/TiB<sub>2</sub> nanocomposites containing 40 mol% Si were prepared after milling of 2g mixture for 10h, 15h, 20h and 25h, respectively. In the case of the mixture containing 33.3 mol % Si, premilled TiB<sub>2</sub> was used instead of the as-received commercial TiB<sub>2</sub> in order to investigate the effect of the particle size of the starting materials. Thus, 4g of commercial TiB<sub>2</sub> (Aldrich, 99%, ~10micron) was milled for 12, 18 and 24h, respectively before milling with Si using 15 balls, corresponding to a charge ratio of 12.5:1. Due to the reactivity of the nano-sized TiB<sub>2</sub> powders with air or oxygen, the premilled powders were collected inside an argon filled glove box. Some portion of the premilled powder was used for x-ray diffraction analysis in order to assess the effect of reduced particle sizes. The nanocomposite of Si using premilled TiB<sub>2</sub> was prepared as follows: 2g of mixture of silicon and premilled titanium boride was sealed with the molar ratio of 1:2 and then milled for the generation of the nanocomposites for 10 h using the same number of balls (diameter: 8 mm) employing a charge ratio of 25:1. A schematic flow sheet of the process used for generating the nanocomposites is provided in Fig 4-2.

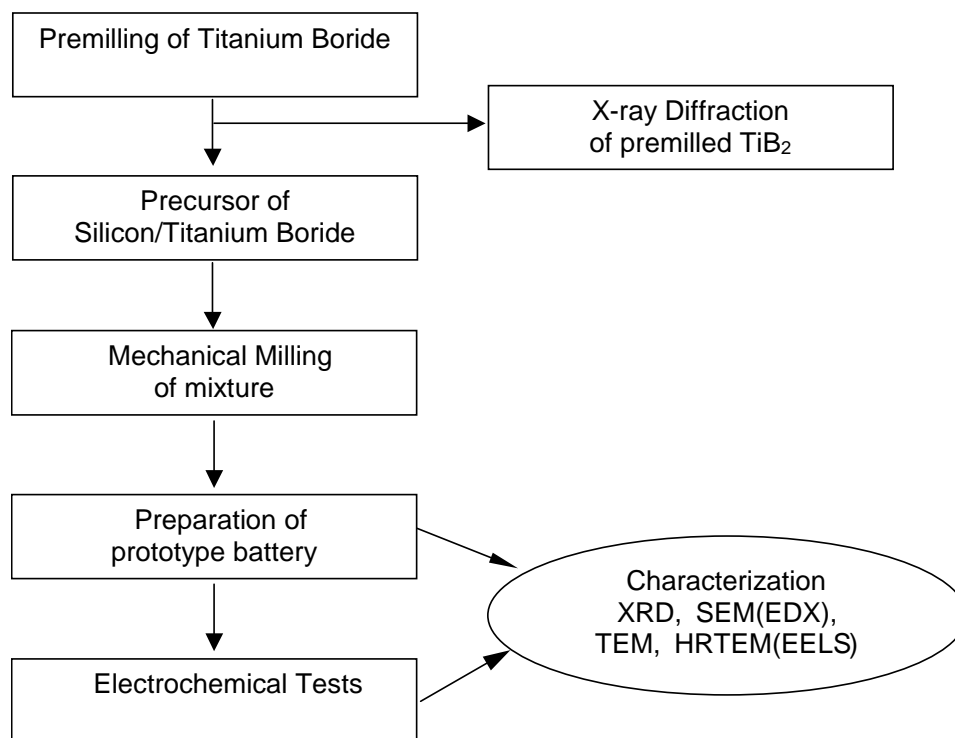


Fig. 4-2. Schematic flow chart of the HEMM process used for synthesizing Si/TiB<sub>2</sub> nanocomposites.

### 3. Silicon / Silicon Carbide (Si/SiC) System

The overall milling process for generating silicon/silicon carbide nanocomposites is very similar to the process used for processing the other nanocomposites described above. 2g of commercial power mixture was sealed in an air-tight vial in a glove box and was mechanically milled subsequently using a charge ratio of 25:1 and 15 hardened steel balls as the milling media (diameter: 8 mm). Two different starting precursors, however were used to generate the nanocomposites containing identical compositions. The first approach uses 2g mixture of silicon (Aldrich, 99.5%, 325 mesh) and silicon carbide (Aldrich, 99%, 400 mesh) in a molar ratio of 1:2, while the other approach utilizes a 2g mixtures of silicon (Aldrich, 99.5%, 325 mesh) and carbon (Aldrich, graphite, 99.9%, 1~2 micron) in a molar ratio of 2:3, selected such that a Si/SiC composite of 1:2 molar ratio is obtained *in-situ* during the

HEMM process. A schematic flow chart of the HEMM process used for generating Si/SiC nanocomposites is shown in Fig. 4-3.

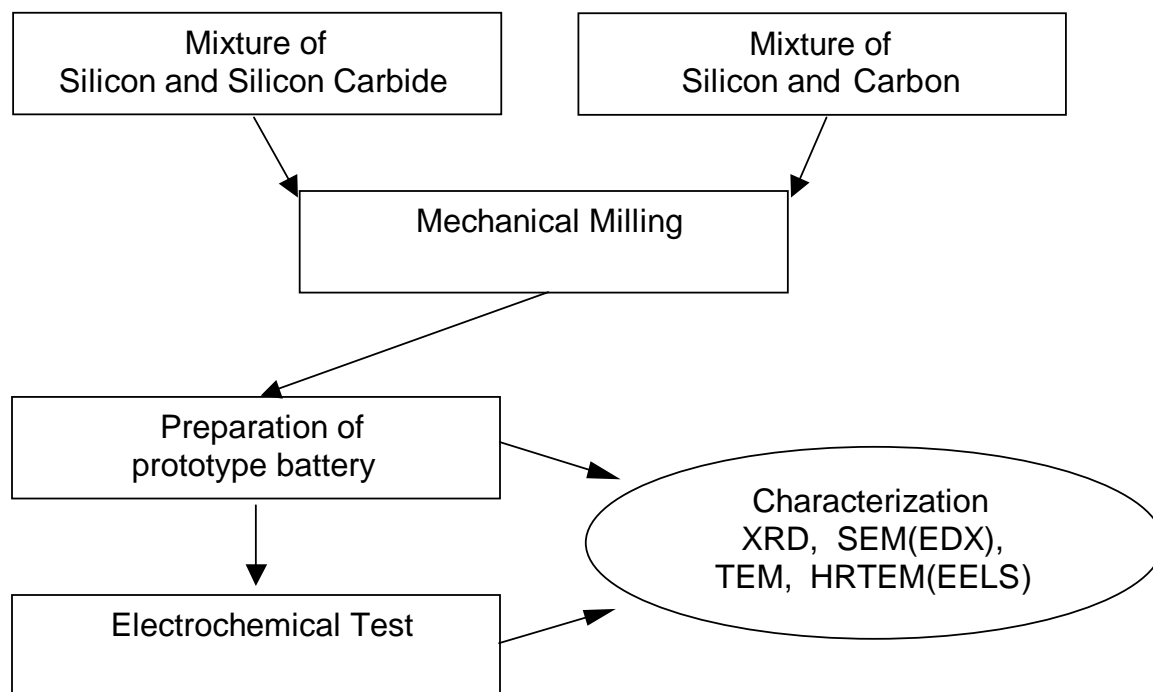


Fig. 4-3. A schematic flow chart of the HEMM process used for synthesizing Si/SiC nanocomposites.

#### **4. 1. 2 Chemical Synthesis of Sn-based Nanocomposites**

As mentioned in chapter 2, a modified hydrazide sol-gel (HSG) and chemical reduction processes have been used to obtain Sn-based nanocomposites. All the starting precursors and the solvents were measured and weighed in the absence of moisture inside an ultra high purity (UHP) argon filled glove box (VAC atmosphere, Hawthorne,

CA, O<sub>2</sub> and moisture content < 10 ppm), while the reactions were executed in a thick-walled air-tight Pyrex glass container (Corning, 1000ml, wall thickness: 5 mm) using the necessary precautions for handling air and moisture sensitive precursors. This is essential since the presence of moisture can easily induce hydrolysis of the anhydrous tin (IV) chloride (Acros, 99%), which is used as the source for Sn.

### **1. The Tin / Titanium Nitride (Sn/TiN) System**

Fig. 4-4 shows the schematic experimental procedure. The hydrazide sol-gel (HSG) approach is utilized. Different amounts of Ti-n-isopropoxide (Ti(OC<sub>3</sub>H<sub>7</sub>)<sub>4</sub>, Aldrich, 99.999%) were used for the synthesis based on the composition of Sn/TiN nanocomposites. 10ml of Ti-n-isopropoxide was used for the generation of Sn/TiN nanocomposite corresponding to molar ratios of Sn and TiN 1:1 and 1:2, while 20ml of Ti-n-isopropoxide was employed for synthesizing the nanocomposite corresponding to Sn:TiN = 2:1 molar ratio. The above amounts of the alkoxide were added to 200ml of acetonitrile (Aldrich, anhydrous, 99.8%), which is followed by the dissolution of tin (IV) chloride (Acros, 99%) into this solution. Hydrazine (N<sub>2</sub>H<sub>4</sub>, Aldrich, anhydrous, 98%) was then carefully added to this solution. The molar ratio of the starting reactants used are 24:1:2, 24:2:1 and 16:1:1 (hydrazine : titanium n-isopropoxide : tin chloride), which corresponds to a volume ratio of (hydrazine : titanium n-isopropoxide : tin chloride) of 25.6ml : 10ml : 7.8ml, 25.6ml : 20ml : 3.9ml, and 17.1ml : 10 ml : 3.9ml, respectively. Excess hydrazine is added since titanium isopropoxide also reacts with hydrazine. The powder obtained after heat-treatment is estimated to generate nanocomposites of molar ratios of Sn and TiN to be 2:1, 1:1 and 1:2, respectively. The addition of hydrazine to the tin (IV) chloride and titanium isopropoxide dissolved in acetonitrile results in a turbid solution owing to the immediate precipitation of a solid. The solution was sealed and stirred for 15h at room temperature to complete the reaction. No additional thermal treatments were induced to prevent any possible particle growth caused by elevated temperature treatments. The resultant solution was then dried in a vacuum oven for 18 h at 100°C.

The as-prepared precursor is perceived to be very hygroscopic and could still be reactive and susceptible to oxidation upon exposure to air. Therefore, extreme precautions were taken while handling the precursor powder to prevent any exposure to moisture. About 2g of the precursor was further heat-treated in UHP-Ar at 600°C, 800°C and 1000°C for 5 h respectively, using a heating/cooling rate of 5°C /min and a gas flow rate of 100ml/min.

### **2. The Tin / Carbon (Sn/C) System**

Several approaches were used for synthesizing Sn/C nanocomposites and each approach is described below.

#### **1) Poly(methacrylonitrile) (PMAN) based approach:**

The procedure consists of dissolving poly(methacrylonitrile) (Polymer Scientific, Mw 20,000) used as a carbon source in 200ml of acetonitrile (Aldrich, anhydrous, 99.8%). This is followed by the dissolution of 9.18 ml (0.05 mole) of tin (IV) chloride (Acros, 99%) into this solution. The amount of polymer used is 0.838g (0.05 mole of carbon), which estimated to achieve a molar ratio of Sn and C to be 1:1 based on the calculated estimate of Sn and C amount in the source materials. The solution is stirred for 1 h since tin (IV) chloride forms a yellow precipitate immediately after addition to acetonitrile. However, the yellow precipitate dissolves back after extended stirring for an hour. To this solution, 8.72 ml (0.4 mole) of Hydrazine (N<sub>2</sub>H<sub>4</sub>, Aldrich, anhydrous, 98%) was carefully added to yield a hydrazine to tin (IV) chloride molar ratio of 8:1. This solution is then stirred for 15h at room temperature and then dried in a vacuum oven at 100°C for 18 h. A precursor weight of ~4g was further heat-treated at 400°C, 600°C and 800°C respectively, in UHP-Ar using a heating rate of 5°C /min for the designated period of 5h, followed by a constant cooling rate of 5°C /min to room temperature. The flow rate of the gas was maintained at 100ml/min. The heat-treated powders were washed with ethanol to remove the unwanted by products such as ammonium chloride (NH<sub>4</sub>Cl) obtained following the reaction of SnCl<sub>4</sub> and N<sub>2</sub>H<sub>4</sub>. A schematic flow chart of the reduction process used for generation Sn/C nanocomposites is also shown in Fig. 4-4.

### 2) Poly(styrene) based approach:

The other approach for generating Sn/C nanocomposite is depicted in Fig. 4-5. 2g of poly(styrene) (PS) resin (Purolite co., MN-200,  $M_w=100,000$ g/mole, >25% of Divinylbenzene, bead size:0.3~1.2mm) was mechanically milled (SPEX CertiPrep, 8000 M) for 30min using 15 hardened steel balls (diameter: 8mm) and a charge ratio of media:powder = 20:1 to pulverize the bead-shaped particles into a fine powder. Tin chloride pentahydrate ( $\text{SnCl}_4 \cdot 5\text{H}_2\text{O}$ , Aldrich, 99%) was used to infiltrate tin into the PS-resin beads and powder. 35g of  $\text{SnCl}_4 \cdot 5\text{H}_2\text{O}$  was dissolved in 20 ml of DI water (5M solution) and then infiltrated with either 3.33 g (0.1 mole of carbon) of PS beads or mechanically milled powder to generate the nanocomposites of a Sn:C =1:1 molar composition. About 2g of the as-prepared precursor was dried in a vacuum oven at 100 °C for 18 h and then heat-treated at 800 °C for 5 h in UHP-Ar in the furnace. The ramp rate was 300°C/hr and the flow rate of the UHP-Ar was 100 ml/min.

The infiltration of alkyl tin compounds was conducted in a similar manner. 2g of PS- resin was mechanically milled (SPEX CertiPrep, 8000 M) for 30min using 15 hardened steel balls (diameter: 8mm) and a charge ratio of media:powder = 20:1. If necessary, the process was conducted repeatedly to obtain more of the PS-resin powder. The PS-resin powder corresponding to 3.33 g (0.1 mole of carbon) was then infiltrated with tetraalkyl tin. Three different organotin precursors were selected depending on their organic chain length, boiling points and decomposition temperatures. Accordingly, 12.1 ml of tetramethyl tin ( $(\text{CH}_3)_4\text{Sn}$ , Alfa Aesar, 98% assay), 23.5 ml of tetraethyl tin ( $(\text{C}_2\text{H}_5)_4\text{Sn}$ , Alfa Aesar, 98% assay) and 39.0 ml of tetra-n-octyl tin ( $(\text{C}_8\text{H}_{17})_4\text{Sn}$ , Gelest, 95% assay), were used to infiltrate the milled PS-resin at room temperature. In order to obtain complete infiltration, the precursor has been stirred using a stirring magnet for 1 h. The composition of the precursor was Sn:C=1:1 based on the theoretical content of Sn in alkyl tin and the real weight of carbon residue obtained after the pyrolysis of PS-resin in UHP-Ar. About 4g of the as-prepared precursor was dried in a furnace for 2h at 150°C in UHP-Ar and then heat-treated subsequently at the desired temperature, 600 or 800 °C in the same furnace. The ramp rate was 300°C/hr and the flow rate of the UHP-



#### Chapter 4. Experimental Procedures

Ar was the same as in the case of the Sn/C nanocomposite derived from PMAN (~100 ml/min). The heat-treated powder was analyzed using XRD and then evaluated for electrochemical response by fabricating electrodes to be tested in a prototype test battery. TGA and TEM studies were also conducted on the nanocomposites for analyzing their thermal, structural and microstructural characteristics.

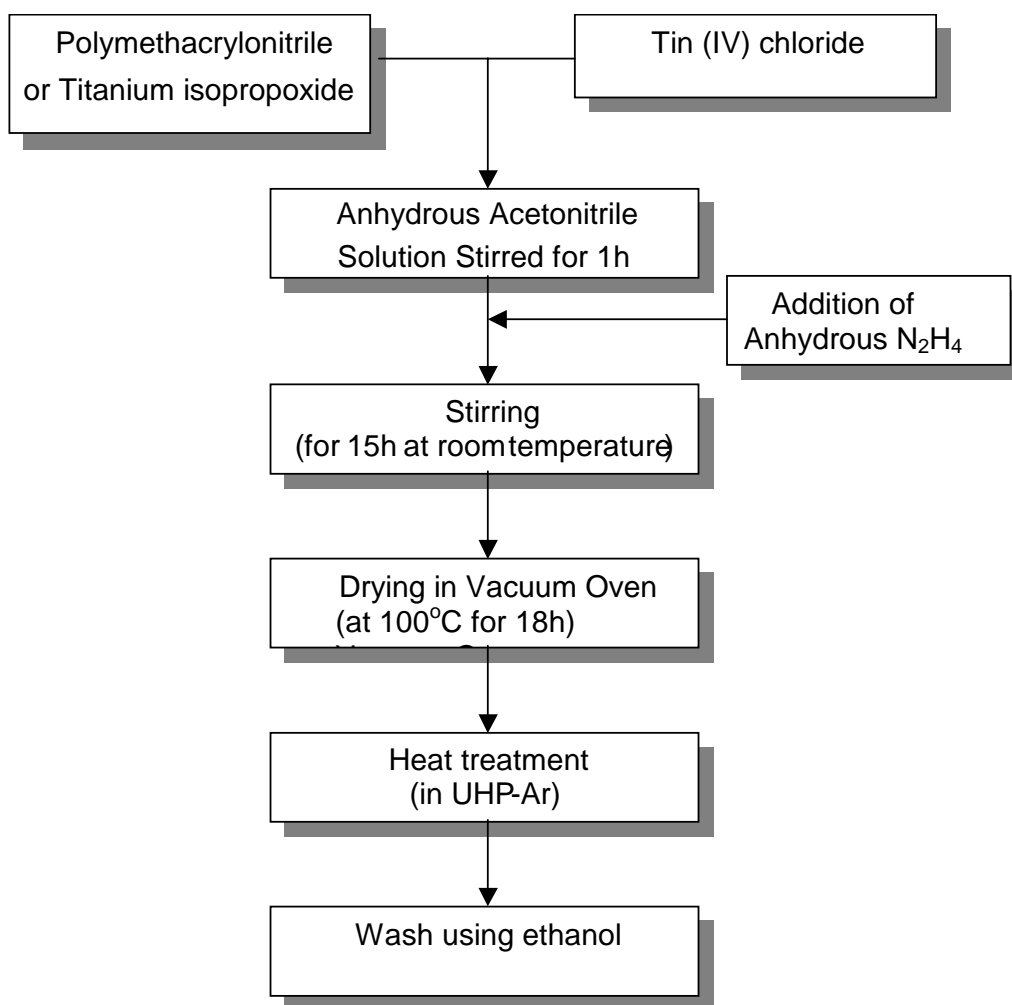


Fig. 4-4. A schematic flow chart showing the chemical synthesis procedure used to obtain Sn/C or Sn/TiN nanocomposites.

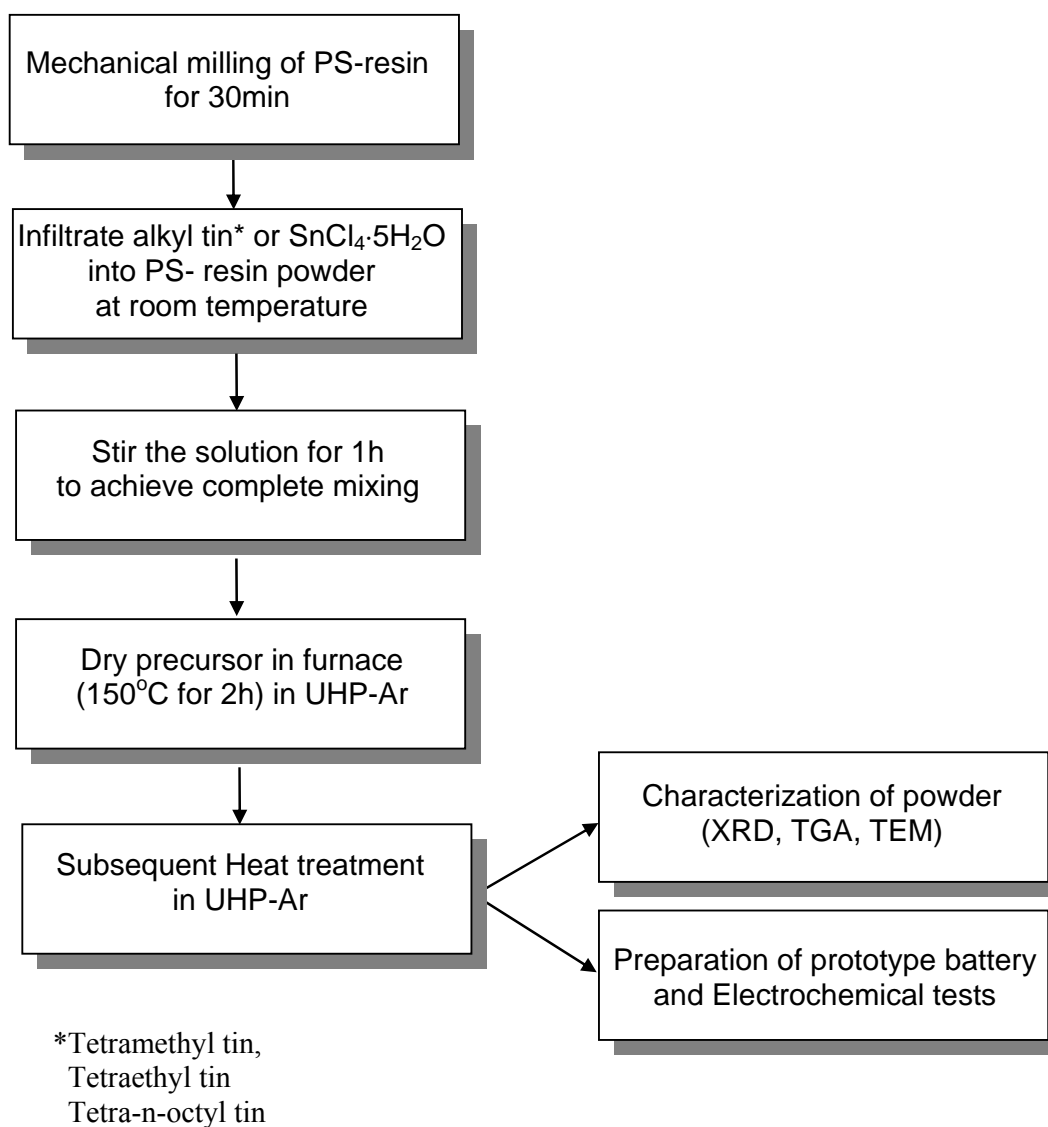


Fig. 4-5. A schematic flow chart showing the chemical synthesis procedure used to obtain Sn/ nanocomposites from alkyl tin and PS-resin.

## **4. 2 Characterization of Nanocomposites**

### **1. TGA/DTA Analysis**

Thermogravimetric analysis (TGA) and differential thermal analysis (DTA) were conducted using the TA instrument setup (TA2960, New Castle, DE). The heating rate was set at 10°C/min for all the thermal analyses, which was conducted in an UHP-Ar gas flow using a flow rate of 100ml/min.

### **2. X-ray Diffraction**

In order to examine the phase evolution and crystallization behavior, a Rigaku  $\theta/\theta$  diffractometer (Cu  $K\alpha_1$  radiation,  $\lambda = 1.5418 \text{ \AA}$ , equipped with a diffracted graphite beam monochromator) was used employing a scanning rate of 0.05°/sec and a collection time of 2 seconds. The powders were normally scanned in the range of  $2\theta = 10^\circ \sim 80^\circ$  using the voltage setting of 35kV and a current of 20mA. Samples synthesized at a later stage were analyzed using the Philips X'PERT PRO XRD system, equipped with the state-of-the-art amorphous Si detector, X'celerator, which allows the collection of x-ray data 100 fold faster than normal typical detectors. The system was used to obtain high-resolution XRD spectra at a scan step of 0.013°/s and a collection time of 50 s. Higher resolution XRD spectra are therefore obtained using the Philips X'PERT PRO system.

### **3. Scanning Electron Microscopy (SEM)**

The morphology and microstructure of the nanocomposites have been studied using a scanning electron microscope (Philips XL30) equipped with an energy dispersive x-ray analyzer (EDX), which allows the quantitative analysis of elements and its distribution in the nanocomposites by mapping each element. Analysis of non-conducting materials was conducted using a conductive coating of Au or C to prevent charge build-up on the particle surface, causing blurring of the image. The nanocomposites prepared in this study are generally electronic conductors and hence no coatings were needed. Samples were prepared by spreading the nanocomposites over

carbon tape on an aluminum stub. An acceleration voltage of 15~25kV is used for observing the images and conducting EDX analysis.

### **4. TEM and HR-TEM Analysis**

TEM analysis was conducted on the nanocomposites in order to study the particle morphology and the distribution of phases within the nanocomposites using a Philips EM420T microscope. The samples were prepared by dispersing the nanocomposite powder in ethanol medium using an ultrasonic bath, followed by placing a few drops of the solution onto a copper grid coated with an amorphous carbon film. The grid is then dried in a vacuum oven for more than 8h at room temperature prior to TEM analysis.

Due to the nano-sized nature of the nanocomposites, high-resolution transmission microscope (JEOL 4000EX) that has a point-to-point resolution at the atomic scale was used employing an acceleration voltage as high as 400kV in order to investigate the interface phases. The HR-TEM is also equipped with an electron energy-loss spectroscopy (EELS) system, which allows mapping of the elements within the particles. Samples for HR-TEM were prepared following procedures identical to the one used for conventional TEM analysis described above.

### **5. Impedance Spectroscopy**

Impedance spectroscopy (IS) analyses of the nanocomposite electrodes have been conducted using a CHI 660A (CH instruments, Austin, TX) electrochemical workstation. Impedance measurements were performed using a 5mV amplitude applied over frequency range of 0.01Hz~100kHz.

IS data have been collected for the electrodes during the first discharge of the constant current cycles at discharge voltages of 1.5, 0.75, 0.5 and 0.02V, respectively. The cells were completely disconnected from the galvanostat for the IS measurements at each discharge voltage and then connected to the impedance analyzer in order to eliminate any possible extensive electronic fluctuations arising due to the electrical connections. After completing the measurements, the setups were connected back to the galvanostat to continue further discharge to lower voltages. Impedance spectra at each

of the discharge voltages that are mentioned above were collected following the identical procedure.

The collected IS have also been analyzed using 'ZVIEW' (Scribner Associates, Inc., Southern Pines, NC) for plotting and analyzing the impedance data. It includes fitting the parameters of the equivalent circuit of each of the electrodes using a complex nonlinear least square (CNLS) method, which provides more accurate values of each parameters, since it fits all the parameters simultaneously.

### **6. 4-pt Probe Measurement**

The electrical resistivity of Si/TiN nanocomposites was measured using the 4-pt probe technique. The nanocomposite powder was compacted into a pellet (diameter: 1 cm) by pressing 1g of the powder employing a uniaxial pressure of 7000 lbs. The pellets were then measured for the electrical resistivity using the 4-pt probe measuring equipment, which has 3-D adjustable probes and a digital source meter (Keithley 2400, voltage from  $\pm 5\mu\text{V}$  (sourcing) and  $\pm 1\mu\text{V}$  (measuring) to  $\pm 200\text{V}$  DC and current ranging from  $\pm 10\text{pA}$  to  $\pm 1\text{A}$ ). The span between the probes used for the measurement was set at 1mm.

### **7. Wettability Measurement**

The wettability of Sn on TiN was investigated by measuring the wetting angle of Sn on the TiN substrate. TiN substrate was prepared by depositing a TiN layer with thickness of  $\sim 6\mu\text{m}$  on a mirror faced alumina substrate (CoorsTek, 99.6%,  $1'\%1'\%0.01'$ , roughness  $< 26\text{nm}$ ) using a sputtering equipment (Perkin Elmer 2400 8L sputtering system). Ti (Goodfellow, 99.999%) target of 5 inches was used to generate TiN film in an atmosphere of ultra high purity  $\text{Ar}+\text{N}_2$  ( $P_{\text{total}}$ : 0.9Pa,  $P_{\text{nitrogen}}$ : 0.1Pa). Sn (Aldrich, 99.5%) powder was dispersed on the sputtered TiN/alumina substrate and heat-treated in UHP-Ar for 5 h at  $800^\circ\text{C}$  in order to obtain complete melting of the Sn powder. The Sn droplets on TiN were examined using scanning electron microscope (Philips XL30) for the measurement of wetting angle.

**8. Brunauer, Emmett and Teller (BET) Specific Surface Area Analysis**

The specific surface area of the nanocomposite powders and the polymeric polystyrene and PMAN precursors was measured using the Brunauer, Emmett and Teller (BET) method ( $N_2$  adsorption, Quantachrome Instruments). 0.5g of samples were used for each measurement, which were dried at 150 °C in a vacuum for 3h before measuring the specific surface area and specific surface area was measured using the 5 pt BET technique.

### **4. 3 Characterization of Electrodes**

#### **1. Anode Preparation**

Electrodes from the synthesized nanocomposites were prepared for electrochemical testing by generating a slurry consisting of 0.5g of as-synthesized powder, 0.042g of acetylene black and 0.032g of polyvinylidene fluoride (PVDF) in 1~1.5ml of N-methyl-2-pyrrolidone (NMP). The resultant slurry was then coated onto the Cu foil (INSULECTRO, electro-deposited, thickness: 175 $\mu$ m), followed by drying in an oven overnight. The coated Cu foil was then punched into disks  $\sim 0.8\text{cm}^2$  in area and then dried inside a vacuum oven at 110  $^{\circ}\text{C}$  for 15h. The dried disks were transferred to a glove box (VAC, Hawthorne, CA, with oxygen and moisture sensors, moisture  $< 0.15\text{ppm}$  and oxygen  $< 0.5\text{ppm}$ ) to assemble the test batteries. The weight of the electrodes were typically in the range of 0.002~0.004g.

#### **2. Battery Assembly for Electrochemical Test**

A “hockey-puck” cell was used for the characterization of the electrochemical properties as shown in Fig. 4-6. This is a 3 electrodes test cell that includes a Li-reference electrode. It should be noted that this is a “half-cell” setup and the Li-foil counter electrode is really the true anode. Thus the active anode material is actually tested as a cathode since it is at a slightly positive potential with respect to lithium. Therefore, the prepared cathodes are tested to analyze the electrochemical behavior. The reference electrode is placed nearby the edge of the cathode (the nanocomposite anode) in order to measure the exact voltage of the electrode while a glass fiber separator (Whatman) is located between the cathode and the anode. A liquid electrolyte consisting of 1M  $\text{LiPF}_6$  in ethylene carbonate/dimethyl carbonate (EC/DMC) with a molar ratio of EC:DMC=2:1 is used for the test.

The Sn/C nanocomposites obtained from alkyl tin and PS-resin were tested for their electrochemical response using a ‘coin cell’ setup (Hohsen Corp., CR2016 type). The setup is a 2-electrodes cell, where the reference electrode is absent. However, Li-

foil is used as a counter electrode, the voltage of the cell is measured with respect to Li-foil. The schematic diagram of the CR 2016 coin cell is shown in Fig. 4-7. The test results appear identical when compared to the results from a hockey puck cell. Polyethylene sheet (Tonen Chemical Corp, thickness: 0.001') is punched into disks for the separator and the same electrolyte is used for the test.

### **3. Characterization of Electrochemical Behavior**

All hockey-puck and coin-cell batteries were cycled at constant current using the galvanostat (Arbin Instrument, TX). Tests were conducted using a constant current density of  $0.25\text{mA}/\text{cm}^2$  or  $0.10\text{mA}/\text{cm}^2$ . All the batteries tested in this study were cycled in the voltage range from 0.02~1.2 V with a 60 s rest period between the charge/discharge cycles.



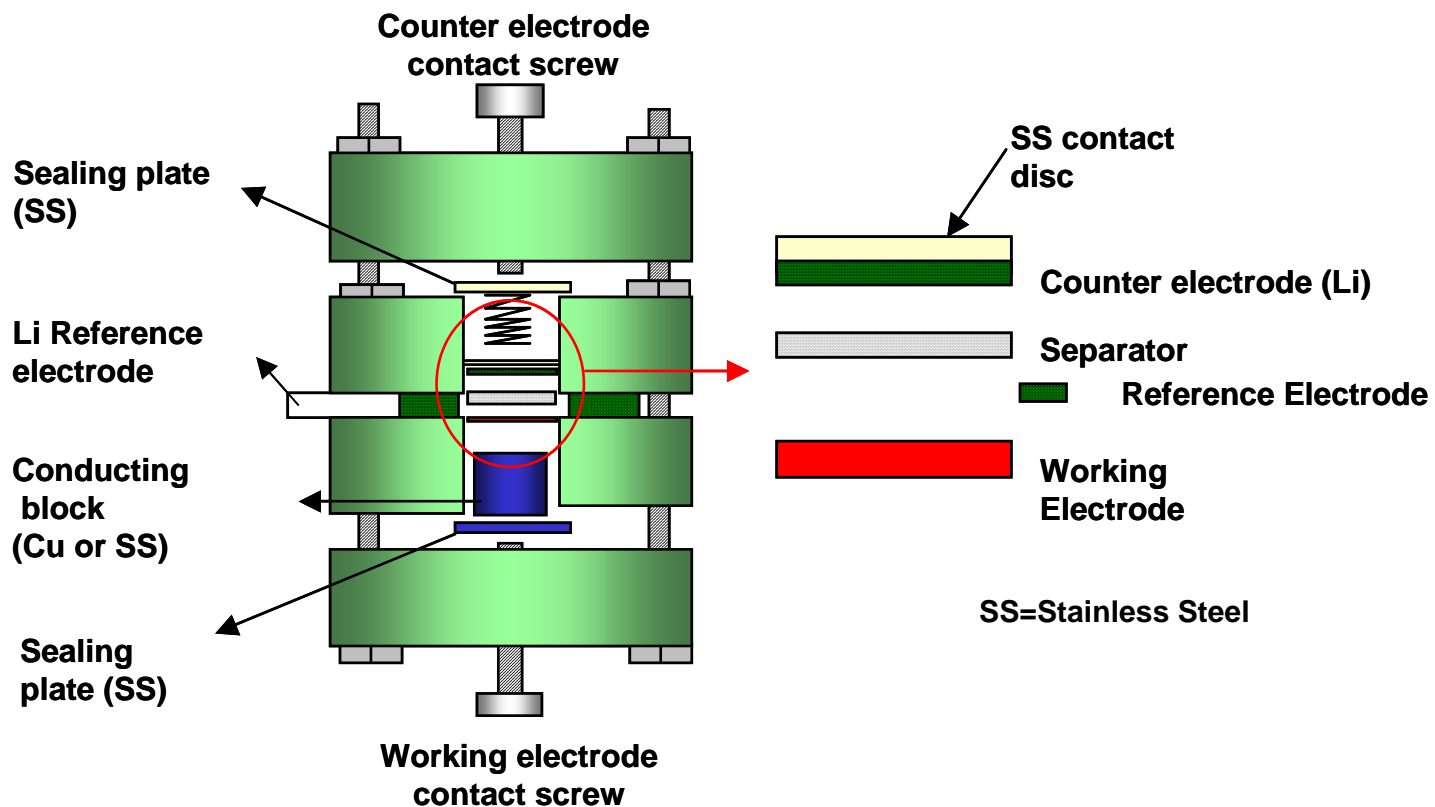


Fig. 4-6. Schematic cross-section of the prototype "hockey-puck" cell used for the characterization of the electrochemical response of the synthesized nanocomposites.

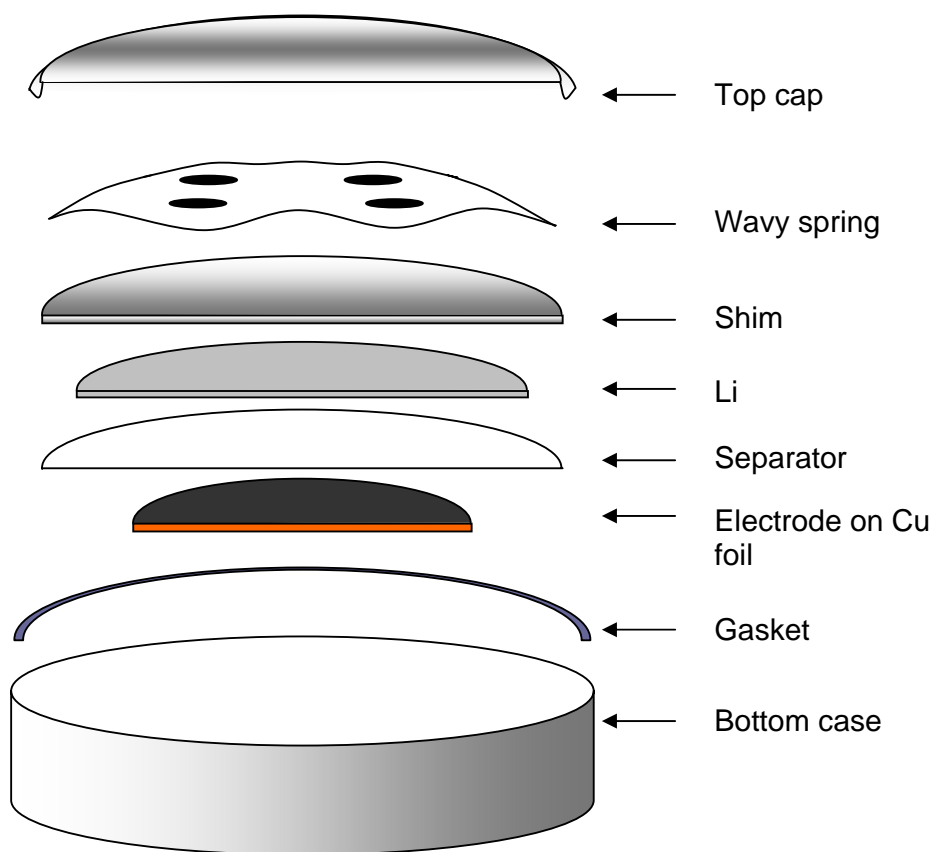


Fig. 4-7. Schematic cross-section of the “CR 2016” type coin cell used for the characterization of the electrochemical response.

## *Chapter 5*

### **Results and Discussion**

#### **Part I. Nanocomposite Electrodes Synthesized using HEMM**

##### **5. 1 Silicon/Titanium Nitride Nanocomposites**

Si/TiN nanocomposites have been synthesized using the high-energy mechanical milling (HEMM) process. The main objective is to develop nanocomposite anodes for Li-ion batteries and therefore it is very important to identify the experimental conditions that yield the best electrochemical performance. The experimental conditions that were optimized include composition of the starting mixture and milling time. Other parameters such as charge ratio and the amount of powder used were kept fixed. It should be noted that there are limited changes possible in the composition of the initial mixture since the nanocomposite electrodes need to have a desirable capacity, which is determined by the amount of active material. As a result, milling time is the most preferred variable that is modified to achieve the desired properties. After identifying the best conditions for synthesizing the electrode, the nanocomposite has been studied in detail using various analytical techniques mentioned in the previous chapter. Results of these analyses would also provide guidelines for further improving the electrochemical performances of the nanocomposite electrodes.

**5. 1. 1 Effect of Composition on the Nanocomposites**

Si/TiN nanocomposites using three different Si and TiN compositions have been generated using the high-energy mechanical milling approach. Fig. 5-1 exhibits the XRD pattern of these three nanocomposites prepared by HEMM for 18h. The peaks observed in each sample are almost identical irrespective of the composition. All the broad peaks shown in the XRD patterns correspond to crystalline TiN, indicating the nanocrystalline nature of the inactive matrix. There are no x-ray peaks visible corresponding to the active component, which suggests that the Si present in the nanocomposites is amorphous. As mentioned in chapter 2, the component that is more brittle undergoes fragmentation at a faster rate, and therefore Si particles become amorphous while TiN remains nanocrystalline. It should also be noted that milling Si alone is not capable of generating amorphous Si, indicating that fine particles of TiN also play an important role as milling media.

Fig. 5-2 shows the capacity vs. cycle number for the different compositions of nanocomposites obtained after milling for 18h. The nanocomposite containing 50 mol% Si (Si:TiN = 1:1) shows the highest initial discharge capacity  $\sim 870\text{mA/g}$ , which decreases very rapidly compared to the other two samples. However, the nanocomposite containing 33 mol% Si has a relatively low initial discharge capacity  $\sim 380\text{mAh/g}$ , which remains stable without undergoing any significant loss up to the 20th cycle. As seen clearly from the plot, the capacity decreases with a decrease in the amount of the active component since only Si reacts with Li during cycling. Based on the concept of ‘active-inactive’ composites, the inactive matrix does not contribute to any electrochemical reaction with Li but only provides the structural integrity leading to the stability of the structure during cycling. Considering that most of the fade in capacity in Li-alloy anodes arises from cracking or crumbling of the active components, structural integrity during electrochemical cycling directly relates to the retention of the capacity. Hence incorporation of a larger amount of the inactive matrix helps to improve capacity retention, as shown in Fig. 5-2, although a primary limitation is the loss in the overall capacity of the nanocomposite.

Fig. 5-3 shows the differential capacity vs. voltage for the first 20 cycles for the nanocomposites containing 50 mol% and 33mol% of Si, respectively obtained after

milling for 18 h. The broad peaks in each plot ( $\cong 0.3, 0.45\text{V}$ ;  $\cong 0.08, 0.2\text{V}$ ) correspond to the reaction of Li with Si, indicating the nanocrystalline nature of Si. The decrease in peak intensity as shown in Fig. 5-3 (a) and (b) is due to the loss in capacity during cycling.

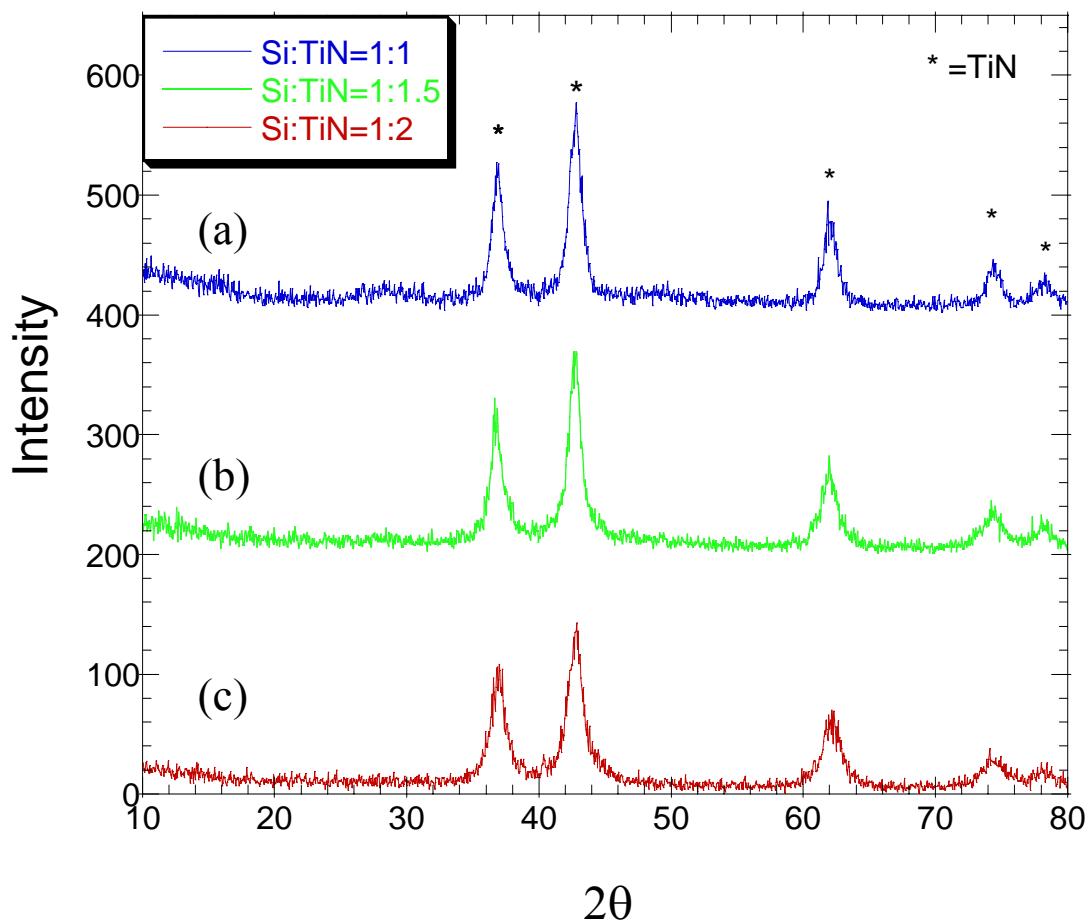


Fig. 5-1 X-ray diffraction patterns of various compositions of Si/TiN nanocomposites obtained after milling for 18h (a) Si:TiN=1:1, (b) Si:TiN=1:1.5 and (c) Si:TiN=1:2, respectively.

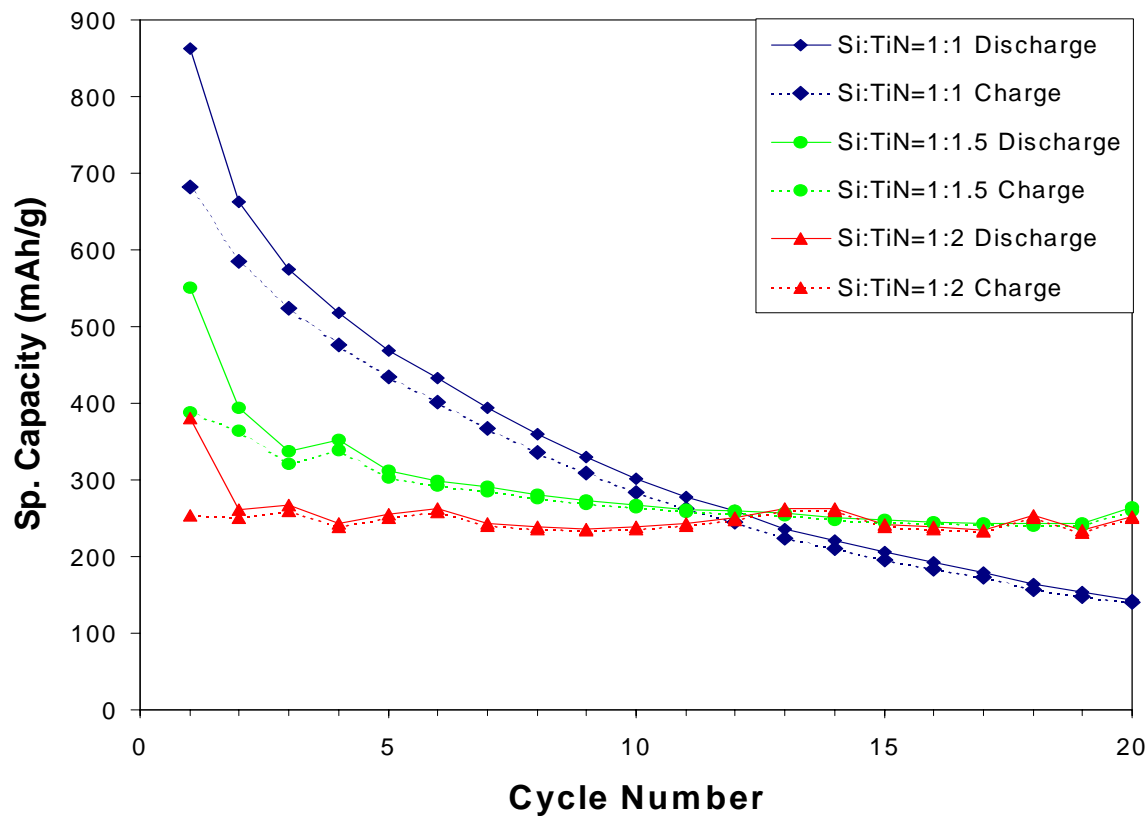
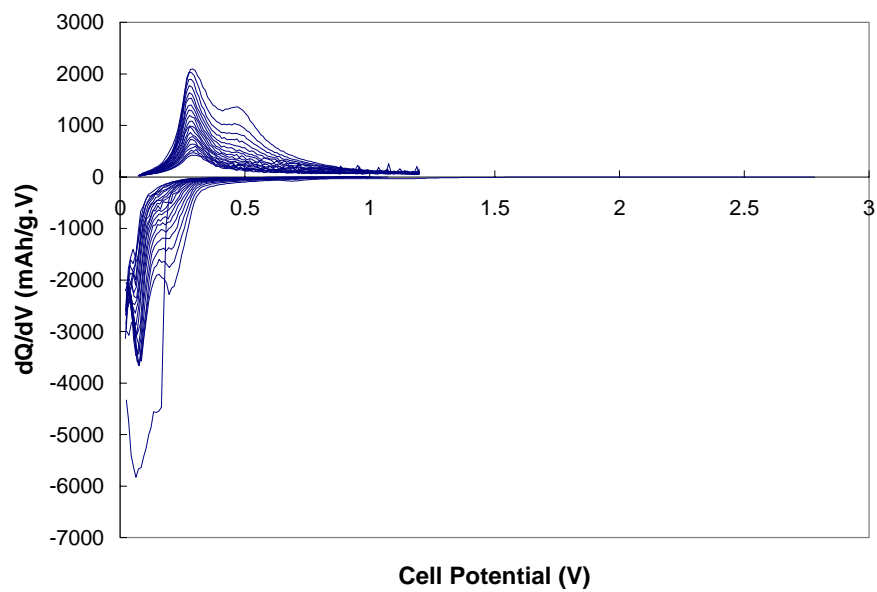
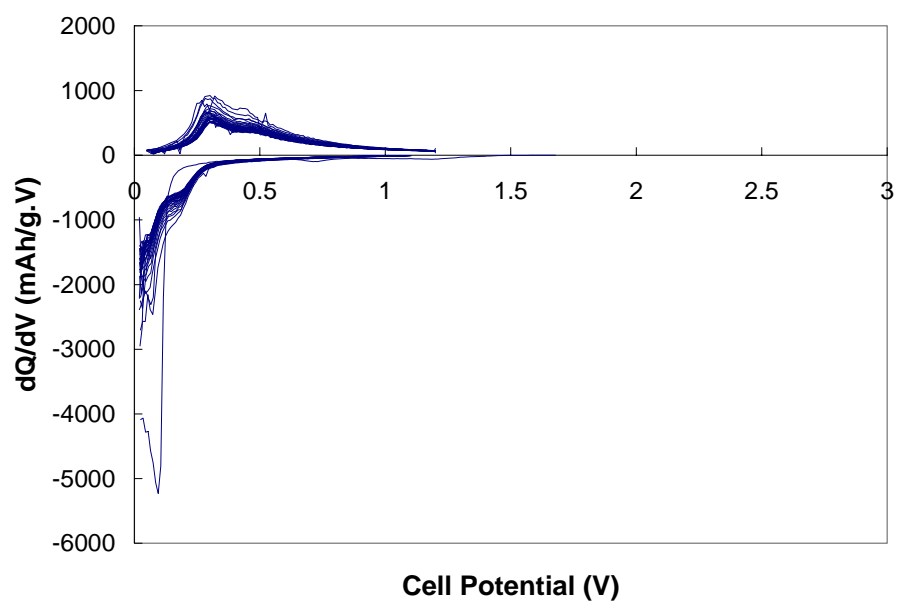


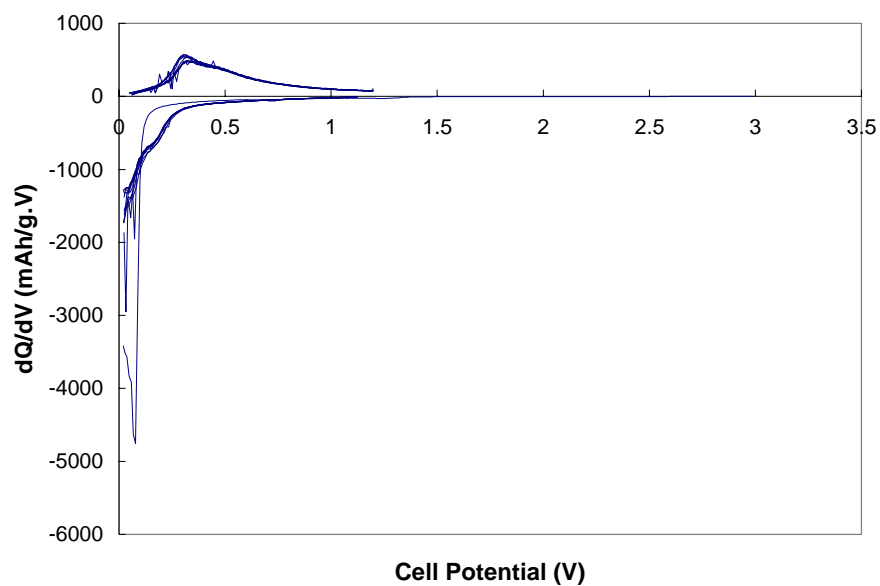
Fig. 5-2 Capacity as a function of cycle number for the different Si/TiN nanocomposites obtained after milling for 18h, (a) Si:TiN=1:1, (b) Si:TiN=1:1.5 and (c) Si:TiN=1:2, respectively. (Current rate:  $250\mu\text{A}/\text{cm}^2$ , Potential: 0.02~1.2 V)



(a)



(b)



(c)

Fig. 5-3 Differential capacity vs. cell potential curves for the first twenty cycles of the different nanocomposites with a molar ratio of (a) Si:TiN=1:1 and (b) Si:TiN=1:1.5, and (c) Si:TiN=1:2 obtained after milling for 18 h. (Current rate:  $250\mu\text{A}/\text{cm}^2$ , Potential: 0.02~1.2 V)



### **5. 1. 2 Effect of Milling Time on the Nanocomposites**

Based on the electrochemical response of various Si/TiN composites, the compositions corresponding to a molar ratio of Si:TiN = 1:2 (i.e. 33.3 mol% Si) exhibited the best electrochemical properties. Hence, the rest of the work was focused on this composition of the composite. In order to analyze the phases present after milling, x-ray diffraction was conducted on the as-milled powders obtained after milling for various time periods (see Fig. 5-4). All the peaks in the patterns correspond to TiN and the broad nature of the peaks suggests the nanocrystalline nature of the TiN powder.

The non-observance of any Si related peak in XRD indicates that Si exists in a nanocrystalline-amorphous form well dispersed inside the powder even after milling for a short time period of only 6 h. This suggests that the HEMM process provides enough energy to generate the nanocomposite powder of Si and TiN. It is not clear based on these results whether Si reacts with TiN to form any Si-N type bonds. Thermal treatments of the nanocomposites described later do provide evidence suggesting the chemical stability of Si and TiN. Based on the XRD patterns, it can be convincingly mentioned that the composites are composed of a nanosized TiN matrix containing a uniform dispersion of amorphous Si independent of the composition. Due to the very small size of the Si crystallites, the impact of volume expansion induced by the phase transitions undergone by the active phase, on the inactive matrix is minimized, and hence the composite can be expected to remain stable during cycling. This is one of the most important requirements for achieving good cyclability in these nanocomposites.

The capacity of the electrodes prepared with these powders is shown in Fig. 5-5. The overall capacity appears to decrease as the milling time is increased, indicating a reduction in the amount of the active Si phase exposed to Li ions. It was therefore decided to investigate the exact cause for this observed response. It could however be speculated at this point that the Si nanoparticles could be buried or enclosed by TiN during milling, thereby preventing their reaction with lithium. Results of electron microscopy and electrochemical impedance analyses discussed later clearly verify this

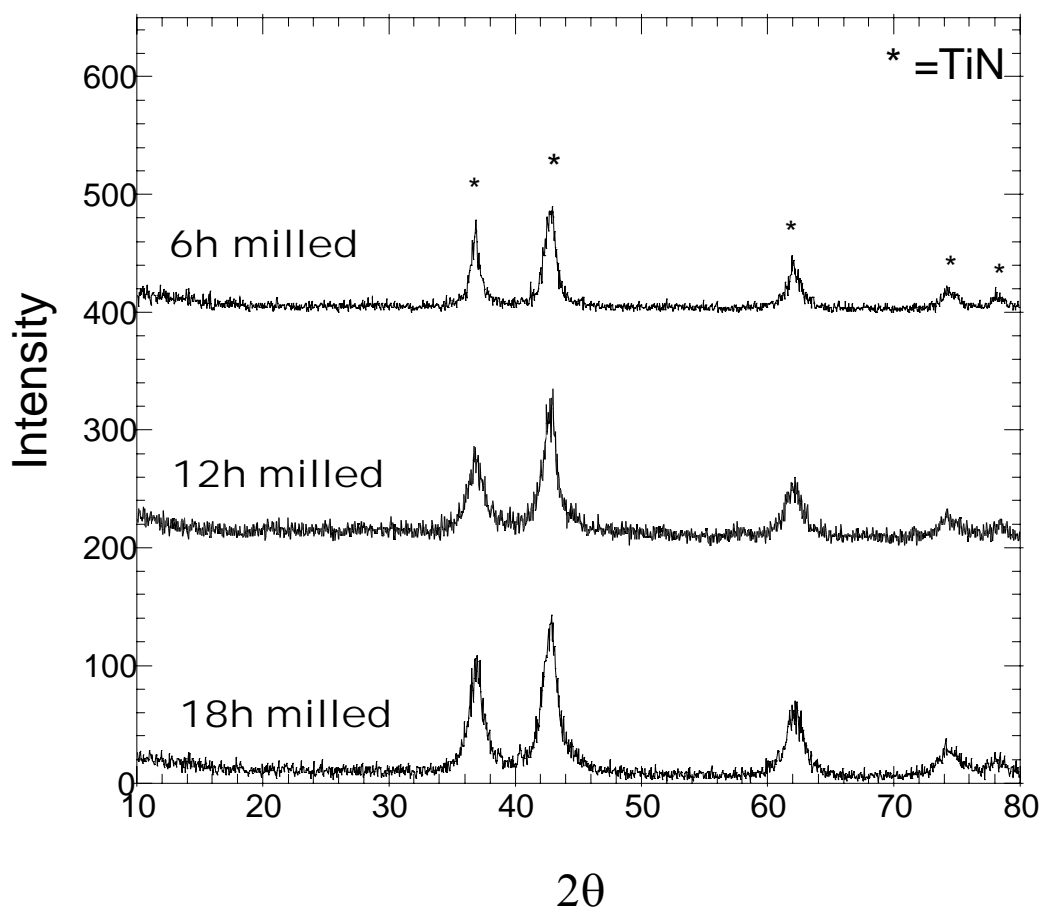


Fig. 5-4 X-ray diffraction patterns of Si:TiN=1:2 composites obtained after milling for 6 h, 12 h and 18 h, respectively.

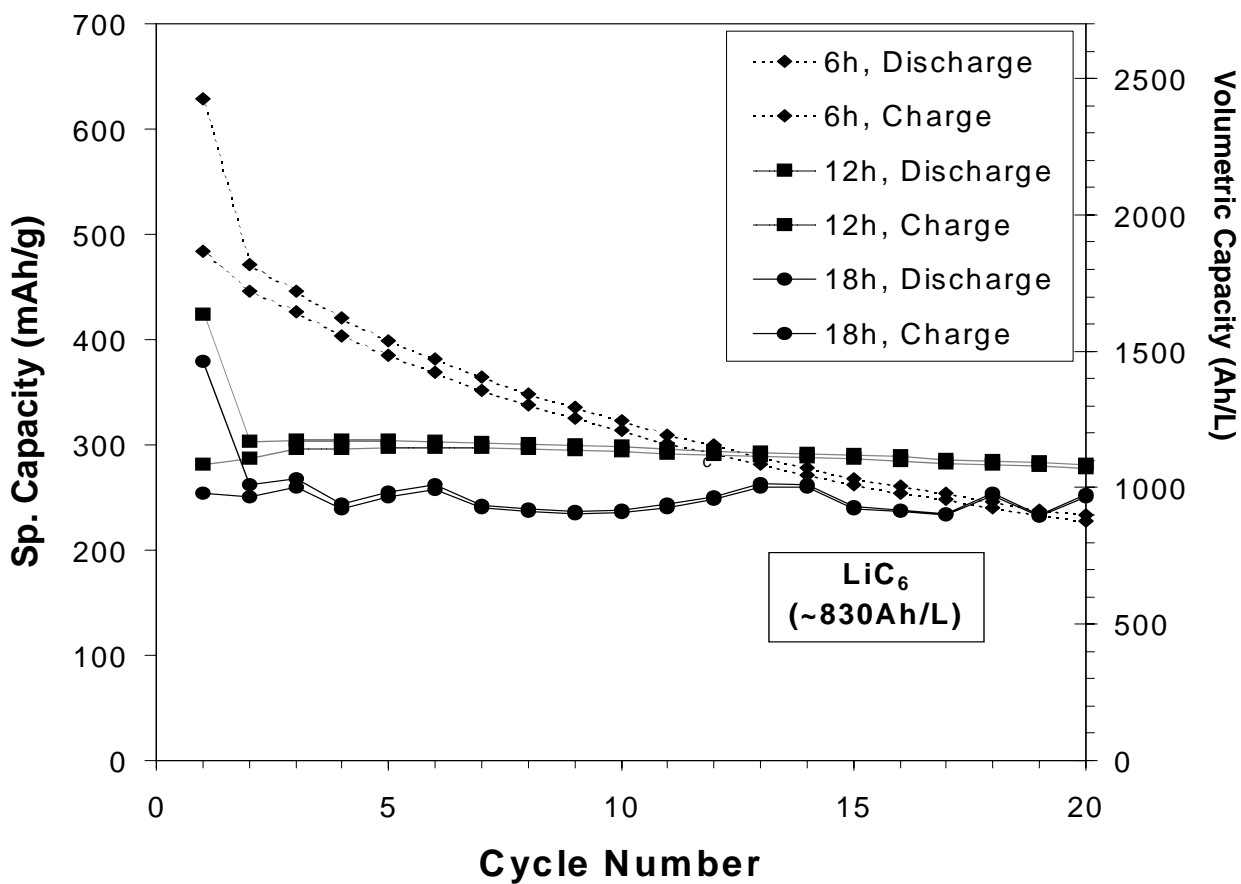


Fig. 5-5 Capacity as a function of cycle number for Si:TiN=1:2 nanocomposites obtained after milling for 6 h, 12 h and 18 h each. (Current rate:  $250\mu\text{A}/\text{cm}^2$ , Potential: 0.02~1.2 V)

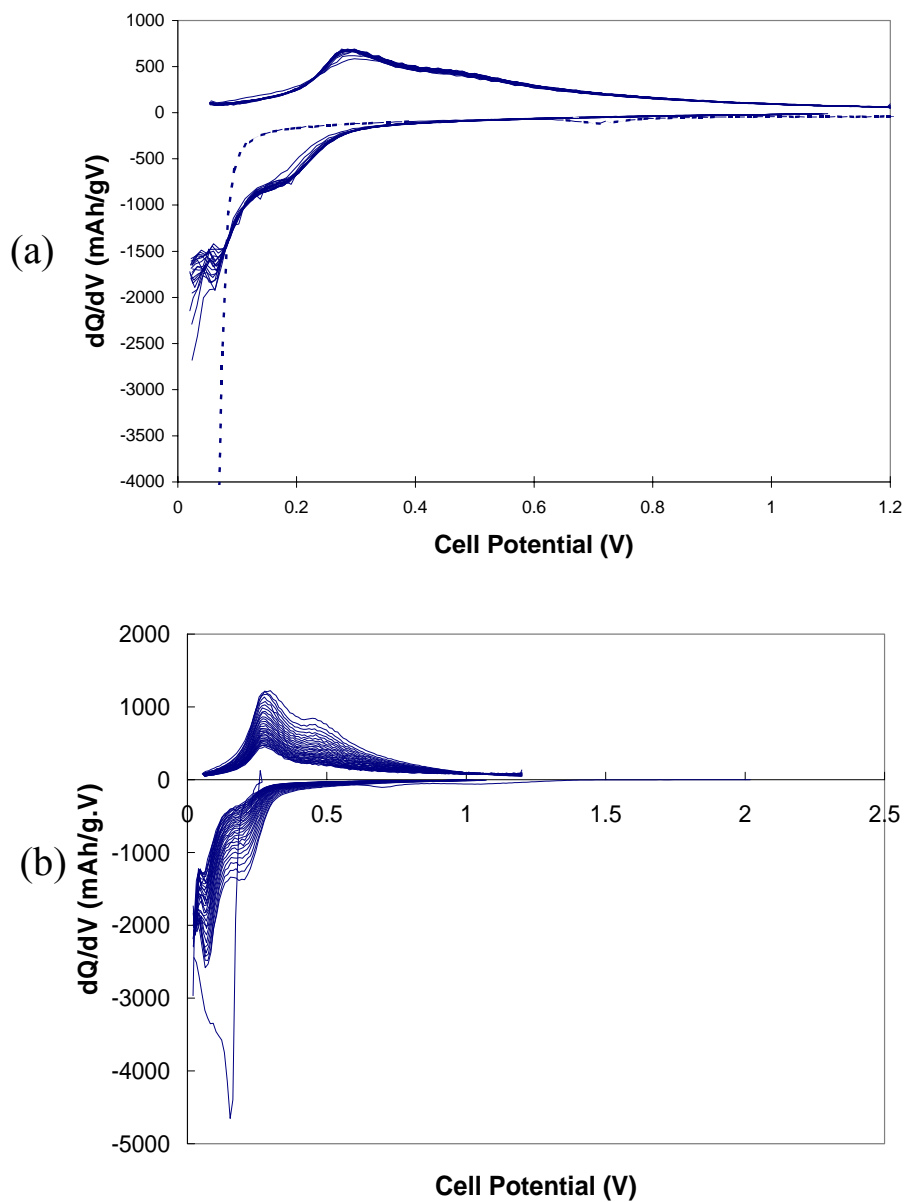


Fig. 5-6 Differential capacity vs. cell potential curves for the first twenty cycles of the nanocomposite with Si:TiN = 1:2 molar ratio obtained after milling for (a) 12 h and (b) 6h. (Current rate:  $250 \mu\text{A}/\text{cm}^2$ , Potential: 0.02~1.2 V)

hypothesis. The composite obtained after milling for 6 h shows fade in capacity, while the samples milled for longer time exhibit good capacity retention. According to the capacity vs. cycle number plot, the composite obtained after milling for 12 h exhibits a moderately high capacity of  $\approx 300$  mAh/g that is retained remarkably well for twenty cycles when cycled at a constant current of  $250\mu\text{A}/\text{cm}^2$  (C-rate of  $\sim\text{C}/10$ ). Although this composition has a smaller gravimetric capacity in comparison to conventional carbon, it exhibits a volumetric capacity (1100Ah/l) that is  $\sim 30\%$  higher than that of carbon (830Ah/l).

Fig. 5-6 (a) shows the differential capacity vs. voltage for all the twenty cycles for the composite containing 33.3 mol% Si obtained after milling for 12 h. The peak observed in the first cycle ( $\approx 0.07\text{V}$ ) is larger in intensity and has a different shape compared to the peaks seen in the subsequent cycles, suggesting the expected irreversible loss in capacity. Besides, there is very broad peak at  $\sim 0.75\text{V}$  during the first discharge that is possibly caused by the formation of a passivation layer, also contributing to the irreversible loss. Dahn et al. reported in their study on  $\text{Sn}_2\text{Fe}$  that peak sharpening in the differential capacity curve corresponds to aggregation of active Sn particles during cycling [1]. However, no peak sharpening occurred in this system even after 20 cycles in our electrodes, indicating the stability of the microstructure without resulting in any aggregation of Si particles. The differential capacity vs. voltage plot of the composite containing 33.3 mol% Si obtained after milling for 6 h is also shown in Fig. 5-6 (b). The decrease in peak intensity suggests the fade in capacity as shown in Fig 5-5. The plot in Fig. 5-7 exhibits the variation in cell potential with specific capacity. The curves show a smooth plateau in the low voltage range as well as good capacity retention. The reason for the first cycle irreversible loss shown in the plot is still unclear and needs more detailed study but one of the many obvious reasons could be the formation of Li-containing passivation layer at the solid electrode-electrolyte interface (SEI) as indicated by the peak  $\approx 0.75\text{V}$  during the first discharge seen in Fig. 5-6 (a).

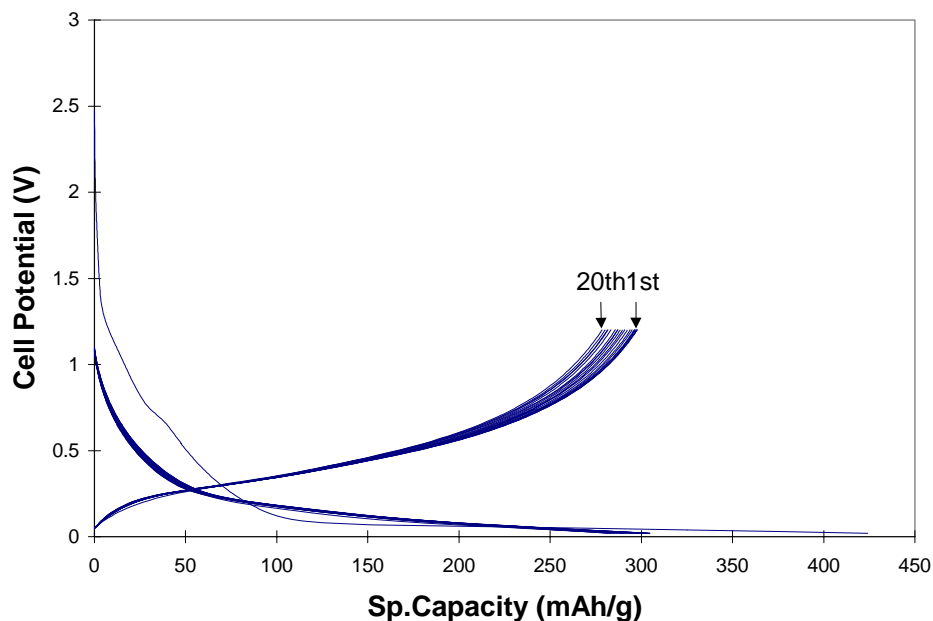
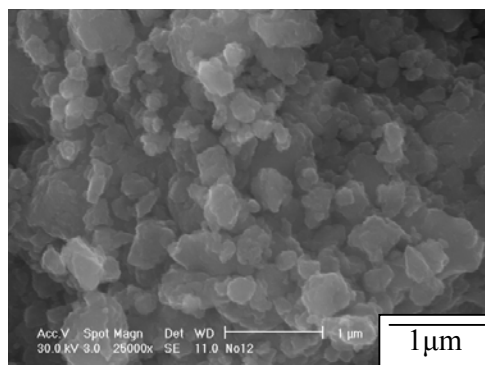


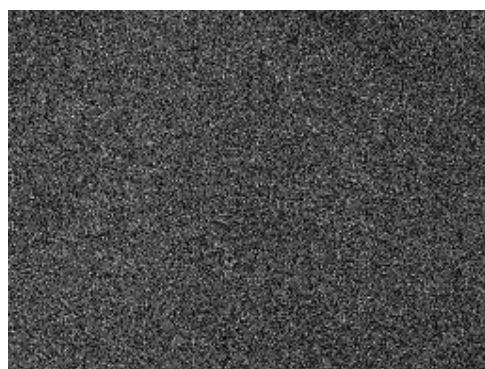
Fig. 5-7 Cell potential vs. specific capacity curves for the first twenty cycles of the nanocomposite corresponding to Si:TiN = 1:2 molar ratio obtained after milling for 12 h. (Current rate:  $250\mu\text{A}/\text{cm}^2$ , Potential: 0.02~1.2 V)

### 5. 1. 3 Analyses of the Morphologies and the Microstructure of the As-Milled Powder and the Electrodes.

The SEM micrograph and the energy dispersive elemental x-ray (EDX) map for silicon and titanium obtained on the 12 h milled powder containing 33.3 mol% Si (Si:TiN=1:2) are shown in Fig. 5-8. The particles are agglomerated although they are extremely small in the range of 100~500 nm. Based on the elemental mapping of Si and Ti, both elements are distributed homogeneously within all particles, suggesting that all



(a)



(b)



(c)

Fig. 5-8 (a) SEM micrograph of the Si:TiN = 1:2 composite showing the nanocrystalline particles (100~300nm). Chemical map of (b) Ti and (c) Si, respectively, using EDX for the Si/TiN composite corresponding to Si:TiN = 1:2 molar ratio obtained after milling for 12 h. (Both images are taken at the same scale.)

**Table 5-1 Results of EDX analysis of the nanocomposite corresponding to a molar composition Si:TiN=1:2 obtained after milling for 12h. (All quantities are given in atomic percentages.)**

At % powder	Ti	N	Si	Fe
Before milling	40	40	20	
After milling*	35.57	41.76	19.41	3.26

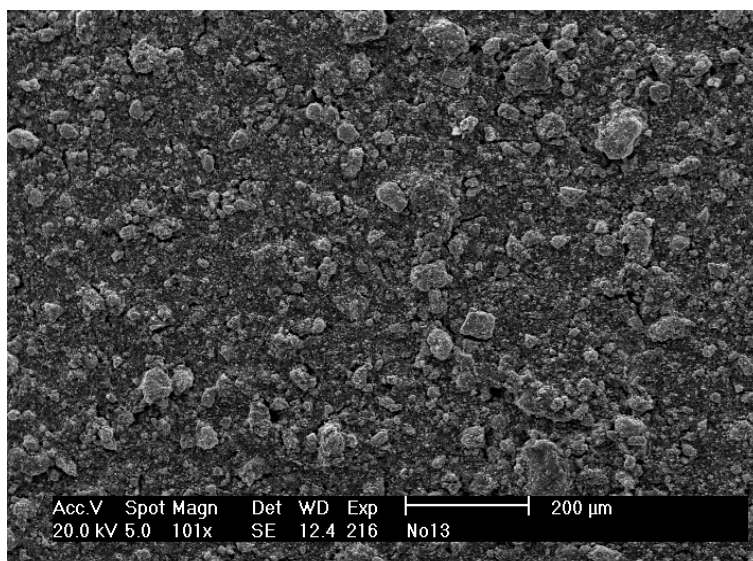
these particles are essentially true composites containing an intimate mixture of Si and TiN according to the EDX analysis. The detailed microstructure will be discussed in the following section.

Table 5-1 shows the elemental composition of the initial Si:TiN=1:2 mixture prior to milling and the as-milled powder obtained after milling for 12h, respectively. The composition of the initial mixture represents calculated values obtained from the original composition of the nanocomposite. The results presented in the Table represent the averaged values obtained from 5 different positions of the sample. The EDX results also indicate the presence of iron ( $\cong 3.3\%$ ) in the as-milled powder, suggesting that iron is incorporated from the vial or the balls used during milling.

In order to analyze any changes in the microstructure or morphology of the particles during cycling, the electrode before and after cycling was observed under the SEM. Fig. 5-9 shows the morphologies of electrodes fabricated from composites containing 33.3 mol% of Si obtained after milling for 12 h. The surface of the electrode after 30 cycles is devoid of any cracks, which are typically observed in other metal-based alloys used as anodes. Moreover, there appears to be no change in the morphology of the particles before and after cycling, which indicates good cycling stability of the composite.



Before cycling



After cycling

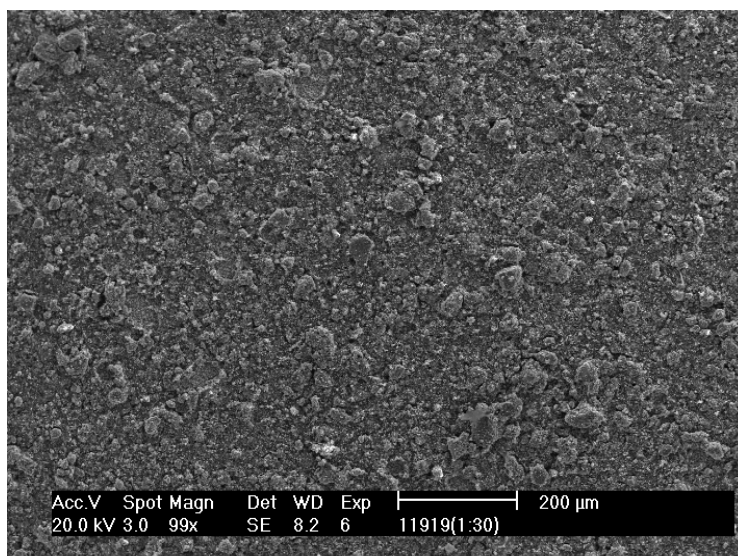


Fig. 5-9 SEM micrographs of the electrode before and after 30 cycles fabricated from the Si/TiN composite corresponding to Si:TiN = 1:2 molar ratio obtained after milling for 12 h.

The XRD pattern collected on the electrode after 30 cycles presented in Fig. 5-10 shows that it is identical to Fig. 5-4. The XRD data was taken from the nanocomposite electrode after electrochemical cycling. The sharp peaks corresponding to the Cu substrate forming the electrode are also shown in the spectrum. Generally, fine particles of the active element undergo coarsening caused by diffusion during cycling thus leading to crystalline peaks after cycling although the active element is either amorphous or nanocrystalline. In the present case, however, no observable changes were observed in the peaks compared to the XRD pattern of the original as-milled powder (Fig 5-4), suggesting that Si remains as very fine particles and does not appear to undergo any clustering during cycling. This excellent stability of the electrode may be attributed to the existence of very finely dispersed amorphous silicon particles within the nanocrystalline TiN matrix.

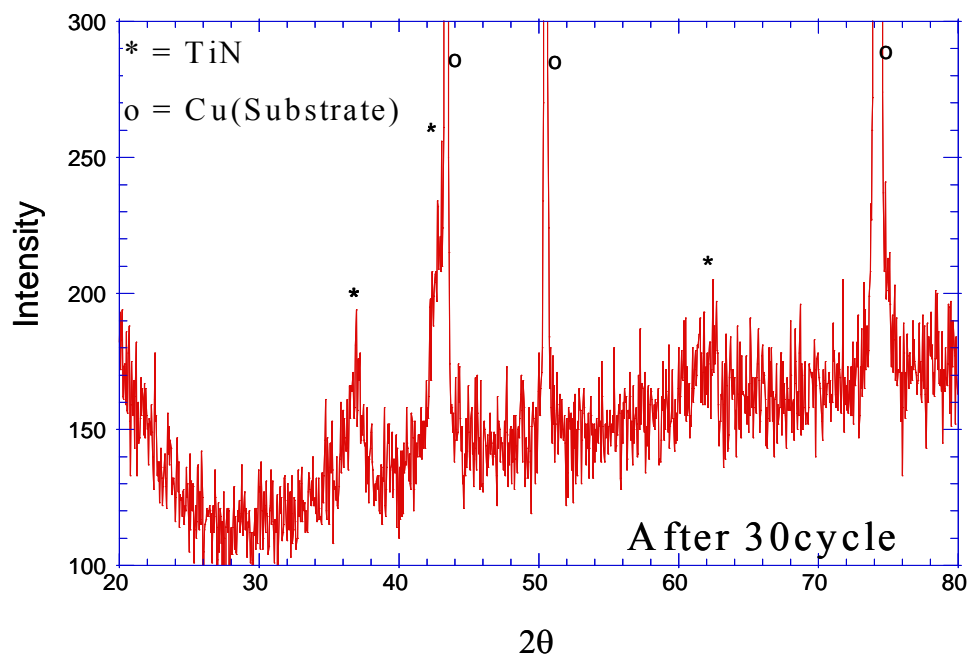


Fig. 5-10 XRD pattern collected on the electrode after 30 cycles prepared with the Si/TiN composite corresponding to Si:TiN = 1:2 molar ratio obtained after milling for 12 h.

Transmission electron microscopy was conducted on this powder to analyze the nanocrystalline state of the composite. Figs. 5-11 (a) and (c) show the TEM bright field image and selected area diffraction pattern collected on the 12 h milled powder containing 33.3 mol% silicon, respectively. The bright field image indicates the presence of very fine size crystallites ( $< 20$  nm) within a single particle, indicating the true nanocomposite nature of this material. The well-defined rings in the selected area diffraction pattern correspond to TiN, which comprises the nanocrystallites. There is no diffraction pattern corresponding to silicon, hence validating its amorphous nature indicated by XRD as well. Fig. 5-11 (b) is the dark field (DF) image corresponding to the crystalline TiN phase. Comparing the region marked with an arrow in the DF and the BF images, it appears that the dark spots in the BF image correspond to TiN crystallites. Although the TEM results suggest that the composite is essentially comprised of nanosized crystallites of TiN and amorphous silicon, it is difficult to ascertain the exact distribution of both phases. Therefore, high-resolution transmission electron microscopy was conducted on the composite using EELS to map the distribution of the elements at the nanoscale.

Fig. 5-12 (a) shows the high-resolution image of the composite containing 33 mol% silicon obtained after milling for 12 h. The dark areas represent the TiN nanocrystallites while the bright regions correspond to amorphous silicon as mentioned above. Lattice fringes from the TiN particles can be observed conforming to the nanocrystalline nature of TiN. Figs. 5-12 (b) and (c) show the high-resolution elemental maps corresponding to silicon and Ti, respectively obtained using electron energy-loss spectroscopy (EELS). The bright regions in the map indicate the high intensity reflecting the amount of each component. The elemental maps therefore show that TiN is distributed homogeneously in the powder and silicon appears to surround the TiN particles. This suggests the influence of mechanical milling on the two materials exhibiting different hardnesses. Silicon exhibits a lower hardness ( $\cong 820$  kg/mm<sup>2</sup>) in comparison to TiN ( $\cong 1900$  kg/mm<sup>2</sup>) as shown in Table 2-6 and thus undergoes significant pulverization. The TiN particles thus appear to be uniformly coated with finely milled amorphous silicon forming the nanocomposite. Generally, the samples need to be sufficiently thin for obtaining good electron energy-loss spectra [2]. This

involves elaborate specimen preparation techniques normally used for bulk samples, which are not applicable for fine powders. Hence, due to the difficulties associated with the sample preparation, the as-milled powder was directly used in this case. As a result, overlapping of the elemental maps can be expected and the boundaries are also possibly diffused. Nevertheless, the elemental maps do reveal two different regions separated distinctly to represent the distribution of silicon and TiN phases. These results are therefore indicative of the stability of the Si/TiN nanocomposite arising from the nanoscale distribution of the two phases achieved by mechanical milling. Results of these studies therefore reveal two aspects. First, the promising nature of Si/TiN nanocomposite as a useful electrochemical system and second, the potential of using mechanical milling as a viable economically feasible approach for synthesizing electrochemically active nanocomposite materials.

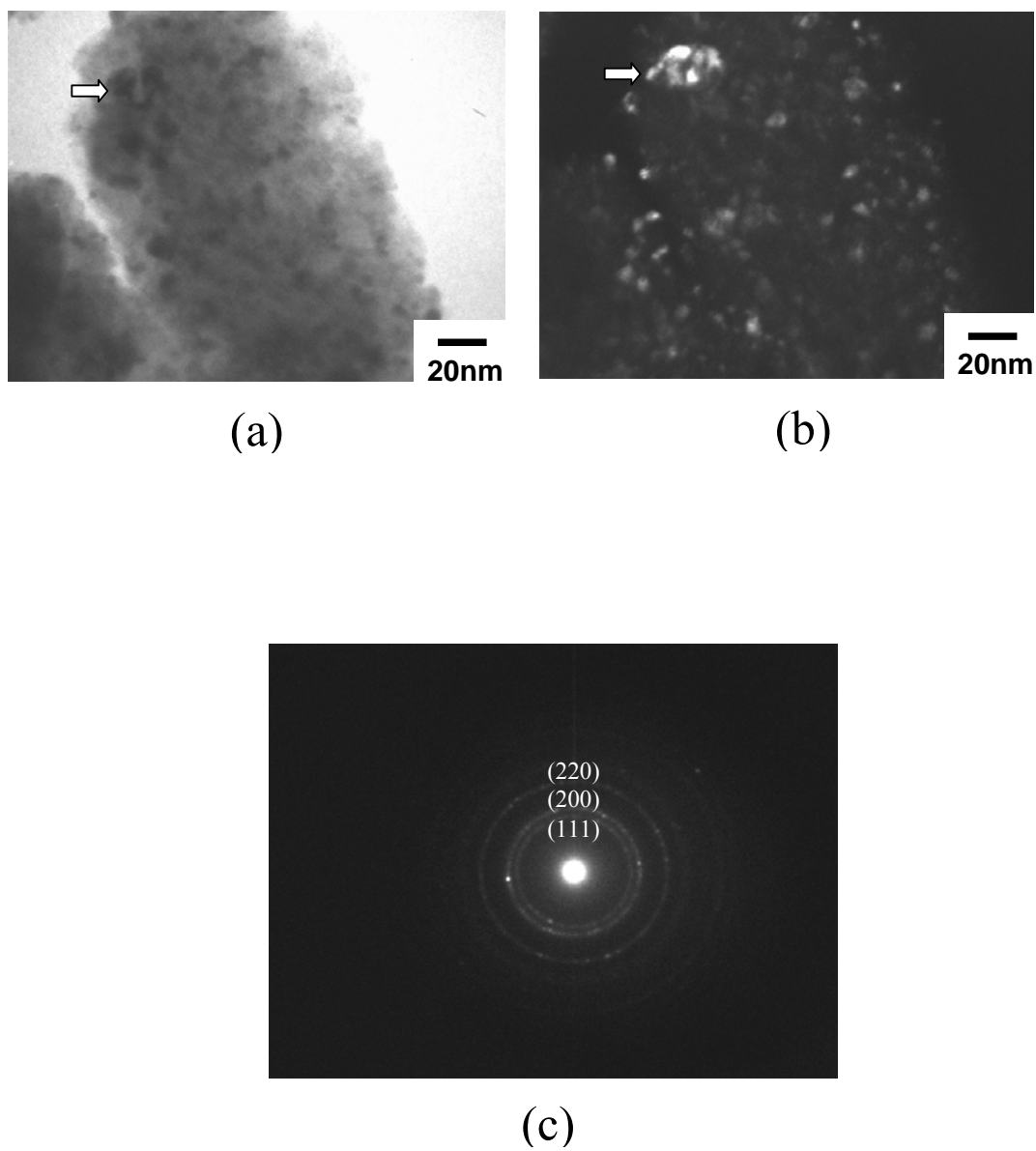


Fig. 5-11 TEM micrographs of the Si/TiN nanocomposite containing 33 mol% Si obtained after milling for 12 h; (a) BF image, (b) DF image, and (c) SA diffraction pattern (camera length = 66cm, reduced to 30% of its original size).

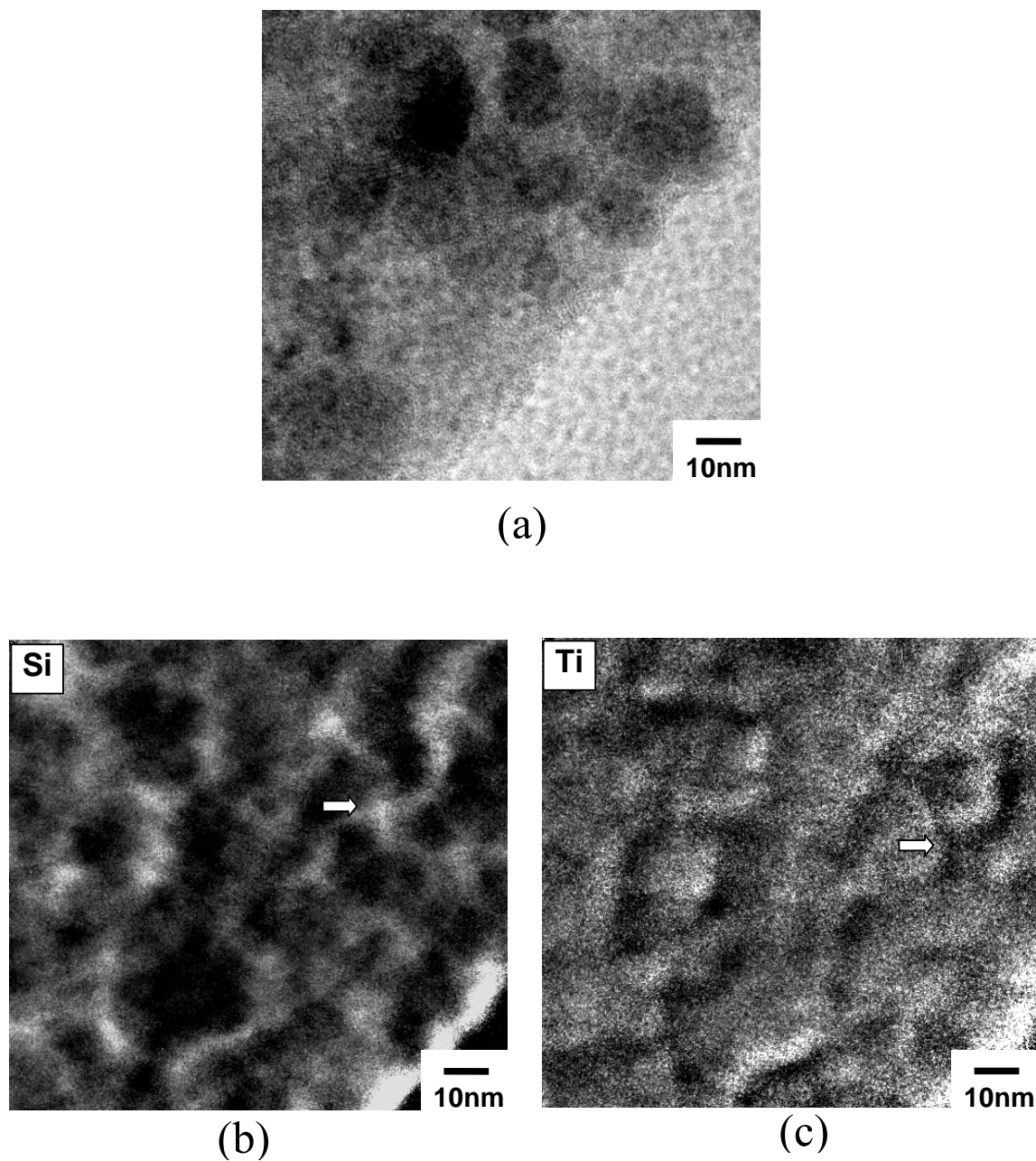


Fig. 5-12 (a) HRTEM micrographs of the Si/TiN nanocomposite containing 33 mol% Si obtained after milling for 12 h, (b) Elemental map of Si, (c) Elemental map of Ti, which are analyzed by electron energy-loss spectroscopy (EELS). (The arrows represent the same position.)

## **5. 2 Silicon/Titanium Boride Nanocomposites**

Based on the results of Si/TiN nanocomposite anodes so far, it is shown that TiN exhibits good properties to justify its use as an inactive matrix in nanocomposite anodes for use in Li-ion batteries. As mentioned previously, materials with good electrical conductivity, mechanical strength and chemical inertness are needed to provide good binding to withstand the stresses attributed to alloying and de-alloying of the active element with Li. Continuing with this line of thought, titanium boride is known to exhibit similar properties as titanium nitride, and could also act as a potential inactive matrix for silicon. Therefore, the concept of active-inactive nanocomposite anodes was extended to this system by synthesizing nanocomposites of silicon and titanium boride. Similar to the earlier study, the overall goal is to develop anode materials exhibiting high capacity. Since titanium boride has similar properties to titanium nitride, Si/TiB<sub>2</sub> nanocomposite anodes were prepared using similar experimental conditions with regards to milling time. In this experiment, we also investigated the effect of initial particle size of the inactive component to enhance the stability of the anode. In addition, microstructural and electrochemical analyses have been conducted to identify the optimum experimental conditions that could yield high capacity.

### **5. 2. 1 Effect of Milling Time on the Nanocomposites**

In the case of the Si/TiN nanocomposites, we have shown that HEMM renders the silicon amorphous. XRD analysis conducted on the Si/TiB<sub>2</sub> system also indicates that Si is rendered amorphous after milling for a time period of only 6 h (see Fig. 5-13). All the peaks in the XRD patterns correspond to TiB<sub>2</sub> and the broad nature of the peaks are clearly indicative of the nanocrystalline nature of the powder. The reason for the formation of nanocrystalline or amorphous Si after milling can be attributed to the mechanical strength and hardness of TiN and TiB<sub>2</sub>, which is shown in Table 2-6 in chapter 2. Since TiB<sub>2</sub> particles act as the milling media, the strength and hardness of the inactive phase accelerates the pulverization of silicon to form very fine amorphous

particles.

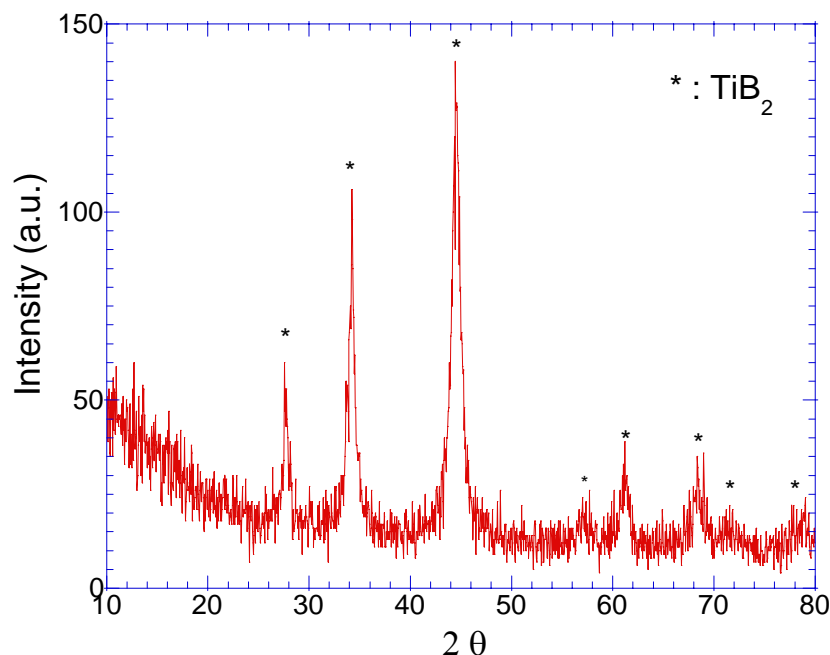


Fig. 5-13 X-ray diffraction patterns of Si:TiB<sub>2</sub>=1:2 composites obtained after milling for 6 h.

The specific gravimetric and the equivalent volumetric capacity of the electrode prepared with the Si/TiB<sub>2</sub> nanocomposites including 40 mol% Si are shown in Fig. 5-14. A larger amount of Si was selected in this case compared to Si/TiN since TiB<sub>2</sub> is heavier in comparison to TiN. A lower amount of the inactive component has therefore been used in comparison to the Si/TiN case. The overall capacity appears to decrease as the milling time is increased, indicating a reduction in the amount of the active phase of silicon. In case of the nanocomposite electrode obtained after milling for 10h, the highest first discharge capacity (~726mAh/g) is observed but the capacity fades rapidly. Besides this value is still lower than the theoretical capacity (891mAh/g) of the



Si/TiB<sub>2</sub> nanocomposites comprising 40 mol% Si. The nanocomposite obtained after milling for 20h nevertheless shows a stable capacity as high as 400mAh/g. As discussed before, the sample milled for a longer time exhibits better capacity retention. Although the reason for the capacity reduction with increasing milling time is not clear yet, one possible explanation is the embedding of Si or the diffusion of Si into the inactive matrix particularly at the active-inactive matrix interface.

Fig. 5-15 shows the differential capacity vs. voltage for 15 cycles for the nanocomposites containing 40mol% of Si obtained after milling for 10 h, 15 h, 20 h and 25 h, respectively. Due to the amorphous/nanocrystalline nature of Si, the reaction of Li with Si is represented as broad peaks in each plot. The nanocomposite electrodes obtained after milling for 10 h and 15 h exhibit a reduction in peak intensity with progressive cycles, indicating fade in capacity, while the electrodes obtained after milling 20 h and 25 h show a stable peak intensity. A broad bump at ~0.75V during the first discharge in all four samples appears to be caused by the passivation layer formation at the solid electrode-electrolyte interface (SEI).

### **5. 2. 2 Morphology and Phase Analyses**

In order to analyze the microstructure, SEM analysis was conducted on the Si/TiB<sub>2</sub> nanocomposite containing 40 mol% Si obtained after milling for 20 h (See Fig. 5-16 (a)). The size of the agglomerates are in the range of 0.3~3 $\mu$ m. The morphology of the powder is characteristic of HEMM derived materials comprising brittle precursors as mentioned in chapter 2.

Energy dispersive x-ray (EDX) mapping of the different elements was conducted to analyze the distribution of the species within the agglomerated particle. EDX mapping analysis was conducted for silicon and titanium obtained after 20 h milling of the powder containing 40 mol% Si (Si:TiB<sub>2</sub>=2:3). The EDX analyses are shown in Fig. 5-16 (b) and (c), respectively. The bright spots correspond to the presence of each element which appear to exist all over the particle. Based on the EDX elemental maps, it can be mentioned that both elements are distributed homogeneously within all particles, indicating the each particle contains a uniform distribution of Si and TiB<sub>2</sub>.

Due to the difficulty in measuring the size of the primary particles within the

agglomerate, high-resolution transmission electron microscopy (HR-TEM) was used to examine the primary particles of the Si/TiB<sub>2</sub> nanocomposite containing 40 mol% of Si

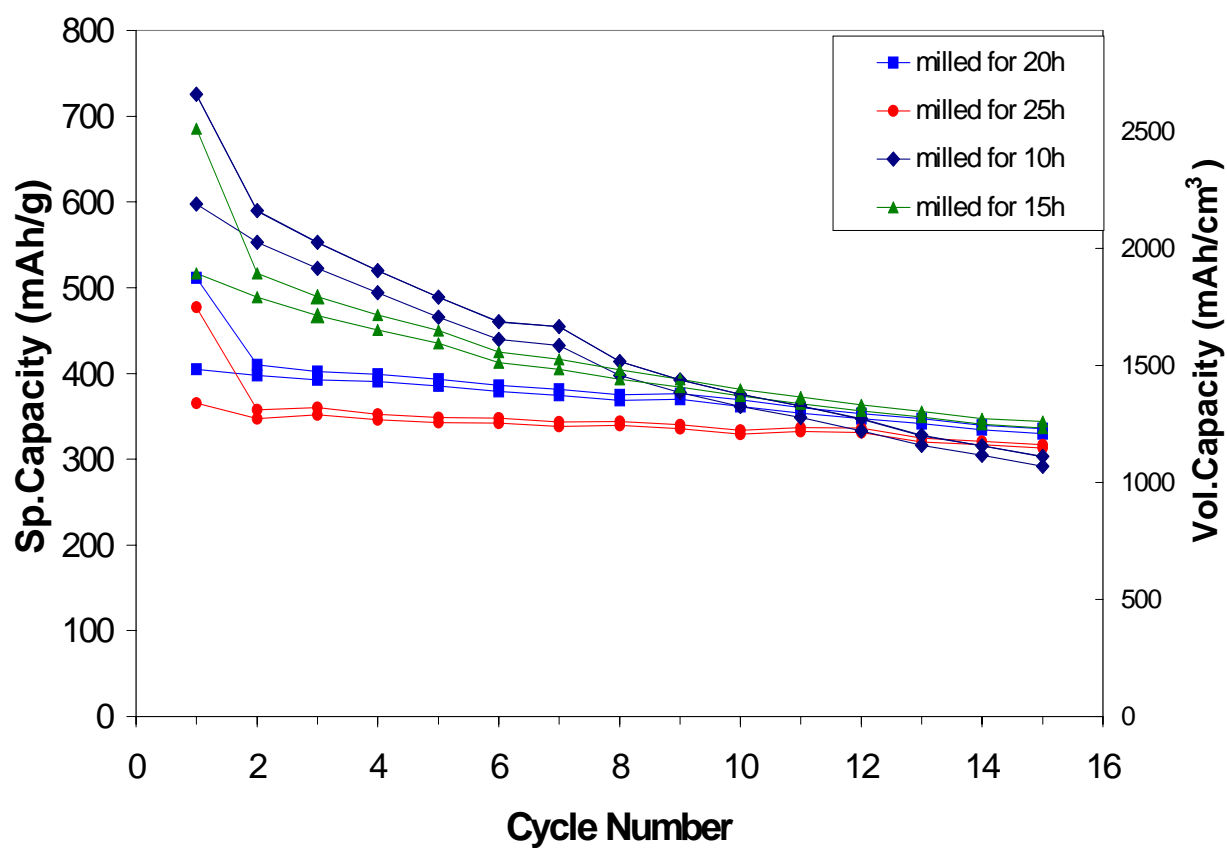
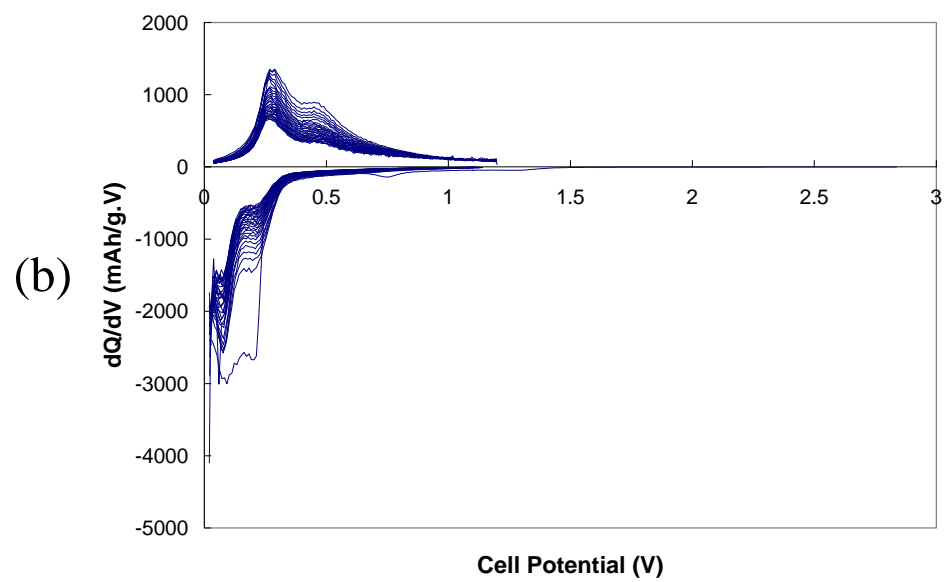
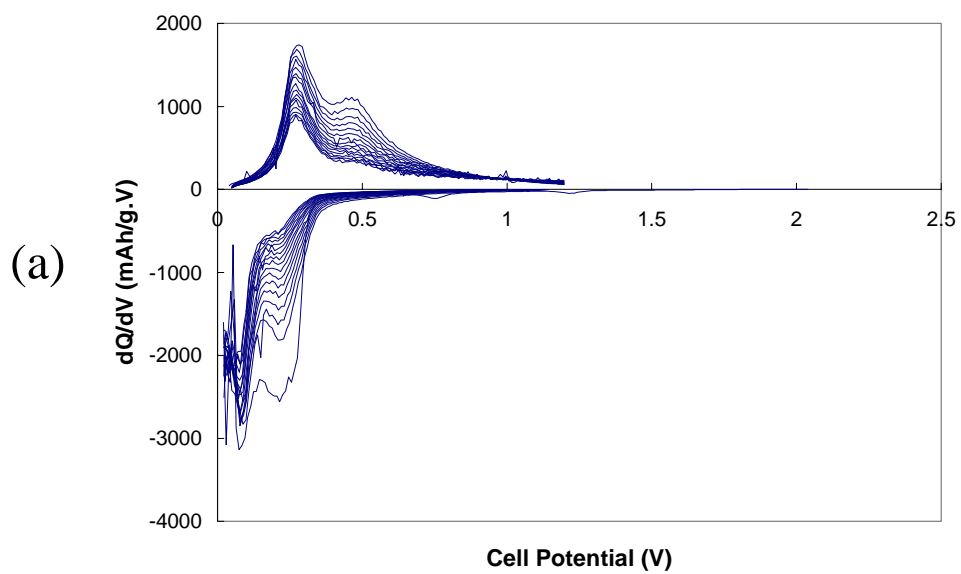


Fig. 5-14 Capacity as a function of cycle number for Si/TiB<sub>2</sub> nanocomposites containing 40 mol% Si obtained after milling for 10 h, 15 h, 20h and 25 h each. (Current rate: 100 $\mu$ A/cm<sup>2</sup>, Potential: 0.02~1.2 V)



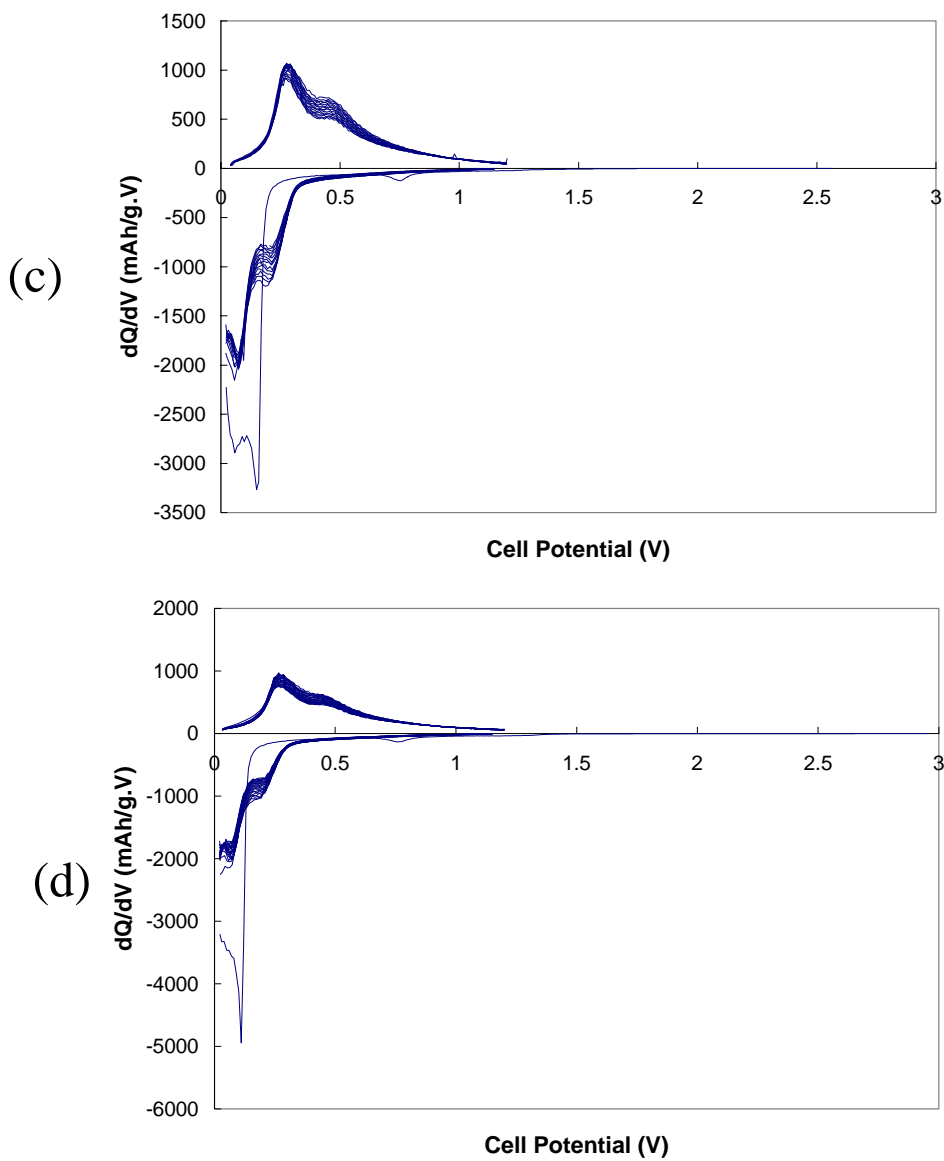


Fig. 5-15 Differential capacity vs. cell potential curves for the first fifteen cycles of the nanocomposite containing  $\text{Si}:\text{TiB}_2 = 2:3$  molar ratio (40 mol % Si) obtained after milling for (a) 10 h , (b) 15 h, (c) 20 h and (b) 25 h, respectively. (Current rate:  $100\mu\text{A}/\text{cm}^2$ , Potential: 0.02~1.2 V)

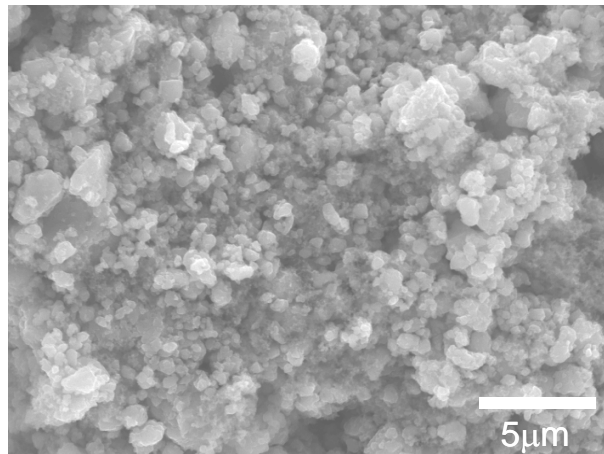
obtained after milling for 20h. Fig 5-17 (a) and (b) show the bright field and dark field images respectively, of the nanocomposite. The agglomerated particle appears to be a very dense nanocomposite comprising nanosized crystallites. The dark field image shows the nanocrystalline  $\text{TiB}_2$  primary particles represented with bright spots, which are very small in the size range of 3~10nm. Fig. 5-17 (c) shows a high magnification bright field image of the nanocomposites taken with the high resolution (HR) TEM. The circular shape fringes corresponds to the  $\text{TiB}_2$  nanocrystallites. Selected area diffraction pattern (SADP) of the nanocomposite exhibits rings, which correspond to nanocrystalline  $\text{TiB}_2$ , indicating that the nanocomposite consists of amorphous Si and nanocrystalline  $\text{TiB}_2$  similar to the XRD result.

The Li-alloy based electrodes in general show structural damage such as cracking or crumbling after electrochemical cycling. The electrode prepared from the nanocomposite containing 40 mol% Si obtained after milling for 20h has been analyzed using SEM to observe cracking if any, of the electrodes. Fig. 5-18 (a) is the SEM micrograph showing the surface of the electrode before cycling and (b) is the SEM image of the electrode after 20 cycles. No distinct change in morphology is observed before and after cycling, suggesting the good structural stability of this nanocomposite electrode, which is responsible for obtaining good capacity retention.

The electrode is also examined by XRD to verify the phase stability of the electrodes. Fig. 5-19 shows the XRD spectra collected from the electrode before and after cycling. The sharp peaks in the XRD pattern correspond to the Cu substrate used for fabricating the electrode coatings. There is no observable change in the XRD patterns before and after electrochemical cycling, suggesting that Si reacts with lithium reversibly without undergoing any noticeable particle growth or secondary phase formation. This result suggests that the phase stability of the nanocomposite arises from the homogeneous distribution of very fine amorphous active (Si) and nanocrystalline inactive ( $\text{TiB}_2$ ) components.

### **5. 2. 3 Effect of Premilling of $\text{TiB}_2$**

In order to investigate the effect of the initial particle size of  $\text{TiB}_2$  on the electrochemical properties of the anodes,  $\text{TiB}_2$  was premilled for different time periods



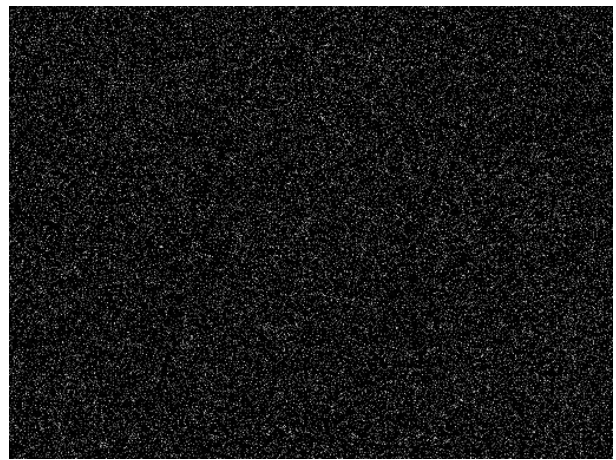
(a)

Si mapping



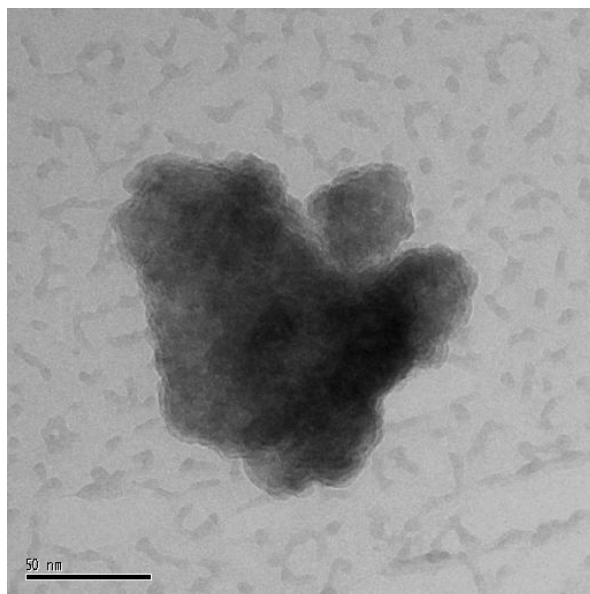
(b)

Ti mapping

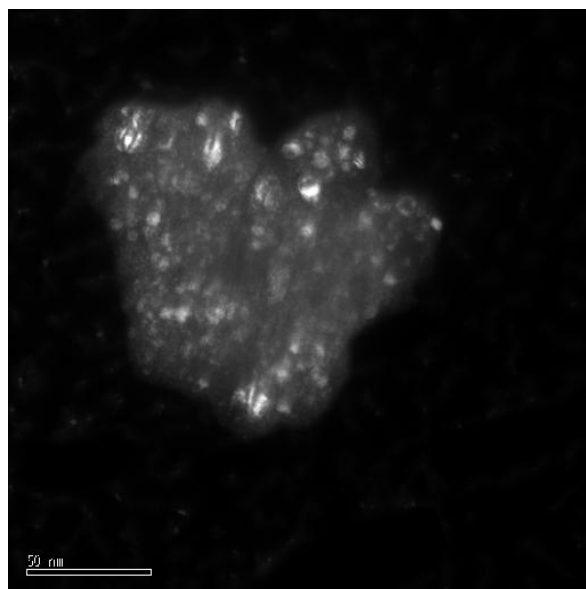


(c)

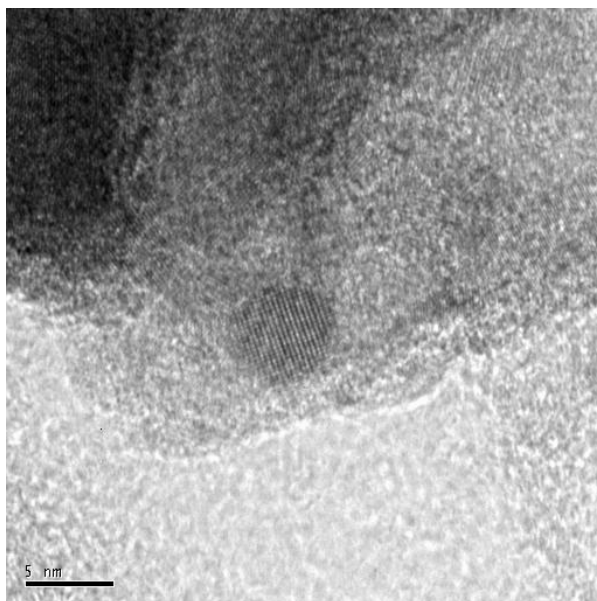
Fig. 5-16 (a) SEM micrograph of the Si:TiB<sub>2</sub> = 2:3 composite obtained after milling for 20h. Chemical map of (b) Si and (c) Ti, respectively, using EDX. (All images are taken at the same scale as shown in (a).)



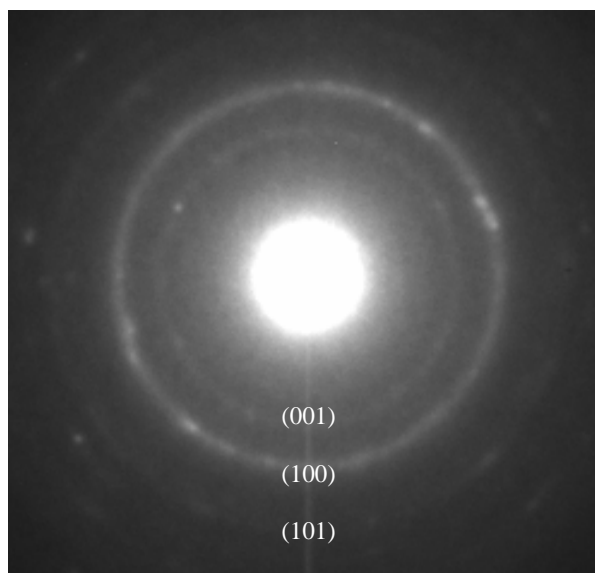
(a)



(b)



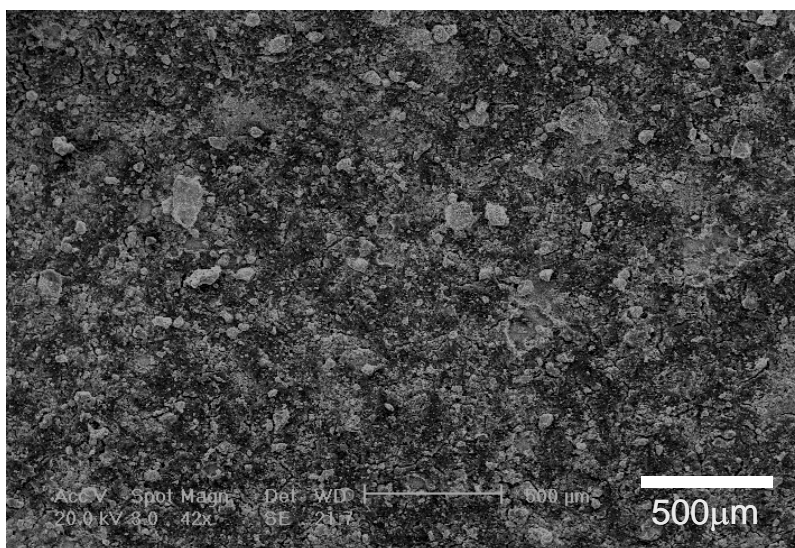
(c)



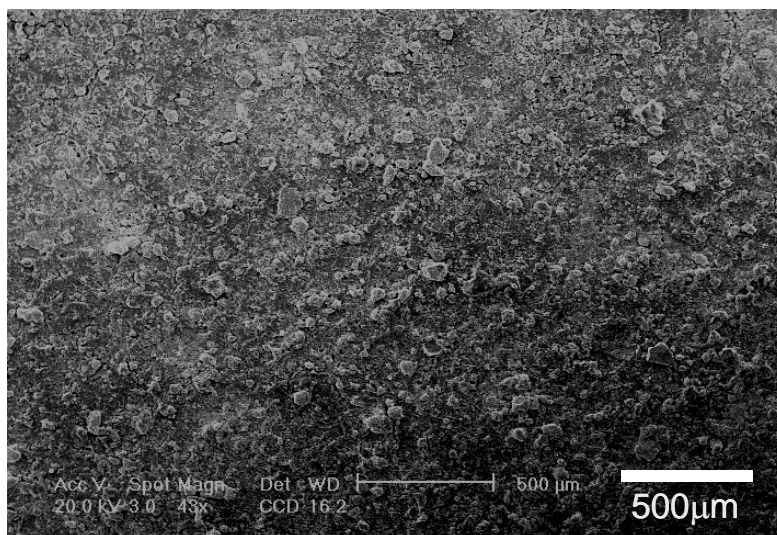
(d)

Fig. 5-17 HR-TEM micrographs of the electrode prepared with the Si/TiB<sub>2</sub> composite corresponding to Si:TiB<sub>2</sub> = 2:3 molar ratio obtained after milling for 20 h (a) bright field image, (b) dark field image, (c) bright field image taken at a higher magnification, and (d) SADP (CL=66 cm) showing nanocrystalline TiB<sub>2</sub>.





(a)



(b)

Fig. 5-18 SEM micrographs of the electrode (a) before and (b) after 20 cycles, comprising Si/TiB<sub>2</sub> nanocomposite corresponding to Si:TiB<sub>2</sub> = 2:3 molar ratio obtained after milling for 20 h.

of 12 h, 18 h and 24 h, respectively. These pre-milled powders were used to generate the Si/TiB<sub>2</sub> nanocomposites instead of commercial TiB<sub>2</sub>. The XRD patterns of these premilled powders are shown in Fig. 5-20 in comparison to commercial TiB<sub>2</sub>. Long scans (scan step: 0.013°, dwell time: 50 sec) have been used to collect the XRD data to reduce the background noise. Since the Scherrer formula allows the calculation of an approximate crystallite size, the sizes of crystallites obtained from premilled powder are tabulated in Table 5-2. The Scherrer formula is expressed as follows [3]:

$$t = \frac{0.9\lambda}{B \cos \theta_B} \quad (5-1)$$

$t$  : particle size

$\lambda$  : wavelength of CuK $\alpha_1$

$B$  : width at  $\frac{1}{2} I_{max}$

$\theta_B$  :  $\theta$  at  $I_{max}$

The  $B$  value has been calculated from the (101) peak in each XRD plot exhibiting the highest peak intensity. The indexed XRD patterns are shown in Fig 5-20. Although the strain effect has not been considered for calculating the crystallite sizes due to the difficulties associated in measuring strain within the particles, the crystallite size nevertheless appears to decrease with increase in milling time. However, the decrease in crystallite size appears to be unaffected when milling is conducted for more than 18h. The reason for this could be attributed to possible plastic deformation occurring in the particles when the crystallites are reduced to the size range of 57Å. As a result, milling action now leads to deformation and probable welding rather than shearing and pulverization of the brittle silicon particles as discussed in chapter 2.

The Si/TiB<sub>2</sub> nanocomposite anodes obtained after milling commercial Si and premilled TiB<sub>2</sub> powder mixtures for 10 h were then tested for electrochemical properties. The composition used for this study is the system containing 33mol% rather than 40 mol% of the active phase because of the reduced milling time necessary to achieve

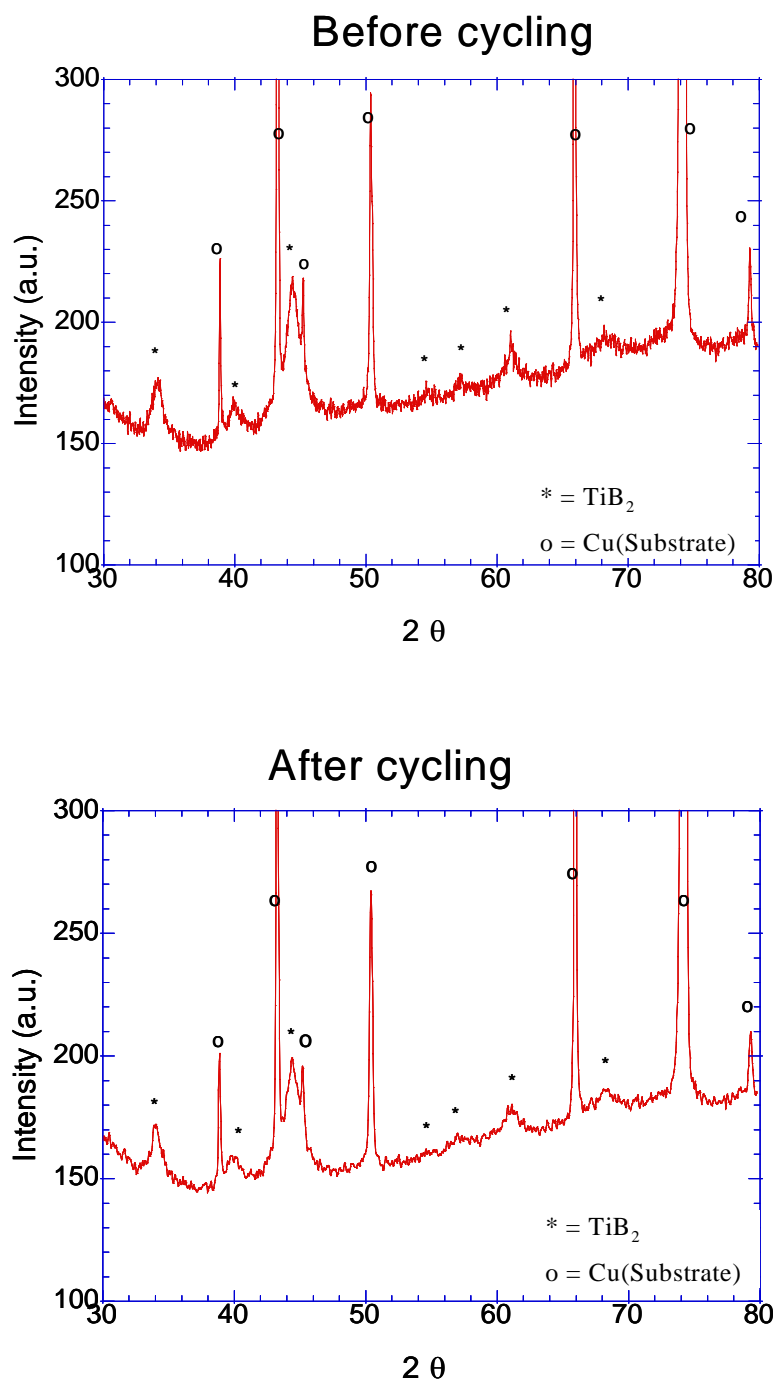


Fig. 5-19 XRD pattern of the electrode before and after 20 cycles prepared with the composite corresponding to  $\text{Si}:\text{TiB}_2 = 2:3$  molar ratio obtained after milling for 20 h.

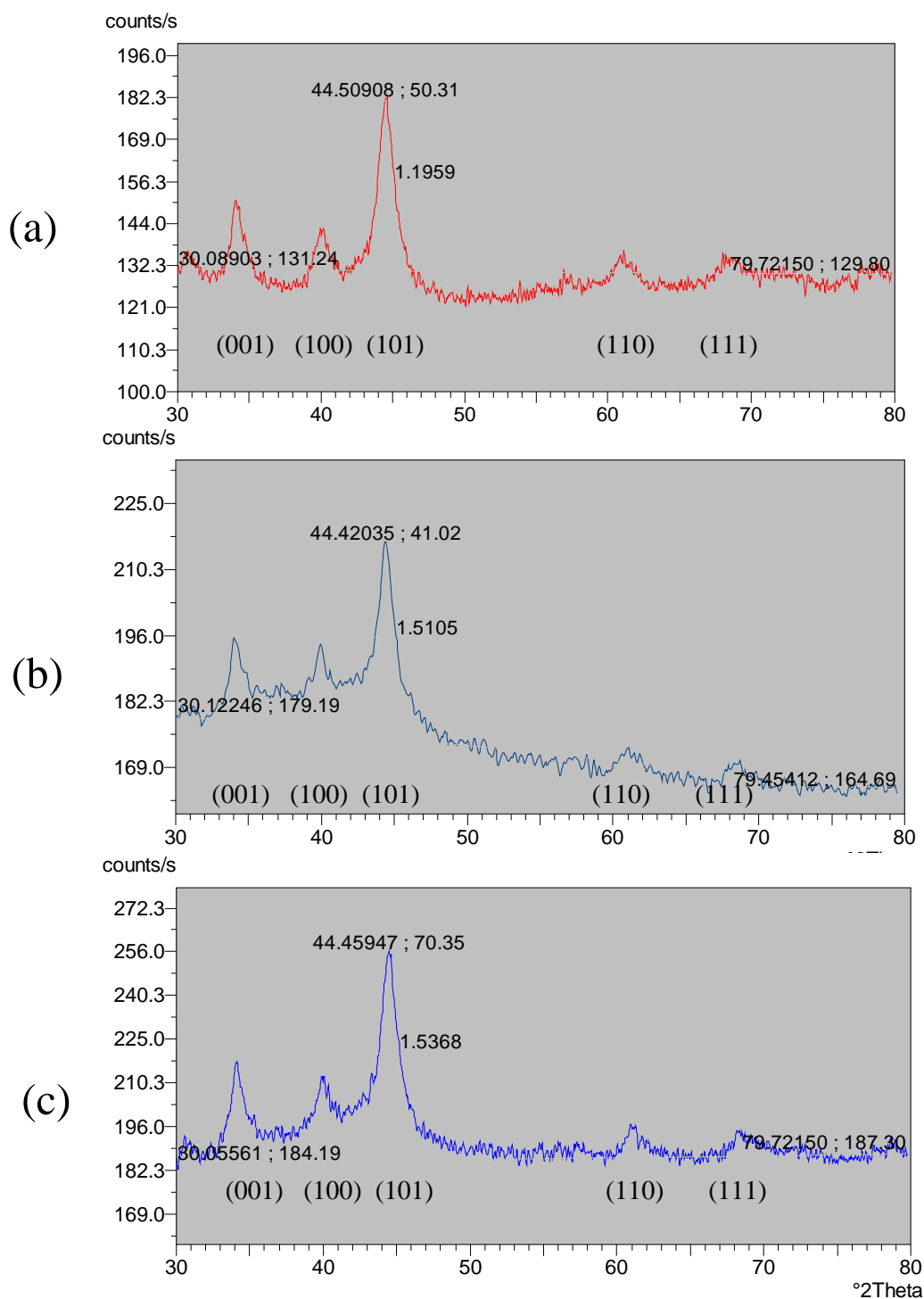


Fig. 5-20 Long scan (scan step:  $0.013^\circ$ , dwell time: 50 sec) XRD patterns corresponding to commercial and premilled TiB<sub>2</sub> powders. The  $B$  values (the peak width at  $I_{max}/2$ ) are marked. (a) premilled for 12h, (b) 18h and (c) 24h, respectively.

**Table 5-2 Approximate crystallite size of the premilled TiB<sub>2</sub> particles obtained after milling for 12h, 18h and 20h, respectively, calculated using the Scherrer formula.**

Milling time	Approximate Particle size
12h	71Å
18h	57Å
24h	56Å

relatively stable capacity. Furthermore, premilling of a large amount of inactive component has a better effect on the capacity. As seen from the plot of capacity vs. cycle number (Fig. 5-21), the sample obtained after milling Si and the 24h premilled TiB<sub>2</sub> for 10h shows better stability in terms of capacity retention, and does not show much capacity loss, which is normally observed in composites obtained after extended mechanical milling. This result indicates that a small particle size of the inactive component provides better stability since the stress induced by the volume expansion of the active phase during cycling is distributed more homogeneously in the nanocomposite containing premilled inactive components. This appears to be a good way to improve the electrochemical stability of the active-inactive nanocomposite anodes.

Fig. 5-22 (a), (b) and (c) shows the differential capacity vs. voltage for all twenty cycles for the composite containing 33.3 mol% Si obtained after milling for 10 h using TiB<sub>2</sub> premilled for 24 h, 12 h and 18h, respectively. The overall shape of the curve is very similar to that of Si/TiN as seen in Fig. 5-6 including the first irreversible loss, suggesting that the broad peaks at ~0.3V, and 0.5V during charge,

and  $\sim 0.1\text{V}$ , and  $0.2\text{V}$  during discharge cycle can be attributed to amorphous Si rather than the inactive components. The peak at  $\sim 1.25\text{V}$  can be attributed to an oxide layer on the surface of the  $\text{TiB}_2$  premilled for 24 h, since ultra fine  $\text{TiB}_2$  can be more easily oxidized during preparation of electrodes in comparison to the samples obtained from  $\text{TiB}_2$  premilled for a shorter time. As shown in the other nanocomposite samples of Si/TiN earlier, the peaks at  $\sim 0.75\text{V}$  correspond to the formation of a passivation film. The peak intensity in the differential capacity plot obtained from the  $\text{TiB}_2$  premilled for 24 h remains stable for all 20 cycles, while the intensity of peaks from the other two samples (see Fig. 5-22, (b) and (c)) slowly decreases as the cycling progresses.

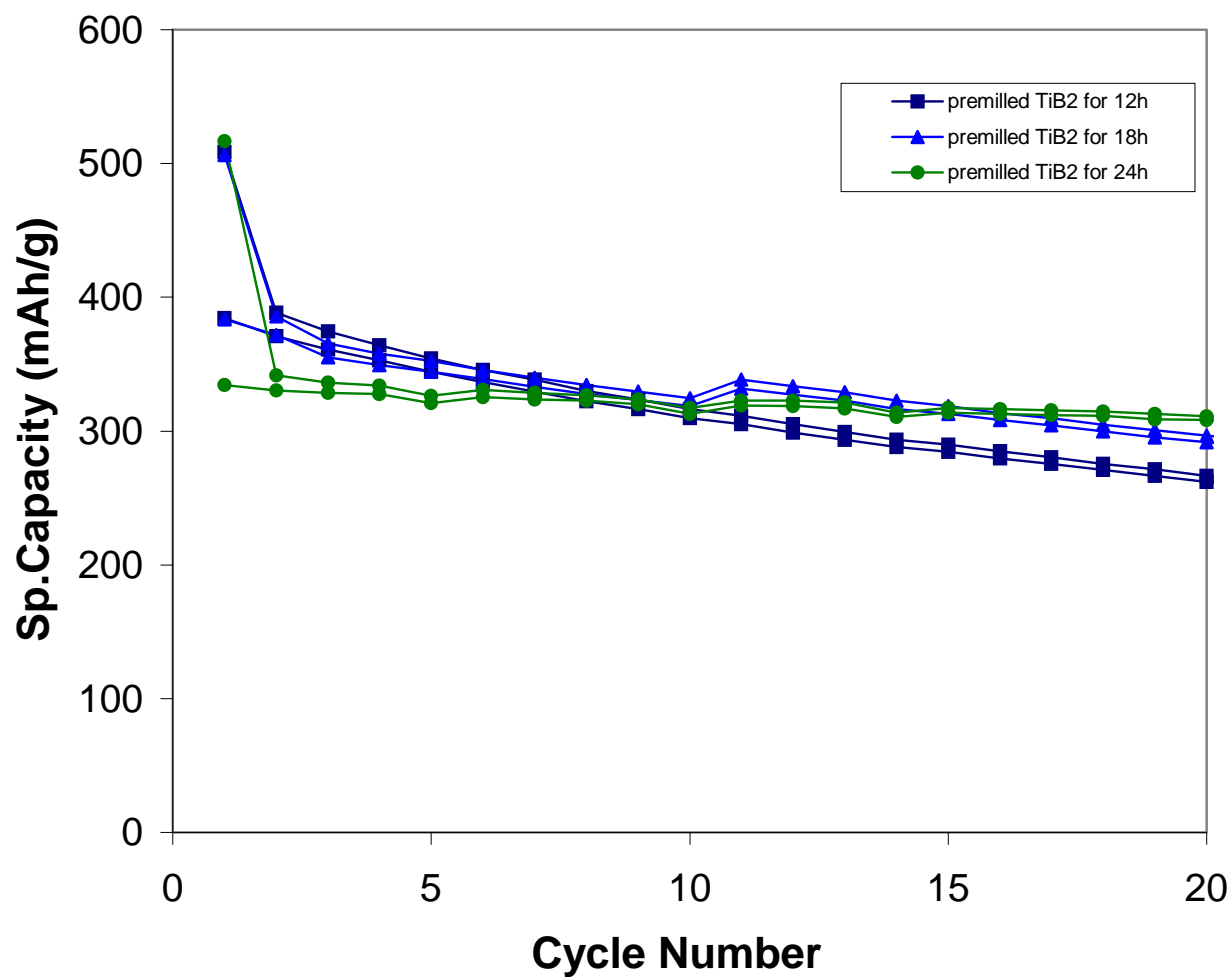
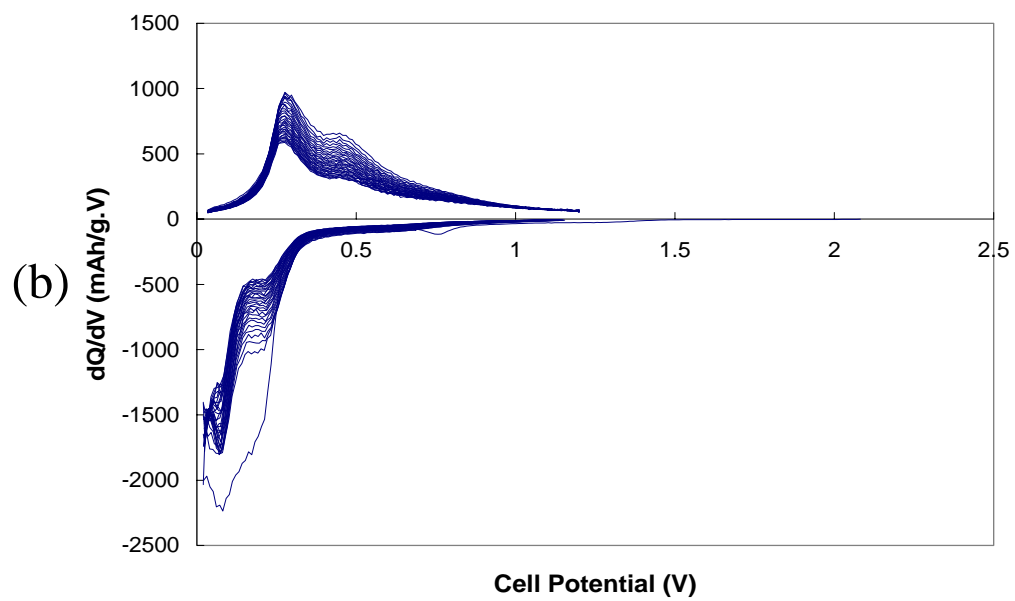
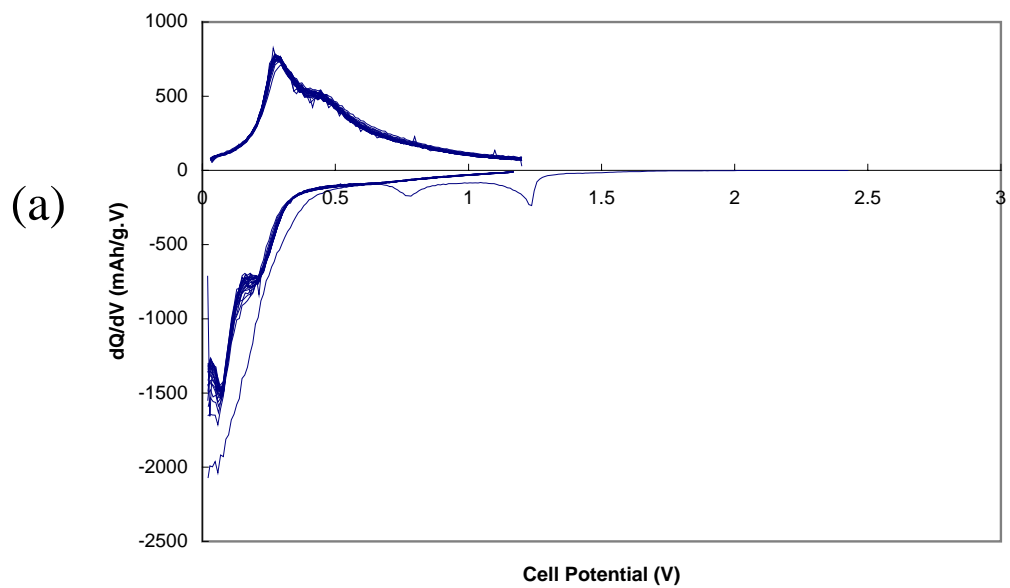


Fig. 5-21 Capacity as a function of cycle number for Si/TiB<sub>2</sub> nanocomposites with a molar ratio 1:2 obtained after milling for 10h. TiB<sub>2</sub> used was pre-milled for 12h, 18h and 24h respectively. (Current rate: 100 $\mu$ A/ cm<sup>2</sup>, Potential: 0.02~1.2 V)





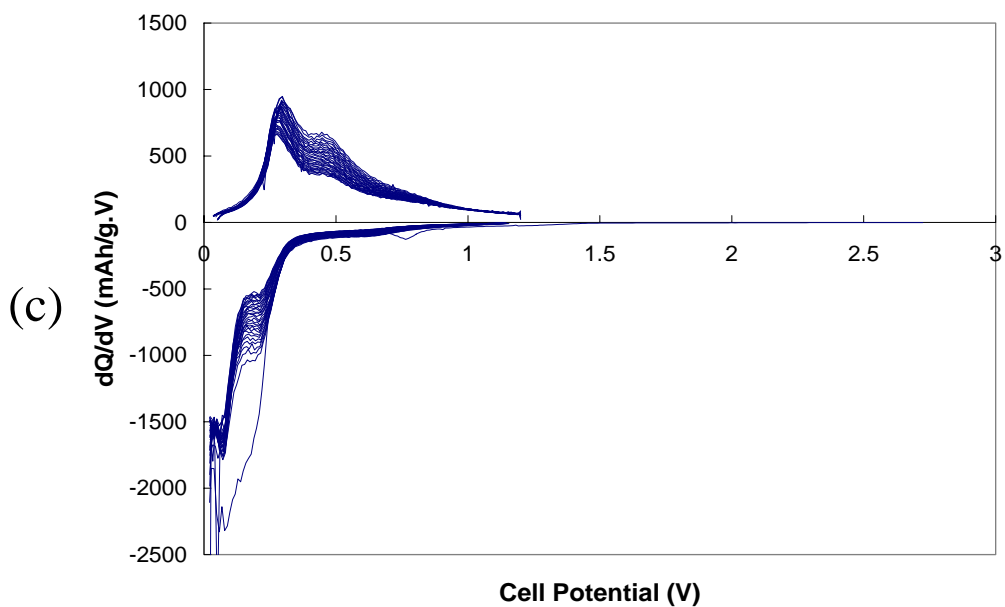


Fig. 5-22 Differential capacity vs. cell potential curves for the first twenty cycles of the nanocomposite containing  $\text{Si}:\text{TiB}_2 = 1:2$  molar ratio obtained after milling for 10 h using  $\text{TiB}_2$  premilled for (a) 24 h, (b) 12 h and (c) 18 h. (Current rate:  $100\mu\text{A}/\text{cm}^2$ , Potential: 0.02~1.2 V)

### **5. 3 Silicon/Silicon Carbide Nanocomposites**

As discussed in the previous sections, Si/TiN and Si/TiB<sub>2</sub> systems are promising and therefore TiN and TiB<sub>2</sub> appear to be good inactive matrix materials for the use of active-inactive nanocomposites as lithium ion anodes. In order to improve the capacity of the anodes further, it is necessary to use lightweight inactive components. Hence the study was focused on using SiC as an inactive material. In addition, SiC is a very hard material exhibiting hardness (2500kg/mm<sup>2</sup>, see Table 2-6) and is also a known wide bandgap semiconductor with electrical resistivity of 10~10<sup>2</sup> Ohm-cm. Nanocomposites containing Si and SiC were therefore synthesized using HEMM. As starting materials, Si, SiC and C were therefore used in order to compare their efficacy in generating Si and SiC nanocomposites.

Two approaches were used to generate the Si/SiC nanocomposites. The first approach utilized Si and SiC while the second approach employed Si and C. The formation of SiC by milling Si and C is generally well known [4, 5], and hence finer SiC powder can be expected by the latter method. SiC is unlikely to react with Si during mechanical milling and being lighter than TiN and TiB<sub>2</sub>, it can be considered a good candidate material for use as an inactive matrix. Hence Si/SiC nanocomposites will be studied to validate the use of SiC as an inactive matrix component.

#### **5. 3. 1 Phase Analysis of As-milled Powders.**

In order to generate Si/SiC nanocomposites using HEMM, two different mixtures have been used as mentioned earlier. The first mixture for HEMM comprises commercial Si and SiC. XRD analysis conducted on the nanocomposite containing 33.3 mol% Si obtained after milling Si and SiC for 24h is shown in Fig. 5-23 (a). The milled powder consists of amorphous-nanocrystalline Si and nanocrystalline  $\beta$ -SiC powder similar to the Si/TiN and Si/TiB<sub>2</sub> nanocomposite systems. The XRD pattern collected on the nanocomposite containing 33.3 mol% Si obtained after milling Si and SiC for 12h, which is not presented, exhibits a very similar pattern to Fig. 5-23 (a), comprising amorphous Si and nanocrystalline SiC. The particle sizes of Si and SiC are likely to be

different due to the milling action though not significant to be observed by x-ray diffraction. Milling the mixture of Si and SiC for 30h also yields a similar XRD pattern

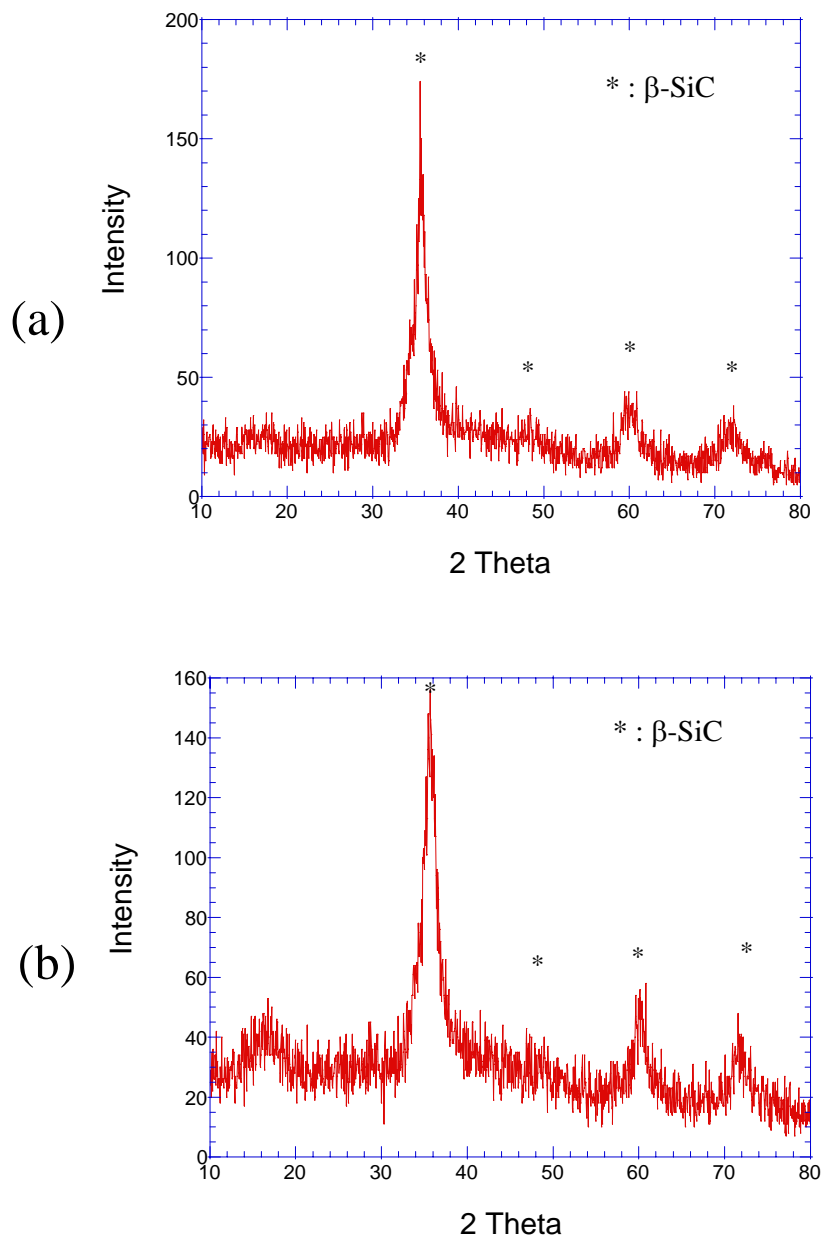


Fig. 5-23 X-ray diffraction patterns of powders milled for 24h using HEMM (a) Si:SiC = 1:2, (b) Si:C = 3:2.

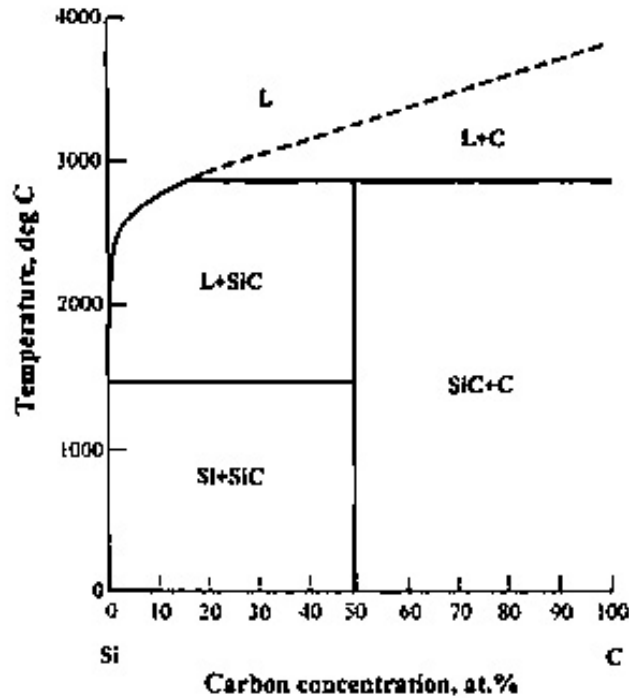


Fig. 5-24 Binary phase diagram of Si-C system [6].

although it is very likely that the particle sizes are different. It should be noted that the brittle Si particles are pulverized rapidly in the presence of SiC of high mechanical strength (Vickers hardness: 3300 kg/mm<sup>2</sup>, Tensile strength: 5~20%10<sup>3</sup> psi). Milling Si alone does not yield amorphous Si even after extended milling for more than 30 h.

The second mixture for generating the Si/SiC nanocomposites is composed of commercial Si and C powders, the composition of which is selected such that the nanocomposite composition after milling is identical to the first mixture. Since Si and C react to form an incongruently melting stoichiometric compound of SiC (Si:C=50:50) as shown in the phase diagram (Fig. 5-24), the composition of the mixture corresponding

to the molar ratio of Si:C=3:2 will generate the Si/SiC nanocomposite containing 33.3 mol% of Si after the mechanochemical synthesis of SiC. It has also been reported that Si and C with an identical molar ratio can generate stoichiometric SiC without any unreacted Si or C [6]. The XRD spectra obtained on the powder which is synthesized using a mixture of Si and C after milling for 24 h (Fig. 5-23 (b)), shows an almost identical pattern with (a), comprising amorphous Si and nanocrystalline  $\beta$ -SiC phases. This result confirms that the mechanochemical reaction between Si and C occurs at the early stages of milling and the SiC formed during milling helps to pulverize the Si powder.

### 5. 3. 2 Electrochemical Characteristics of the Si/SiC Nanocomposites

Fig. 5-25 (a) shows the specific capacity vs. cycle number for the Si/SiC nanocomposites synthesized using Si and SiC. All the samples milled exhibit a molar ratio 1:2. The advantages of using SiC as the matrix component is to prevent any possible reaction between Si and the matrix as seen from the Si-C phase diagram and to reduce the weight of the inactive matrix component. As a consequence, capacity retention is enhanced even after extended milling while maintaining the desired capacity. However, as seen from the plot, the capacity decreases with increase in milling time suggesting other possible reasons contributing to the decrease in capacity such as embedding of the active Si phase. Experiments to identify the exact cause for this reduction in capacity will be explained in the next section. Although there is a small fade in capacity, the samples milled for 30h show a capacity as high as  $\sim 370\text{mAh/g}$  after 15 cycles using a constant current of  $100\mu\text{A/cm}^2$  corresponding to a C-rate of  $\sim\text{C}/25$ .

As discussed in the Si/TiB<sub>2</sub> nanocomposites prepared using premilled TiB<sub>2</sub> powders, the initial particle size of the inactive matrix before milling affects the electrochemical stability of the capacity of the anode. It was therefore decided to explore the use of Si and C as starting materials for milling instead of Si and SiC, since SiC generated during the milling process is expected to be much finer. The anode synthesized using Si and C mixture is tested and its electrochemical characteristics are

shown in Fig. 5-25, (b). The molar ratio of the initial composition used for milling corresponds to Si:C = 3:2, which ultimately yields an overall molar ratio of Si/SiC of 1:2 assuming complete consumption of C with Si to form SiC. Although it is difficult to unequivocally distinguish the two different samples made by the different experimental approaches, it appears that Si/SiC nanocomposites prepared using Si and C mixture show better capacity retention due to the fine particle size of the inactive component although they exhibit similar capacity values of ~370mAh/g after 15 cycles using a constant current of  $100\mu\text{A}/\text{cm}^2$  corresponding to a C-rate of ~C/25.

The differential capacity of the nanocomposite samples prepared from Si:SiC=1:2 obtained after milling for 20 h, 25 h and 30 h and from a Si:C=3:2 sample obtained after milling for 12 h and 24 h, are shown in Fig. 5-27 from (a) to (e), respectively. The plots that correspond to the electrodes with stable capacity (see Fig. 5-26 (c) and (e)) appear to be almost identical, suggesting that the two samples are very similar from the viewpoint of electrochemical behavior. The two broad peaks during charge and discharge cycles ( $\cong 0.08\text{V}$ ,  $0.2\text{V}$ ;  $\cong 0.3\text{V}$ ,  $0.45\text{V}$ ) are attributed to the reaction of amorphous Si with Li. Therefore it can be concluded that the Si/SiC nanocomposite obtained from Si:C=3:2 mixture exhibits better capacity retention than the one obtained from Si:SiC=1:2 mixture. This is mainly due to the fine size of the inactive component, which is generated in-situ during the HEMM process, although the electrochemical response from the differential capacity appears to be similar. In the following section, therefore results of the microstructural study conducted will be presented for the Si/SiC nanocomposite obtained after milling Si:C=3:2 mixture for 24h.

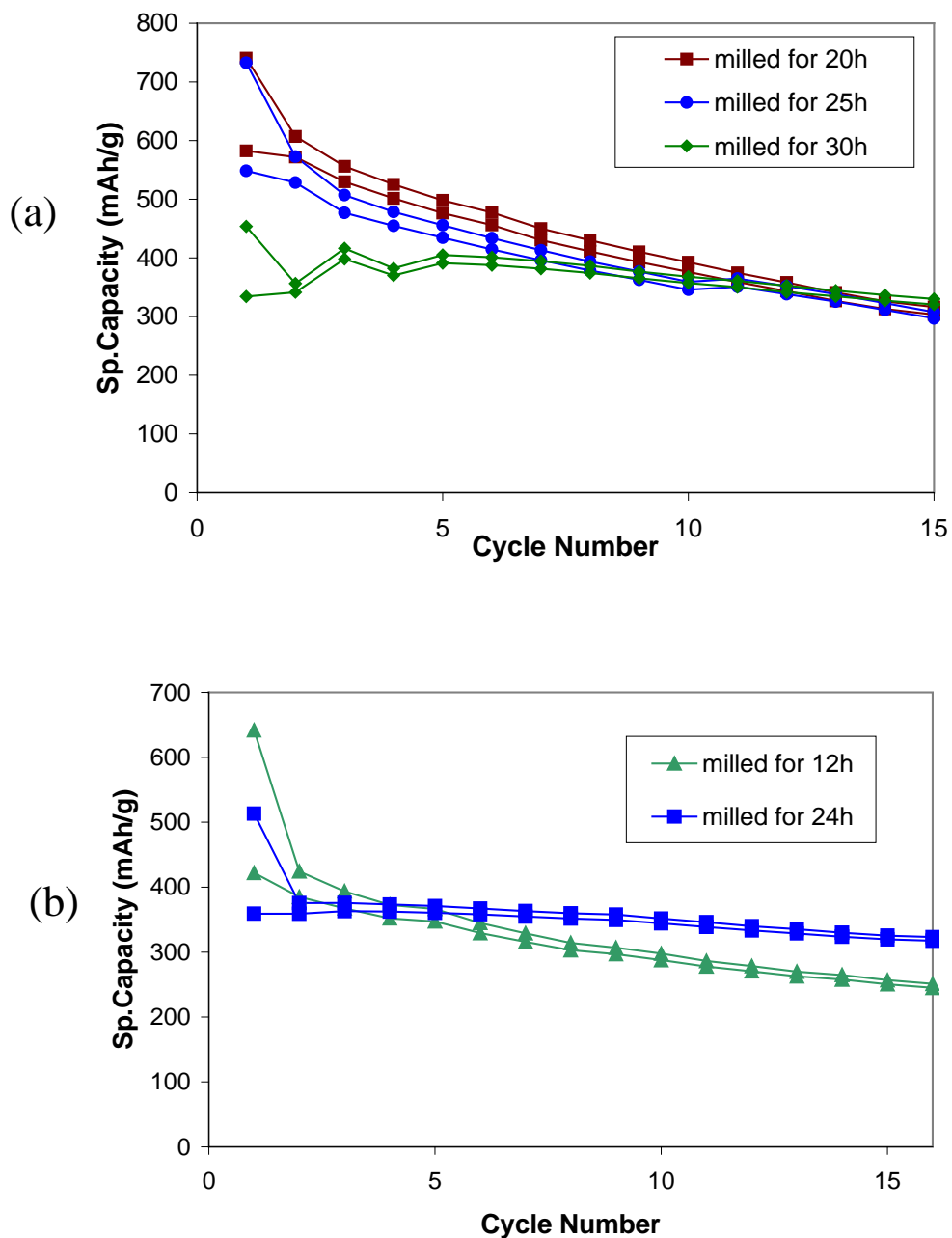
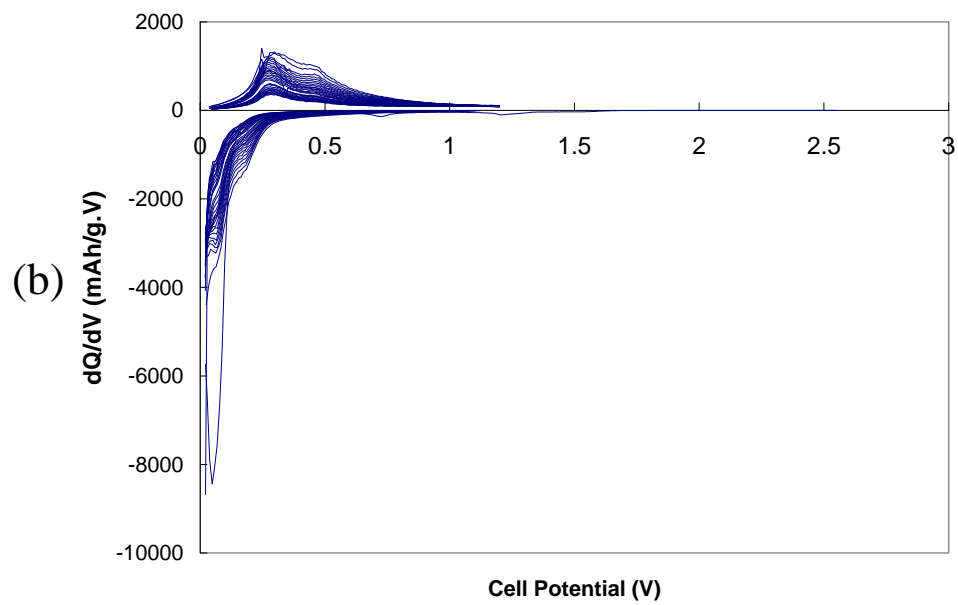
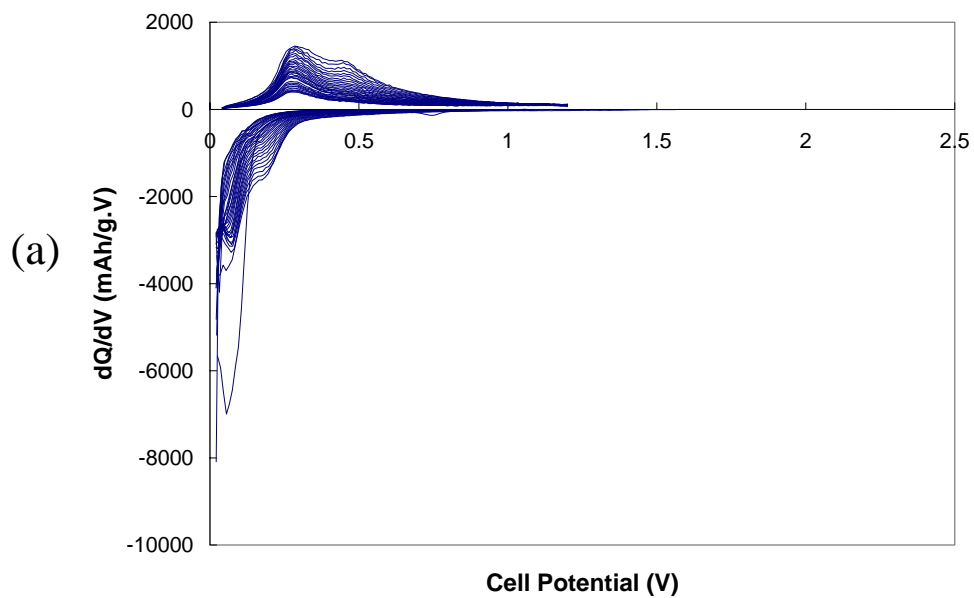
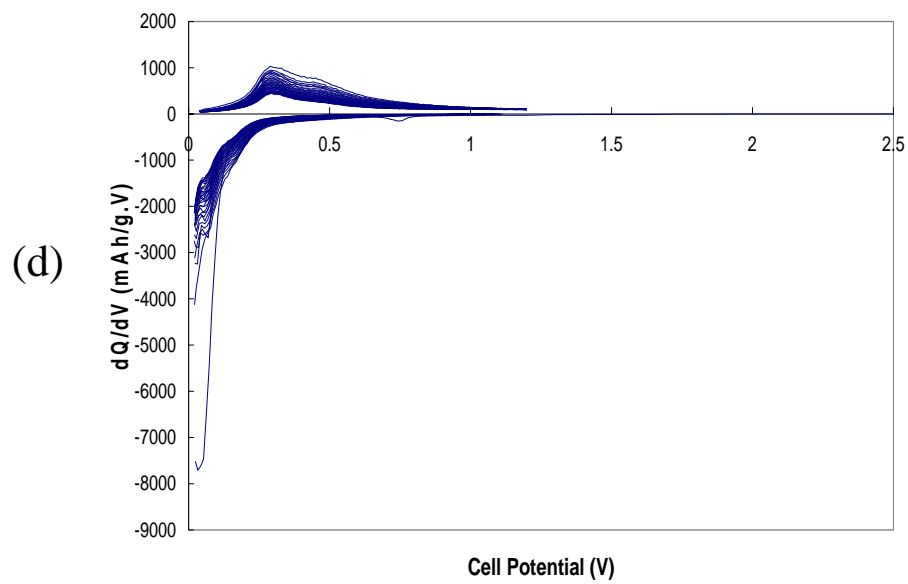
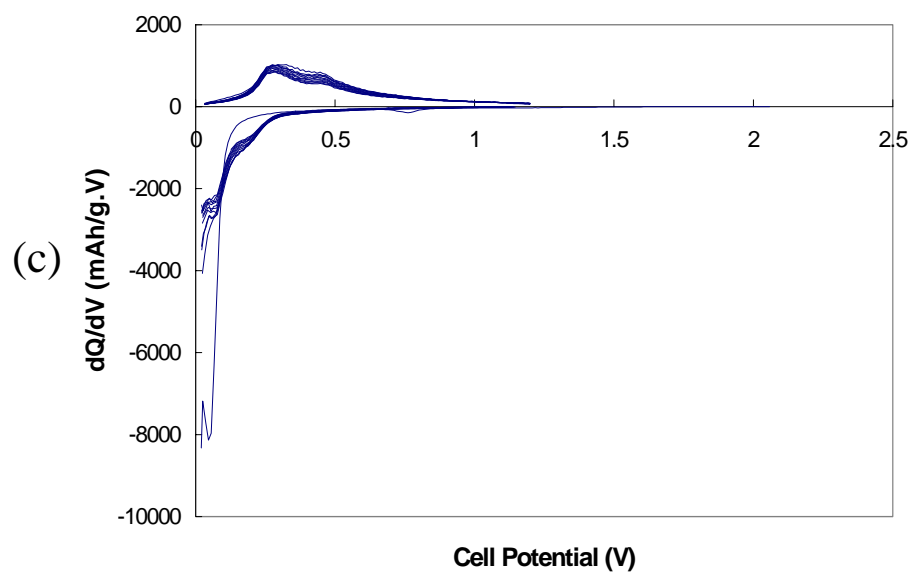


Fig. 5-25 Capacity as a function of cycle number for Si/SiC nanocomposites obtained after milling (a) Si and SiC using the molar ratio of Si:SiC=1:2, (b) Si and C using the molar ratio of Si:C=3:2. (Current rate:  $100\mu\text{A}/\text{cm}^2$ , Potential: 0.02~1.2 V)







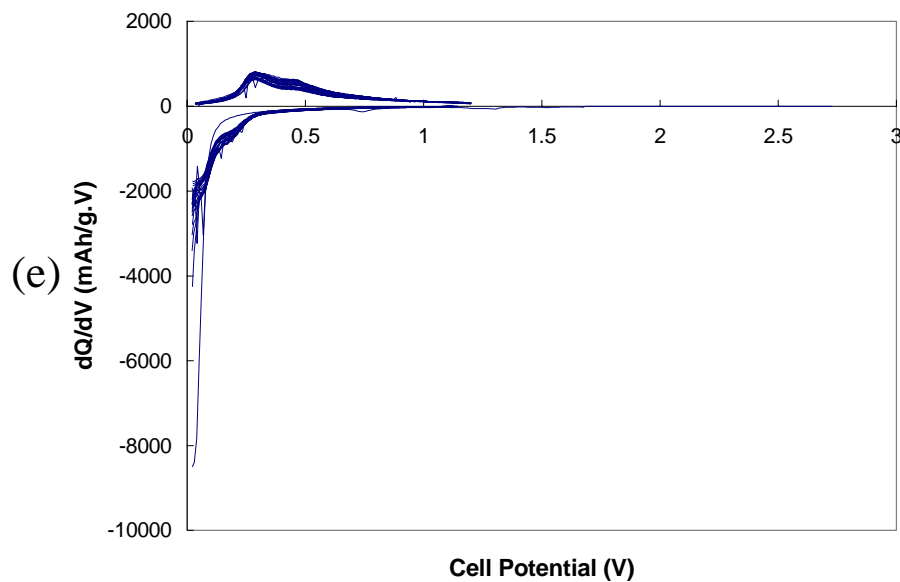


Fig 5-26 The differential capacity plots of the nanocomposites prepared from Si:SiC=1:2 obtained after milling for (a) 20 h, (b) 25 h and (c) 30h. The differential capacity plots obtained from Si:C=3:2 obtained after milling for (d) 12 h and (e) 24 h. (Current rate:  $100\mu\text{A}/\text{cm}^2$ , Potential: 0.02~1.2 V)

### **5. 3. 3 Microstructural/Morphological Analysis of the Si/SiC Nanocomposites**

In order to investigate the microstructure of the Si/SiC nanocomposite obtained from Si and C, high-resolution transmission electron microscopy (HR-TEM) was conducted on the nanocomposite of Si:C=3:2 ratio obtained after milling for 24h and the resulting micrographs are shown Figs. 5-27. The bright field image and dark field image indicate the presence of very fine size SiC crystallites (10 ~ 20 nm) seen as dark and white regions in the BF and DF images, respectively within the agglomerates ( $\cong$  100nm) (see Fig. 5-27 (a) & (b)), which is similar to the other nanocomposites obtained after HEMM discussed in the previous sections. The selected area diffraction pattern (SADP) exhibits well-defined rings with some spots corresponding to  $\beta$ -SiC (see Fig. 5-27 (d)), suggesting the nanocrystalline nature of the  $\beta$ -SiC nanosized particles. No presence of crystalline Si is seen in the SADP validating the amorphous nature of Si as indicated by XRD. The image in Fig. 5-27 (c) shows the agglomeration of Si/SiC nanocomposite particles, although the dark regions corresponding to SiC nanocrystallites are not shown clearly in comparison to the BF image (Fig 5-27 (a)) due to the lower magnification. The nanocomposite has been examined at high magnifications due to the fine particle size and severe agglomeration of the particles. At the same time, the distribution of carbon has been studied using EELS to map the presence of SiC and Si in the nanocomposite.

Fig. 5-28 (a) shows the high-resolution image of the nanocomposite corresponding to Si:SiC=1:2 obtained after milling Si and C in the molar ratio of Si:C=3:2 for 24 h. The areas showing the lattice fringes correspond to the nanocrystalline  $\beta$ -SiC that has a particle size of 5~10nm. The surrounding areas correspond to amorphous Si is not as clearly visible in the BF image. Hence elemental map of carbon has been obtained using electron energy-loss spectroscopy (EELS), the results of which are shown in Fig. 5-28 (b). Carbon was selected as the element for mapping in these nanoscale regions since silicon is present in both the active and inactive matrix components. Hence, in the case of Si, a clear map was not achieved. The bright regions correspond to SiC nanocrystallites, which indicate the regions with high concentration of carbon as mentioned earlier in the case of Si/TiN nanocomposites. The

elemental map of carbon reveals two distinct regions according to carbon concentration where Si and SiC are homogeneously distributed in the composite at a nanoscale. The microstructure of the nanocomposite appears to be slightly different from that of the Si/TiN nanocomposites. In the case of the Si/TiN, TiN particles are uniformly coated with finely milled amorphous silicon, whereas in the Si/SiC nanocomposites, the  $\beta$ -SiC particles are irregular in shape. This may be possibly caused by the in-situ chemical reaction between silicon and carbon that is responsible for generating  $\beta$ -SiC nanocrystallites in contrast to TiN. TiN nanocrystallites are generated by pulverization of TiN polycrystals while SiC nanocrystallites are generated from the diffusional chemical reaction between Si and C during HEMM. Hence  $\beta$ -SiC particles tend to have an irregular shape as shown in Fig. 5-27.

These results suggest that the Si/SiC nanocomposites comprise two phases, amorphous Si and nanocrystalline  $\beta$ -SiC analogous to the case of Si/TiN and Si/TiB<sub>2</sub>. The study also indicates that the HEMM process is a useful method to generate nanocomposites by reacting Si and carbon to form SiC, an electrochemically inactive component.

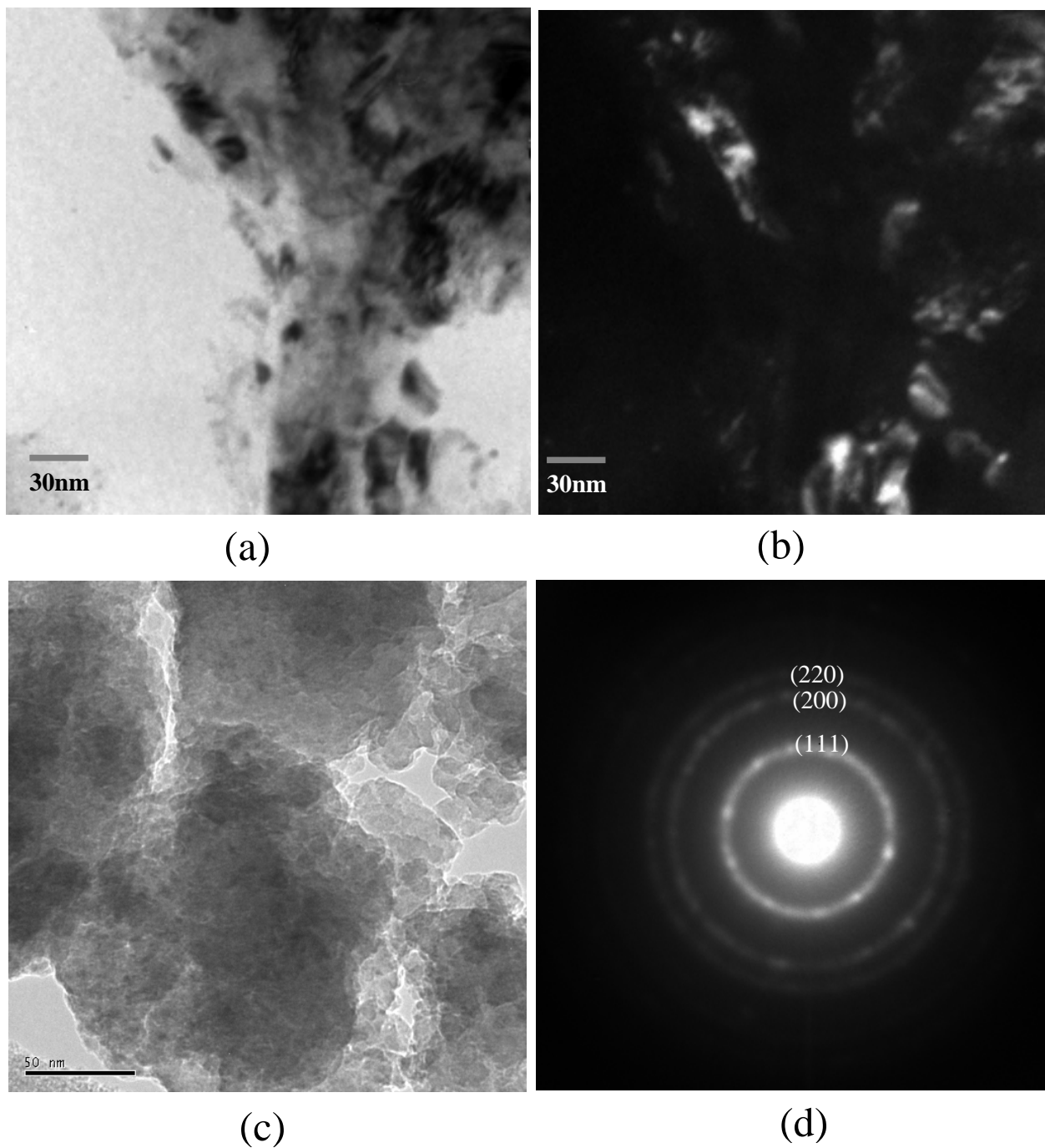
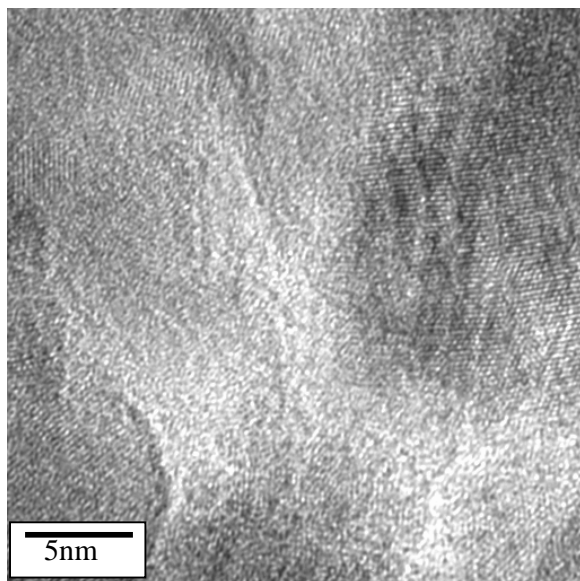
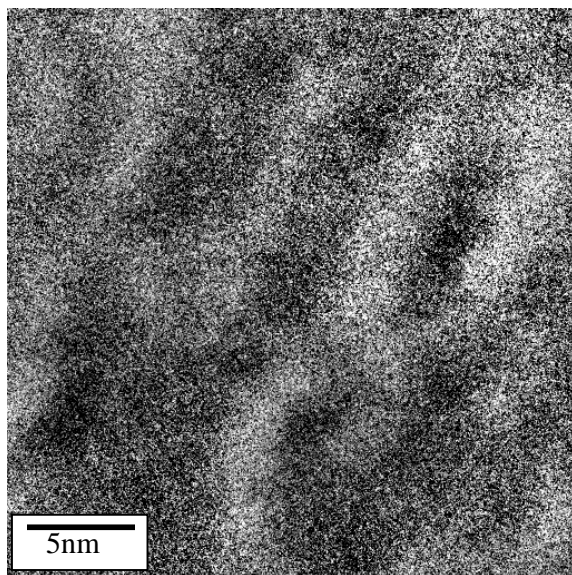


Fig. 5-27 TEM micrographs of the Si/SiC nanocomposite obtained after milling Si and C in the molar ratio (Si:C=3:2) for 24 h; (a) BF image, (b) DF image, (c) BF image at a lower magnification, and (d) SA diffraction pattern (camera length = 66cm, reduced to 70% of its original size).



(a)



(b)

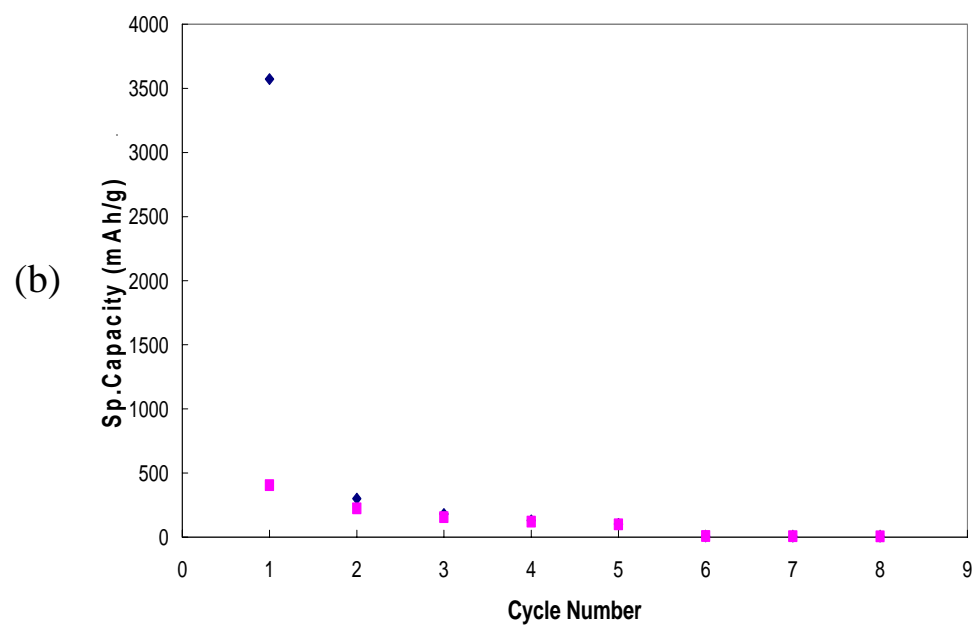
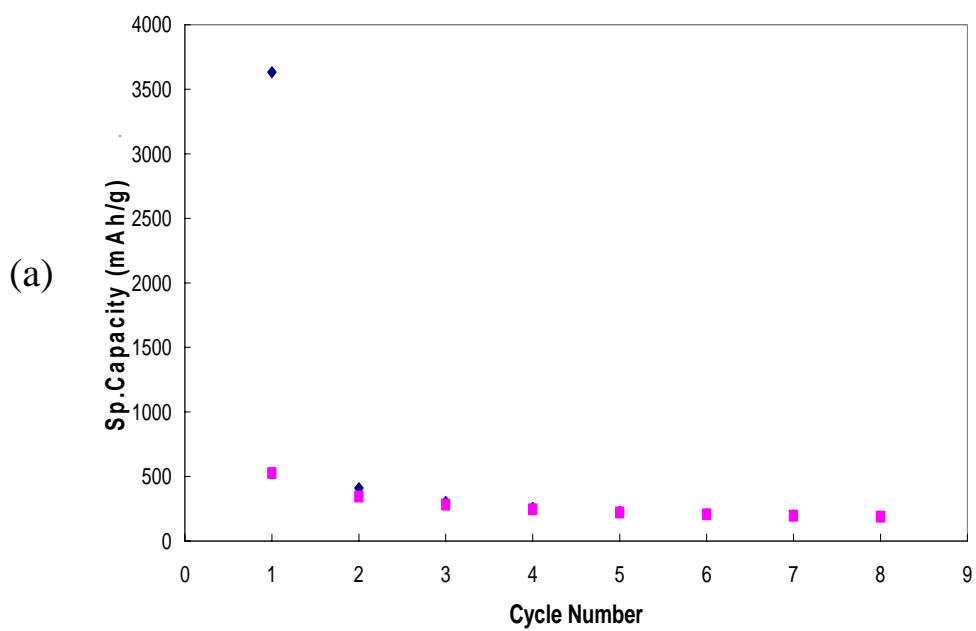
Fig. 5-28 (a) HRTEM micrographs of the Si/SiC nanocomposite obtained after milling Si and C in the molar ratio (Si:C=3:2) for 24 h, (b) Elemental map of carbon, which are analyzed by electron energy-loss spectroscopy (EELS).

## **5. 4 Study of the Inactivity of Nanocomposites Generated by Extended HEMM**

The nanocomposite anodes that have been discussed so far show good capacities and capacity retention when HEMM was conducted controlling the composition and milling time. However the capacities of the nanocomposites are still lower than the estimated theoretical capacities because of several possible reasons: 1) prolonged milling leads to shearing of the active material causing loss of contact among powder particles resulting in high interface resistance, 2) the diffusion of Si into the inactive matrix components causes the formation of other inactive phase/s at the interface of the Si and the inactive matrix components, 3) Si is probably embedded or surrounded by inactive components due to HEMM, resulting in a barrier to the electrochemical reaction of Li with Si, and 4) introduction of defects (disorder, stacking fault, dislocation) during HEMM which may contribute to some inactivity of Si.

Although further study is clearly necessary to identify the exact reason for the loss in capacity after HEMM, it should be noted that some of the factors mentioned above may be of less importance compared to others. Shearing of active materials causing loss of contact is less likely to occur since even brittle materials undergo plastic deformation when the particles are very fine as discussed in chapter 2 [7]. Besides, the particles may have good contact when they are embedded or surrounded by the inactive components. We examined the electrochemical behavior of crystalline Si and amorphous Si for their capacity (see Fig. 5-29 (a) and (b)) [8], and our studies indicate that both forms of Si are very similar in capacity, suggesting that the reaction of Li with Si is not affected by the lack of crystallinity of Si. The differential capacity plots of crystalline and amorphous samples are shown in Fig. 5-29 (c). Although there is slight difference in peak positions and intensities, both curves are very similar indicating that the electrochemical reaction of Li with either amorphous or crystalline Si is also similar. The second factor is related closely to the third because diffusion of Si into the inactive matrix implies the burial of Si atoms within the matrix components. However, extensive analyses are required to validate the proposed reasons proposed above. In this section, therefore, detailed analyses will be conducted using several techniques, particularly

related to the inactivity of nanocomposites after extended milling.





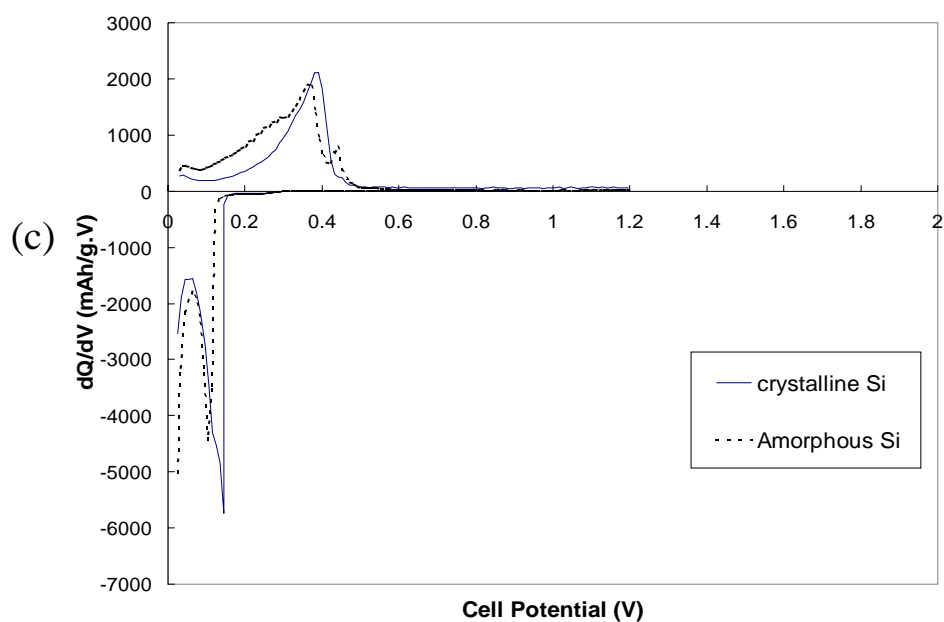


Fig. 5-29 Capacity as a function of cycle number for commercially obtained (a) crystalline and (b) amorphous silicon. (c) Differential capacity plots of commercially obtained amorphous and crystalline Si. Note the first discharge capacity of both samples is similar. (Current rate:  $250\mu\text{A}/\text{cm}^2$ , Potential:  $0.02\sim 1.2\text{ V}$ )

#### 5. 4. 1 Electrical Resistivity of Nanocomposites

In order to investigate the change in electrical resistivity of the Si/TiN nanocomposites containing 33 mol. % of Si obtained after different milling times, the 4-point probe technique has been used. The most common form of four-point probe method is the in-line type as illustrated in Fig. 5-30. There are two different modes for measuring resistivity based on the thickness of samples namely, bulk and thin film forms. Since the pellets of the nanocomposites that were used for the 4-point probe experiments have thicknesses larger than the probe spacing, the resistivity has been calculated using the relations valid for bulk samples. The equation used for the experiment is given below, where the probes can be assumed to be sitting on a material of semi-infinite volume [9]:

$$\rho = \frac{V}{I} \left[ \frac{2\pi}{1/s_1 + 1/s_3 - 1/(s_1 + s_2) - 1/(s_2 + s_3)} \right] \quad (5-2)$$

$$\rho = \frac{V}{I} 2\pi s \quad (\text{When } s_1 = s_2 = s_3 = s)$$

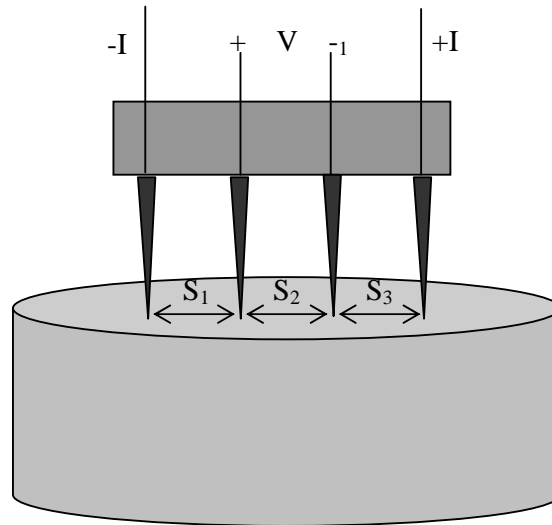


Fig. 5-30 Schematic drawing of the four point probe layout used for bulk resistivity measurement.

As described in the experimental section, the Si/TiN nanocomposites corresponding to Si:TiN=1:2 molar ratio obtained after milling for 4 h, 6 h, 9 h and 18 h, respectively were pressed into pellets using 7000lbs pressure. The density of each sample is 3.10, 3.31, 3.31 and 3.30 g/cm<sup>3</sup>, respectively and the average density (3.20 g/cm<sup>3</sup>) corresponds to almost 75% of the theoretical density (4.27 g/cm<sup>3</sup>) of the Si/TiN nanocomposites corresponding to Si:TiN=1:2. These pellets were therefore measured for their electrical resistivity using the 4-pt probe technique, assuming that the density is high enough to achieve reasonable resistivity value.

Fig. 5-31 shows the resistivity of Si/TiN nanocomposites obtained after milling for 4, 6, 9 and 18 h. Each resistivity data point is obtained using equation (5-2) and represents an average value of 15 measurements from 3 different regions of the samples. As seen from the plot, the resistivity appears to remain unchanged as milling time increases within experimental error. From the previous section, it is known that the crystallite size appears to decrease with increase in milling time, however, the decrease in particle size is almost negligible after prolonged milling. In other words, the effect of milling on particle size reduction becomes redundant after extended milling.

When a composite is composed of an insulator (or semiconductor) and conductor, the overall electrical behavior of the electronic composite is governed by percolation via the formation of a continuous network of conducting particles throughout the insulating component. Hence the overall conductivity or resistivity of the composites is dominated by the volume fraction of the conducting element as well as by the microstructure of the composite [10]. In the case of the Si/TiN nanocomposite, since all samples have the same composition of Si and TiN and the microstructure of the nanocomposites obtained using HEMM could be considered similar despite possible differences in particle size, the resistivity of the composites remains unchanged regardless of the milling time. It should also be noted that the resistivity values ( $\cong 0.0052 \sim 0.0055 \text{ } \Omega \text{ m}$ ) of the nanocomposites are much higher than the theoretical resistivity of TiN ( $2.3 \times 10^{-7} \text{ } \Omega \text{ m}$ ) [11] due to possible contact resistance of the probes although the resistivity shown in the plot is quite low, indicating that the nanocomposites obtained after milling are still good electronic conductors. It should be noted that these electronic conductivity measurements were conducted on pressed

pellets whose density values are 75% of the theoretical density. Thus the resistivity values can be considered to be apparent and originating mainly from grains with all different orientations as well as contribution from grain boundary resistance [12-14]. The resistivity values though apparent and not representative of a fully dense composite, nevertheless provide a reasonable picture of the variation in electronic conductivity of the nanocomposites obtained with different milling times. Since the density and microstructure of all the nanocomposites are similar, a constant deviation from actual values of a dense nanocomposite can safely be assumed for all the nanocomposites obtained after milling for different time intervals. Similar approaches have been used to characterize the electronic conductivity of many new nitride materials in the literature and hence the values presented here can be used to make appropriate valid comparisons and study the representative trends with varying milling times [12-14].

In the previous section, several possible reasons for the electrochemical inactivity of the composites after prolonged milling are mentioned and the one possible reason is the increase in the electrical resistivity that is caused by the high contact resistance between the particles after extended milling. However, the resistivity appears to remain unchanged after milling even for 18 h, although the sample is completely inactive sample from an electrochemically point of view. Therefore, it can be concluded that the increase in electrical resistivity is not responsible for the inactivity of the nanocomposites.

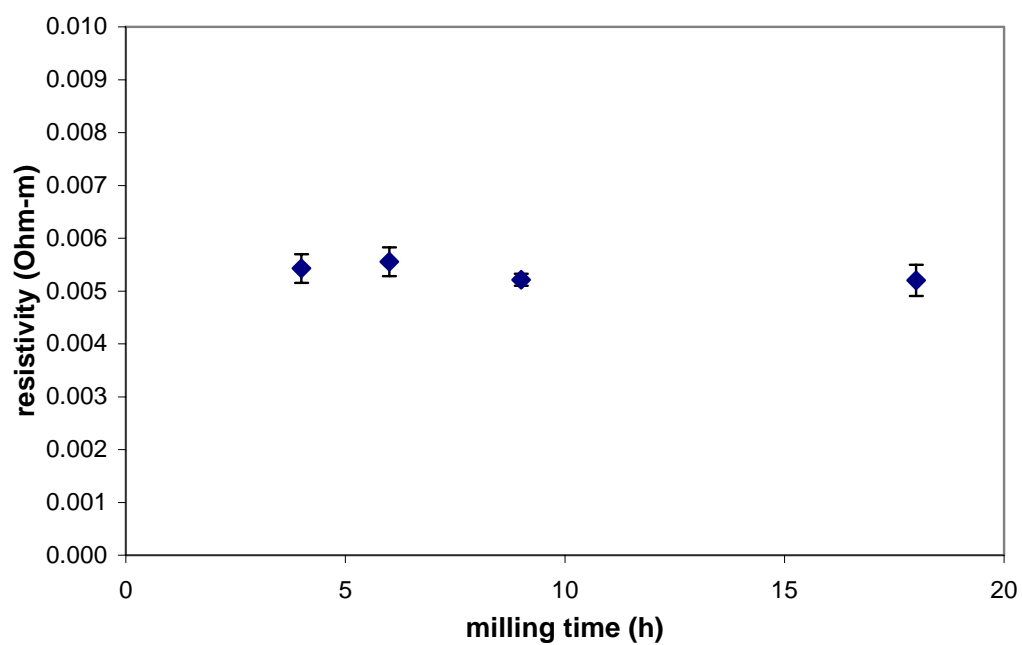


Fig. 5-31 The resistivity of the Si:TiN=1:2 nanocomposites obtained after milling for 4, 6, 9 and 18 h, respectively.

#### **5. 4. 2 Impedance Analyses of Nanocomposites**

The kinetics of lithium insertion into an electrode is dominated by the lithium ion transport through the electrolyte, the electrode/electrolyte interface and the electrode material. Impedance spectroscopy (IS) techniques have been widely used for investigating kinetics of primary or secondary batteries since IS allows us to correlate each electrical component of the cells with parameters such as resistance, capacitance, conductance, etc., obtained using simple electrical measurement.

As discussed in the previous section, the nanocomposites obtained after extended mechanical milling exhibit negligible electrochemical capacities, indicating that there is no significant reaction between Li and Si during electrochemical cycling. In order to investigate the complex variables that result in the inactivity of the electrodes, two Si/TiN nanocomposite samples that were obtained after different milling times were analyzed using impedance spectroscopy. One is an electrochemically active sample exhibiting a stable capacity of ~300mAh/g obtained after milling for 6 h and the other is an inactive sample obtained after milling for 9 h. It should be noted that the milling time for the stable and inactive sample is different from what we discussed in the previous section, since the milling conditions described here are for a different setup of the HEMM equipment. Mechanical milling is a complex process and the results are affected by a number of variables such as charge ratio, the number of balls, the size and weight of the milling media and even the power of the motor used for the specific machine.

The electrochemical capacity of these two electrodes is exhibited in Fig. 5-32. The electrodes were measured for their impedance during the first discharge to examine the effect of extended milling on the impedance spectra. It should be noted that the electrodes used for impedance analysis have the same weight in order to maintain the total amount of electrode material for both cases constant, which allow the impedance values of the two electrodes to be compared very easily. Fig. 5-33 shows the impedance spectra collected from the electrodes during first discharge when the voltage is set at 1.5, 0.75, 0.5 and 0.02 V in the frequency range of 100kHz ~ 0.01Hz. When the discharge potential changes from 1.5 to 0.02V, the IS of both samples show one depressed semi-circle and an extended portion of a tail, which is related to the Warburg impedance. In order to analyze the IS result, the model of the equivalent circuit has been established.

The detailed explanation of each component and the accompanying related mathematical related expressions are provided in appendix C. The effect of passivation layers on the impedance spectra can generally be represented by resistance (R) and capacitor (C) elements in the equivalent circuit and the spectra consist of two or multi semi-circles in this case [15-18]. However the impedance spectra shown here have only one semi-circle or arc, and thus the effect of passivation layers in the impedance analysis appears to be negligible in the spectra. All the spectra could be deconvoluted with the equivalent circuit as depicted in Fig. 5-34. The  $R_{\Omega}$  component corresponds to higher frequency region ( $> \sim 30\text{kHz}$ ), the semi-circle represents the parameters, charge transfer resistance,  $R_{ct}$  and constant phase element, CPE in the intermediate frequency range ( $\sim 30\text{kHz} \sim 10\text{Hz}$ ), which are assigned to the charge transfer reaction during the  $\text{Li}^+$  insertion process. In the low frequency range ( $< \sim 10\text{Hz}$ ), Warburg Impedance,  $Z_w$ , becomes most significant, which is related to  $\text{Li}^+$  ion diffusion into the electrode. The values of each parameter have been obtained by complex nonlinear least square (CNLS) method, using the 'Zview' program based on the equivalent circuit model.

The evolution of  $R_{ct}$  is shown in Fig. 5-35 (a) for the electrodes obtained after milling for 6h and 9h denoted as 'active' and 'inactive' sample respectively, during the first discharge process, where  $R_{ct}$  values are obtained by fitting the impedance data to the model.  $R_{ct}$  is indicative of the inherent reaction speed in an electrode reaction. In other words, a high  $R_{ct}$  value represents a slow reaction. In contrast to a mass transfer reaction that involves diffusion of ionic species, charge transfer reaction indicate electron transfer to the absorbed ionic species or vice versa at the electrode/electrolyte interface. As seen from the plot,  $R_{ct}$  of the active electrode decreases at the voltage of 0.75V because  $\text{Li}^+$  ions begin to react with Si in the active sites and electrons are transferred to form the Li-Si alloys. As the discharge voltage decreases,  $R_{ct}$  appears to increase since the number of Si atoms in the active sites decreases after the reaction with  $\text{Li}^+$  ions. Similarly, the  $R_{ct}$  of the inactive electrode obtained after milling for 9h exhibits a slight decrease at the discharge voltage of 0.75V and an increase as the voltage decreases further. However, the  $R_{ct}$  values are almost 5 fold higher when compared to that of the active electrode since the number of active Si atoms are much less in the case of inactive electrode because of embedding of Si during prolonged milling of the Si/TiN mixture. Hence it can be concluded that embedding of Si leads to

the high  $R_{ct}$  values, which prevent the reaction of  $Li^+$  ions with Si in the electrode. Brug et al. [19] mention that the double layer capacitance ( $C_{dl}$ ) of the CPE can be expressed by the following equation, where  $Y_o$ ,  $n$  are the characteristic parameters for the CPE [19-21].

$$Y_o = (C_{dl})^n \left( \frac{1}{R_{\Omega}} + \frac{1}{R_{ct}} \right)^{1-n} \quad (5-3)$$

The change of  $C_{dl}$  with respect to the discharge voltage is shown in Fig. 5-35 (b).  $C_{dl}$  is known to be inversely proportional to the thickness of electrical double layer, and in the case of the ‘inactive’ sample, there is a larger accumulation of  $Li^+$  ions at the electrode interface, thus resulting in a smaller double layer capacitance as shown in the figure [22]. In addition,  $C_{dl}$  is also inversely proportional to the quantity of  $R_{ct}$ , however, the effect of  $R_{ct}$  on the  $C_{dl}$  is negligible in the equation (5-3) since the quantity of  $1/R_{ct}$  is much smaller compared to  $1/R_{\Omega}$  and  $C_{dl}$  of both electrodes therefore can be determined by other factors such as  $Y_o$ ,  $n$  and  $R_{\Omega}$  rather than  $R_{ct}$ .

The diffusivity of  $Li^+$  ions is measured from ‘ $\tau$ ’, which has been obtained from the Warburg impedance under finite-space condition as explained in the appendix. In this case, the Warburg impedance can be expressed by [23-27]:

$$Z_{FSW} = R_D \left( \frac{j\omega l^2}{D_{Li^+}} \right)^{-1/2} \coth \left( \frac{j\omega l^2}{D_{Li^+}} \right)^{-1/2} \quad (5-4)$$

where  $R_D$  is the low frequency limit of  $Z_w$  and  $\tau (= l^2/D)$  is a diffusion time constant. Therefore the diffusivity of Li ions can be calculated from the Warburg coefficient ( $\tau$ ) and  $l$ , measured from the ‘hockey puck’ cell setup using the equation,  $D = l^2/\tau$ . The value of ‘ $l$ ’ was determined to be 0.558mm measured between the working electrode (Si/TiN) and the counter electrode (Li). Since the tail portion of the data can show a non-linear response attributed to factors other than diffusion of  $Li^+$ , only the initial data of the tail part has been used to obtain the diffusion coefficient in the relatively high frequency range. The diffusivity of  $Li^+$  obtained from both ‘active’ and ‘inactive’ electrodes is shown in Fig. 5-35 (c) exhibiting the diffusivity values of  $10^{-6} \sim 10^{-8}$



$\text{cm}^2/\text{sec}$  during  $\text{Li}^+$  insertion, which is comparable to values of the chemical diffusion coefficient of  $\text{Li}^+$  in  $\text{Li}_{4.4}\text{Sn}$  alloy system measured by the coulometric titration technique, reported in the literature [28]. In both samples, the diffusivity decreases as  $\text{Li}^+$  insertion progresses since the number of available sites of Si at the surface for diffusion decreases. A longer diffusion path for Li ions to form alloys with Si therefore causes a decrease in diffusivity. Although the diffusivity of the ‘active’ electrode appears to be slightly higher, there is no significant difference indicating that the diffusion of  $\text{Li}^+$  ions in the electrodes is not a major factor contributing to the inactivity of the nanocomposite after prolonged milling.

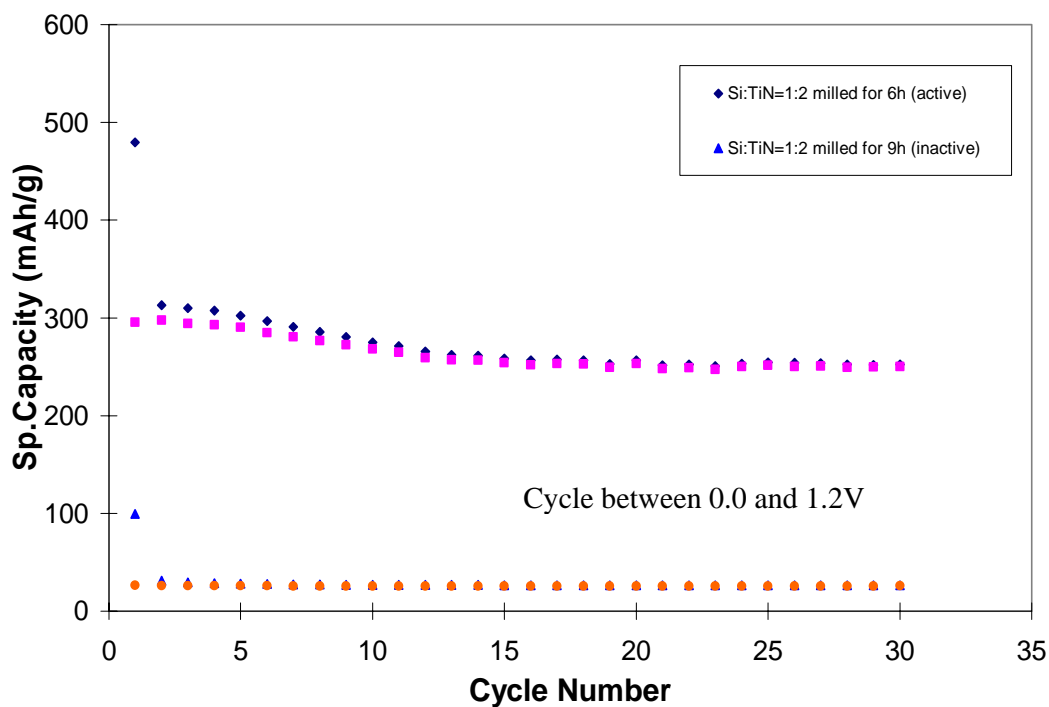


Fig. 5-32 Capacity as a function of cycle number for Si/TiN nanocomposites containing 33 mol% Si obtained after milling for 6 h and 9 h each. (Current rate:  $100\mu\text{A}/\text{cm}^2$ , Potential: 0.02~1.2 V)

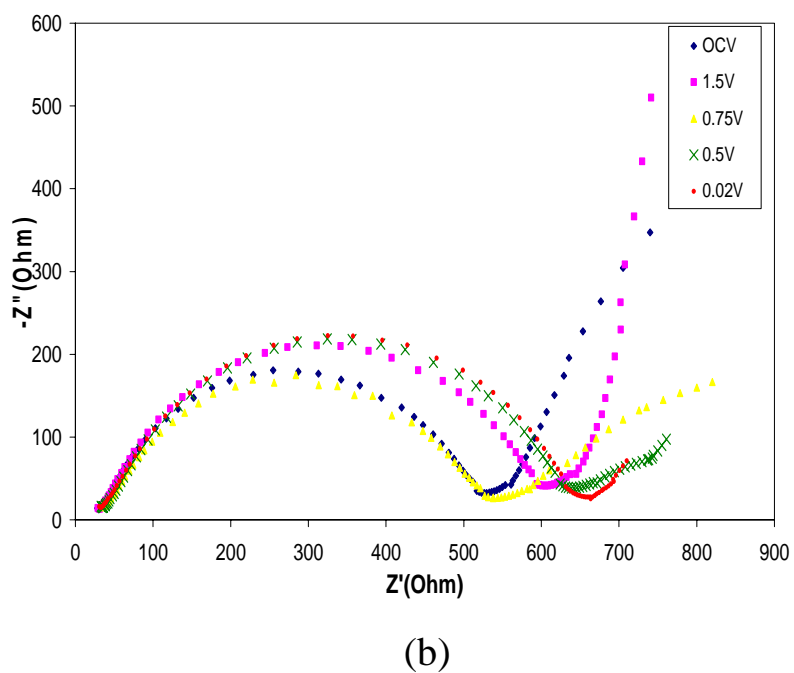
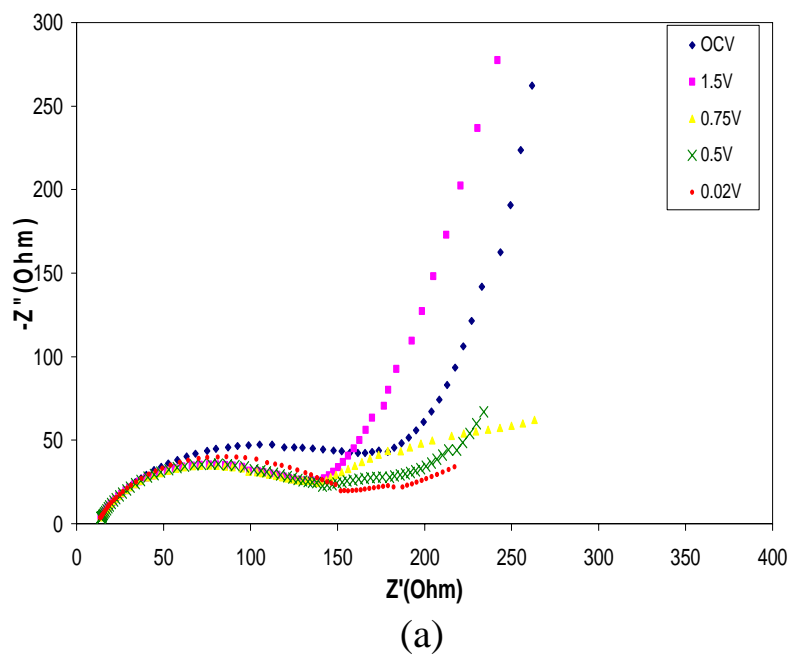


Fig. 5-33 Impedance spectra collected at different discharge voltages on the Si/TiN (Si:TiN=1:2) nanocomposite electrode obtained after milling for (a) 6h, (b) 9h respectively, during the first discharge process.

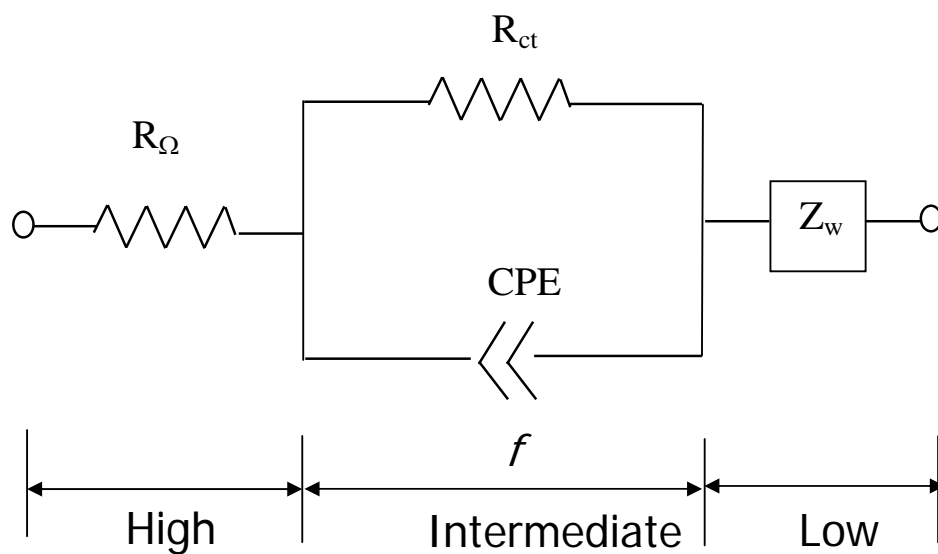
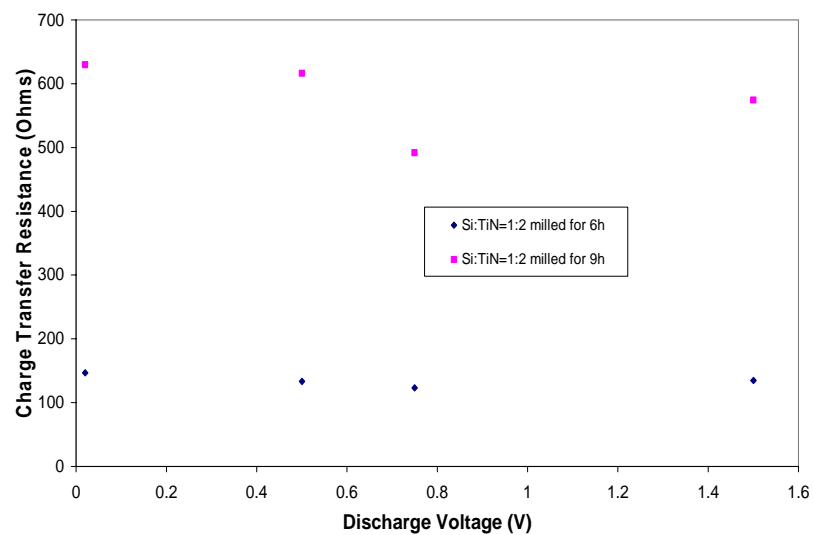
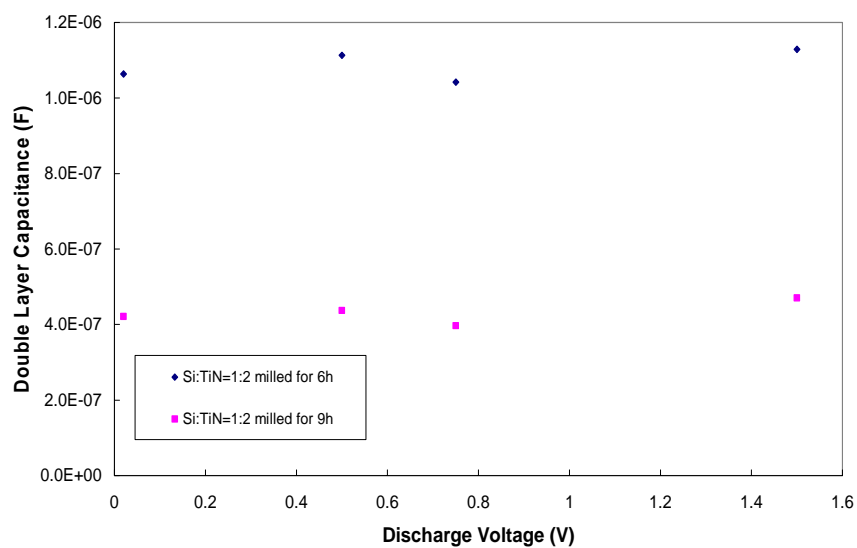


Fig. 5-34 Equivalent circuit used for the interpretation of the Si/TiN nanocomposite electrodes. ( $R_{\Omega}$ : ohmic resistance,  $R_{ct}$ : charge transfer resistance, CPE: constant phase element,  $Z_w$ : Warburg impedance and  $f$ : frequency)

(a)



(b)



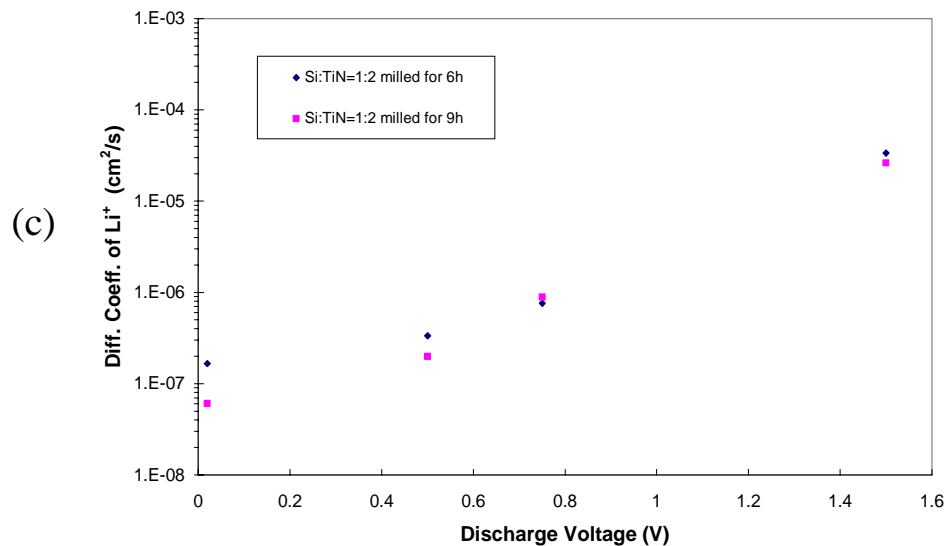


Fig. 5-35 The plots of (a) Charge transfer resistance ( $R_{ct}$ ) vs. discharge potential, (b) Double layer capacitance vs. discharge potential, and (c) Diffusion coefficient of  $\text{Li}^+$  ions vs. discharge potential of the Si/TiN (Si:TiN=1:2) electrodes obtained after milling for 6 h and 9 h, respectively.

### **5. 4. 3 Chemical Stability of the Active-inactive Nanocomposites**

Understanding the interfacial phenomena between the active and inactive components is very important since the stability and performance of the nanocomposites are directly linked to the nature of the active-inactive component interface. Wetting is therefore a key factor important for understanding the interfacial phenomena especially between the ceramic and the metal useful for analyzing the performance of a number of ceramic-metal matrix composites for high temperature and thin-film applications, etc [29-35]. Wetting is a consequence of short-range intermolecular interactions between ions or atoms, and is a significant parameter that exhibits the chemical affinity of different materials. Although wetting behavior of nanosized systems is not known, the general understanding of wetting behavior of active and inactive elements will be useful in justifying the thermodynamic and chemical stability of the selected active and inactive components studied.

As mentioned in chapter 2, the chemical stability between the active and inactive components is important since any reaction between the active and inactive elements may not be desirable in order to obtain nanocomposite materials with high electrochemical capacity using either HEMM or pyrolysis. Although the inactive component, SiC, was prepared by the reaction between Si and C in the case of Si/SiC nanocomposites, there was no further reaction of Si with the SiC synthesized in-situ during HEMM. Wetting experiments to ascertain the chemical inertness of the active and inactive components was conducted using TiN and Sn as the model system primarily since Si has a high melting temperature  $\sim 1410^{\circ}\text{C}$  [29] and thus wetting experiments would need much higher temperatures beyond the melting point of Si. The synthesis of Sn/TiN nanocomposites and their electrochemical response will be presented in the next section.

In order to study the wetting behavior of Sn on TiN, TiN film that has a thickness of  $\sim 6\mu\text{m}$  has been deposited onto polished polycrystalline alumina substrate (CoorsTek, 99.6%,  $1'\times 1'\times 0.01'$ , roughness  $< 26\text{nm}$ ) using R.F sputtering, whose experimental details are given in chapter 3. XRD analysis of the sputtered TiN film shows broad peaks of the TiN phase with preferred (110) orientation due to the

abnormally large (220) peak intensity seen in the XRD pattern shown in Fig. 5-36 in comparison to the normal TiN x-ray pattern. 0.2g of commercially obtained Sn (Aldrich, 99.8%, 325 mesh) powder was then power sprinkled on the TiN film, followed by heat-treatment in UHP-Ar atmosphere at a temperature of 800°C for 5h to achieve complete melting and equilibrium wetting. The sample was then quenched by air cooling to room temperature and analyzed using SEM for wetting behavior. The SEM image of Sn droplets on TiN film is shown in Fig. 5-37.

The interfacial energy between Sn and TiN ( $\sigma_{\text{Sn-TiN}}$ ) can be expressed in terms of surface energy of Sn ( $\sigma_{\text{Sn}}$ ), and surface energy of TiN ( $\sigma_{\text{TiN}}$ ) and the contact angle ( $\theta$ ) of Sn droplets on the TiN film using the familiar Young's equation:

$$\cos \theta = \frac{\sigma_{\text{TiN}} - \sigma_{\text{Sn-TiN}}}{\sigma_{\text{Sn}}} \quad (5-5)$$

wherein the surface energy of Sn ( $\sigma_{\text{Sn}} = 506 \text{ mJ/m}^2$ ), and surface energy of TiN ( $\sigma_{\text{TiN}} = 6990 \text{ mJ/m}^2$ ) were obtained from reports in the literature [36] and the contact angle ( $\theta$ ) was measured from the SEM images. The average value of wetting angle obtained from 8 measurements from different locations on the surface of the film is  $\sim 137.2^\circ$ , which corresponds to the interfacial energy between Sn and TiN ( $\sigma_{\text{Sn-TiN}}$ ) of  $\sim 7.37 \text{ J/m}^2$ . The result above indicates very poor wettability of Sn, indicating that Sn is not likely to react with TiN due to the high interfacial energy. The wetting angle of Sn/TiN system is also comparable to that of Ag/TiN, which has negligible wettability [31].

The work of adhesion ( $W_{\text{Sn-TiN}}$ ) and spreading coefficient ( $S_{\text{Sn/TiN}}$ ) are additional parameters that provide information about the stability of the system and are given by following equations [32-34].

$$\begin{aligned} W_{\text{Sn-TiN}} &= \sigma_{\text{Sn}} (1 + \cos \theta), \\ S_{\text{Sn/TiN}} &= W_{\text{Sn-TiN}} - 2\sigma_{\text{TiN}} \end{aligned} \quad (5-6)$$

The calculation using above result gives  $W_{\text{Sn-TiN}}$  of  $\sim 134.74 \text{ mJ/m}^2$  and  $S_{\text{Sn/TiN}}$  of  $-13.85 \text{ J/m}^2$ , where a negative spreading coefficient means that Sn will not spread over TiN. This information of wetting of Sn and TiN can be used to understand the wetting behavior of Si and TiN as well.

As mentioned before, heating Si up to a temperature much higher than the melting point of Si is necessary to obtain complete information on the wetting behavior of Si on TiN. This being a difficult experimental proposition, was therefore not conducted. However chemical stability of the Si/TiN system has been studied by conducting a phase analysis using XRD after high temperature treatment at temperature  $\cong 1500^\circ\text{C}$ . Fig. 5-38 shows the XRD spectrum obtained after heat-treatment of commercial Si (0.09g, Aldrich, 99.5%, 325 mesh) and TiN (0.42g, Aldrich, 99.5%, 325 mesh) powders corresponding to 1:2 molar ratios at  $1500^\circ\text{C}$  in UHP-Ar for 5h. The sharp peaks seen in the XRD plot can all be assigned to crystalline Si and TiN. No other phase is seen in the scan, indicating that there is no reaction between Si and TiN during heat-treatment at an elevated temperature higher than the melting point of Si. From the results above, it can be construed that TiN is thermodynamically/chemically stable when used with Sn and Si. The chemical inertness exhibited by Sn + Si to TiN therefore suggest that TiN is a good inactive material for use in the synthesis and study of nanocomposite electrode materials.



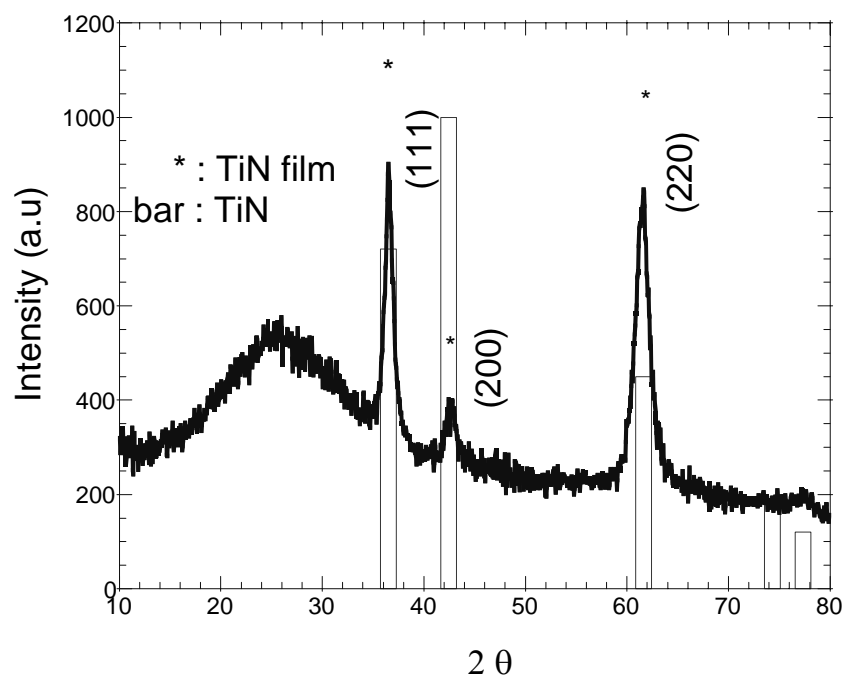


Fig. 5-36 XRD spectrum collected on the TiN thin film obtained after sputtering from a Ti target in Nitrogen atmosphere onto polycrystalline dense  $\text{Al}_2\text{O}_3$ . Note the crystallographic data for TiN is shown by bars.

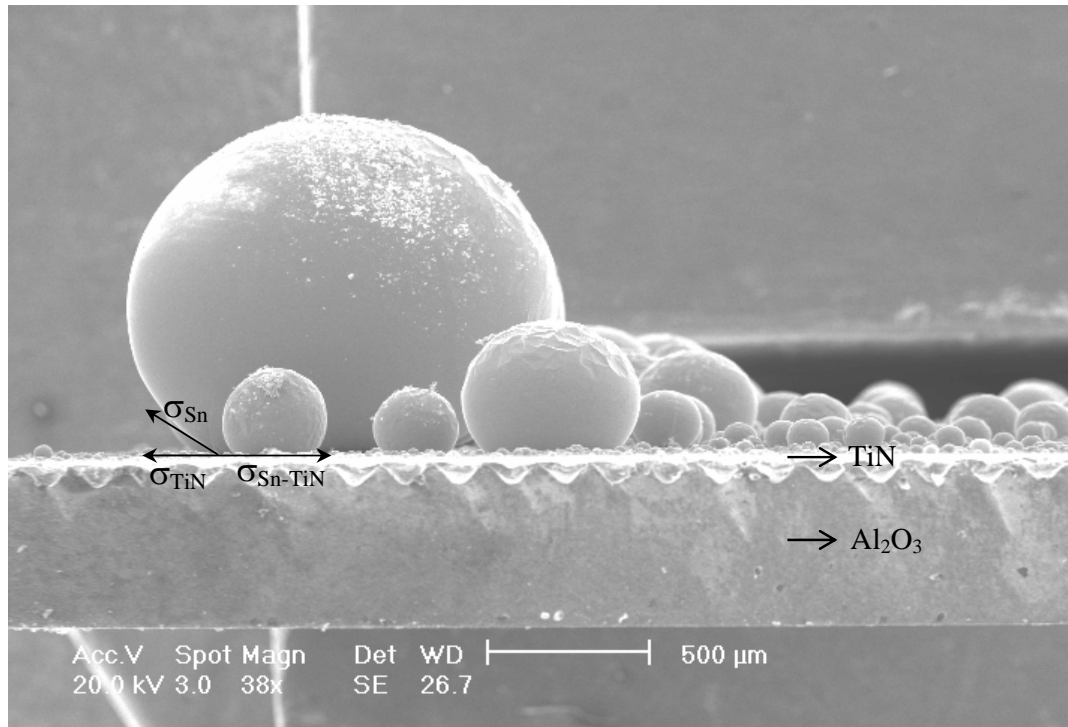


Fig. 5-37 SEM micrograph showing the Sn-TiN interface. Note the formation of Sn droplets with contact angle of  $137.2^\circ$  indicating the non-wetting of Sn on TiN.

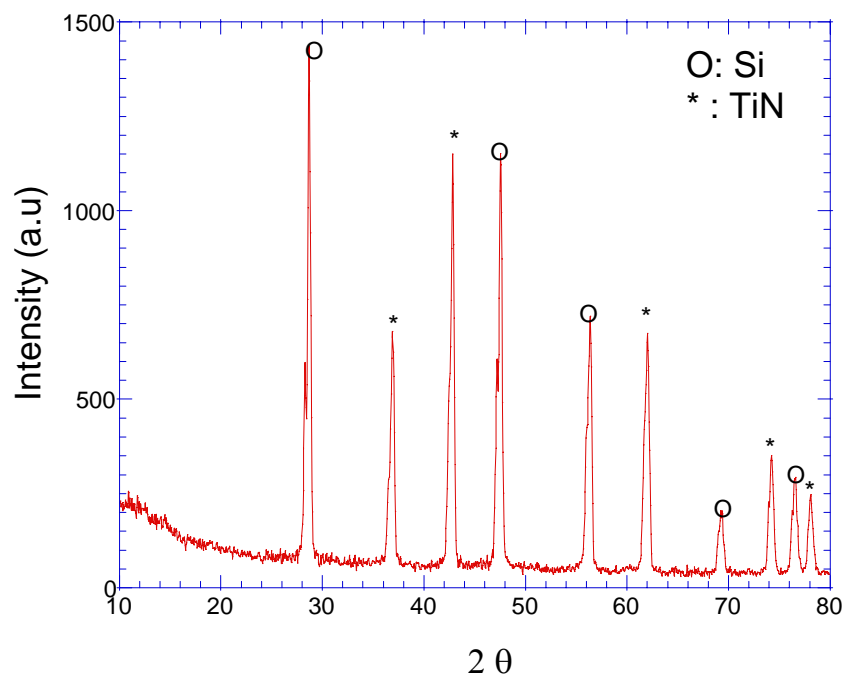


Fig. 5-38 XRD pattern of Si and TiN mixture obtained after heat-treatment at 1500°C for 5 h in UHP-Ar.

#### **5. 4. 4 High Resolution TEM (HR-TEM) Analyses**

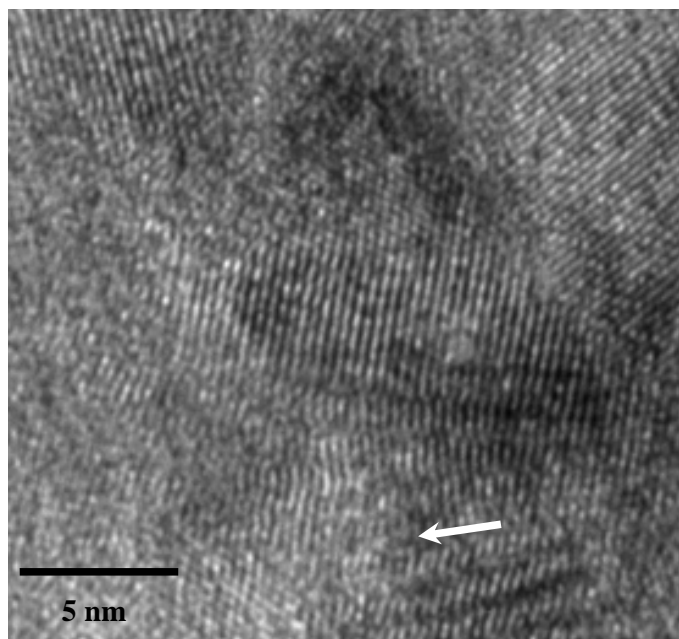
In order to confirm the results obtained from the above sections, HR-TEM study has been conducted on the Si/TiN corresponding to Si:TiN=1:2 nanocomposite sample obtained after milling for 9h. Since the electrode is electrochemically inactive as mentioned, the microstructural analysis will elucidate the possible reasons for the inactivity observed in addition to the evidences provided by the impedance analyses, electrical resistivity measurements and the chemical stability experiments conducted at high temperatures. From the results so far, the most plausible reason for the inactivity observed in the Si/TiN nanocomposites is the embedding of active Si by nano-sized TiN crystallites during HEMM.

The bright field image of the nanocomposite, which is seen in Fig. 5-39 (a), provides an example of the embedded Si cluster in the matrix, which is indicated by an arrow. Embedding of Si does not imply that Si clusters are completely sealed by TiN grains but rather that Si clusters are surrounded by TiN particles, which leads to the inactivity of Si due to the kinetics limitation of the reaction of Li with Si. Although embedding of Si with TiN nanocrystalline particles is not shown clearly by the bright field image, EELS mapping of Si provides a better picture illustrating the isolation of Si clusters surrounded by TiN crystallites (see Fig. 5-39, (b)). The bright dotted areas in Fig. 5-39 (b) with an arrow correspond to the isolation of Si clusters by TiN particles, which are indicated by dark areas. This type of embedding can be caused by continuous pulverization and deformation of less brittle materials such as silicon during the high-energy mechanical milling process by very hard material such as TiN, as mentioned in chapter 2. Another example of embedded Si cluster can be seen in Fig. 5-39 (c), indicated by an arrow and the corresponding EELS map of Ti taken from identical regions indicated by an arrow (see Fig. 5-39 (d)). The EELS map of Ti also suggests the isolation of Si clusters as seen by the dark region surrounded by white spots corresponding to Ti (see Fig. 5-39 (d)).

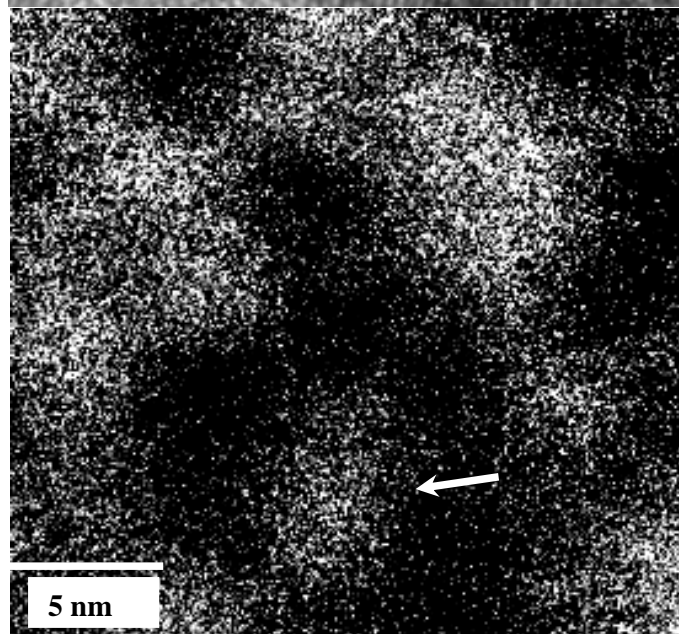
The clean interface between a nanocrystalline TiN particle identified by fringes and amorphous Si is shown and indicated by an arrow in Fig. 5-40. As discussed in the previous section, the Si/TiN nanocomposite exhibits remarkable chemical stability of Si to TiN during heat-treatment to temperatures higher than the melting temperature of

Si, which indicates that there is no chemical reaction or formation of any secondary phase at the interface. Based on the HR-TEM image, the interface shows no interfacial layer or secondary phase, indicating that Si and TiN do not undergo any chemical reaction during HEMM. The HR-TEM result does indeed suggest that embedding of Si is the main possible reason for the electrochemical inactivity observed after prolonged milling.

(a)



(b)



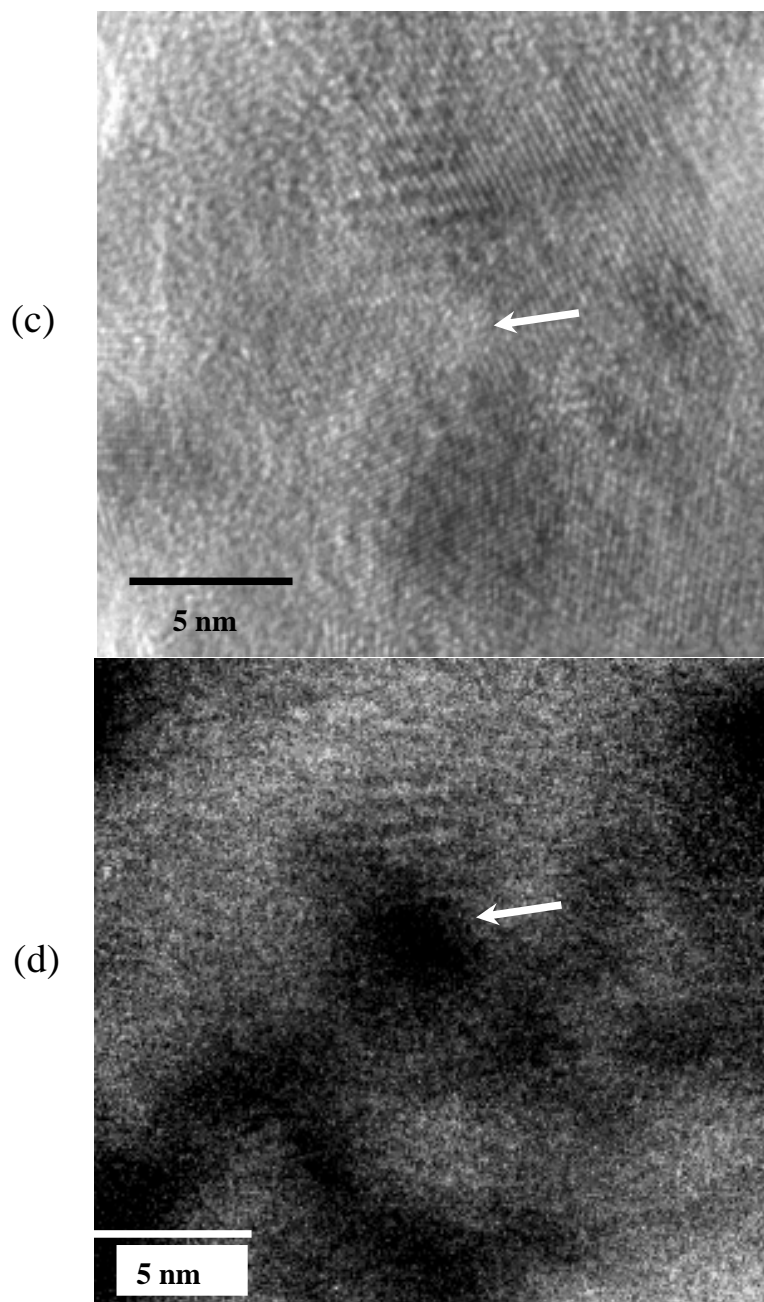


Fig. 5-39 (a) and (c) HRTEM micrographs of the Si/TiN nanocomposite containing 33 mol% Si obtained after milling for 9 h, (b) EELS elemental map of Si obtained from (a), (d) EELS elemental map of Ti obtained from (c). (The arrows represent the same position in (a) and (b), (c) and (d), respectively.)

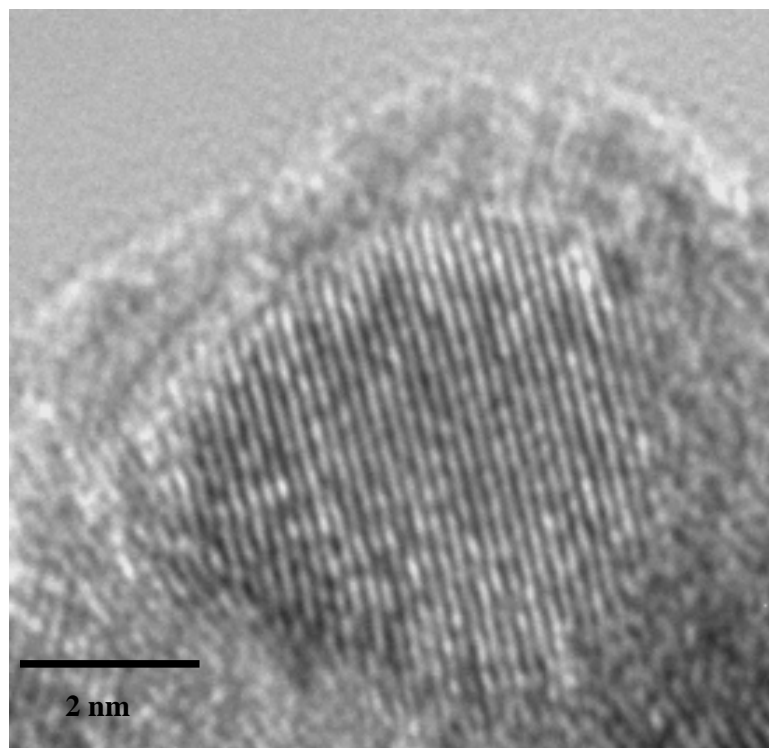


Fig. 5-40 HRTEM micrographs of the interface between nanocrystalline TiN and amorphous Si, taken from the Si/TiN nanocomposite containing 33 mol% Si obtained after milling for 9 h.



#### **5. 4. 5 Addition of Particle Size Reducers**

Results of several analyses conducted so far have verified that embedding of Si is indeed the main reason for the electrochemical inactivity of nanocomposites obtained after extended HEMM. In order to validate the proposed embedment of Si, a simple experiment was designed. Small amount of particle size reducers such as sodium chloride (NaCl) or sodium iodide (NaI) were used along with the initial mixture used for HEMM. After milling, these particle size reducers are leached out by water or alcohol to expose the possibly embedded Si particles. The rationale being that the removal of the particle size reducer by dissolution after milling will result in the generation of smaller particles allowing easy access for lithium to the embedded Si clusters. This concept was first demonstrated for Si/TiN and Si/SiC nanocomposites.

Fig. 5-41 shows the change in capacity of the Si/TiN composite containing 33.3 mol% Si obtained after milling for 12h before and after addition of the particle size reducer, NaCl. It should be noted however that the nanocomposite now shows a different capacity from the system shown in Fig. 5-5, since a different milling machine was used for this study. Nevertheless, increase in capacity after addition of 5 wt% NaCl is clearly evident in the plot, suggesting that the particle size reducer affects the increase in capacity by exposing embedded Si during mechanical milling. In addition, it should be noted that the increase in capacity is more significant in inactive Si/TiN sample than the case of Si/SiC, which will be shown below, due to the larger amount of embedded Si, which contributes to a larger capacity after the embedded Si is exposed.

The differential capacity of the nanocomposite samples prepared from Si:TiN=1:2 after milling for 12 h containing 0 wt.% and 5 wt.% of NaCl as particle size reducer are shown in Fig. 5-42 (a) and (b), respectively. The plot obtained from the electrode without adding any particle size reducer exhibits a typical differential capacity plot characteristic of a double layer capacitor, whose capacity is as low as ~100 mAh/g. The absence of any significant peaks in the plot suggest that the capacity is probably attributed to a surface reaction resulting in a non-faradic double layer capacitance rather than due to an electrochemical reaction of Li with Si. While there is no distinct peak in Fig 5-42 (a), the differential capacity plot of the electrode obtained using 5 wt% NaCl exhibits typical broad peaks during charge and discharge process (see Fig. 5-42 (b)),

which are attributed to the reaction between Li and amorphous Si.

This concept of the particle size reducer is also applied to the Si/SiC composite containing Si:SiC=1:2 molar ratio obtained by milling Si:C = 3:2 after 24h milling. The composite shows a low capacity as shown in Fig 5-43 even though the conditions used are identical to those used to generate the data shown in Fig. 5-25. This as mentioned above is due to the use of a new milling machine whose milling energies were considerably higher. The overall capacity of the Si/SiC nanocomposite increases with an increase in the amount of NaI, suggesting that a higher fraction of Si reacts with Li by adding the particle size reducer. However, the nanocomposite containing 10 wt% NaI shows fade in capacity probably because the presence of NaI at the interface prevents the formation of the composite due to a higher concentration of the particle size reducer used during mechanical milling. Nevertheless, the nanocomposite containing 5 wt% NaI does indeed have a higher capacity and exhibits better stability than the one without the particle size reducer. Although the reason for the stability of the nanocomposite containing 5 wt% NaI is not clear at this point, it can be hypothesized that fine porous channels created by the particle size reducer and the surrounding nanocrystalline matrix could result in better capacity retention.

The differential capacity of the nanocomposite samples prepared from Si:C=3:2 after milling for 24 h containing 0 wt%, 5 wt.% and 10 wt.% of NaI as particle size reducer are shown in Fig. 5-44 (a), (b) and (c), respectively. The differential capacity plot of the nanocomposite containing 0 wt% NaI obtained from Si:C=3:2 after milling for 24 h exhibits broad peaks at 0.3V and 0.45V (see Fig. 5-44 (a)), corresponding to the reaction between amorphous Si and Li as mentioned earlier. The plot obtained from the electrode using 5 wt% particle size reducer (Fig. 5-44 (b)) exhibits a different profile compared to other differential capacity plots obtained from the Si/SiC nanocomposites shown in Fig 5-44. The absence of any significant peaks in the plot suggest that the capacity is probably attributed to a surface reaction resulting in a non-faradic double layer capacitance rather than due to an electrochemical reaction of Li with Si. Although the particle size reducer appears to induce the formation of nanocomposites with high surface area, the exact role of a particle size reducer needs to be investigated and further study is clearly warranted. While there is no distinct peak in Fig 5-44 (b) two broad peaks corresponding to the charge and discharge cycles of the

electrode fabricated from the nanocomposite containing 10 wt.% NaI are clearly observed, which can be attributed to the reaction of amorphous Si with Li (see Fig. 5-44 (c)).

Based on the results, it can be also concluded that the decrease in capacity after extended mechanical milling is caused by embedding of the active element in the nanocomposite anodes. Furthermore, the addition of particle size reducer does help to increase the capacity by exposing the embedded active component. It should therefore be noted that the addition of particle size reducers to the nanocomposite before HEMM process can also contribute to the optimization of the capacity in all the systems studied here.

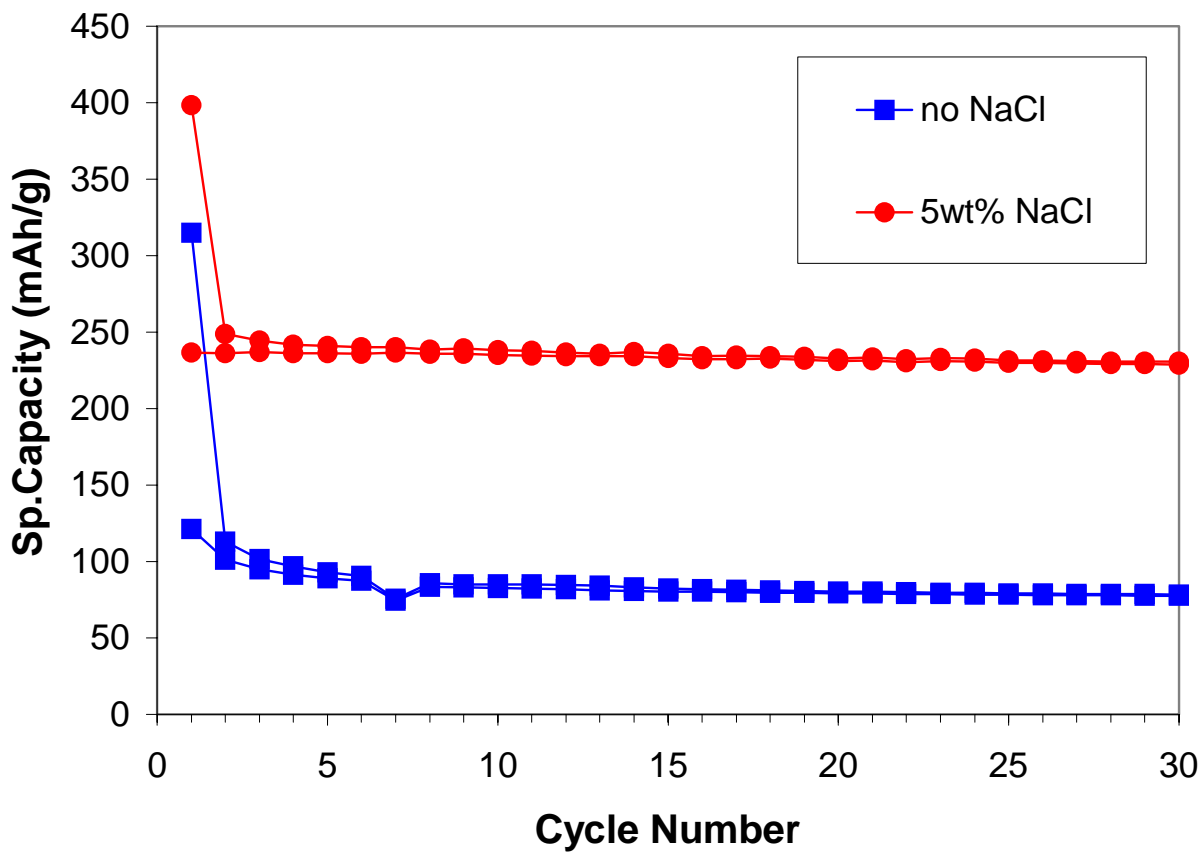


Fig. 5-41 Capacity as a function of cycle number for Si/TiN nanocomposites obtained after milling for 12 h using Si:TiN=1:2 mixture. (Current rate:  $100\mu\text{A}/\text{cm}^2$ , Potential: 0.02~1.2 V)

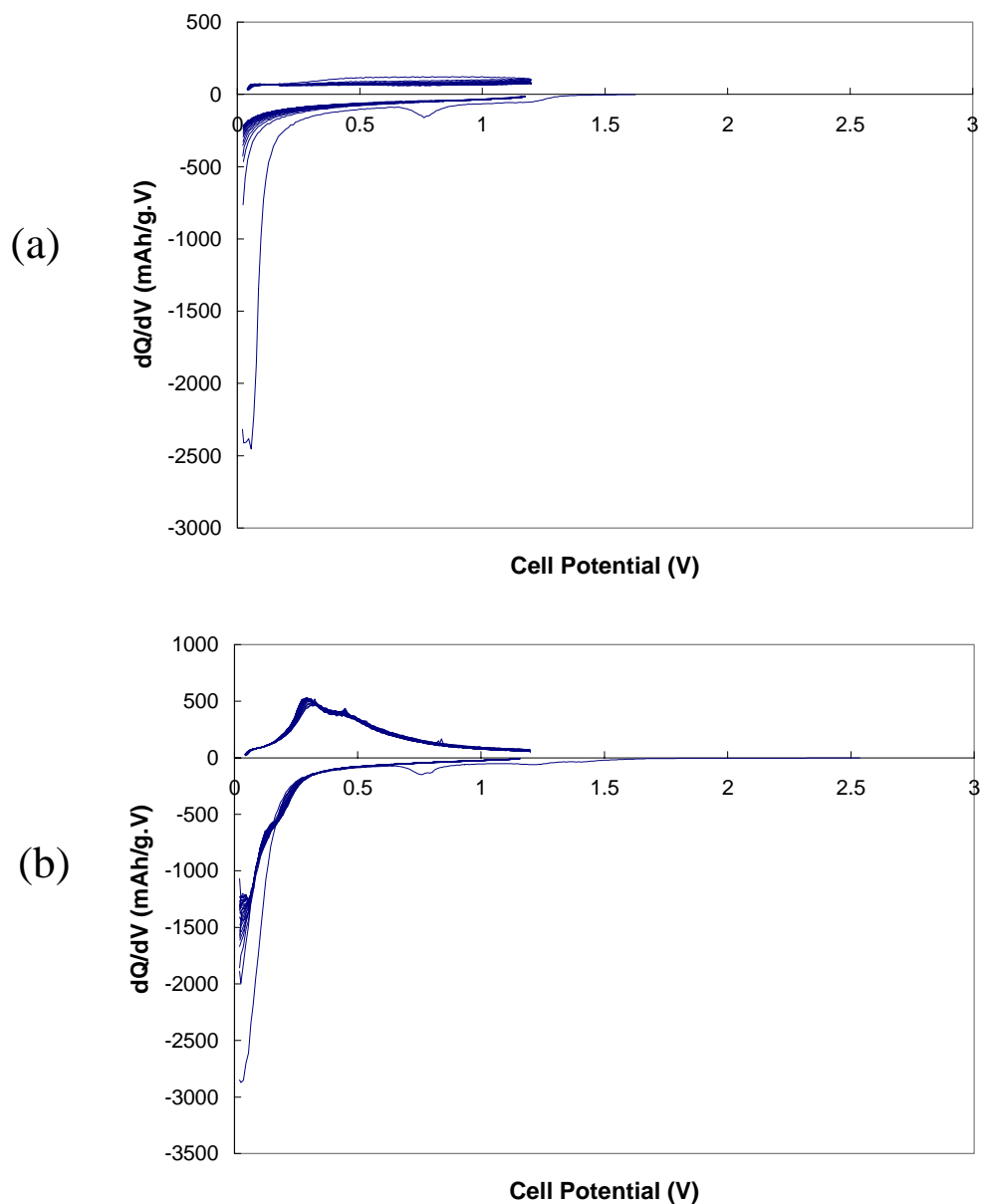


Fig 5-42 The differential capacity plots of the nanocomposites prepared from Si:TiN=1:2 obtained after milling for 12 h using a particle size reducer corresponding to (a) 0 wt.% NaCl and (b) 5 wt.% NaCl. (Current rate:  $100\mu\text{A}/\text{cm}^2$ , Potential: 0.02~1.2 V)

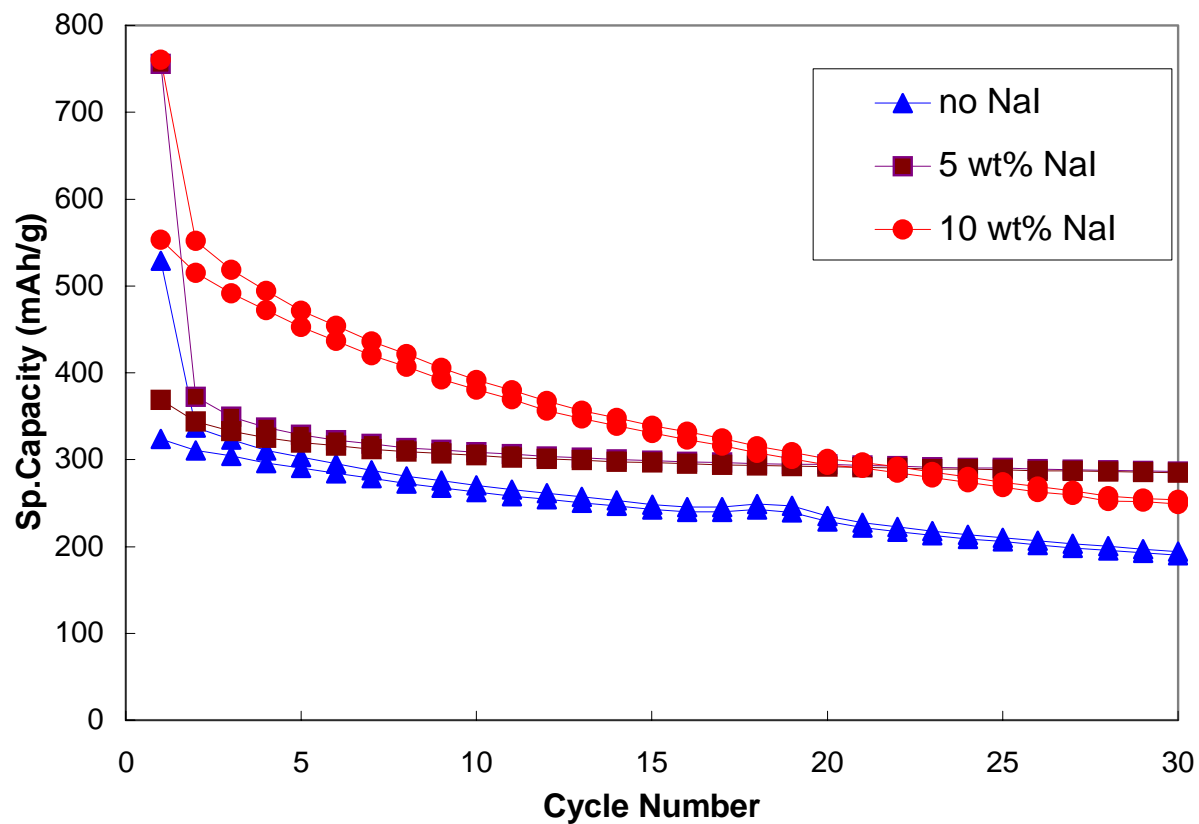
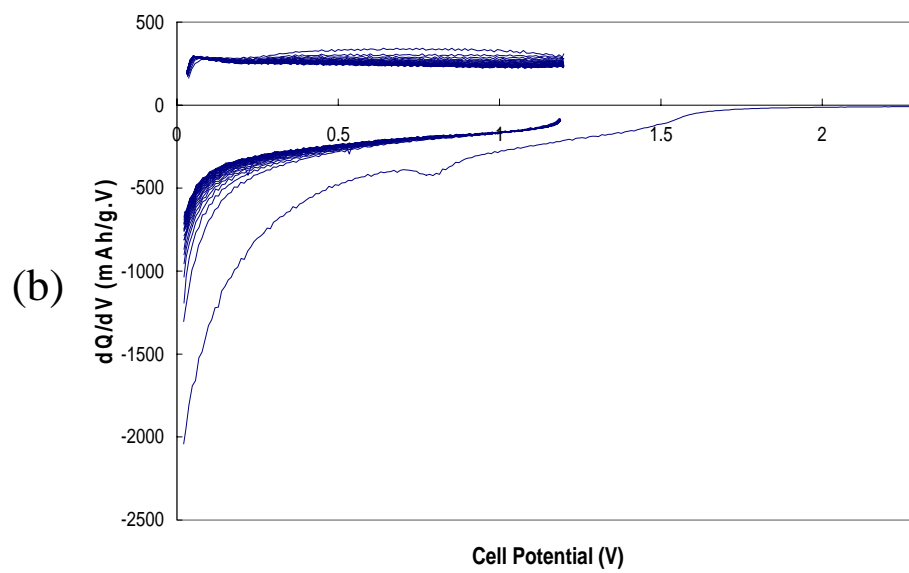
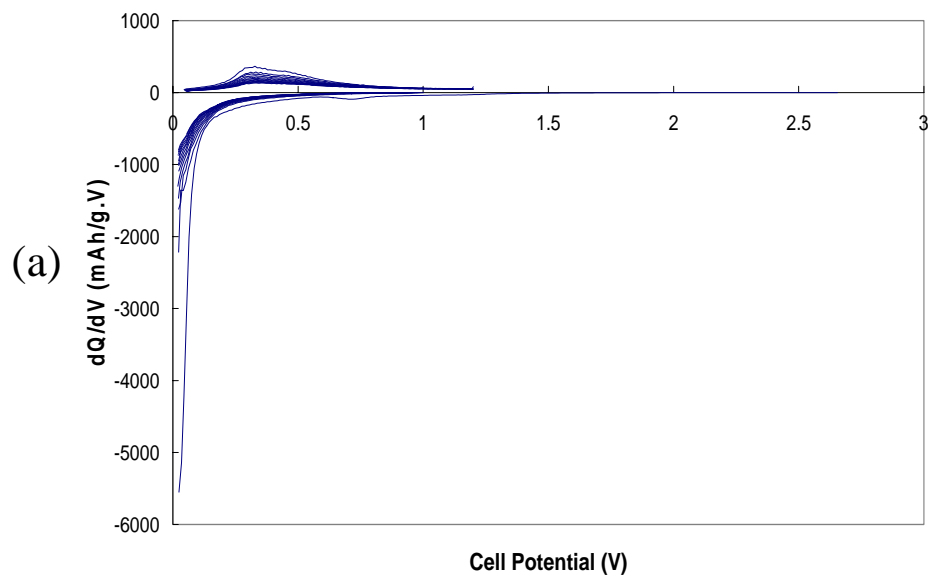


Fig. 5-43 Capacity as a function of cycle number for Si/SiC nanocomposites obtained after milling 24 h using Si:C=3:2 mixture. (Current rate:  $100\mu\text{A}/\text{cm}^2$ , Potential: 0.02~1.2 V)



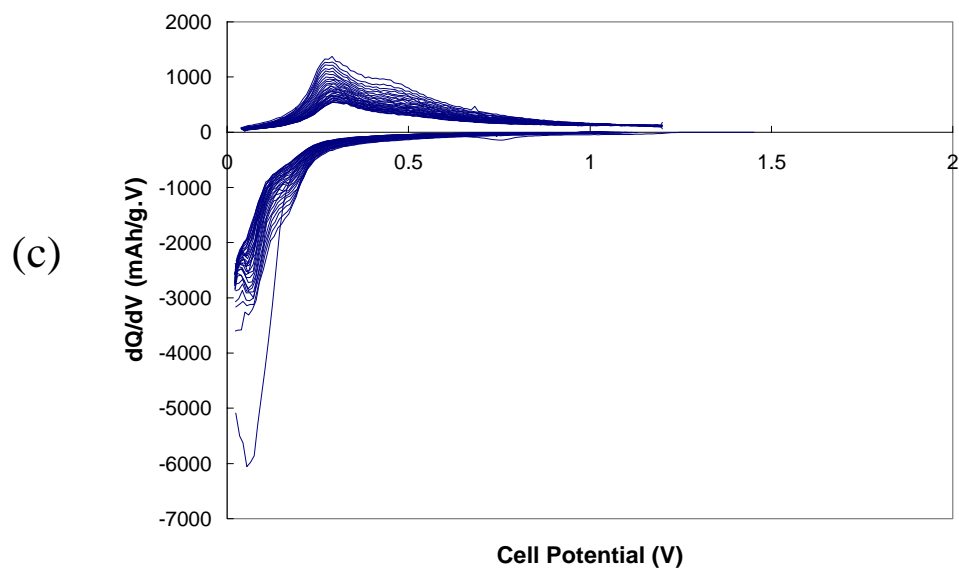


Fig 5-44 The differential capacity plots of the nanocomposites prepared from Si:C=3:2 obtained after milling for 24 h using a particle size reducer of (a) 0 wt% NaI, (b) 5 wt% NaI and (b) 10 wt% NaI. (Current rate:  $100\mu\text{A}/\text{cm}^2$ , Potential: 0.02~1.2 V)



## **Part II. Sn-based nanocomposite electrodes obtained by Chemical Synthesis**

### **5. 5 Tin/Non-oxide Nanocomposites**

As discussed before, Sn is also well known for its electrochemical reaction with Li and therefore has been used as an active component in the preparation of ‘active-inactive’ nanocomposite anodes [37-43]. However, a limitation of Sn-based nanocomposites is that they cannot be generated by high-energy mechanical milling (HEMM) due to the ductile and malleable nature of Sn. Sn typically lumps up to form a ball and sticks to the walls of the container during mechanical milling. Furthermore, the low melting point of Sn (231°C) also facilitate this process since local heating during mechanical milling causes the temperature to easily exceed the melting point of Sn. On the other hand, Sn can be easily reduced chemically using common reducing agents such as alkali metals (Li and Na), alkaline-earth, hydrazine, sodium borohydride (NaBH<sub>4</sub>) and even late transition metals such as Zn [44, 45]. Therefore, a chemical route has been chosen for synthesizing the nanocomposites containing Sn. Transition metal non-oxide and carbon have been selected as the inactive components for generating the Sn-based nanocomposites. Both matrices are good candidates since they are electrochemically inactive and can be effective if they can be synthesized at low enough temperatures to prevent coarsening and aggregation of Sn.

#### **5. 5. 1 Sn/TiN Nanocomposites**

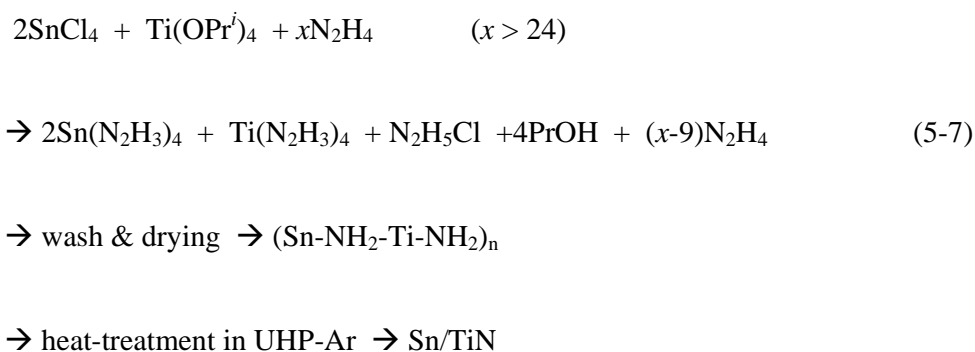
It was shown that TiN is a good candidate matrix in the case of Si/TiN nanocomposite anodes obtained by HEMM. However Sn is not suitable for HEMM and the process cannot be utilized for the synthesis of Sn/TiN nanocomposites. Hence chemical routes have been selected as alternative approaches for generating the Sn/TiN nanocomposite anodes.

The sol-gel method is known for its ability useful to generate oxide ceramics

and our research group has shown that this technique can be easily used to synthesize non-oxide materials such as transition metal sulfides (thio sol-gel) and nitrides (hydrazide sol-gel). The nitrides prepared by this process show very high specific surface area ( $\sim 250\text{m}^2/\text{g}$ ) and exhibit very fine particle sizes less than 50nm (see appendix A). Therefore the hydrazide sol-gel method enables the generation of nanocrystalline Sn/TiN composites. Tin tetrachloride and titanium isopropoxide have been reacted with anhydrous hydrazine in the presence of anhydrous acetonitrile. Since the as-prepared precursor is likely to be metal complexes, further heat-treatment is necessary to generate nitrides. Sn tetrachloride is likely to form elemental Sn instead of tin nitride because tin nitride is unstable and easily decomposes into tin metal [46, 47]. One of the objectives of the study is to synthesize Sn/TiN nanocomposites by the hydrazide sol-gel (HSG) method and analyze their applicability as anode materials.

### 1. Formation of Sn/TiN nanocomposites

The following reaction is proposed to provide the basic mechanism for the co-precipitation reaction leading to the generation of Sn/TiN nanocomposite corresponding to Sn:TiN = 2:1 by the HSG process.



As discussed earlier, the metathetic reduction of tin halides is used for the synthesis of Sn while the hydrazide sol-gel process is employed for generating TiN. The hydrazide precursor was obtained by reacting both tin (IV) chloride and titanium

isopropoxide, which were dissolved in anhydrous acetonitrile, with excess amount of anhydrous hydrazine. On adding hydrazine to the solution of  $\text{SnCl}_4$  and  $\text{Ti}(\text{OPr}^i)_4$  in acetonitrile, the solution gradually turns white and then purple, indicating the formation of the complexed titanium hydrazide precursor. After stirring for 15h at room temperature, the remnant liquid is evaporated in vacuum at  $100^\circ\text{C}$  and the as-prepared precursor is collected. The amount of Sn and TiN was varied to form composites with Sn:TiN = 1:1, 1:2 and 2:1. Fig. 5-45 shows the capacity vs. cycle number plots of Sn/TiN nanocomposites corresponding to Sn:TiN=1:2 and 1:1, respectively. The electrochemical capacities in both cases are very low, indicating that the amount of tin in the composites is significantly lower than the nominal composition. However, the Sn:TiN = 2:1 composition showed the best electrochemical property, and is discussed below. Thus the discussions in the subsequent sections are therefore focused on this particular composition.

### 2. Phase Evolution of Sn/TiN Precursor

Fig. 5-46 shows the XRD patterns of the nanocomposites comprising Sn:TiN=2:1 obtained after heat treatment at  $800^\circ\text{C}$  and  $1000^\circ\text{C}$  in UHP-Ar for 5 h, respectively. The XRD analysis of the other compositions also exhibits similar patterns. XRD data collected on the nanocomposite heat-treated at  $800^\circ\text{C}$  exhibits broad peaks, which are caused by nanocrystalline TiN and Sn (Fig. 5-46 (a)). Sharp Sn peaks however are observed after heat-treatment at  $1000^\circ\text{C}$  as seen in Fig. 5-46 (b), suggesting that Sn particles have undergone significant growth. The crystallization temperature of Sn observed from XRD results is much higher than the melting temperature of Sn, also indicating that the growth of amorphous/nano particles Sn is suppressed by the presence of C, which may arise from the unreplaced alkoxy groups of titanium alkoxide.

### 3. Electrochemical Characteristics of the Sn/TiN nanocomposites

The capacity of Sn:TiN = 2:1 nanocomposites are shown in Fig. 5-47. All samples show stable capacity without any noticeable fade, indicating that the Sn particles are stable during the charge and discharge cycling without undergoing any

particle growth or cracking. The sample obtained after heat treatment at 800°C exhibits higher stable

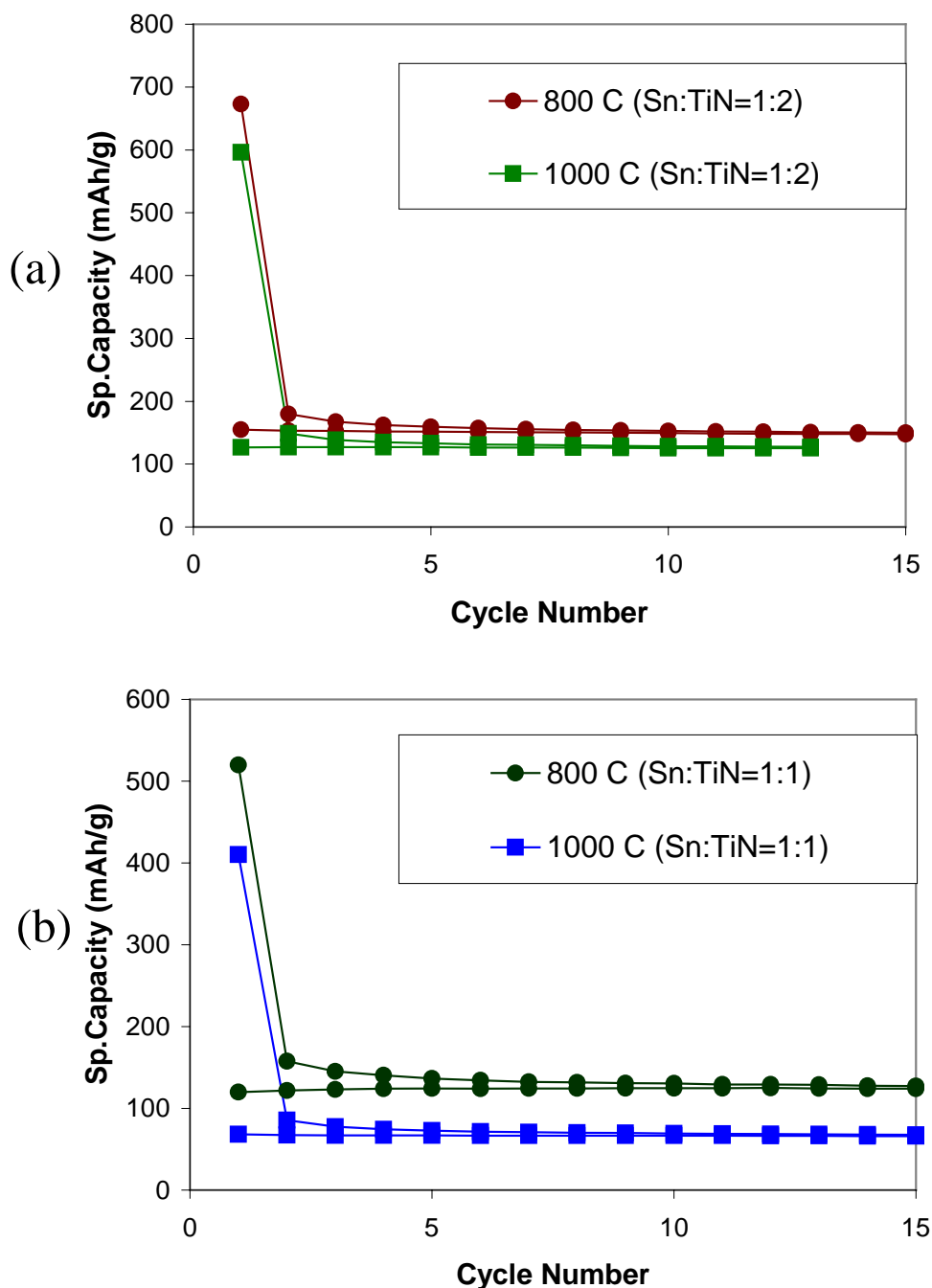


Fig. 5-45 Capacity as a function of cycle number for Sn/TiN nanocomposites corresponding to (a) SnTiN = 1:2 and (b) Sn:TiN = 1:1 obtained after heat treatment for 5 h in UHP-Ar at 800 and 1000°C, respectively. (Current rate : 100 $\mu$ A/ cm<sup>2</sup>, Potential : 0.02~1.2 V)

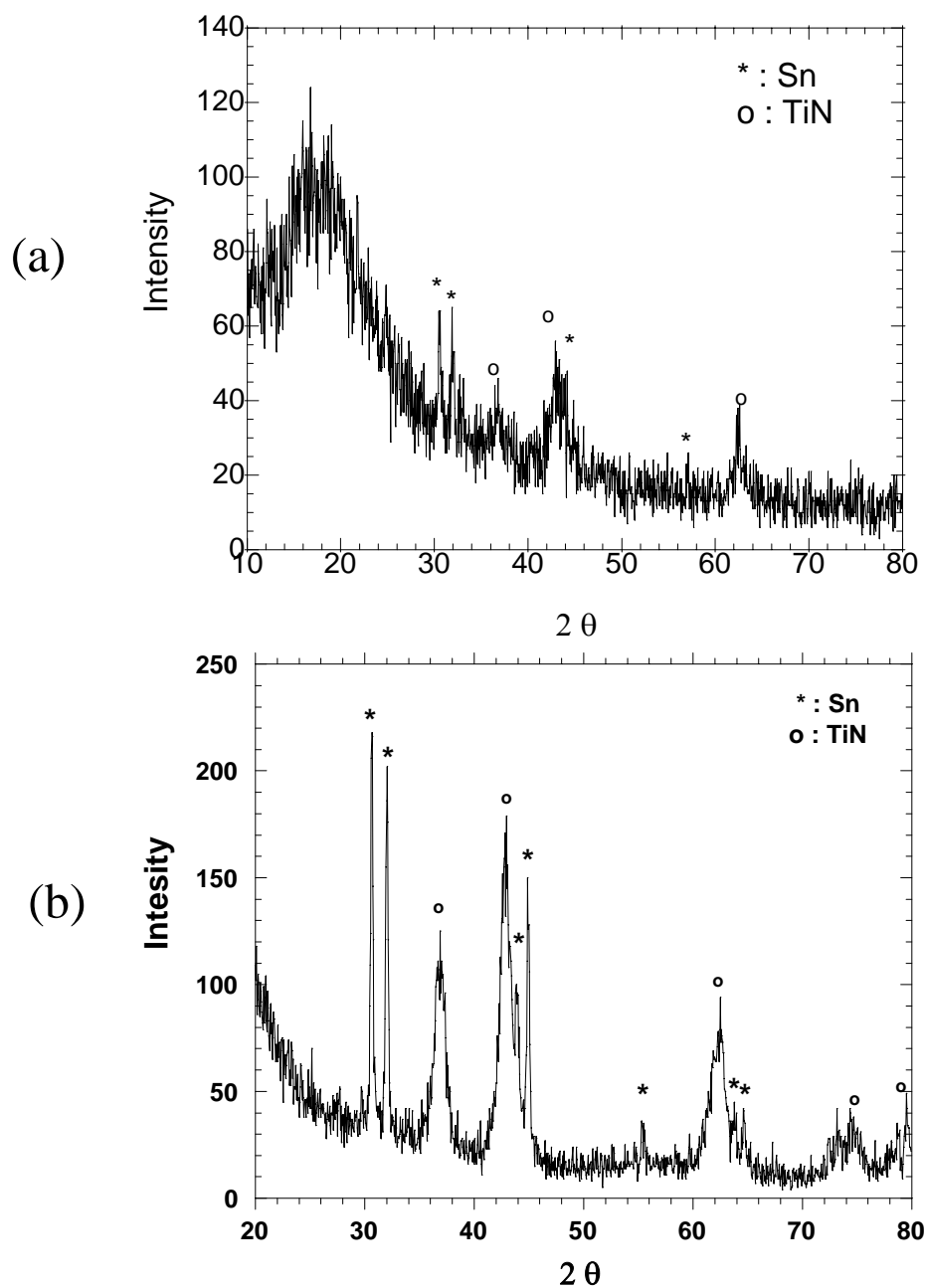


Fig. 5-46 X-ray diffraction patterns of Sn/TiN nanocomposites corresponding to Sn:TiN = 2:1 obtained after heat treatment for 5 h in UHP-Ar at (a) 800 and (b) 1000 °C, respectively.

capacity of ~290 mAh/g than the composite heat-treated at 1000°C, which exhibits a stable capacity of ~ 250mAh/g due to the possible loss of Sn during heat-treatment at the higher temperature of 1000 °C. However the nanocomposite electrode obtained after heat-treatment at 1000°C exhibits a lower irreversible loss of ~49% in capacity, suggesting that heat-treatment helps to remove by-products such as residual halides, hydrazine, hydro chloride and also probably helps to minimize the disordered carbon species arising from the unreplaced or adsorbed alkoxides. In addition, the reduction in surface area after heat-treatment at higher temperature may also be responsible for the decrease in the first irreversible loss. Surface area plays a very important role in passivating the surface due to adsorbed electrolyte layer as discussed later. It should be noted that the overall capacity is relatively low compared to that of the Sn/C nanocomposite described in the next section containing a molar ratio of Sn:C=1:2 even though the content of Sn is higher. The exact reasons are not clear yet however, the loss of Sn during heat-treatment is more significant in the case of Sn/TiN nanocomposites, which may be caused by the different binding characteristics of Sn and the inactive component.

Fig 5-48 shows the differential capacity vs. cell potential of the Sn:TiN =2:1 composition discussed above. Electrodes fabricated from powders obtained after heat treatment at 800°C exhibit very broad peaks (See Fig 5-48 (a)). The broad peaks occurring during charge and discharge correspond to the reaction between Li and the nano/amorphous Sn particles as discussed earlier. The differential capacity plot of the electrode derived from powders obtained after heat-treatment at 1000°C however exhibits sharp peaks (Fig 5-48 (b)). The sharp peaks during cycling are suggestive of the growth of Sn particles in the Sn/TiN nanocomposites and this result is consistent with the sharp Sn peaks seen in the XRD patterns validating the presence of coarse Sn crystallites.

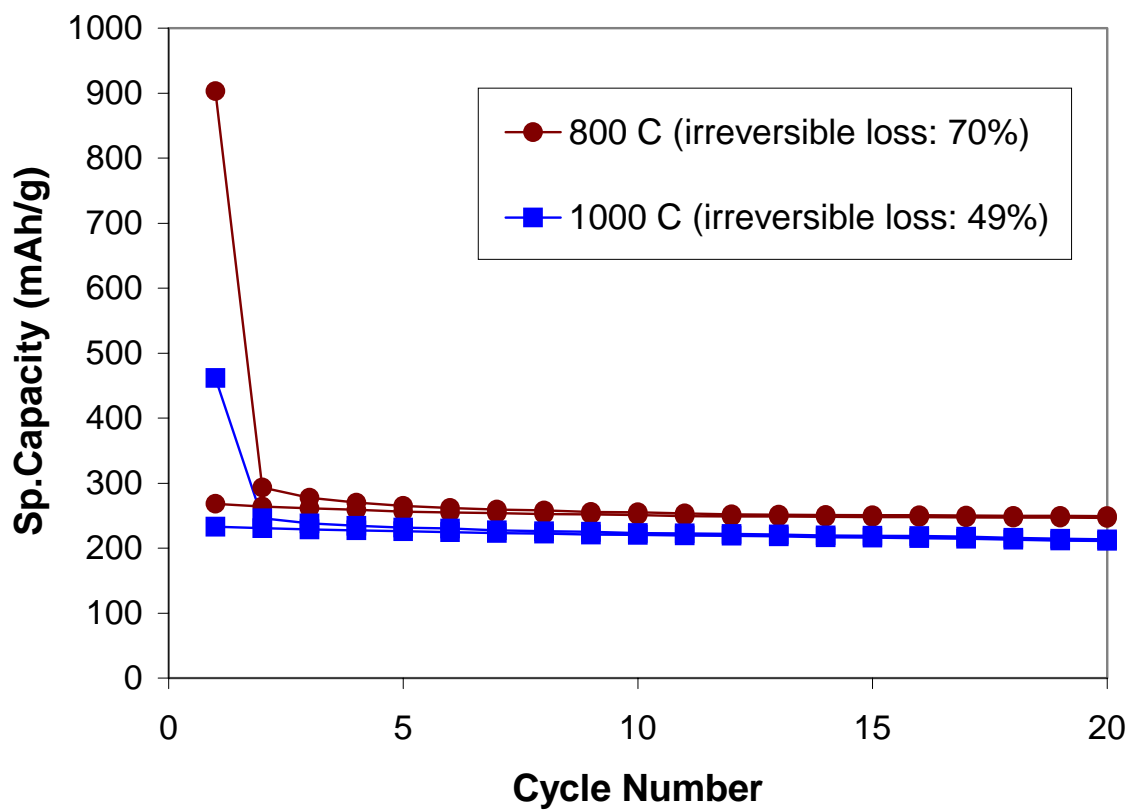
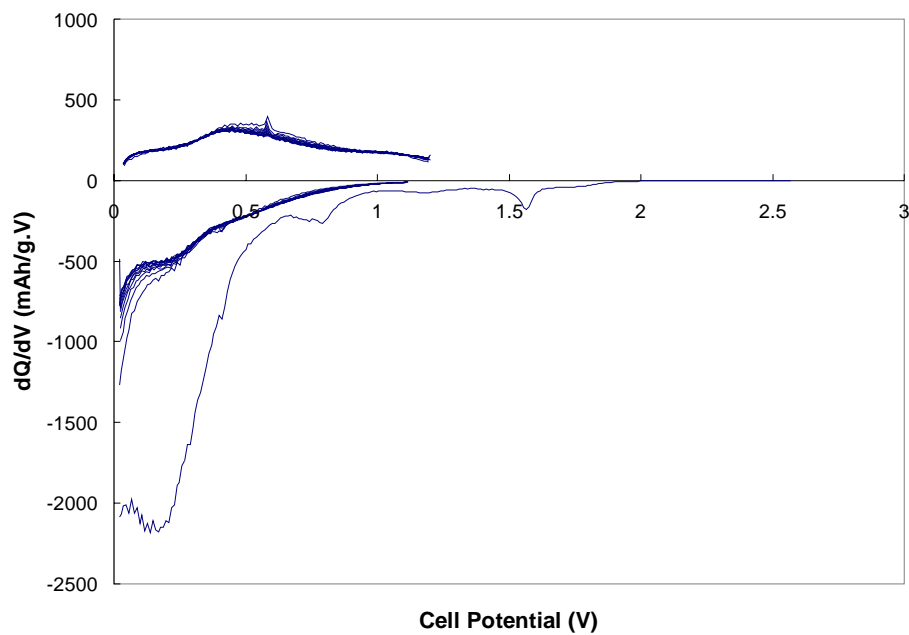
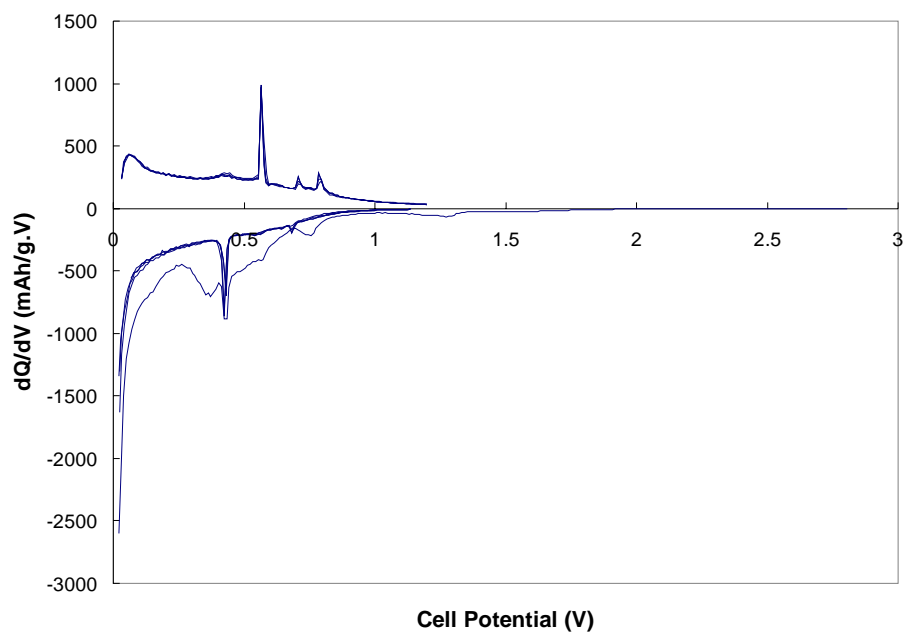


Fig. 5-47 Capacity as a function of cycle number for Sn/TiN nanocomposites obtained after heat treatment for 5 h in UHP-Ar at 800 and 1000°C, respectively. The first irreversible loss of each nanocomposite is shown in the box. (Current rate : 100 $\mu$ A/ cm<sup>2</sup>, Potential : 0.02~1.2 V)



(a)



(b)

Fig. 5-48 Differential capacity vs. cell potential curves of the Sn/TiN nanocomposites obtained after heat treatment for 5 h in UHP-Ar at (a) 800 and (c) 1000°C, respectively. (Current rate :  $100\mu\text{A}/\text{cm}^2$ , Potential : 0.02~1.2 V)



## **5. 5. 2 Sn/C Nanocomposites**

### **5. 5. 2. 1. Tin (IV) Chloride + Poly(methacrylonitrile)**

Based on the results of the Sn/TiN nanocomposite synthesized by the hydrazide sol-gel process described above, the Sn/TiN nanocomposite anodes show lower capacity (<290mAh/g) than the electrodes corresponding to the Si/TiN, Si/TiB<sub>2</sub> and Si/SiC systems prepared by HEMM because of the significant loss of Sn resulting from the high heat treatment temperatures. The detailed experimental results have been discussed in the preceding sections.

On the other hand, C can be easily generated by thermal decomposition of various polymers [48-50] since C is the main non-volatile component of polymers generated by pyrolysis. In this study, poly(methacrylonitrile) has been used for the synthesis of Sn/C nanocomposites since it is easily soluble in organic solvents that are typically used for the synthesis of Sn by chemical reduction.

#### 1. The formation of Sn/C nanocomposites

As discussed in chapter 2, the metathetic reduction of tin halides is used for the synthesis of Sn/C nanocomposites. Polymethacrylonitrile (PMAN,  $M_w = 20,000$  g/mol), which originally consists of white granules, dissolves completely in anhydrous acetonitrile, which is used as a solvent for this reaction. The solution becomes transparent since PMAN breaks down to monomers, dimers or  $n$ -mers upon dissolution. These  $n$ -mers stays inert throughout the chemical reactions and are pyrolyzed to form carbon after heat treatment. The hydrazide precursor of Sn was obtained by reacting tin (IV) chloride with excess anhydrous hydrazine in anhydrous acetonitrile in the presence of solubilized polymer. With the addition of hydrazine to the solution of SnCl<sub>4</sub> in acetonitrile, the halide forms an adduct with acetonitrile in a 1:1 molar ratio as reported in the literature [51]. The formation of the adduct however does not affect the

subsequent reactions [52]. The yellow solution gradually turns white, indicating the formation of the hydrazide complex. After stirring for 15h at room temperature, the remnant liquid is evaporated in vacuum at 100°C and the as-prepared precursor is collected. The overall reaction can be written as follows:

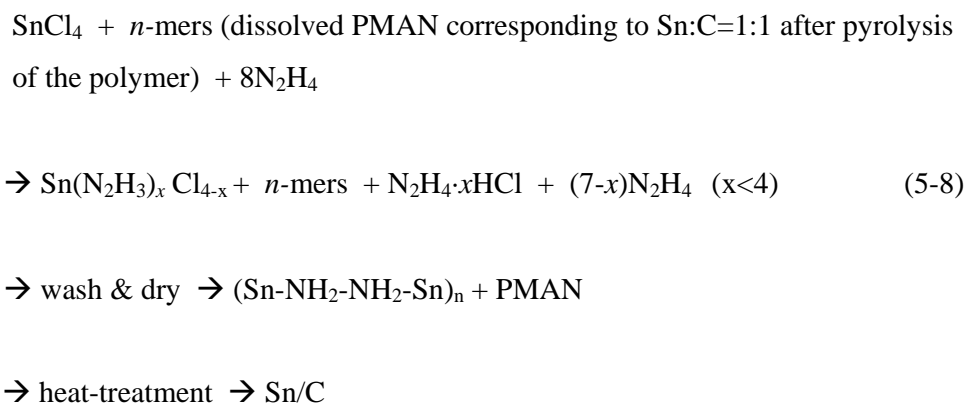


Fig. 5-49 shows a schematic representation of the processes involved in the formation of the Sn/C nanocomposites. The Sn precursors are obtained as a result of the chloride-hydrazide ( $\text{Cl} \leftrightarrow \text{N}_2\text{H}_3$ ) replacement reaction, while the polymers remain unchanged in the solubilized state. The *n*-mers condense to its polymeric state after removal of all the liquid and in combination with the as-prepared precursor forms the Sn/C composite eventually via controlled heat treatments.

## 2. Phase Evolution of the As-prepared Precursor

Thermogravimetric (TGA) and differential thermal analyses (DTA) are conducted on the as-prepared precursor of Sn/C nanocomposites as well as the polymethacrylonitrile (PMAN) polymer alone (See Fig. 5-50). The precursors were heated in UHP-Ar to 1000°C using a heating rate of 10°C/min. The TGA/DTA result of PMAN shows a typical decomposition behavior of polymers except that the yield of carbon residue after pyrolysis is very low (< 0.2 mg, ~2%). However, the yield of carbon appears to increase when the polymer undergoes pyrolysis to form a composite with the Sn-complex according to the TGA result of the as-prepared precursor of Sn/C nanocomposites (Fig. 5-50 (b)), which exhibits a gradual weight loss compared to the

result obtained from thermal decomposition of PMAN alone (Fig. 5-50 (a)). The large weight loss beginning around 250°C appears to be mainly caused by the decomposition of the polymethacrylonitrile (PMAN) and the removal of hydrazide groups in the as-prepared precursor. In addition, evaporation of the hydrazine hydrochloride ( $N_2H_4 \cdot xHCl$ ) species occurs around the temperature of 200°C. The continuous weight loss after 400°C is attributed to the removal of carbonaceous species. These carbonaceous species, which form the inactive component of the nanocomposite, play an important role in preventing the growth of Sn particles as will be discussed later. The first and the second endothermic peaks around 100°C and 240°C correspond to the melting of PMAN and the evaporation of hydrazine hydrochloride species, respectively [53, 54].

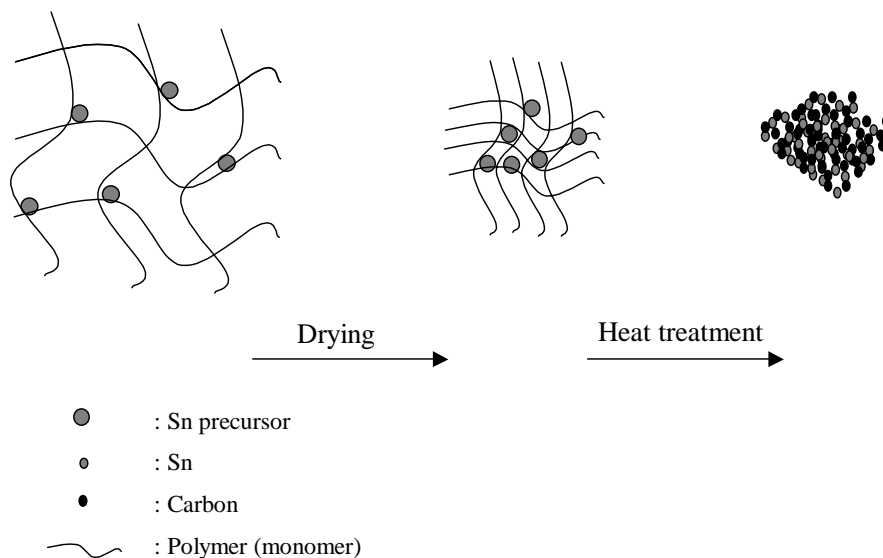


Fig. 5-49 A schematic representation of the processes involved in the formation of Sn/C nanocomposite using the chemical approach.

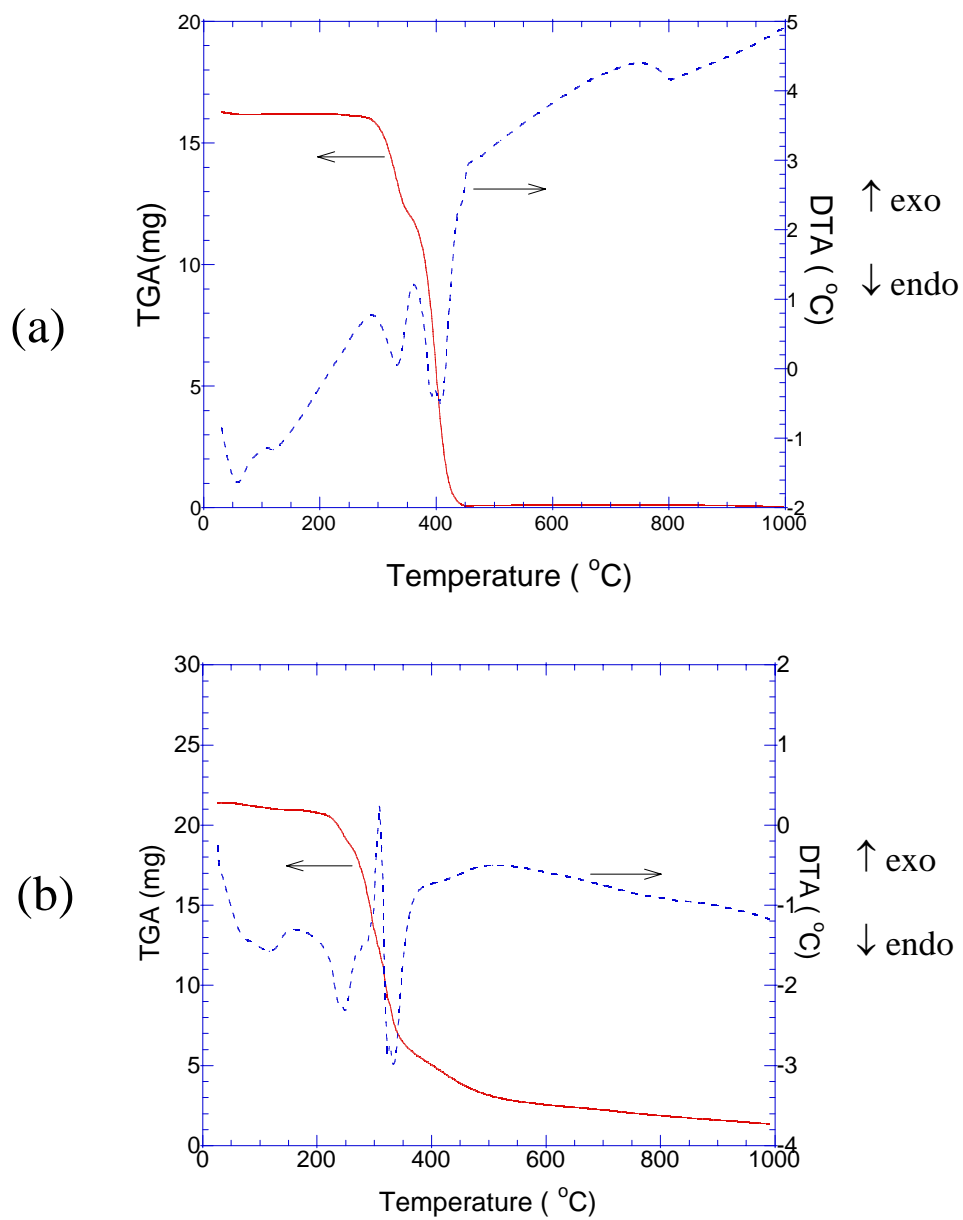


Fig. 5-50 The TGA/DTA analyses of the (a) polymethacrylonitrile and (b) as-prepared precursor showing the formation of C and Sn/C nanocomposites, respectively.

The endothermic reaction around 240°C appears to be caused by the removal of hydrazide groups from the Sn-containing precursor. The sharp endotherm at 320°C is attributed to the decomposition of PMAN. No further reaction was observed at temperature beyond 400°C. There is a gradual weight loss beyond 400°C, which appears to correspond to loss of either carbonaceous species or/and Sn.

It is very important to identify suitable heat treatment temperatures of the precursor since heat treatment at low temperatures may cause incomplete removal of the unwanted species such as hydrocarbon arising from the polymer. On the other hand, nano-particles of Sn will grow by thermal treatment at high temperatures. The heat-treatment temperature is therefore important for controlling the morphology and crystal structure of the Sn/C nanocomposites. Since the precursor does not undergo any reactions beyond 400°C, higher temperature could be appropriate for heat-treating the as-prepared precursor. As mentioned above, however, the slow weight loss beyond 400°C could be caused by loss of Sn, which may reduce the capacity of the Sn/C nanocomposites while also losing the nanoscale structure. Therefore, the heat-treatment temperature of the precursor is very important to achieve high capacity and stability.

Fig. 5-51 shows the XRD patterns of the nanocomposites obtained after heat treatment at 400, 600 and 800°C in UHP-Ar for 5 h, respectively. The nanocomposites heat-treated at 400 and 600°C do not show any XRD peaks, suggesting the amorphous nature of Sn and C. However, Sn begins to crystallize after heat-treatment at 800°C as shown in the XRD results (Fig. 5-51 (c)). The crystallization temperature of Sn is much higher than the melting temperature of Sn (231°C) and it indicates that the growth of amorphous/nano particles Sn is suppressed by the presence of C as mentioned above. The exact role of carbon in preventing growth of Sn will be studied as part of the future work.

### 3. Electrochemical Characteristics of the Sn/C nanocomposites

The Sn/C nanocomposites corresponding to Sn:C=1:1 were tested for their electrochemical responses using a current rate of 100  $\mu\text{A}/\text{cm}^2$  ( $\cong$  C-rate of C/18) and the capacity vs. cycle numbers of Sn/C nanocomposites is exhibited in Fig. 5-52. All samples show relatively stable capacity (0.14 ~ 0.16 % loss/cycle), indicating that the

Sn particles are homogeneously dispersed and remain stable during the charge and discharge cycles. The sample obtained after heat treatment at 600°C exhibits higher capacity than the composite heat-treated at 400°C since the latter contains higher fraction of inactive species including carbon and others species such as hydrocarbons, which arises from the incomplete decomposition of the polymer. The electrode fabricated from the powder after heat treatment at 800°C however shows a slightly lower capacity ( $\cong 528\text{mAh/g}$ ) than the sample that is heat-treated at 600°C ( $\cong 568\text{mAh/g}$ ). This is probably due to Sn lost by evaporation because of high temperature heat treatment as indicated by TGA/DTA results.

There is however a large irreversible capacity loss ( $\cong 48.8\% \sim 60.4\%$ ) in the Sn/C electrodes prepared by this chemical approach, which decreases slightly with increase in heat-treatment temperature. Although the reason for the large irreversible loss is not clear yet, it is likely that the disordered carbon with high specific surface area resulting from pyrolysis is the main cause of the irreversible loss due to its irreversible reaction with lithium [55]. Besides, electrodes processing high surface area also cause the excessive formation of passivation layer during the first discharge process. Results of BET surface area measurement conducted on the Sn/C nanocomposites obtained after heat treatment at 400°C, 600°C and 800°C in UHP-Ar for 5 h shows that the samples have a specific surface area of  $62.55\text{ m}^2/\text{g}$ ,  $60.49\text{ m}^2/\text{g}$  and  $44.56\text{ m}^2/\text{g}$ , respectively. This result is indicative of the fact that the decrease in specific surface area is closely related to the reduction in the first irreversible loss. Therefore, the decrease in the first irreversible loss with increase in heat treatment temperature can be explained by the growth of the particles size in the nanocomposite and the subsequent decrease in the passivation layer.

Fig 5-53 shows the differential capacity vs. cell potential of the three electrodes discussed above. Electrodes obtained after heat treatment at 400 and 600°C exhibit similar peaks (See Fig 5-53 (a) and (b)). The broad peaks occurring during charge and discharge correspond to the reaction between Li and the nano/amorphous Sn particles as discussed in the nanocomposites obtained by HEMM. The broad peaks in the range of 0.7~1.2 V during the first discharge appear to be caused by the reaction of Li with hydrocarbon species and/or disordered carbon. The differential capacity plot of the

electrode obtained from heat-treatment at 800°C however does not show this type of broad peaks (Fig 5-53 (c)). Furthermore, the area under the curve in the differential capacity vs. voltage plot spanning 0.7~1.2 V range is also lower compared to the 400°C and 600°C heat-treated electrodes suggesting the slight reduction in the irreversible loss consistent with the result shown in Fig. 5-52. The sharp peaks during cycling suggest the growth of Sn particles in the Sn/C nanocomposites, which is consistent with the XRD data.

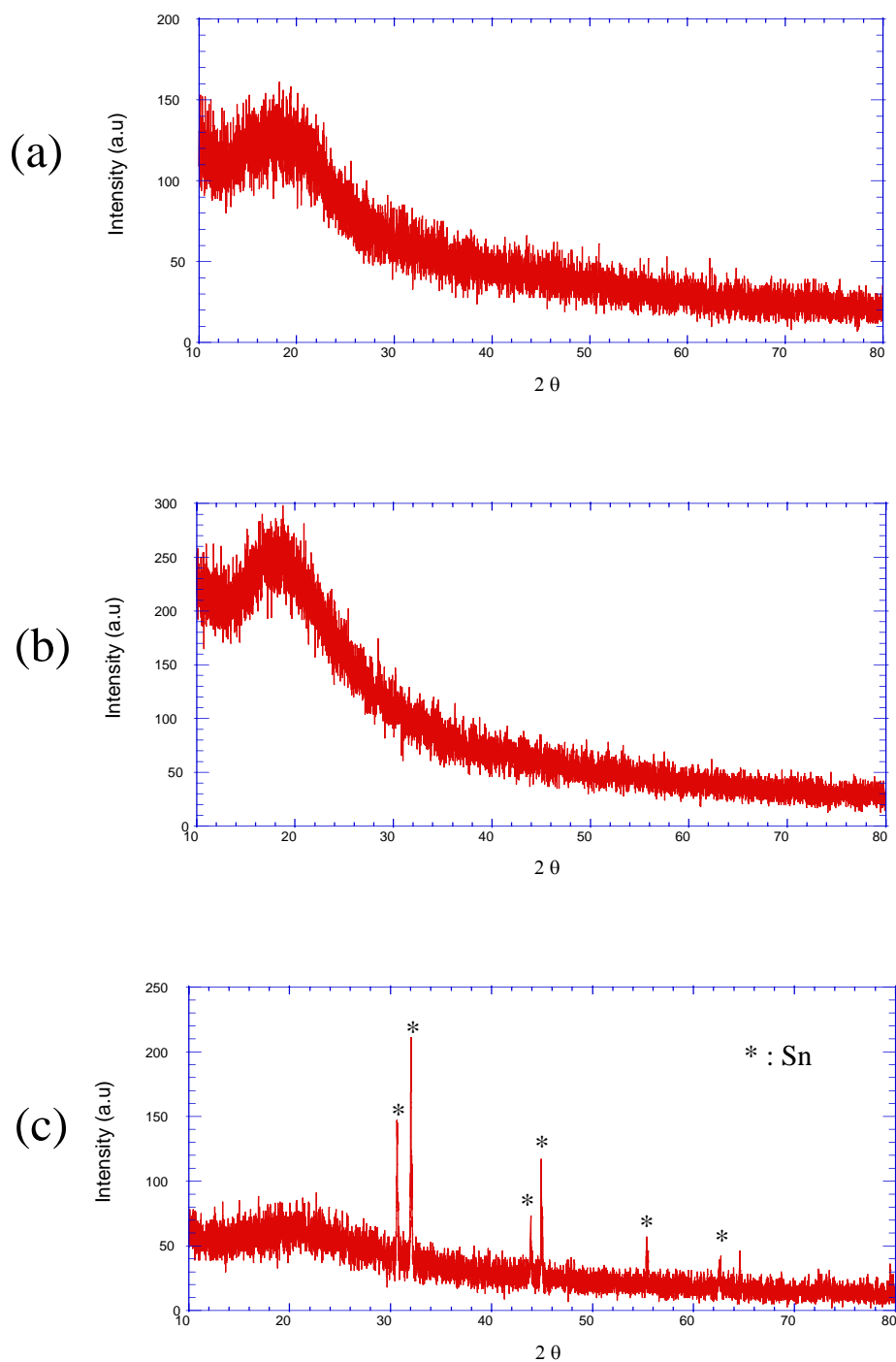


Fig. 5-51 X-ray diffraction patterns of Sn/C nanocomposites obtained after heat treatment for 5 h each in UHP-Ar at (a) 400, (b) 600 and (c) 800°C, respectively.



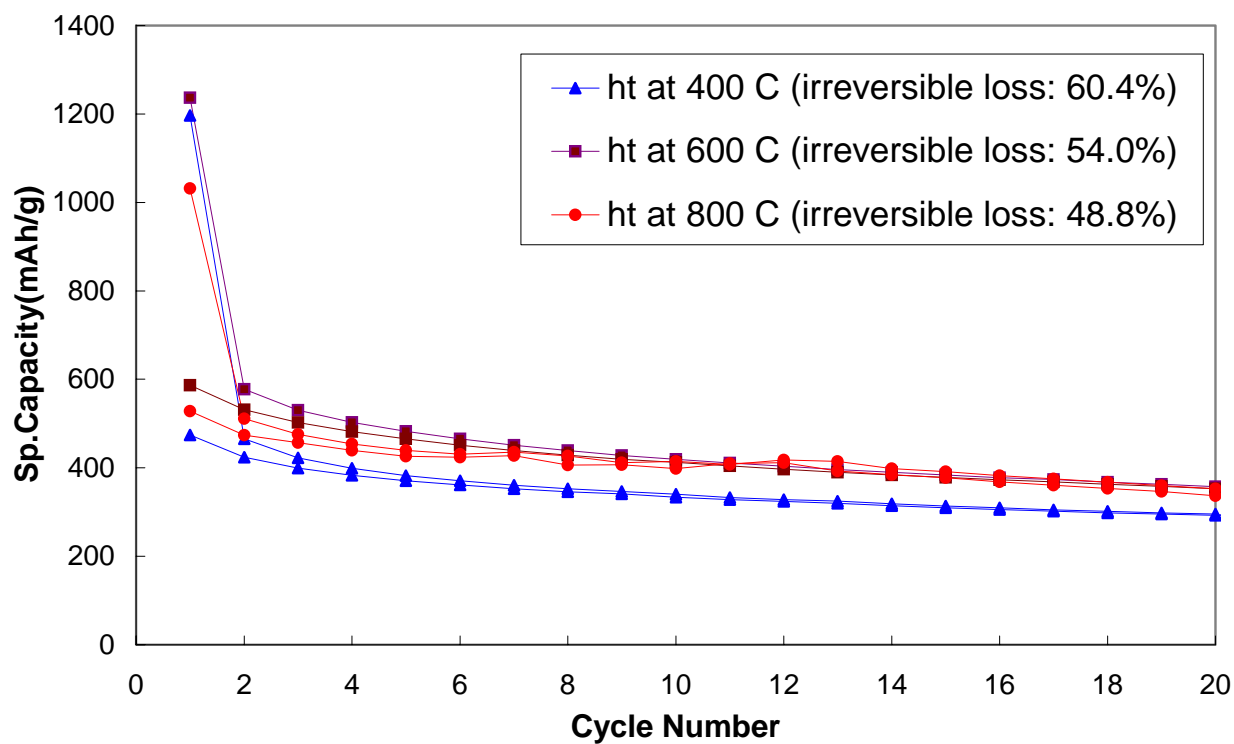
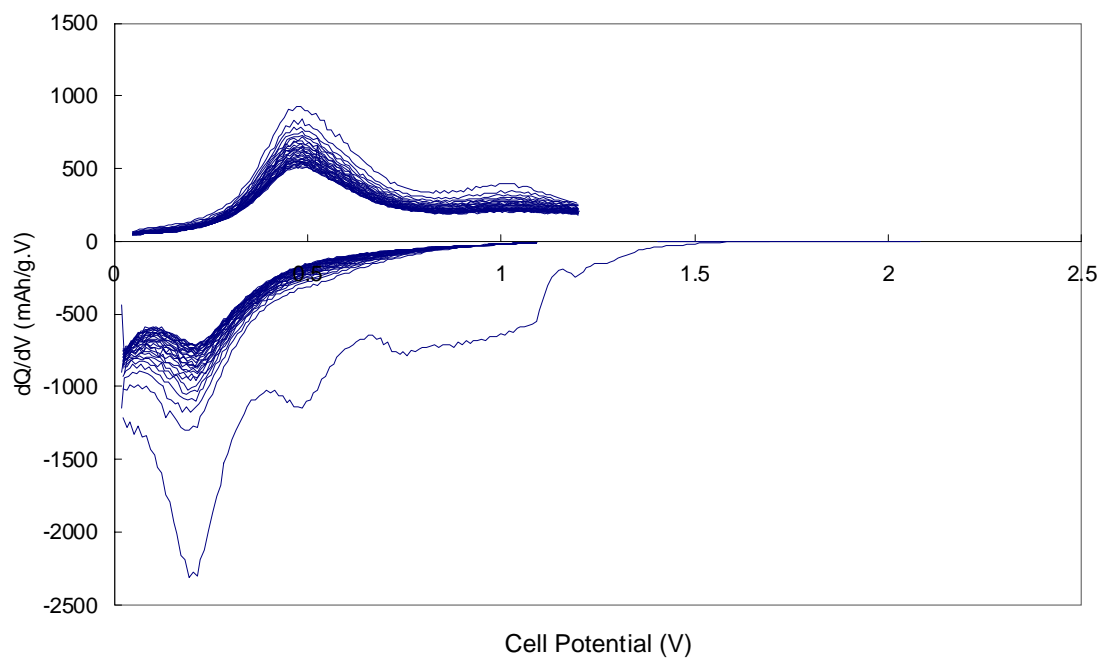
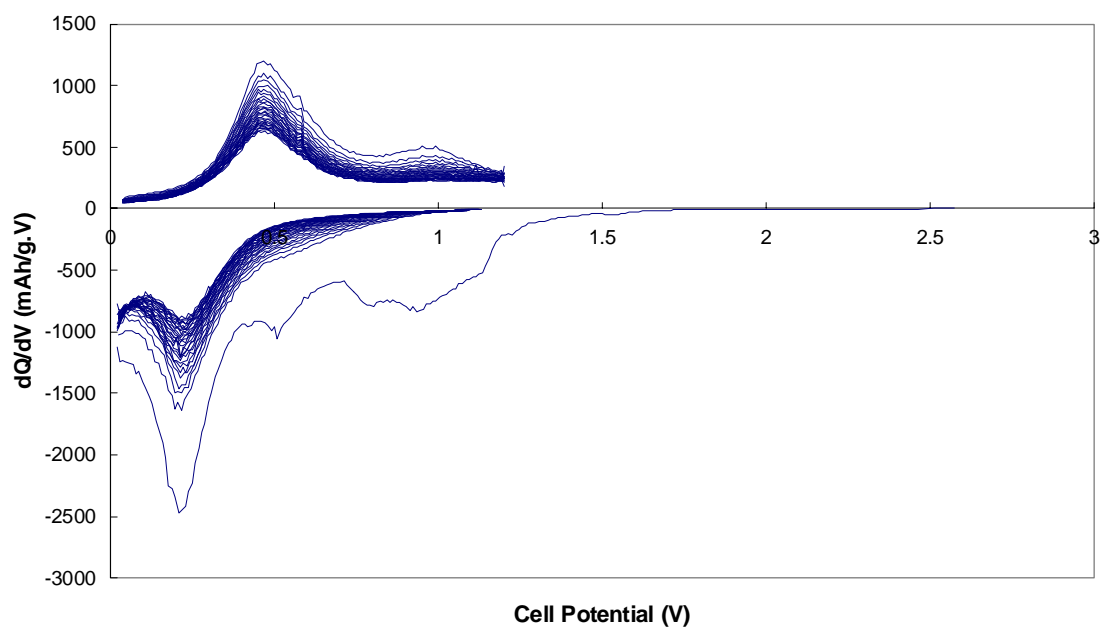


Fig. 5-52 Capacity as a function of cycle number for Sn/C nanocomposites obtained after heat treatment for 5 h each in UHP-Ar at 400, 600 and 800°C, respectively. The first irreversible loss of each nanocomposite electrode is shown in the box. (Current rate : 100 $\mu$ A/ cm<sup>2</sup>, Potential : 0.02~1.2 V)



(a)



(b)

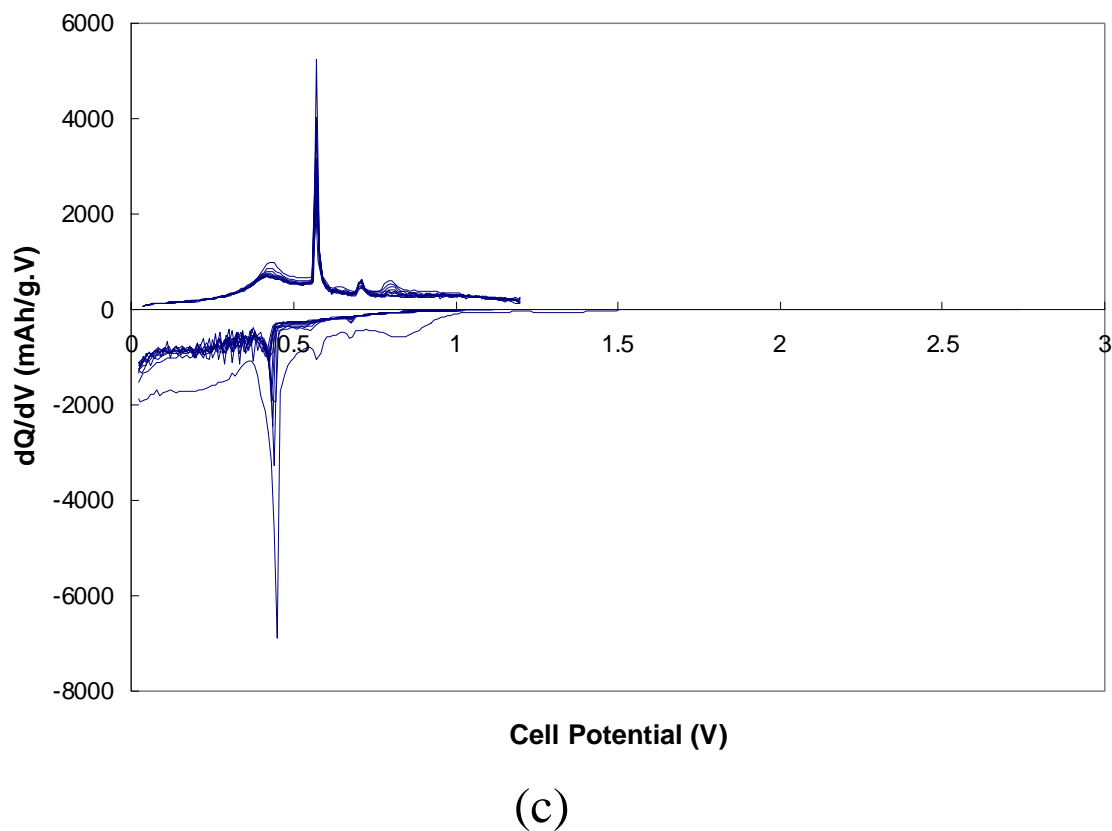


Fig. 5-53 Differential capacity vs. cell potential curves of the Sn/C nanocomposites obtained after heat treatment for 5 h each in UHP-Ar at (a) 400, (b) 600 and (c) 800°C, respectively. (Current rate :  $100\mu\text{A}/\text{cm}^2$ , Potential : 0.02~1.2 V)

### **5. 5. 2. 2. Sn/C Nanocomposites Derived from Alkyl tin + PS-resin**

#### 1. Materials Selection for Sn/C nanocomposites

Although the Sn/C nanocomposites obtained from tin chloride and PMAN exhibit high capacity and stability, there are major problems related to the first cycle irreversible loss. The cause of the first cycle irreversible loss as discussed in the previous sections could be related to the high surface area and the disordered structure of carbon obtained from PMAN. Besides, hydrocarbon and chlorine species in the nanocomposite can also react irreversibly with Li during the first discharge, although most of chlorine in the precursor would be removed during heat-treatment. Therefore, it is necessary to identify an alternative approach for generating Sn/C nanocomposites.

One of the approaches will be to identify porous cross-linked polymers that will decompose to yield carbon at a reasonable yield (>35%). In addition, the porous polymer should be able to accommodate tin precursors that will ultimately yield Sn/C nanocomposite after pyrolysis. Several researchers have studied the use of phenolic resins to generate carbonaceous materials for used as anode [56-58], and have claimed that the electrochemical properties such as irreversible loss can be controlled by appropriate heat-treatments. In this study, cross-linked polystyrene (PS)-based resin material has been used for the synthesis of carbon matrix component since cyclic carbon ring structure in the PS will form a structure similar to graphite upon pyrolysis and also the hydrogen content in the PS-resin is much less than PMAN, which could result in a lower irreversible capacity loss [59]. The schematic molecular structure of PS-resin is shown in Fig. 5-54. Besides, the yield of carbon after pyrolysis will be larger due to its cross-linked structure in comparison to PMAN. In order to study the decomposition of PS-resin, thermo gravimetric analysis has been conducted on the PS-resin (27.7 g) in UHP-Ar atmosphere using a heating rate of 10°C/min . The TGA plot is shown in Fig. 5-55. There is a large weight loss that initiates at ~450°C, which corresponds to the decomposition of PS-resin to form carbon. Furthermore, the yield of carbon is about 36% by weight. The heat-treatment temperature for the generation of C from PS-resin should be higher than the temperature of decomposition in order to ensure generation of

carbon. Hence a heat-treatment temperature higher than  $\sim 550^{\circ}\text{C}$  should be selected, where the decomposition of PS-resin is almost complete.

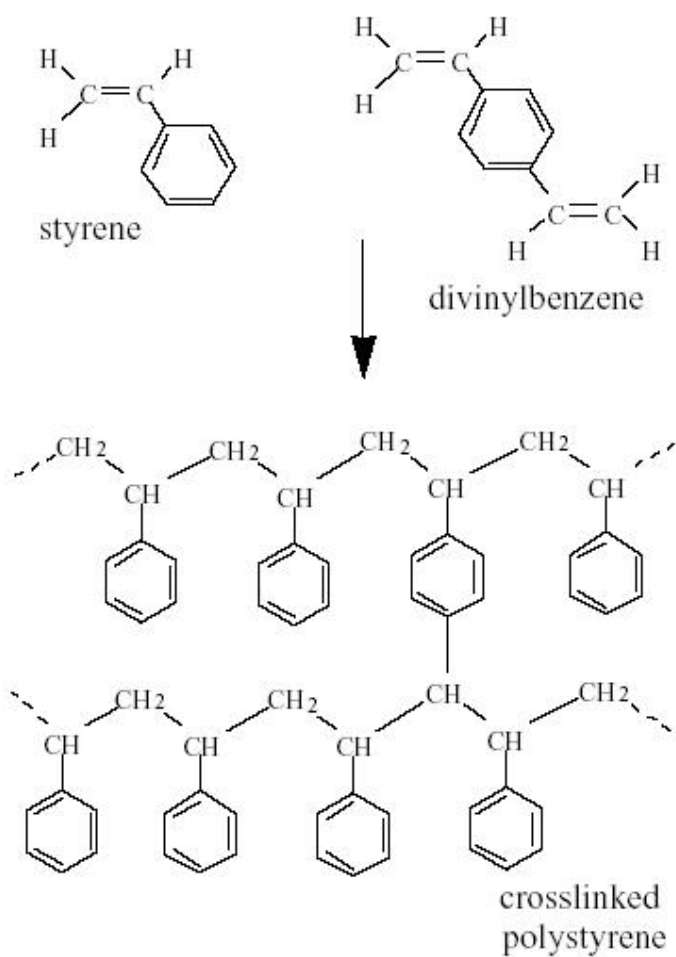


Fig. 5-54 Schematic structure of PS-resin cross-linked by divinylbenzene.

Since cross-linked PS-resin does not dissolve in common organic solvent but swells partially (~5%) in solvents such as water, methanol and acetone [60], it is necessary to infiltrate the pores of the PS-resin by the use of a tin source preferably in a liquid state. PS-resin is available in the form of beads (diameter: 0.3~1.2 mm) and the internal pores within allow a limited amount of liquid that can be infiltrated into the pores. This leads to loss of Sn that can be finally contained in the composite. In order to increase the amount of liquid that could be infiltrated into the PS-resin, fine sized PS-resin may be necessary, which could lead to an increase in the absorption of the liquid tin source on the surface due to the high surface area of the PS-resin powder. Our preliminary study on the infiltration of a solution of hydrous tin chloride ( $\text{SnCl}_4 \cdot 5\text{H}_2\text{O}$ ) dissolved in DI water into the PS-resin shows that the amount of tin in the resultant pyrolyzed polymer is larger when the tin solution is infiltrated into the powdered PS-resin, which is obtained after HEMM for 30 min, in comparison to infiltration of the liquid tin precursor directly into the PS-resin beads. The BET surface area measurements show that the as-received PS-resin beads from the commercial vender and the powder obtained after mechanical milling for 30 min have the specific surface area of  $853 \text{ m}^2/\text{g}$  and  $961 \text{ m}^2/\text{g}$ , respectively. These values indicate that the surface area of the PS-resin increases after mechanical milling. This extremely high surface area of the PS-resin powder appears to be suitable for infiltration. This can be realized from the capacity difference seen in Fig. 5-56. The nanocomposite synthesized initially (Fig. 5-56 (a)) is obtained by infiltration of the PS-beads with 5M water solution of  $\text{Sn}_2\text{Cl}_4 \cdot 5\text{H}_2\text{O}$  followed by pyrolysis in UHP-Ar for 5h at  $800^\circ\text{C}$ , while the second composite (Fig. 5-56 (c)) is obtained following the same experimental condition except that PS-resin powder after mechanical milling for 30 min is used.

The first charge capacity of the second nanocomposite is ~15% higher than that of the nanocomposite obtained from the PS-resin beads. This suggests that the amount of tin in the Sn/C nanocomposites after pyrolysis of the precursor derived by infiltration of the mechanically milled PS-resin is larger than that of the nanocomposite obtained by infiltration and pyrolysis of the beads. Differential capacity plots of both nanocomposites (Fig 5-56 (b) and (d)) show sharp peaks during charge (~ 0.6V, 0.72V

and 0.8V) and discharge ( $\sim 0.4V$ ,  $0.5V$  and  $0.65V$ ) cycles although the peak intensity collected on mechanically milled PS-resin infiltrated with  $Sn_2Cl_4 \cdot 5H_2O$  is higher, supporting the fact that the amount of tin in this nanocomposite is higher as mentioned above.

Fig. 5-57 shows the pore channels existing in PS-resin beads and PS-resin powder that is obtained after milling for 30min. The PS-beads may have pore channels existing within the beads in the internal 3-D structure. However there is only limited number of pore channels available for infiltration on the surface (see Fig 5-57 (a)). On the other hand, the PS-resin powder obtained after mechanical milling has more pore channels, which is attributed to exposure of pore channels within beads during milling and the formation of pore channels between the fine particles as shown in Fig. 5-57 (b). Therefore, it can be concluded that the PS-resin powder is more suitable for infiltration of liquid precursors since the pore channel density is higher in comparison to the PS-resin beads.

Alkyl tin compounds have been studied to generate fine Sn for Pt-Sn catalyst [61, 62] and have been used as a tin source for this research instead of tin chloride. Based on our preliminary study, all alkyl tin compounds can decompose into tin in the presence of carbon species. Hence several alkyl tin compounds have been selected to generate Sn/C nanocomposites. These includes tetramethyl tin  $((CH_3)_4Sn)$ , tetraethyl tin  $((C_2H_5)_4Sn)$  and tetra-n-octyl tin  $((C_8H_{17})_4Sn)$ . Two important aspects have been considered for the infiltration of alkyl tin into PS-resin. 1) The molar volume of alkyl tin compound is important, which dictates the amount of tin that will be obtained in the final pyrolyzed Sn/C composites. 2) The other aspect is the decomposition temperature since it decides the temperature of formation of tin during heat-treatment. If the decomposition temperature is low then the tin content in the composite may decrease during subsequent heating because of the evaporation of tin. However, the decomposition temperature and mechanisms involved in the pyrolysis of alkyl tin to yield metallic tin is not clearly understood. Nevertheless, the boiling point has been used to select the alkyl tin compound that will yield optimum amount of tin in the final pyrolyzed composite. Since all alkyl tin compounds are liquids, no external solvent was used for the infiltration experiments.

Fig. 5-58 exhibits the electrochemical response of the composites derived from

various alkyl tin sources with a nominal Sn/C composition of Sn:C=1:1. The nominal composition used for all these experiments has been determined using the theoretical Sn content in the alkyl tins and the yield of carbon from the PS-resin after pyrolysis, since the PS-resin does not have a fixed chemical formula or composition as discussed in the experimental section. All the precursors were prepared by infiltration of each alkyl tin compound into the PS-resin powder obtained after milling for 30 min. The Sn/C nanocomposites were generated after heat-treatment at 600°C in UHP-Ar for 5 h, where the PS-resin decomposes completely to form carbon. The insets show the differential capacity vs. cell potential plots of the Sn/C nanocomposites obtained from tetramethyl tin and tetra-n-octyl tin, respectively. The differential capacity plot corresponding to the Sn/C nanocomposite obtained from tetraethyl tin is discussed at the end of the following section. The sharp peaks during charge (~ 0.6V, 0.72V and 0.8V) and discharge (~ 0.4V, 0.5V and 0.65V) cycles suggest the reaction between Li and crystalline tin during electrochemical cycling.

The Sn/C nanocomposite derived from tetramethyl tin shows an initial discharge capacity higher than 300 mAh/g however the capacity decreases slowly after 7 cycles (see Fig. 5-58 (a)). Although tetramethyl tin is advantageous for the infiltration of tin due to its low molar volume (120.63ml/mol), the Sn/C nanocomposite does not show high capacity. This appears to be attributed to loss of tin during subsequent pyrolysis after the decomposition of tetramethyl tin at a temperature as low as 74°C. The reason for capacity fade is not clear however the particle growth may have caused the fade in capacity since tin particles form at early stage of pyrolysis due to its low decomposition temperature.

The Sn/C nanocomposite generated from tetraethyl tin on the other hand exhibits a stable capacity of ~480 mAh/g as shown in Fig. 5-58 (b). Based on the electrochemical analysis, tetraethyl tin exhibits the highest capacity due to its relatively low molar volume (235.48ml/mol) and high boiling temperature (181°C) compared to other alkyl tin precursors whose molar volume and boiling temperature are as follows: tetramethyl tin: 120.63ml/mol, 74°C; tetra-n-octyl tin: 389.54ml/mol, 224°C. The nanocomposite derived from tetra-n-octyl tin shows very low capacity (see Fig. 5-58 (c)), which appears to be caused by its high molar volume. Since there is limited volume of pores available in the PS-resin powder as mentioned before, the amount of tin



obtained from the infiltration of tetra-n-octyl tin might be negligible. Therefore it can be concluded that the alkyl tin compounds such as tetra-n-octyl tin with high molar volume is not useful for generating Sn/C nanocomposite despite its high decomposition temperature. Therefore, alkyl tin compounds such as tetraethyl tin, which have a small molar volume and high decomposition temperature appear to be more appropriate for the purpose of infiltration of tin into the PS-resin powder. In the following sections, the Sn/C nanocomposite obtained from tetraethyl tin and PS-resin powder has been studied further for its phase evolution behavior, microstructure and electrochemical response.

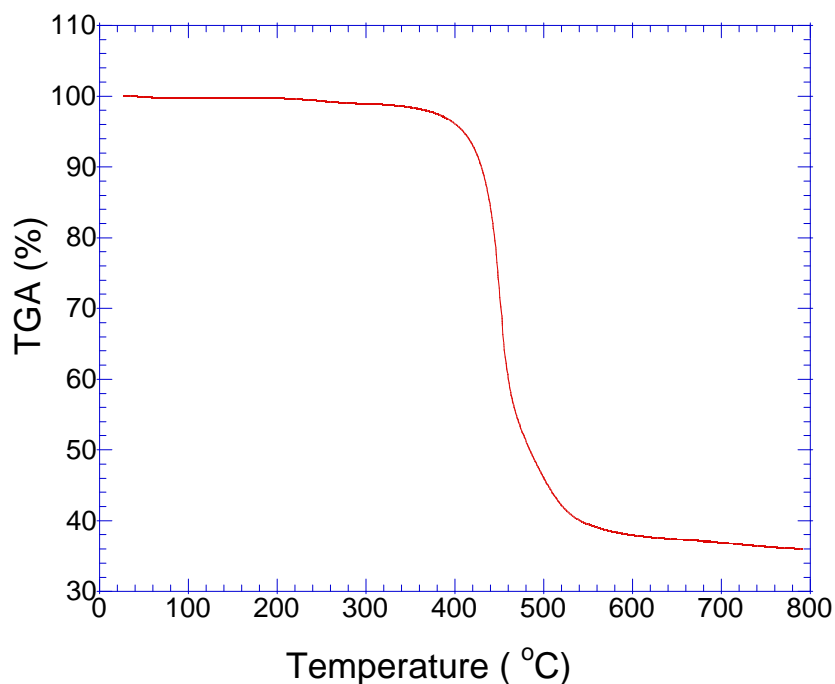
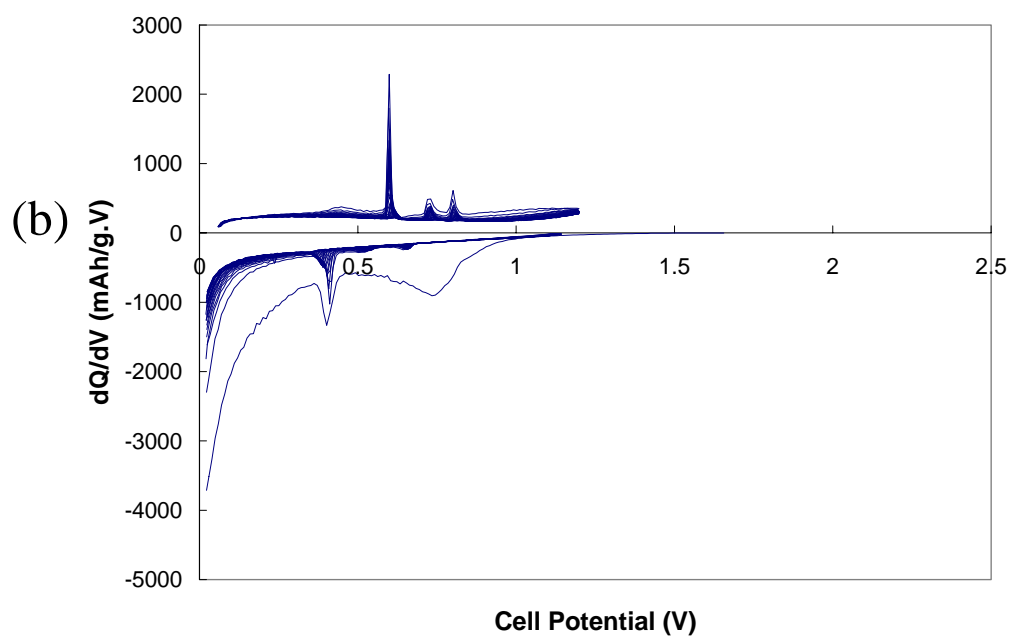
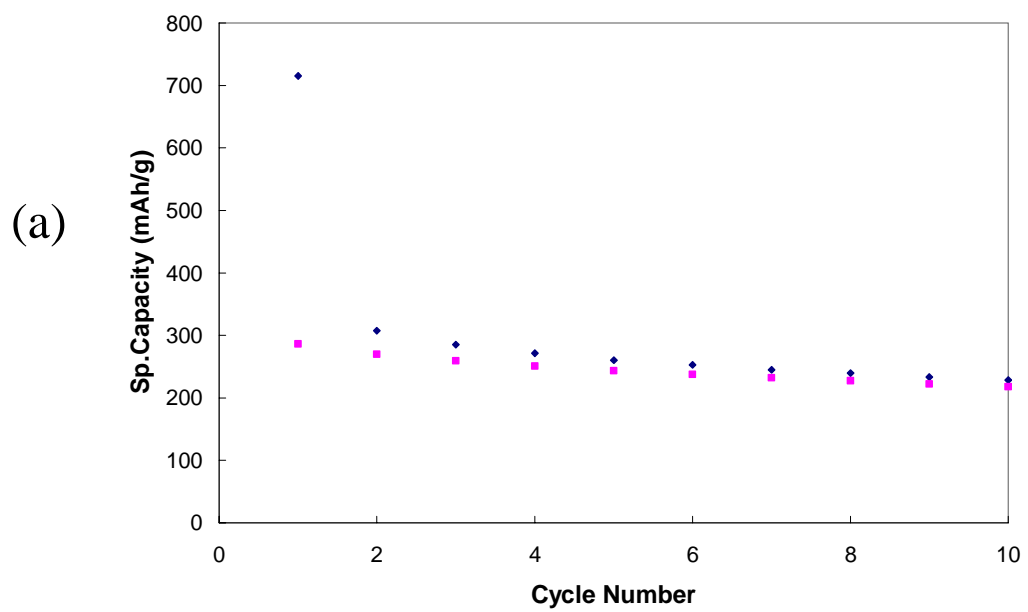


Fig. 5-55 The TGA analysis of the PS-resin in UHP-Ar showing the formation of carbon.



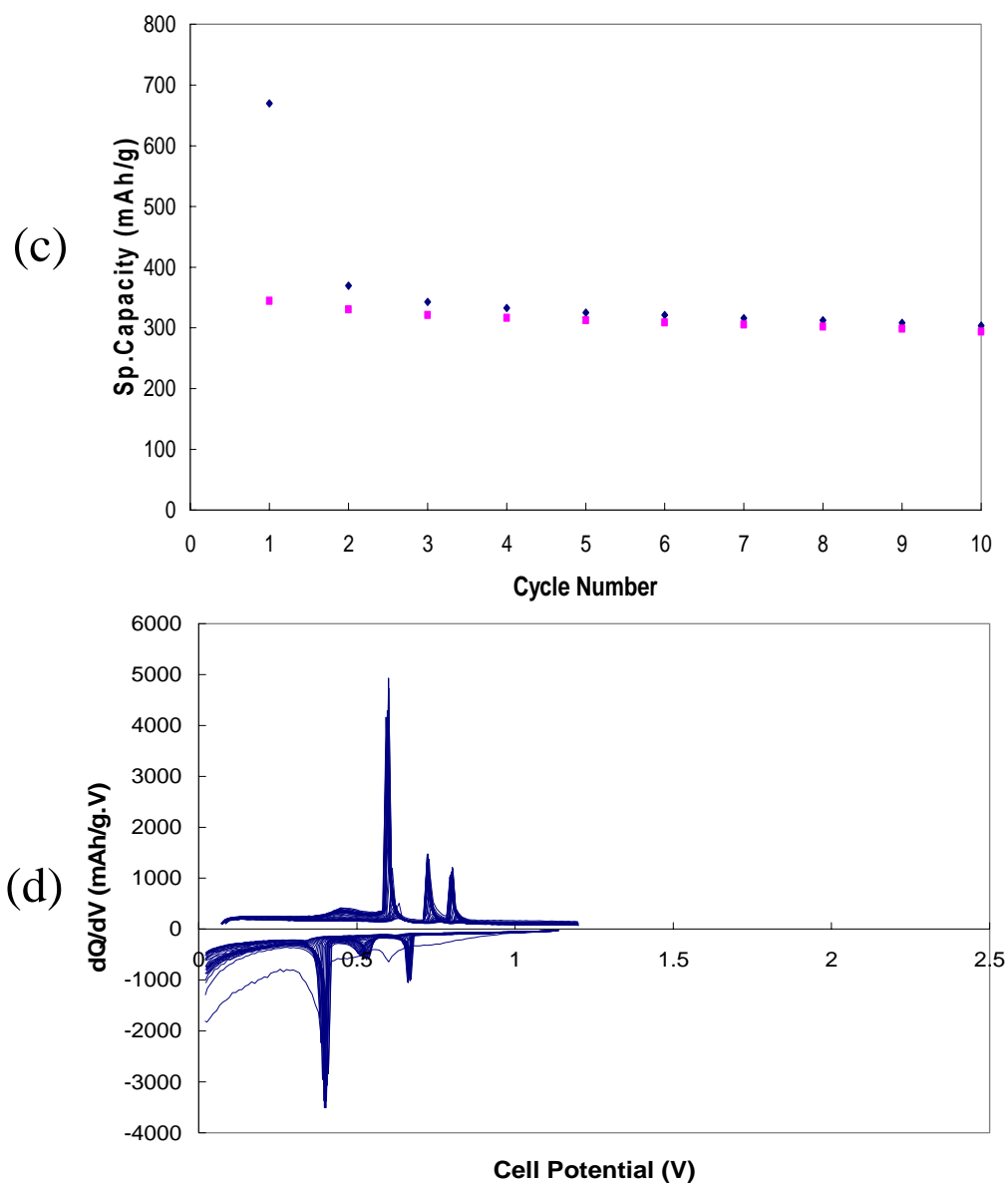


Fig. 5-56 Capacity as a function of cycle number for Sn/C nanocomposites obtained from (a)  $\text{Sn}_2\text{Cl}_4 \cdot 5\text{H}_2\text{O}$  + PS-resin beads and (b) corresponding differential capacity plot; (c)  $\text{Sn}_2\text{Cl}_4 \cdot 5\text{H}_2\text{O}$  + mechanically milled PS-resin powder and (d) corresponding differential capacity plot, respectively. Both nanocomposites were obtained after heat treatment for 5 h in UHP-Ar at  $800^\circ\text{C}$ . (Current rate :  $100\mu\text{A}/\text{cm}^2$ , Potential : 0.02~1.2 V)

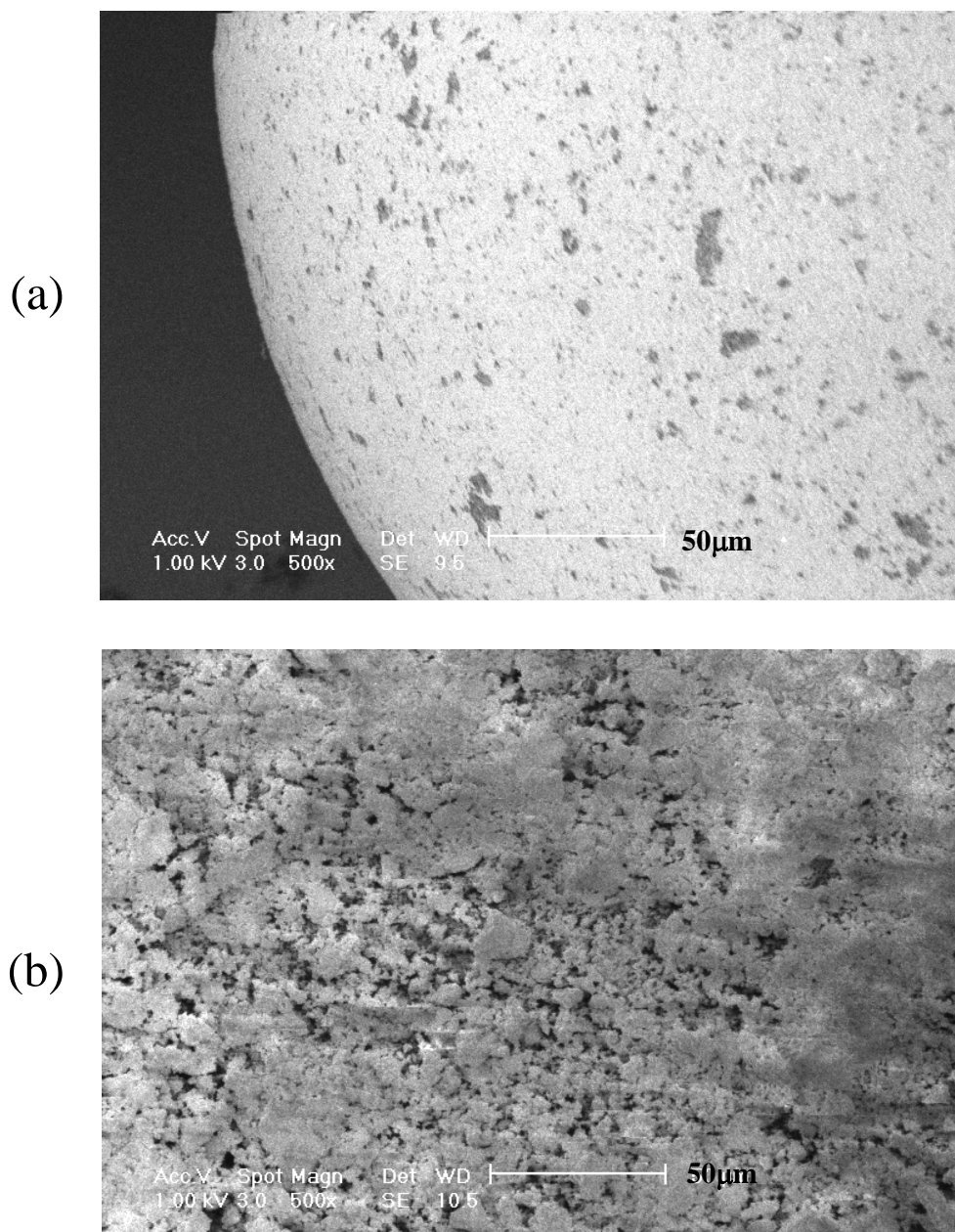
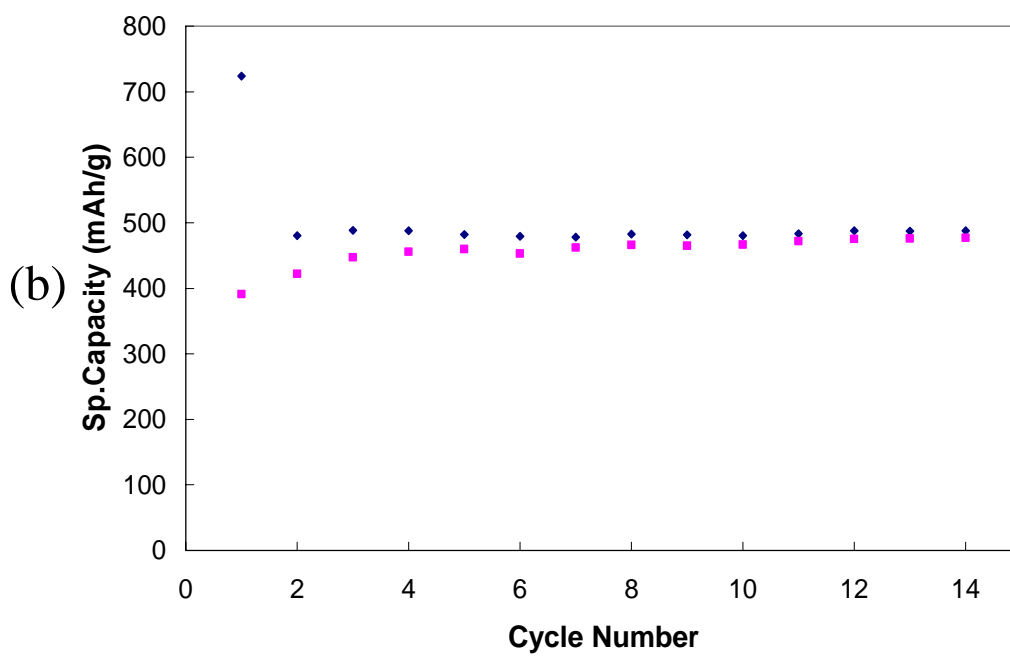
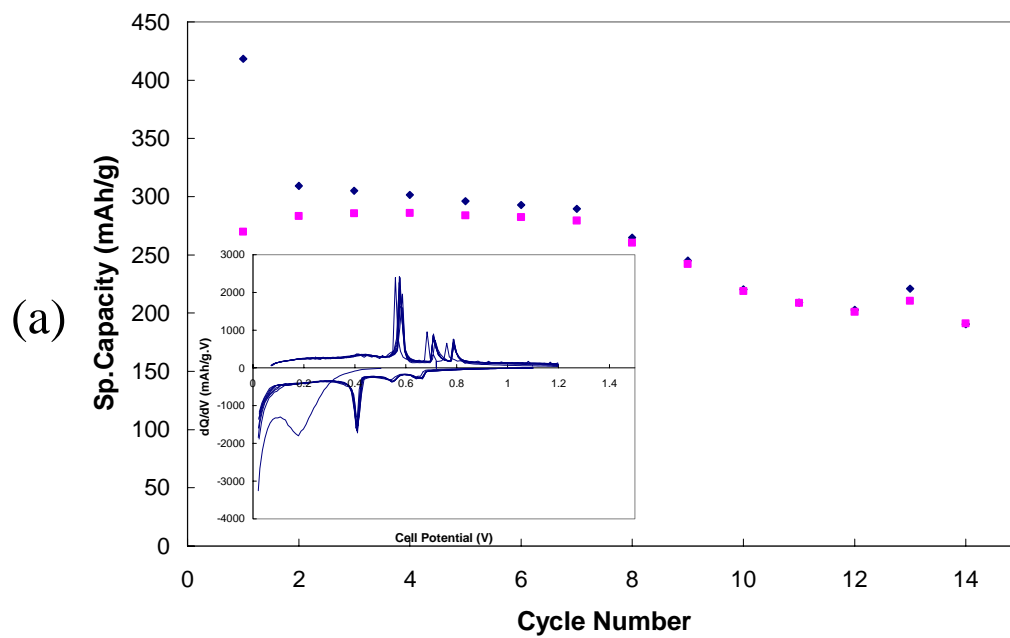


Fig. 5-57 SEM micrographs showing pores in (a) PS-resin beads and (b) mechanically milled PS-resin powder. Note the density of pores is higher in the case of PS-resin powder obtained after mechanical milling for 30 min.



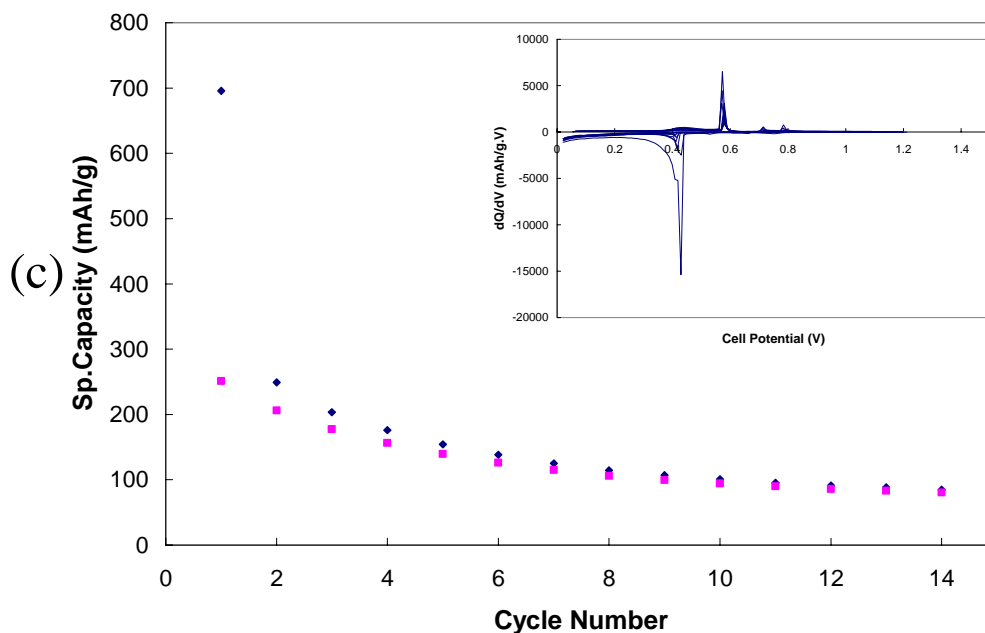


Fig. 5-58 Capacity as a function of cycle number for Sn/C nanocomposites corresponding to a Sn:C =1:1 composition obtained from mechanically milled PS-resin powder infiltrated with (a) tetramethyl tin, (b) tetraethyl tin, and (c) tetra-n-octyl tin, respectively, followed by pyrolysis for 5 h in UHP-Ar at 600°C. The insets show the differential capacity vs. cell potential plots for each of the nanocomposites. (Current rate : 100 $\mu$ A/cm<sup>2</sup>. Potential : 0.02~1.2 V)

### 2. Phase Evolution and Microstructure of Sn/C nanocomposites

The Thermogravimetric analysis of the precursor (27.1mg) obtained after infiltrating tetraethyl tin into the fine PS-resin powder has been conducted to investigate the decomposition of tetraethyl tin and PS-resin in UHP-Ar atmosphere using a heating rate 10°C/min and a flow 100ml/min. As seen in Fig. 5-59, there are two significant weight losses, seen at ~100°C and ~400°C, respectively. The first weight loss corresponds to the decomposition of tetraethyl tin and the second one is attributed to the decomposition of the PS-resin. Although the boiling point of tetraethyl tin is 181°C, the decomposition appears to commence at a lower temperature. The nominal composition of Sn/C nanocomposite is Sn:C=1:1, calculated based on the molecular formula of tetraethyl tin. Since PS-resin does not change its mass up to 200°C as shown in Fig. 5-55, the first weight loss is attributed to the removal of four ethyl groups from the tetraethyl tin. Based on the TGA result, the approximate actual composition of the Sn/C nanocomposite obtained after heat-treatment at 600°C is Sn:C=1:5.56. This therefore indicates that the amount of tin is much less than the initial nominal composition (Sn:C=1:1) since tin can be lost by evaporation during decomposition or subsequent heat-treatment.

Result of XRD analysis of the Sn/C nanocomposite obtained after heat-treatment at 600°C is shown in Fig. 5-60. The sharp peaks in the spectra correspond to the crystalline tin phase while carbon essentially remains amorphous. However, the broad peaks shown around ~24° and ~44° correspond to (100) and (110) planes of carbon single layer, which are not stacked in a parallel manner as in graphite [57, 59]. The mono graphene layers in the composite may contribute to the overall capacity by providing reversible sites for Li intercalation.

In order to investigate the microstructure of the Sn/C nanocomposite obtained after heat-treatment for 5h at 600°C in Ar, bright field image and its selected area diffraction pattern (SADP) were taken using TEM shown in Fig. 5-61. The dark spherical regions in the BF image correspond to tin particles with a size of ~200nm embedded inside a large carbon particle ( $\cong 2 \sim 10 \mu\text{m}$ ). The SADP pattern corresponds to metallic tin. The microstructure shown in the micrograph is also indicative of the mechanisms leading to the formation of the Sn/C nanocomposite during heat-treatment.

It appears that tetraethyl tin decomposes first to form metallic tin, which then deposits on the surface of PS-resin powder. At higher temperatures during pyrolysis, the PS-resin powder decomposes and agglomerates to generate the specific microstructure shown in Fig. 5-61 (a). Since Sn particles are embedded within the thick carbon particle, it is very difficult to image the tin particles. However, the SADP (Fig. 5-61 (b)) consisting of spots and diffused halos clearly suggest that crystalline tin particles coexist within the amorphous carbon particles. The SADP analysis therefore validates the XRD results.



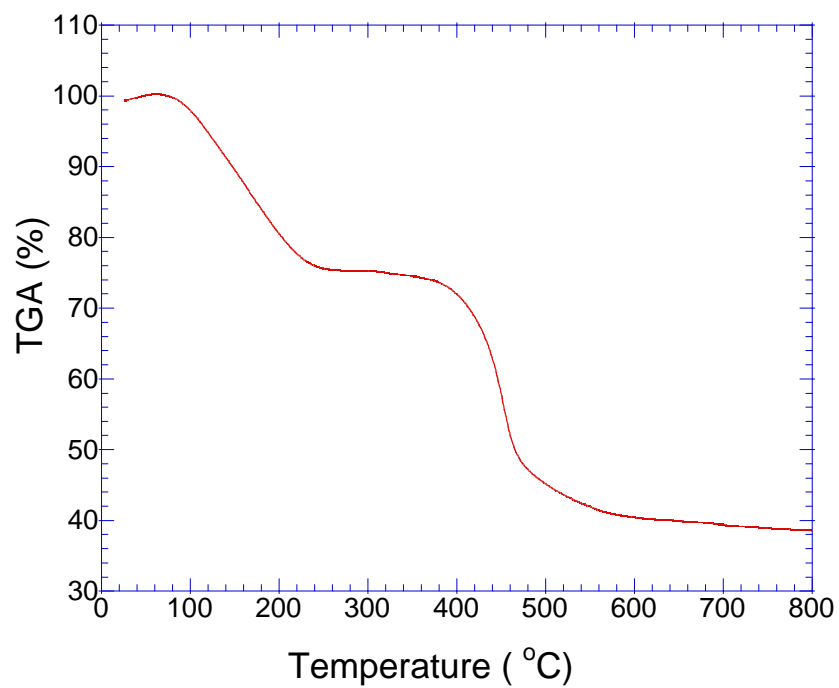


Fig. 5-59 The TGA analysis of the precursor obtained from PS-resin infiltrated with tetraethyl tin corresponding to the composition of Sn:C=1:1 in UHP-Ar using a heating rate of 10°C/min.

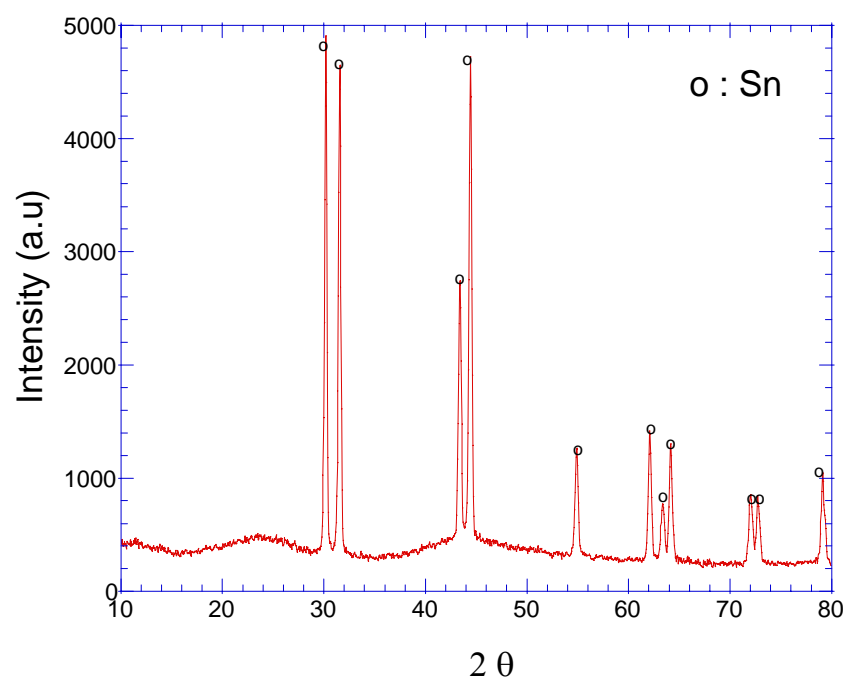
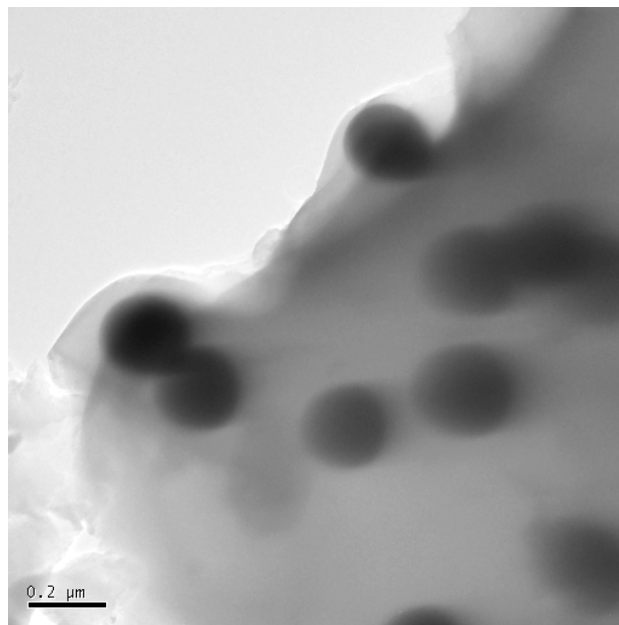
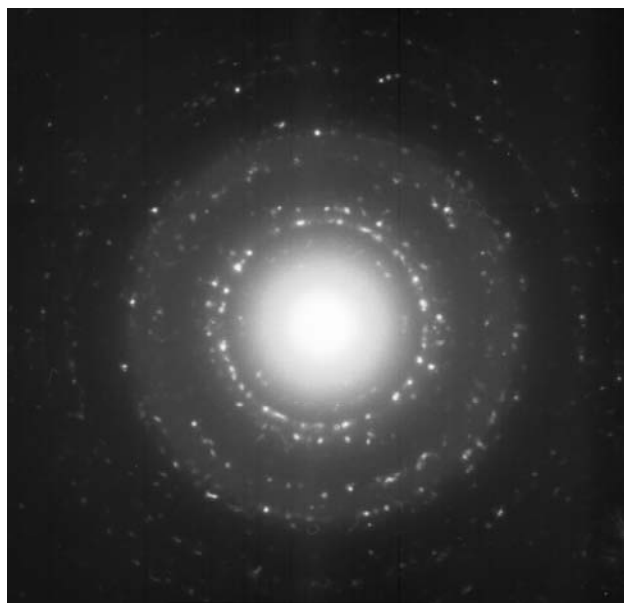


Fig. 5-60 X-ray diffraction pattern of Sn/C nanocomposite obtained from PS-resin infiltrated with tetraethyl tin corresponding to a composition of Sn:C=1:1, after heat treatment for 5 h in UHP-Ar at 600 °C.



(a)



(b)

Fig. 5-61 TEM micrographs of the Sn/C nanocomposite obtained from PS-resin infiltrated with tetraethyl tin corresponding to a composition of Sn:C=1:1 after heat treatment for 5 h in UHP-Ar at 600 °C; (a) BF image, (b) SA diffraction pattern (camera length = 61cm, reduced to 40% of its original size).

### 3. Electrochemical Response of the Sn/C Nanocomposite

The Sn/C nanocomposite derived from the PS-resin powder infiltrated with tetraethyl tin after heat-treatment at 600°C for 5h in Ar has been analyzed for its electrochemical properties using a current rate of 100  $\mu\text{A}/\text{cm}^2$  ( $\cong$  C-rate of C/13). The capacity vs. cycle number of Sn/C nanocomposites is exhibited in Fig. 5-62, (a). The nominal composition used for synthesizing the composite corresponds to Sn:C=1:1, although the actual composition is 1:5.56 determined from the TGA result as discussed in the previous section. Based on the actual composition, the theoretical capacity of the composite should be 636mAh/g considering that the capacity is only associated with tin in the composite, which is slightly lower than the first discharge capacity ( $\sim$ 718 mAh/g) shown in the plot. However the carbon derived from PS-resin pyrolyzed at 600 °C for 5 h in UHP-Ar also exhibits an initial discharge capacity of 750 mAh/g although a stable capacity  $\sim$ 300 mAh/g is ultimately realized according to our preliminary result (see Fig. 5-63 (a)). There are no peaks in the differential capacity plot obtained from the carbon (see Fig. 5-63 (b)), indicating the amorphous nature of the carbon. Thus the overall capacity is likely to originate from carbon as well as tin. It can be mentioned that the capacity of the Sn/C nanocomposite derived from tetraethyl tin is less than the sum of the theoretical capacity and the capacity contributed from carbon although the contribution from carbon cannot be determined exactly. The reason for the discrepancy between the actual and the estimated capacity is not clear at this moment, however partial embedding of Sn inside the large carbon particles appears to be one of the causes of this difference. The first irreversible loss of the nanocomposite appears to be caused by carbon since a similar trend is seen when the pyrolyzed carbon is electrochemically tested as shown in Fig. 5-63. The irreversible loss in carbon materials may be caused by disordered carbon structure seen in amorphous carbon [58] or the presence of hydrogen attach to carbon that is also common in carbon derived from resins [57, 59].

The Sn/C nanocomposite electrode exhibits a gravimetric capacity of  $\sim$ 480mAh/g with a good capacity retention (0.15%loss/cycle), which is equivalent to 1450 Ah/l in volumetric capacity. This capacity is significantly higher ( $\cong$  75%) than that of carbon as indicated in the plot. The result supports the TEM result, that the Sn

particles are homogeneously dispersed within the carbon particle, which leads to good capacity retention. However, the embedment of tin within the carbon matrix may also be the reason for the observed lower discharge capacity compared to its theoretical capacity.

Fig. 5-62 (b) shows the differential capacity of the Sn/C nanocomposites obtained after heat-treatment at 600°C for 5h in Ar. The sharp peaks during charge and discharge processes are attributed to the nanocrystalline tin in the composite. Although there are no peaks related to the carbon, the background is caused by carbon, indicating that carbon also contributes to the overall capacity. The peak intensity does not change during cycling, which suggests the good cyclability of the nanocomposite. It can be concluded based on this result that this Sn/C nanocomposite prepared from the tetraethyl tin and PS-resin powder is very promising for use as anode in Li-ion application and there is clearly a need for optimization. This will be a part of the future studies recommended.

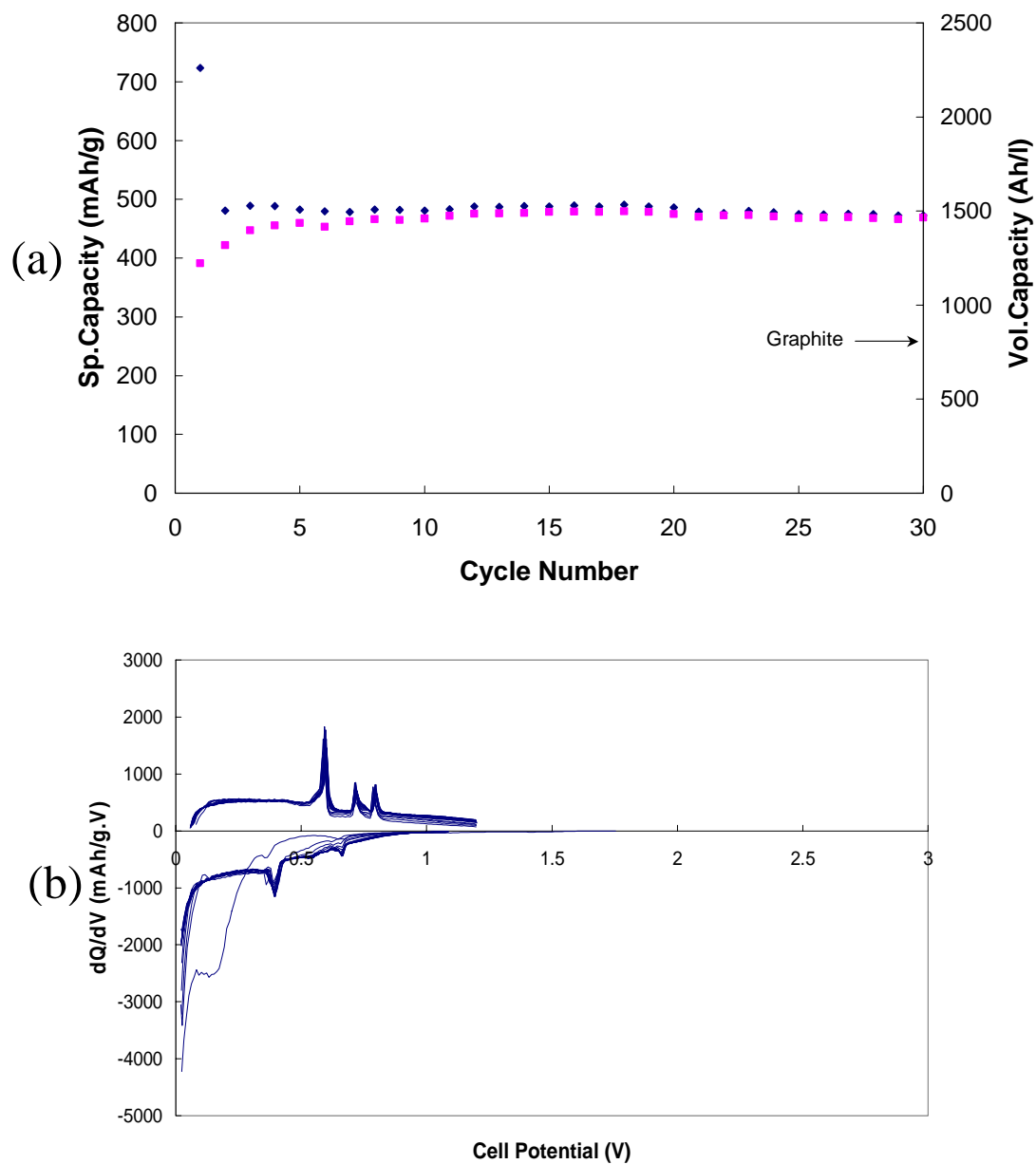


Fig. 5-62 (a) Plots of capacity as a function of cycle number, (b) Differential capacity vs. cell potential curves obtained from the PS-resin infiltrated with tetraethyl tin corresponding to the composition of Sn:C=1:1 after heat treatment for 5 h in UHP-Ar at 600 °C. (Current rate :  $100\mu\text{A}/\text{cm}^2$ , Potential : 0.02~1.2 V)

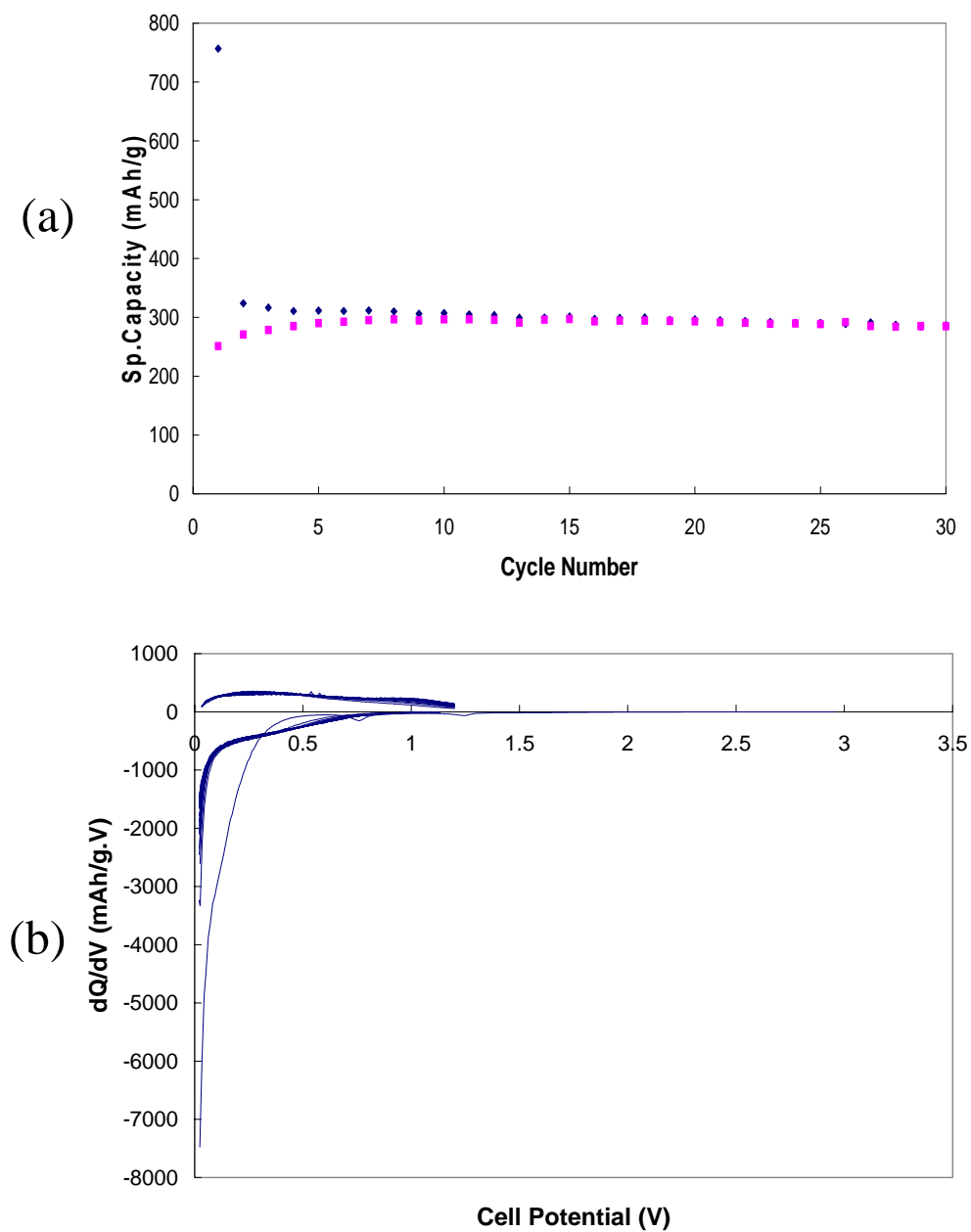


Fig. 5-63 (a) Plot of capacity as a function of cycle number (b) Differential capacity vs. cell potential curves obtained from the carbon obtained after heat-treatment of PS-resin at 600°C for 5h in Ar. (Current rate : 100 $\mu$ A/ cm<sup>2</sup>, Potential : 0.02~1.2 V).

**References**

1. O. Mao, R. A. Dunlap, and J. R. Dahn, *J. Electrochem. Soc.*, 146, 405 (1999).
2. D. B. Williams and C. B. Carter in *Transmission Electron Microscopy*, p. 655, (Plenum Press, NY, 1996).
3. B. D. Cullity in *Elements of X-ray Diffraction*, Second Ed., p. 284, (Addison-Wesley, MA, 1978).
4. R. Ren, Z. Yang and L. L. Shaw, *J. Amer. Ceram. Soc.*, 85, 819 (2002).
5. L. L. Shaw, Z. Yang and R. Ren, *J. Amer. Ceram. Soc.*, 85, 709 (2002).
6. E. Eskandarany, M. S. Suniyama and K. Suzuki, *J. Mater. Res.*, 10, 659 (1995).
7. C. Suryanarayana, *Prog. Mater. Sci.*, 46, 1 (2001).
8. I. Kim and P. N. Kumta, Carnegie Mellon University, unpublished work, (1999).
9. *Handbook of Thin Film* ed by L. I. Maissel and R. Glang, McGraw-Hill, Inc., New York, pp. 13-6~13-7, 1970.
10. W. J. Kim, M. Taya, K. Yamada and N. Kamiya, *J. Appl. Phys.*, 83, 2593 (1998).
11. T. Graziani and A. Bellosi, *J. Mater. Sci.*, 14, 1078 (1995)
12. D. S. Bem, H. P. Olsen and H-C zur Loye, *Chem. Mater.*, 7, 1824 (1995).
13. D. S. Bem, C. M. L-Onnerud, H. P. Olsen and H-C. zur Loye, *Inorg. Chem.*, 35, 581 (1996).
14. G. Liu, X. Zhao and H. A. Eick, *J. Alloys Compounds*, 187, 145 (1992).
15. K. Dokko, M. Umeda, Y. Fujita, M. Mohamedi, I. Uchida and J. R. Selman, *Electrochim. Acta*, 47, 933 (2001).
16. M. Umeda, K. Dokko, Y. Fujita, M. Mohamedi, I. Uchida and J. R. Selman, *Electrochim. Acta*, 47, 885 (2001).
17. A. Mohamedi, S. Lee, D. Takahashi, M. Nishizawa, T. Itoh and I. Uchida, *Electrochim. Acta*, 46, 1161 (2001).
18. C. Wang, A. J. Appleby and F. E. Little, *Electrochim. Acta*, 46, 1793 (2001).
19. G. J. Brug, A. B. D. Eeden, M. S-Rehbach and J. H. Sluyters, *J. Electroanal. Chem.*, 176, 275 (1984).
20. A. Lasia, *J. Electroanal. Chem.*, 397, 27 (1995).
21. M. Mohamedi, S-J. Lee, D. Takahashi, M. Nishizawa, T. Itoh and I. Uchida, *Electrochimica Acta* 46, 1161 (2001).



22. H. Li, X. Huang and L. Chen, *J. Power Sources*, 81-82, 340 (1999).
23. J. R. MacDonald, *Impedance Spectroscopy: Emphasizing Solid Materials and Systems*, (John Wiley & Sons Inc., New York, 1987).
24. 'Zview for Windows' Operating Manual ver. 2.2, (Scribner Associates Inc., Southern Pines, 2000).
25. C. Ho, I. D. Raistrick and R. A. Huggins, *J. Electrochem. Soc.*, 127, 343 (1980).
26. I. Rubinstein, J. Rispon and S. Gottesfeld, *J. Electrochem. Soc.*, 133, 729 (1986).
27. M. D. Levi, G. Salitra, B. Markovsky, H. Teller, D. Aurbach, U. Heider and L. Heider, *J. Electrochem. Soc.*, 146, 1279 (1999).
28. A. Anami, S. C-Baker, and R. A. Huggins, *J. Electrochem. Soc.*, 134, 3098 (1987).
29. J. G. Li, *J. Mater. Sci. Lett.*, 11, 903 (1992).
30. P. G. de Gennes, *Rev. Mod. Phys.*, 57, 827 (1985).
31. P. Xiao and B. Derby, *Acta Mater.*, 44, 307 (1996).
32. P. C. Hiemenz and R. Rajagopalan, *Principles of Colloid and Surface Chemistry*, 3<sup>rd</sup> ed., (Marcel Dekker, Inc., New York, 1997).
33. Y. V. Naidich and N. Y. Taranets, *J. Mater. Sci.*, 33, 3993 (1998).
34. J. G. Li and H. Hausner, *Mater. Lett.*, 14, 329 (1992).
35. N. Eustathopoulos, M. G. Nicholas and B. Drevet, *Wettability at High Temperature*, (Pergamon, Amsterdam, 1999).
36. M. Marlo and V. Milman, *Phys. Rev. B*, 62(4), 2899 (2000).
37. O. Mao, R. L. Turner, I. A. Courtney, B. D. Fredericksen, M. I. Buckett, L. J. Krause and J. R. Dahn, *Electrochem. Solid-State Lett.*, 2, 3 (1999).
38. O. Mao and J. R. Dahn, *J. Electrochem. Soc.*, 146, 405 (1999).
39. O. Mao and J. R. Dahn, *J. Electrochem. Soc.*, 146, 414 (1999).
40. O. Mao and J. R. Dahn, *J. Electrochem. Soc.*, 146, 423 (1999).
41. K. D. Kepler, J. T. Vaughey and M. M. Thackeray, *Electrochem. Solid-State Lett.*, 2, 307 (1999).
42. J. Yang, , M. Wachtler, M. Winters and J. O. Besenhard, *Electrochem. Solid-State Lett.*, 2, 161 (1999).

43. G. M. Ehrlich, C. Durand, X. Chen, T. A. Hugener, F. Spiess and S. L. Suib, J. Electrochem. Soc., 147, 886 (2000).
44. M. Christianson, D. Price and R. Whitehead, J. Organomet. Chem., 102, 273 (1975).
45. E. Borsella, A. Nesterenko and R. Larciprete, Chem. Phys. Lett., 199, 605 (1992).
46. . J. C. Remy and J. J. Hantzpergue, Thin Solid Films, 30, 197 (1975).
47. R. S. Lima, P. H. Dionisio and W. H. Schreiner, Solid State Comm., 79, 395 (1991).
48. F. A. Cotton and G. Wilkinson, Advanced Inorganic Chemistry, 5<sup>th</sup> ed., (Wiley, New York, 1988).
49. S. E. Hayes, H. Eckert and W. R. Even Jr, J. Electrochem. Soc., 146, 2435 (1999).
50. K. R. Zavadil, A. R. Guidotti and W. R. Even Jr, MRS Symposium Proceedings, 496, 539 (1998).
51. K. F. Purcell and R. S. Drago, J. Am. Chem. Soc., 88, 919 (1996).
52. M. A. Sriram, P. N. Kumta and E. I. Ko, Chem. Mater. 7, 859 (1995).
53. N. Grassie, I. C. McNeill, J. Polymer Sci., 33, 171 (1958).
54. B. B-Garcia, F. J. B-Barros, F. J. H-Rolando, A. M. P-Galn and C. V-Calahorro, Thermochemica Acta, 339, 95 (1999).
55. T. S. Ong and H. Yang, J. Electrochem. Soc., 149, A1 (2002).
56. Z. Wang, X. Huang and L. Chen, J. Power Sources, 81-82, 328 (1999).
57. T. Zheng, Q. Zhong and J. R. Dahn, J. Electrochem. Soc., 142, L211 (1995).
58. M. Noel and V. Suryanarayanan, J. Power Sources, 111, 193 (2002).
59. Y. Liu, J. S. Xue, T. Zheng and J. R. Dahn, Carbon 34, 193 (1996).
60. Technical Data, The Purolite co., Bala Cynwyd, PA 19004
61. J. L. Margitfalvi, I. Kolosova, E. Talas and S. Gobolos, Appl. Cata. A, 154 L1 (1997).
62. J. L. Margitfalvi, I. Borbath, M. Hegedus and A. Tompos, Appl. Cata. A, 229, 35 (2002).